Modeling Plasmas with Strong Anisotropy, Neutral Fluid Effects, and Open Boundaries

Eric T. Meier

A dissertation submitted in partial fulfillment
of the requirements for the degree of

Doctor of Philosophy

University of Washington

2011

Program Authorized to Offer Degree:
Aeronautics & Astronautics

University of Washington
Graduate School

This is to certify that I have examined this copy of a doctoral dissertation by

Eric T. Meier

and have found that it is complete and satisfactory in all respects,
and that any and all revisions required by the final
examining committee have been made.

Chair of the Supervisory Committee:

_____
Uri Shumlak

Reading Committee:

_____
Uri Shumlak

_____
Thomas R. Jarboe

_____
Richard D. Milroy

Date: _____

In presenting this dissertation in partial fulfillment of the requirements for the doctoral degree at the University of Washington, I agree that the Library shall make its copies freely available for inspection. I further agree that extensive copying of this dissertation is allowable only for scholarly purposes, consistent with "fair use" as prescribed in the U.S. Copyright Law. Requests for copying or reproduction of this dissertation may be referred to Proquest Information and Learning, 300 North Zeeb Road, Ann Arbor, MI 48106-1346, 1-800-521-0600, to whom the author has granted "the right to reproduce and sell (a) copies of the manuscript in microform and/or (b) printed copies of the manuscript made from microform."

Signature________________________________

Date___________________________________

University of Washington

Abstract

Modeling Plasmas with Strong Anisotropy, Neutral Fluid Effects, and Open
Boundaries

Eric T. Meier

Chair of the Supervisory Committee:
Professor Uri Shumlak
Aeronautics & Astronautics

Three computational plasma science topics are addressed in this research: the challenge of
modeling strongly anisotropic thermal conduction, capturing neutral fluid effects in colli-
sional plasmas, and modeling open boundaries in dissipative plasmas. The research efforts
on these three topics contribute to a common objective: the improvement and extension
of existing magnetohydrodynamic modeling capability. Modeling magnetically confined
fusion-related plasmas is the focus of the research, but broader relevance is recognized and
discussed. Code development is central to this work, and has been carried out within the
flexible physics framework of the highly parallel HiFi implicit spectral element code.

In magnetic plasma confinement, heat conduction perpendicular to the magnetic field is
extremely slow compared to conduction parallel to the field. The anisotropy in heat con-
duction can be many orders of magnitude, and the inaccuracy of low-order representations
can allow parallel heat transport to "leak" into the perpendicular direction, resulting in
numerical perpendicular transport. If the computational grid is aligned to the magnetic
field, this numerical error can be eliminated, even for low-order representations. However,
grid alignment is possible only in idealized problems. In realistic applications, magnetic
topology is chaotic. A general approach for accurately modeling the extreme anisotropy
of fusion plasmas is to use high-order representations which do not require grid alignment
for sufficient resolution. This research provides a comprehensive assessment of spectral el-

ement representation of anisotropy, in terms of dependence of accuracy on grid alignment, polynomial degree, and grid cell size, and gives results for two- and three-dimensional cases.

Truncating large physical domains to concentrate computational resources is often necessary or desirable in simulating natural and man-made plasmas. A novel open boundary condition (BC) treatment for such domain truncation, lacuna-based open boundary conditions (LOBC), is presented. LOBC provide effective open BC for dissipative MHD and other hyperbolic and mixed hyperbolic-parabolic systems of partial differential equations. Based on manipulating Calderon-type near-boundary sources, LOBC damp hyperbolic effects in an exterior region attached to the simulation domain, and apply BC appropriate for the remaining parabolic effects (if present) at the exterior region boundary. LOBC and several alternative open BC are tested in gas dynamics and dissipative MHD problems, and their performance is compared. LOBC are found to give stable, low-reflection solutions even in the presence of strong parabolic behavior, while alternative open BC are either highly reflective or unstable.

Only a few specialized computational tools are available for capturing the effects of neutral particles in plasmas. The goal of this research has been to develop and apply a generalized, computationally tractable model based on first principles that serves as a first step toward more sophisticated models. This dissertation presents the derivation of a plasma-neutral fluid model from the Boltzmann equation, allowing for charge exchange, ionization, and recombination. Single-species, singly-ionized plasma and its parent neutral atoms are modeled. Mass, momentum, and energy exchange between the plasma and neutral species are tracked in a numerically stable, conservative implementation. The implementation has been applied to parallel-plate and coaxial plasma acceleration, ion spin-up in field-reversed configuration (FRC) plasmas with rotating magnetic field (RMF) current drive, and the interaction of FRC plasmas with neutral gas in the Electrodeless Lorentz Force (ELF) thruster. ELF simulations are compared with preliminary experimental results.

TABLE OF CONTENTS

LIST OF FIGURES

LIST OF TABLES

ACKNOWLEDGMENTS

I extend my deepest thanks to the many people who have made this research possible. My advisor, Uri Shumlak, has gone above and beyond the call of duty in providing me with inspiration, education, and guidance for this research. Slava Lukin, who was a postdoc with the PSI-Center, has also had a profound positive influence on me, showing me the ropes of computational plasma science. I also appreciate the influence of many Aeronautics and Astronautics (A&A) faculty members and especially: Alan Glasser, who has provided a historically and technically rich view of kinetic theory in plasma science, and has been a wise mentor; Tom Jarboe, the director of the PSI-Center, who has been instrumental in ensuring a practical, experiment-focused approach to this computational research; Richard Milroy, who has been a leading example for me in extracting useful information from computational plasma science tools; and Adam Bruckner, long-time A&A chair, who brought me on board in 2005. Thanks to my fellow graduate students and friends in Seattle for making the last six years such a pleasure. Thanks to Susan Griffith for maintaining our computers and providing always-interesting diversions. Thanks to the Achievement Rewards for College Scientists (ARCS) foundation, and my specific donors, Mr. and Mrs. George Mueller, for the three-year fellowship that they so generously bestowed upon me. Special thanks to my mother, father, and siblings who have been extremely supportive of my career in science and engineering, and in all that I have decided to tackle, and to Anita for being my best friend and a wonderful inspiration in my life.

DEDICATION

To my parents and grandparents

Chapter 1

INTRODUCTION

Motivation for this research is given in Section 1.1. Specific research contributions are summarized in Section 1.2. An overview of the primary computational tool used for the research, the high-order spectral (finite) element code, HiFi [1, 2, 3], is presented in Section 1.3. The research presented in this dissertation is all strongly related to the dissipative magnetohydrodynamics (MHD) model, which is presented in Section 1.4. Section 1.5 introduces a plasma configuration, the field-reversed configuration (FRC), which receives significant attention in this dissertation.

Chapters 2 – 6 present in detail the research contributions summarized in Section 1.2. Prior and foundational research on each topic is presented, and the new research is described in detail. In Chapter 7, the significance of the research contributions is summarized.

1.1 Motivation

Plasma is ubiquitous in the universe. Hundreds of billions of stars in our galaxy alone gravitationally confine plasma, releasing energy through nuclear fusion. Energetic particles escape stellar surfaces, forming plasma that streams into space. The plasma streaming from the Sun, called the solar wind, interacts with the Earth's magnetic field to create a magnetosphere. Erratic behavior of the solar wind disturbs the magnetosphere, causing aurorae (northern and southern lights) and geomagnetic storms [4, 5]. Plasma science improves our understanding of this complex space environment.

Plasma-based technologies are used in a variety of engineering fields. For example, in aerospace engineering, plasma propulsion can be used instead of chemical propulsion to dramatically reduce the propellant mass necessary for a given mission [6]. Plasma has also been harnessed in fluorescent lighting, plasma televisions, and in industrial processes such

as semiconductor manufacturing.

The primary motivation for the work in this dissertation is the prospect of controlled nuclear fusion, which has been under development for over 60 years [7]. Fusion power is attractive because of the abundance of fuel and the low environmental impact of the technology. Fusion energy machines have generated significant fusion power [8], but a commercially viable power plant design has not yet been demonstrated. Over the past century, the energy consumption rate of humanity has grown enormously. Largely, that appetite has been satisfied by burning fossil fuels. There is a growing consensus that unabated growth of fossil-fuel-based energy consumption would be both environmentally and economically hazardous, and alternatives are being sought. (For a thorough discussion of energy-related challenges facing America and the world, see Ref. [9].) The development timeline for commercial fusion power is uncertain, but steady or increased funding could enable commercial fusion power by 2050. Although it is a relatively long-term prospect, fusion has the potential, when it does become available, to be a panacea for world energy problems. Continued interest and funding seem certain.

Improved comprehension of plasma physics phenomena encountered in fusion technology is attained through three interdependent approaches: experimental research, theoretical research, and computational research. Experimental research is critical, of course, because the final goal of the research is a tangible reality that can be produced only through experimentation. Experimental scientists have developed a wide array of tools and techniques to measure plasma behavior, but are still frequently mystified by what they see. Theoretical scientists have developed mathematical models to help unravel some of the mysteries. Some of the models, however, are not amenable to hand calculation. Computer simulations have revolutionized our ability to extract information from theoretical models. Merriam-Webster gives the following definition of simulate: "to give or assume the appearance or effect of, often with the intent to deceive." The goal of simulation is to recreate an interesting physical process on a computer in a way that allows the computational scientist to observe the system behavior at a level of detail that is far beyond that achievable by experimental scientists. The availability of computational power has increased exponentially over the past decades. This enhances our ability to either extract useful information or, as the definition

(unwittingly) suggests, thoroughly deceive ourselves. Efficiently harnessing computational power requires a high degree of ingenuity, theoretical and experimental understanding, and close alliance of computation with theory and experiment.

Improving computational techniques and developing new models for simulating fusion-related plasmas is the basic objective of the research presented in this dissertation, although the work is relevant to plasma propulsion, astrophysical plasmas, and space plasmas in general. The research is conducted as part of the Plasma Science and Innovation Center (PSI-Center) [10], a center funded by the United States Department of Energy to develop predictive simulation capability for plasma science experiments. With predictive capability, the design cycle can be accelerated so that the physics knowledge needed for fusion can be more rapidly and cost effectively revealed.

1.2 Research contributions

The three primary contributions of this research to the field of computational plasma physics are stated briefly below, and are addressed in detail in Chapters 2 – 6.

Contribution 1:

A study has been conducted to quantify the benefits of using a spectral element representation for modeling strongly anisotropic thermal conduction in terms of the total degrees of freedom needed to achieve a desired accuracy, and the effect of grid alignment (and misalignment) with the anisotropy.

Strong anisotropy (especially anisotropic thermal conduction) is present in many plasmas. Earlier research (see Section 2.1) has shown that spectral element spatial representation[1] is effective for modeling the strongly anisotropic thermal conduction. The PSI-Center has chosen to focus development effort on codes that employ spectral elements largely because of this useful quality. Research presented in Chapter 2 builds upon earlier work, providing a thorough analysis of the ability of spectral elements to manage the numerical

---

[1]As discussed in Section 1.3, the terminology "spectral element" will be used interchangeably with "high-order finite element".

challenge of extreme anisotropy in two and three dimensions, while varying the grid orientation with respect to the anisotropy. In addition to the quantitative analysis, the sources of inaccuracy are qualitatively explained.

Contribution 2:

An "open" boundary condition (BC) has been developed that is suitable for modeling nonlinear dissipative MHD using a spectral element spatial discretization.

Boundaries of computational domains frequently represent physical walls. Sometimes, however, computational domain boundaries represent artificial boundaries. For example, to focus computational resources on the edge region of a fusion plasma, an artificial boundary might represent the interface between the edge plasma and the core plasma. Open boundary conditions (BC) are applied at artificial boundaries.

When the dominant physics is hyperbolic, open BC techniques based on characteristic decomposition, an inherently hyperbolic concept, are appropriate. Incoming and outgoing characteristics are treated separately. Such techniques fail when parabolic (dissipative) effects play a significant role. An alternative approach that properly bounds mixed hyperbolic-parabolic problems is presented in this research.

Contribution 3:

A model has been developed for capturing neutral fluid effects in a straightforward extension of the nonlinear dissipative MHD plasma model. Mass, momentum, and energy equations are evolved for separate plasma and neutral fluids, and the effects of ionization, recombination, and charge exchange reactions on plasma density, momentum and energy evolution are captured. This plasma-neutral model can be easily applied to a variety of plasma experiments.

Several aspects of modeling partially ionized plasma present challenges above and beyond those usually associated with MHD modeling. First, an appropriate model must be derived, which accounts for the transactions between species. These transactions involve complicated inelastic collisions[2]. The approach taken in this research is to limit the inelastic

---

[2]Even the stoic Braginskii (known for his pioneering paper about transport processes in plasmas [11]) describes inelastic collision terms as "extremely complicated".

collision types considered — electron-impact ionization, radiative recombination, and resonant charge exchange are allowed — and to limit the states accessible to the particles — only singly charged ions and neutral particles are considered. Furthermore, implementation challenges exist. Explicit time advancement of multiple reacting species is often numerically unstable. Also, many existing codes are specialized (e.g., for dissipative MHD), and cannot be easily modified to accommodate the additional complicated physics of plasma-neutral interaction. The code used for this research, HiFi, is well-suited to meet these implementation challenges. HiFi, described in Section 1.3, uses an implicit time advance which assures numerical stability. Also, the code is designed to facilitate implementation of new physical models like the plasma-neutral model.

1.3 Primary computational tool: HiFi

In 2007, the PSI-Center began using the HiFi code [1, 2, 3]. (Before extension of the code to 3D, it was called SEL.) HiFi is the computational framework in which this research is conducted. This section provides a basic description of the code. Lukin [2] gives a much more detailed description. The simulations discussed in this dissertation are primarily 2D calculations. This 2D research is expected to translate trivially to 3D.

HiFi is a framework for solving general partial differential equations (PDEs). In a "physics" module that is separate from the core numerical solver routines, users can specify any set of equations in flux-source form. For example, an acceptable form is

$$\frac{\partial \mathbf{q}}{\partial t} + \nabla \cdot \mathbb{F}\left(\mathbf{q}, \frac{\partial \mathbf{q}}{\partial \mathbf{x}}\right) = \mathbf{S}\left(\mathbf{q}, \frac{\partial \mathbf{q}}{\partial \mathbf{x}}\right), \tag{1.1}$$

where $\mathbf{q}$ is the vector of variables, the tensor $\mathbb{F}$ is the flux, $\mathbf{S}$ is the source, and t and $\mathbf{x}$ refer to time and space. In the physics module, input variables are defined, equations for the boundary and interior are set, and Jacobians (i.e, derivatives of the boundary or interior fluxes and sources with respect to the variables) are defined.

Appendix A briefly describes how to acquire and compile HiFi, and how to run and postprocess a simulation, using the physics module pn.f as an example. pn.f contains the plasma-neutral model presented in Section 5.3 and derived in Section 5.2.

1.3.1 Spatial discretization

Space is discretized with the spectral element technique [12, 13]. The properties of spectral elements are essentially identical to high-order finite elements. (In this context, the term "spectral" implies high-order representation.) Sometimes spectral elements and high-order finite elements are called hp finite elements, where the h refers to the cell size and the p refers to the degree of the polynomial representation within each cell. hp implies that the options exist to either reduce the cell size or increase the polynomial order to improve resolution. Karniadakis et al. [12] give an overview of spectral element development, which can be summarized as follows: When compared to purely spectral methods, spectral element methods allow discretization of complex geometries with relative ease and a variety of grid adaptation strategies can be accommodated while maintaining the benefits of high-order accuracy. However, as for all high-order methods, implementation is generally more complicated than for low-order methods, and the techniques can be relatively sensitive to boundary condition implementations.

HiFi uses the Jacobi polynomial basis function set $\{\Lambda^i\}$ as shown in Figure 1.1. The basis for 2D representation is found by the tensor product $\{\alpha^k\} = \{\Lambda^i\}\{\Lambda^j\}$. Physical variables U are represented as expansions in this basis set with amplitudes u^i. That is, $U = u^i \alpha^i$. At cell boundaries, the variables have nonlinear variation only tangential to the boundary. Matching the linear basis function amplitudes at cell boundaries ensures C^0-continuity.

As usual for finite element techniques [13, 14], the problem is cast in a variational formulation, known as weak form, which involves integrating the PDE(s) over the domain. The integration requires quadrature points — specific locations at which the physical variable values are computed. Enough quadrature points must be used to yield an accurate integration. Typically, the number of quadrature points (in each direction) must be equal to or greater than the polynomial degree that is chosen.

HiFi uses an adaptive grid generation technique called static rezoning. Unlike adaptive mesh refinement strategies, static rezoning does not subdivide existing grid cells. Instead, the existing cells are concentrated or rarified as required to minimize the error. The name is drawn from the fact that grid generation is done between time steps as necessary rather
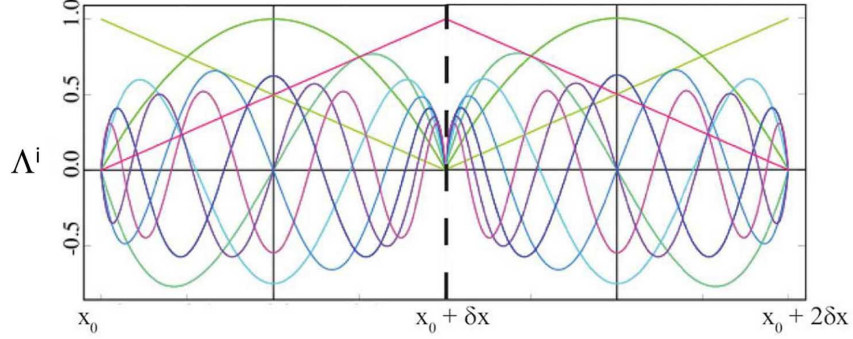
Figure 1.1: A one-dimensional illustration of the Jacobi polynomial basis functions used in HiFi. Two adjacent cells are shown. All but the linear basis functions vanish at cell boundaries. (Credit: V. S. Lukin, A. H. Glasser.)

than simultaneously evolving the grid and the physical variables. (Static rezoning is not employed in the simulations described in this dissertation; it is described here to complete the description of HiFi.)

1.3.2 Time discretization

For the HiFi temporal advance, the user can choose an implicit scheme based on either the θ-method or the second-order backward differencing (BDF2) formula. The second-order non-dissipative Crank-Nicolson method — the θ-method with $\theta = 1/2$ — is used throughout this research. For the θ-method, the system is advanced from time step n to $n + 1$ according to

$$\mathbb{M}\frac{\mathbf{q}^{n+1} - \mathbf{q}^n}{\Delta t} = \theta\mathbf{r}(t^{n+1}, \mathbf{q}^{n+1}) + (1 - \theta)\mathbf{r}(t^n, \mathbf{q}^n), \tag{1.2}$$

where $\mathbb{M}$ is the mass matrix, and $\mathbf{r}$ is the right-hand side of the problem. A Newton-Krylov iterative technique is used to solve this equation for $\mathbf{q}^{n+1}$. For the mth Newton-Krylov iteration, the residual is

$$\mathbf{R}^{m+1} = \mathbb{M}(\mathbf{q}^{m+1} - \mathbf{q}^n) - \Delta t \left[\theta\mathbf{r}(\mathbf{q}^{m+1}) + (1 - \theta)\mathbf{r}(\mathbf{q}^n)\right]. \tag{1.3}$$

The residual is driven to zero (within a user-specified tolerance) iteratively. The solution at the mth iteration is

$$\mathbf{q}^{m+1} = \mathbf{q}^m - \mathbb{J}^{-1}\mathbf{R}^{m+1}. \tag{1.4}$$

The initial guess is $\mathbf{q}^m|_{m=0} = \mathbf{q}^n$. The Jacobian of the iteration is

$$\mathbb{J} = \frac{\partial \mathbf{R}^{m+1}}{\partial \mathbf{q}^{m+1}} = \mathbb{M} - \Delta t\theta\frac{\partial \mathbf{r}(\mathbf{q}^{m+1})}{\partial \mathbf{q}^{m+1}}. \tag{1.5}$$

The Jacobian is inverted using the PETSc [15] software with an appropriate linear solver. PETSc is also used for the nonlinear iteration process. Once the solution $\mathbf{q}^{m+1}$ is found that achieves the required tolerance, the solution at time step $n + 1$ is set as $\mathbf{q}^{n+1} = \mathbf{q}^{m+1}$.

All spatial degrees of freedom in the problem are coupled through the Jacobian. The parallel efficiency of the code is enhanced by employing static condensation to facilitate inverting the Jacobian. Full details of static condensation are available in the dissertation by Lukin [2] and the references therein. Essentially, because of the C^0-continuity of the spatial representation, global coupling results only from the linear basis functions at cell boundaries. This reduced, globally-coupled problem is solved in parallel, and local solves are used to determine the solutions in cell interiors.

1.3.3   Boundary conditions

HiFi allows boundary conditions (BC) that fall into two basic categories: "flux BC" and "explicit local BC".

As shown in Figure 1.1, the solution at the edges of every cell, including boundary cells, is represented by a single linear basis function. Explicit local BC enforce user-chosen boundary condition equations at boundary quadrature points. This dictates the linear basis function amplitudes at the boundary. An example of the explicit local BC is setting a Dirichlet BC on the normal component of velocity: $v_n = 0$.

As mentioned in Section 1.3.1, HiFi solves PDE(s) in weak form. Integrating over the volume,

$$\int_V \left(\frac{\partial \mathbf{q}}{\partial t} + \nabla \cdot \mathbb{F} \right) dV = \int_V \mathbf{S} \ dV. \tag{1.6}$$

Using the divergence theorem,

$$\int_V \frac{\partial \mathbf{q}}{\partial t} dV + \oint_S \mathbb{F} \cdot \hat{\mathbf{n}} \ dS = \int_V \mathbf{S} \ dV, \tag{1.7}$$

where $\hat{\mathbf{n}}$ is the outward-pointing normal unit vector. In Eqn. (1.7), the normal flux ($\mathbb{F} \cdot \hat{\mathbf{n}}$) is integrated over the boundary surface. As the name suggests, the flux BC involves specifying this normal flux at the boundary and including the related term in the integration.

1.4 Dissipative MHD model

The set of equations presented in this section is called the dissipative magnetohydrodynamic (MHD) model and will be referred to frequently in this thesis. Detailed derivations of dissipative MHD are available from various sources [11, 16, 17]. Dissipative MHD can be expressed in terms of a continuity equation, momentum equations, a generalized Ohm's law, and total energy evolution, which can be written, respectively, as

$$\frac{\partial \rho}{\partial t} + \nabla \cdot (\rho \mathbf{v}) = 0, \tag{1.8}$$

$$\frac{\partial}{\partial t}(\rho \mathbf{v}) + \nabla \cdot \left\{ \rho \mathbf{v} \mathbf{v} + \mathbb{I} \left(p + \frac{\mathbf{B}^2}{2\mu_0} \right) - \frac{\mathbf{B}\mathbf{B}}{\mu_0} - \xi[\nabla \mathbf{v} + (\nabla \mathbf{v})^\mathsf{T}] \right\} = 0, \tag{1.9}$$

$$\frac{\partial \mathbf{A}}{\partial t} = \mathbf{v} \times \mathbf{B} - \eta \mathbf{j}, \tag{1.10}$$

$$\frac{\partial e}{\partial t} + \nabla \cdot \left\{ \mathbf{v} \left(e + p + \frac{\mathbf{B}^2}{2\mu_0} \right) - \mathbf{B} \left(\mathbf{B} \cdot \mathbf{v} \right) \right.$$
$$\left. - \left[\kappa_\| \hat{\mathbf{b}}\hat{\mathbf{b}} + \kappa_\perp \left(\mathbb{I} - \hat{\mathbf{b}}\hat{\mathbf{b}} \right) \right] \cdot \nabla T + \eta \mathbf{j} \times \mathbf{B} \right\} = 0, \tag{1.11}$$

where the dependent variables are density (ρ), momentum ($\rho \mathbf{v}$), magnetic vector potential ($\mathbf{A}$), and total energy (e). $\mathbb{I}$ represents the identity tensor. The magnetic field is defined by $\mathbf{B} = \nabla \times \mathbf{A}$, and current density by $\mu_0 \mathbf{j} = \nabla \times \mathbf{B}$. Magnetic vector potential is related to

the electric field by $\mathbf{E} = -\partial\mathbf{A}/\partial t$. Here, $\mathbf{B}^2 = \mathbf{B}\cdot\mathbf{B}$. ξ, η, $\kappa_\parallel$, and $\kappa_\perp$ are coefficients for viscosity, resistivity, parallel thermal conductivity, and perpendicular thermal conductivity, respectively. The definition of total energy is $e = p/(\gamma - 1) + \rho\mathbf{v}^2/2 + \mathbf{B}^2/(2\mu_0)$, where γ is the ratio of specific heats. $\gamma = 5/3$ is used in this work except where explicitly specified. The pressure, p, is defined in terms of e. This pressure represents the sum of ion and electron pressures, which are assumed to be equal.

The dissipative MHD equations are normalized when implemented in HiFi. In the normalized equations, if the dissipation coefficients, ξ, η, $\kappa_\parallel$, and $\kappa_\perp$, shown in Eqns. (1.9) – (1.11) are uniform, they are equivalent to inverse Reynolds, magnetic Reynolds, parallel Péclet, and perpendicular Péclet numbers, respectively. The thermal conductivities are applied parallel or perpendicular to the magnetic field direction defined by $\hat{\mathbf{b}} = \mathbf{B}/|\mathbf{B}|$. For thermal conductivity to remain well defined where the magnetic field magnitude approaches zero, $\kappa_\perp$ must approach $\kappa_\parallel$. For this reason, $\kappa_\perp$ is defined as $\kappa_\perp = \kappa_\perp^m \kappa_\parallel/[(\mathbf{B}/B_0)^2\kappa_\parallel + \kappa_\perp^m]$, where B_0 is the characteristic magnetic field, and $\kappa_\perp^m$ is a "magnetized" value of the perpendicular thermal conductivity. Assuming $\kappa_\parallel \gg \kappa_\perp^m$, this expression for $\kappa_\perp$ has the following useful properties: where $|\mathbf{B}|/B_0 \to 1$, $\kappa_\perp \to \kappa_\parallel$, and where $|\mathbf{B}|/B_0 \approx 1$, $\kappa_\perp \approx \kappa_\perp^m$. Besides having these properties, the expression mimics the behavior of the formulas for perpendicular heat conduction given by Braginskii [11], in the sense that $\kappa_\perp \propto 1/\mathbf{B}^2$. This simple thermal conductivity is useful, but when higher accuracy is needed, parallel and perpendicular thermal coefficients should be calculated with more physically realistic formulas such as those presented by Braginskii [11]. In some of the plasma-neutral model applications of Chapter 6, the Braginskii formulas are, in fact, employed.

In the HiFi implementations of dissipative MHD discussed in this dissertation, artificial dissipation is often employed to reduce numerical noise. The continuity equation with density diffusion proportional to the coefficient D_ρ is

$$\frac{\partial\rho}{\partial t} + \nabla\cdot(\rho\mathbf{v} - D_\rho\nabla\rho) = 0. \tag{1.12}$$

The momentum equation with artificial viscosity proportional to the coefficient ξ_a is

$$\frac{\partial}{\partial t}(\rho\mathbf{v}) + \nabla \cdot \left\{ \rho\mathbf{v}\mathbf{v} + \mathbb{I}\left(p + \frac{\mathbf{B}^2}{2\mu_0}\right) - \frac{\mathbf{B}\mathbf{B}}{\mu_0} \right.$$
$$\left. -\xi[\nabla\mathbf{v} + (\nabla\mathbf{v})^\intercal] - 2\xi_a\mathbb{I} \circ (|\nabla\mathbf{v}| \circ \nabla\mathbf{v}) \right\} = 0, \tag{1.13}$$

where "∘" indicates entrywise tensor multiplication. Appendix B contains a discussion and derivation of this artificial viscosity. These artificial dissipation terms can prevent spurious oscillations (like Gibbs phenomena) and related numerical instabilities in solutions. The coefficients D_ρ and ξ_a are typically set to small values such that artificial dissipation is small compared to the physical dissipation in the system.

Notice that if the magnetic field is zero, the magnetic vector potential evolution is unnecessary and the equations reduce to equations of gasdynamics.

1.5 The field-reversed configuration (FRC)

Because the field-reversed configuration (FRC) plasma confinement method is featured in several simulations presented in Chapters 4 and 6, it is briefly introduced here. Details about the configuration can be found in the review papers by Steinhauer [18] and Tuszewski [19], and in the dissertation by Weber [20], who focuses on the ELF thruster concept presented in Section 6.4, but gives a useful overview of relevant FRC physics and technology. Figure 1.2 shows the flux and pressure of an FRC in the $r - z$ plane. The dashed contour that converges on axis at X-points represents the separatrix, which bounds a region with isolated magnetic topology. Within the separatrix are nested toroidal flux surfaces, one of which is indicated in the figure. The O-point is a field null that occurs in the center of the nested flux surfaces. A useful analogy to the FRC is the Hill's vortex.[3] Where the Hill's vortex has streamlines that confine fluid density, the FRC has closed magnetic field lines that confine hot plasma.

Rotating magnetic field (RMF) current drive [18, 19] is relevant to two of the applications of Chapter 6, and is introduced here. An FRC with RMF current drive is depicted in Figure 1.3. Again, a slice of the FRC in the $r - z$ plane is shown. Curves varying from green to blue

---

[3]A smoke ring is a common example of a Hill's vortex.
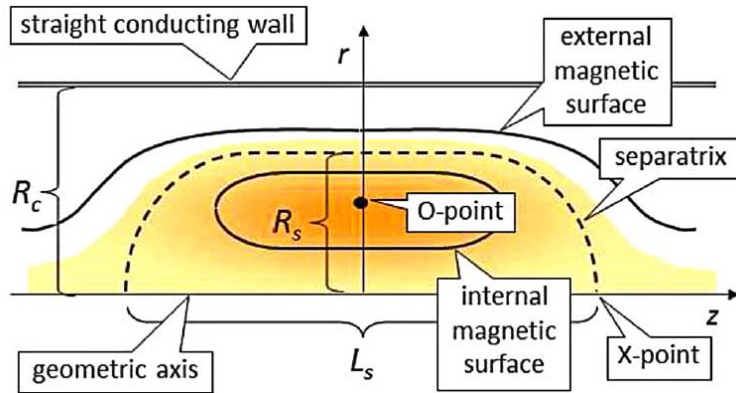
Figure 1.2: Field-reversed configuration schematic. Orange shading indicates pressure. Poloidal magnetic flux is shown in black contours. High plasma pressure is contained by the toroidal flux surfaces. For the purposes of this illustration, the axial ends of the domain may be considered periodic. (Credit: L. C. Steinhauer [18])

are within the separatrix and represent nested toroidal flux surfaces. The rotating magnetic field (RMF) is imposed at a rotation frequency that couples strongly with electrons and weakly with ions, driving current. RMF current drive can be used to form FRCs and to sustain FRC current no matter how the FRC was formed.

The simulations of Chapters 4 and 6 that feature FRCs require appropriate initial conditions. In particular, FRCs in MHD equilibrium (or "quasi-equilibrium" as discussed below) are initialized. These FRC equilibria are generated with a Grad-Shafranov (G-S) solver developed by Marklin [22]. An exceptional feature of the Marklin G-S solver is that it allows user specification of the axial position of the separatrix. The pressure in equilibria generated with the Marklin G-S solver is modified in a way that warrants explanation. In MHD equilibrium, pressure is a function of flux. Between the separatrix flux value and the wall flux value, pressure in a typical equilibrium might vary from a non-zero value to zero (or to a constant with respect to flux).[4] In this case, the equilibrium pressure and associated

---

[4]In a realistic FRC, the pressure and pressure gradient are non-zero outside the separatrix. In fact, cross-field heat flux is always present, causing pressure on the open field lines near the separatrix.
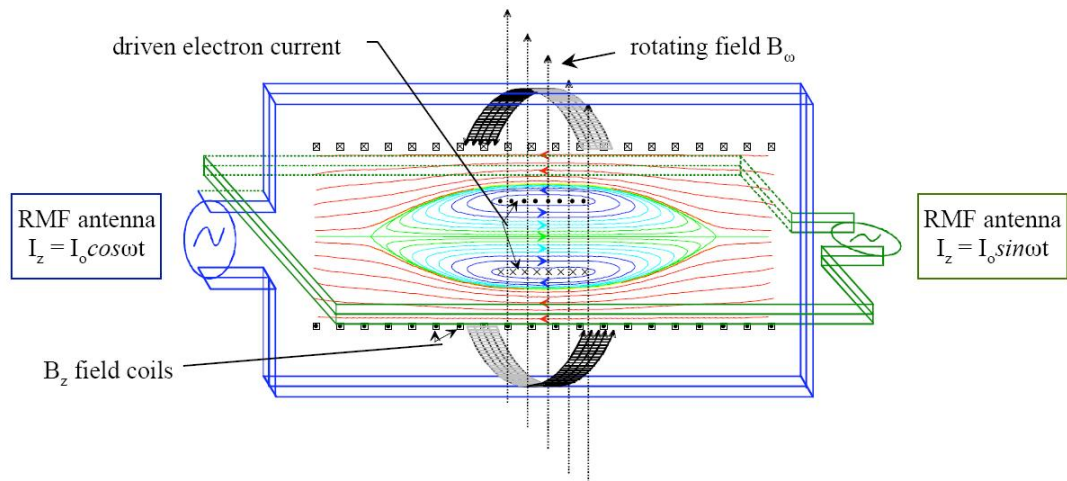
Figure 1.3: FRC with rotating magnetic field (RMF) current drive. The field rotates as indicated, causing electron rotation and, if ions are relatively still, driving net current. (Credit: A. Hoffman [21])

pressure gradient outside the separatrix would extend on the open field lines to the axial ends of the computational domain of the G-S solver. If an isolated FRC is desired, this pressure gradient on the open field lines should be truncated. To achieve this truncation, the solver has been specialized so that the equilibrium pressure can be ramped from the usual G-S solution to zero (or a constant with respect to flux) over a user-specified axial range. If the pressure is truncated in this way, the initial condition is not an ideal MHD equilibrium. Equilibria truncated in this way will be referred to as quasi-equilibria.

Chapter 2

MODELING ANISOTROPY WITH SPECTRAL ELEMENTS

In magnetically confined plasma, charged particles travel easily parallel to the magnetic field lines that form nested magnetic surfaces, while their perpendicular motion is restricted. Thus, strongly anisotropic behavior is a signature property of magnetically confined plasma. In these systems, characteristic rates of heat conduction parallel and perpendicular to the local magnetic field direction can differ by as many as nine orders of magnitude [23]. In computational simulations, any spurious leakage of parallel heat flow into the perpendicular direction inhibits predictive capabilities. When modeling anisotropic behavior with low-order spatial discretization schemes, prohibitively high spatial resolution is often required to achieve the desired degree of accuracy. Local grid alignment with the principal axis of anisotropy dramatically reduces resolution requirements [24]. However, in systems where the field dictating the anisotropy is topologically complex, only approximate grid alignment is possible and solution representations with exponential spatial convergence rates may be necessary. As shown below, spectral element spatial representation can be used to accurately model this anisotropy, even without grid alignment, while minimizing computational expense.

A study has been conducted to assess the accuracy of numerical solutions of a highly anisotropic thermal diffusion equation using the spectral element spatial discretization method, with attention to the effects of the overall spatial resolution, polynomial degree, and computational grid directionality. (Note that this research has been published earlier in somewhat condensed form [25].) It is shown that, for a given number of spatial degrees of freedom, increasing polynomial degree while reducing the number of elements results in exponential reduction of numerical error. Alignment of the grid with the principal direction of anisotropy is shown to further improve the accuracy of the solution. These effects are qualitatively explained and numerically quantified in 2- and 3-dimensional calculations with

straight and curved anisotropy.

Section 2.1 provides relevant background information. Section 2.3 describes the test problems used. In Section 2.4, an analytical basis is developed for interpreting the results, which are presented in Section 2.5.

2.1 Prior and foundational work

Modeling in the presence of significant anisotropy is required in a variety of fields including image processing [26], electromagnetics [27], medical imaging [28], geological science [29], and plasma science [23]. Earlier research on modeling anisotropic behavior has recognized the benefits of high-order elements. For example, Sovinec et al. [23] successfully employ high-order finite elements to compute nonlinear tearing mode evolution, which involves complex magnetic topology and strong anisotropy. As discussed by Kreiss [30], increasing element order allows a reduction of total degrees of freedom to reach a given accuracy, and can often lead to an improvement of overall computational efficiency.

Special methods have been proposed to allow low-order elements to accurately capture anisotropic behavior — see Günter et al. [31], for example. However, the present research concentrates on a computational framework that is broadly applicable.

There are two aspects of extremely anisotropic thermal diffusion that are beyond the scope of this research, but are nevertheless important to consider here: 1) extremely high parallel heat conduction is generally associated with extremely low collisionality, and the associated closure is non-local; 2) so-called "positivity" is not necessarily preserved in general high-order implementations as presented in this research — i.e., heat can be transported "uphill" from regions of low temperature to regions of high temperature, violating the second law of thermodynamics and possibly causing negative temperatures. The first issue is considered in detail in work by Held and Ji [32, 33]. The second issue is addressed, for instance, by Sharma [34]. In recent work, del-Castillo-Negrete and Chacón [35] present a novel approach for addressing non-local closures, positivity, and the basic problem addressed in this research of spurious perpendicular heat transport in the presence of extreme anisotropy, especially in the presence of chaotic magnetic field where field-aligned grids are not feasible. A drawback of the approach presented by del-Castillo-Negrete and Chacón is

that it is applicable only when perpendicular thermal heat conduction is zero (or sufficiently close to zero relative to the parallel conduction).

2.2   Thermal diffusion model

The equation studied is the thermal diffusion equation,

$$\frac{\partial T}{\partial t} + \nabla \cdot (-\mathbb{D} \cdot \nabla T) = 0. \tag{2.1}$$

Here, T is temperature, and $\mathbb{D}$ is the anisotropic thermal diffusion tensor. In 3D,

$$\mathbb{D} = \begin{pmatrix} D_\parallel \cos^2(\phi) + D_\perp \sin^2(\phi) & \left(D_\parallel - D_\perp\right) \sin(\phi) \cos(\phi) & 0 \\ \left(D_\parallel - D_\perp\right) \sin(\phi) \cos(\phi) & D_\parallel \sin^2(\phi) + D_\perp \cos^2(\phi) & 0 \\ 0 & 0 & D_\perp \end{pmatrix}.$$

$D_\parallel$ and $D_\perp$ are parallel and perpendicular diffusion coefficients, and ϕ is the angle from the positive x-direction to the direction of high parallel diffusion (i.e., the principal axis of the diffusion tensor), which is constrained to be in the $x - y$ plane. $\phi = 0°$ indicates perfect alignment of the grid with the principal axis. In 2D, $\mathbb{D}$ reduces to the 2-by-2 tensor in the upper left of the 3-by-3 3D tensor.

2.3   Test problem descriptions

The first two test problems are designed to test uniform anisotropy with a straight principal axis. In magnetized plasma, this corresponds to an idealized case in which magnetic field lines are straight. The first problem is 2D, and the second is 3D. In these problems, the initial temperature profile is uniform in the direction of the principal axis and varies in the perpendicular direction. The relative alignment of the principal axis with the computational grid is varied. The third problem involves anisotropy with a varying principal direction, which verifies the ability of spectral element discretization to accurately capture anisotropic diffusion when grid alignment is non-uniform.
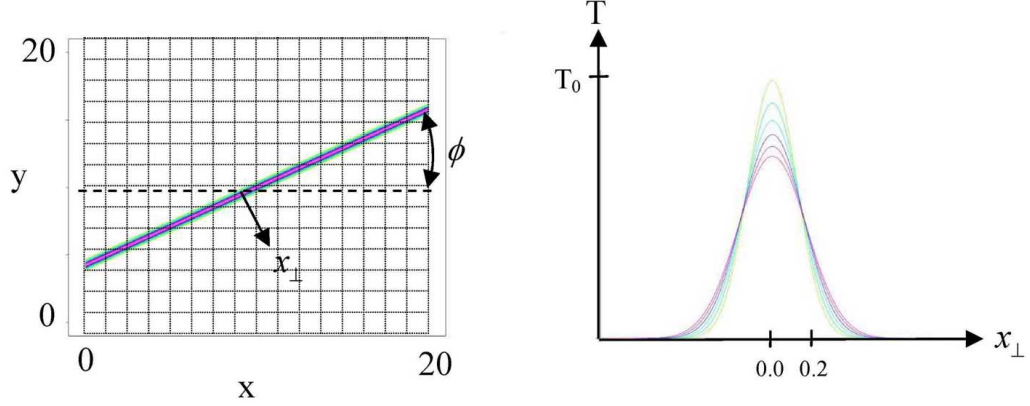
Figure 2.1: Setup for test problem one (TP1). On the left is the domain and initial condition with temperature contours shown. Plotted on the right are slices of temperature perpendicular to the principal direction of anisotropy as time progresses. (The decrease in peak temperature is exaggerated for illustration.) Initial peak temperature is $T_0 = 1$. The Gaussian profile is always centered at $x = 10$, $y = 10$.

2.3.1 Domain and initial condition

The domain and initial condition for test problem one (TP1) are shown in Figure 2.1. Perpendicular to the principal direction of anisotropy, the temperature profile is a Gaussian: $T = \exp\left(-x_\perp^2/\lambda^2\right)$ where $x_\perp$ is the distance from the Gaussian peak, and λ is the characteristic width of the Gaussian. Note that the peak temperature is one. The initial analytical temperature profile is uniform in the principal direction of anisotropy. The domain is square with 20 length units per side, and the characteristic width of the Gaussian temperature profile is 0.2. The relatively large domain size makes boundary effects negligible. Grid alignment is varied from 0 to 60 degrees. (As expected, results for $\phi = 60°$ are identical to results when $\phi = 30°$.)

Test problem two (TP2) is similar to TP1 except that the domain is 3D such that isosurfaces of the Gaussian temperature profile are cylindrical. Figure 2.2 shows the problem setup. The principal direction of anisotropy is rotated 30 degrees from the $x-$direction in
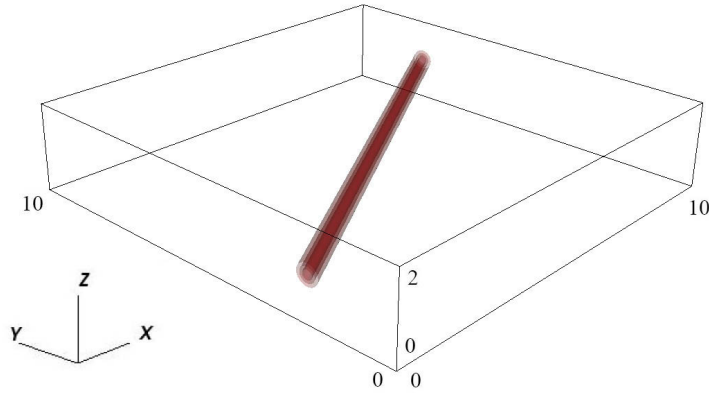
Figure 2.2: Setup for test problem two (TP2). Temperature is shown in nested semi-transparent red isosurfaces. The Gaussian temperature profile is cylindrical instead of linear as in TP1. Initial peak temperature is $T_0 = 1$. The mesh is composed of cubic grid cells. The angle of the Gaussian to the principal direction of anisotropy is fixed at $\phi = 60°$.

the $x - y$ plane ($\phi = 30°$). The grid alignment is not varied. This problem demonstrates spectral element performance in 3D. As in TP1, the characteristic width of the Gaussian temperature profile is 0.2. The $x - y$ domain is a 10-by-10 square. (In TP1, a 20-by-20 square is used; TP2 is more computationally demanding, and a 10-by-10 domain is found to sufficiently remove boundary effects.) Rotation of the Gaussian occurs only in the $x-y$ plane and the chosen $z-$direction domain extent of 2 units is large enough to prevent boundary effects.

The test problem three (TP3) initial condition is shown in Figure 2.3. In this 2D problem, the Gaussian peak is a function of radius from the center of the domain. The Gaussian peak is at 1 unit from the center and the characteristic width is 0.2 as in TP1 and TP2. As shown in Figure 2.3, this forms a circular "ridge" of high temperature. The principal diffusion axis is aligned in the polar direction, that is, aligned with the circular temperature contours. The $x - y$ domain is a 3-by-3 square, which is large enough to prevent boundary effects. This circular ridge profile is used instead of a centered Gaussian peak because of unexpected solution behavior with the centered Gaussian peak — the peak
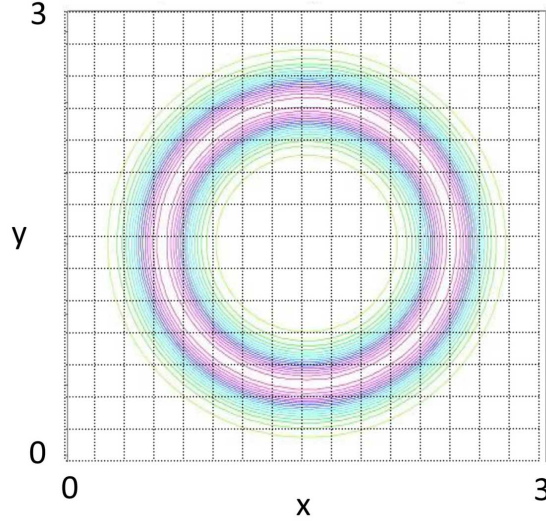
Figure 2.3: Setup for test problem three (TP3). Temperature contours are shown. Initial peak temperature is $T_0 = 1$. The peak of the Gaussian profile is 1 unit from the center of the domain.

temperature of the profile is observed to increase if the Gaussian is centered, or if the circular ridge radius is not sufficiently displaced from the domain center. The qualitative behavior (i.e., the rise in peak temperature) of a problem like TP3, but with the Gaussian peak centered, is discussed in Section 2.5, and the results are plotted.

2.3.2 Boundary conditions

A zero flux boundary condition, $\hat{\mathbf{n}} \cdot (\mathbb{D} \cdot \nabla T) = 0$ is applied to all boundaries (edges in the 2D problems and surfaces in the 3D problem), implying that the domain is perfectly insulating.

2.3.3 Resolution

The resolution in the $x-$, $y-$ and $z-$directions is identical in these simulations. The range of polynomial degree (np) studied is np=2 to 6. Element size (h) ranges from approximately 0.07 to 0.33. The domain size in the three different test problems varies, so the total number

of elements in each direction varies. A fundamental measure of resolution is the number of elements per unit length, nx/L. The number of elements per unit length is the same in all directions. The number of degrees of freedom per unit length (dof) is another useful measure of resolution, and is defined as $dof = nx * np/L$. $dof = 18$, 24, and 30 are studied.

2.3.4 Time evolution

Data is collected with uniform, constant parallel thermal diffusion ($D_\parallel = 1$) and zero perpendicular thermal diffusion ($D_\perp = 0$). When numerical error allows heat flux in the transverse direction, the Gaussian profile diffuses. The total simulation duration is the same for all runs — 10 time units. The time step is fixed at 0.1 time units.

2.4 Analytical considerations

Though not mathematically rigorous, the following analysis provides an intuitive feel for the source of numerical perpendicular thermal diffusion.

For finite elements representations of order np, error is of order $O(h^{np+1})$, provided the following conditions are met [14]: the converging quantity is well behaved, i.e., has finite strain energy; the basis functions are sufficiently uniform; and the solution is sufficiently smooth. Because the C^0-continuous spectral element code, HiFi, solves PDEs in weak form such that only first derivatives of dependent variables are needed, the strain energy constraint is satisfied globally. The requirements on basis function uniformity and solution smoothness are easily met in the simulations for this work which involve rectangular (and hexahedral) cells with fixed aspect ratio and infinitely differentiable Gaussian profiles. In realistic applications, the challenges of maintaining solution smoothness and basis function uniformity require attention to mesh generation and provision of sufficient spatial resolution (perhaps via mesh adaptation).

The source of perpendicular numerical diffusion error due to anisotropy is best understood by rewriting Eqn. (2.1) in terms of a numerical solution, $\tilde{T} = T - \delta T$, where T is a solution that exactly satisfies $\nabla \cdot \left(-\mathbb{D}_\parallel \cdot \nabla T \right) = 0$, where $\mathbb{D}_\parallel$ is just $\mathbb{D}$ with $D_\perp = 0$, and δT is the numerical error of order $O(h^{np+1})$. Setting $D_\perp = 0$, the evolution equation for $\tilde{T}$ is

$$\frac{\partial \tilde{T}}{\partial t} + \nabla \cdot \left(-\mathbb{D}_\parallel \cdot \nabla \tilde{T} \right) = 0,$$

or equivalently,

$$\frac{\partial \tilde{T}}{\partial t} + \nabla \cdot \left(\mathbb{D}_\parallel \cdot \nabla \delta T \right) = 0.$$

The finite element gradient operators are analytically exact, and the tensor $\mathbb{D}_\parallel$ is also analytically specified. Therefore, diffusion can arise only due to the numerical error, δT, in representing the temperature itself.

As illustrated in Figure 2.4, for a uniform anisotropy as in the first test problem, numerical error only arises when the computational mesh is misaligned with the anisotropy. The same relatively low-resolution mesh is used in Figures 2.4a and 2.4b. When the computational mesh is aligned with the anisotropy, as in Figure 2.4a, the same perpendicular temperature profile is perfectly replicated at all parallel locations, and $\nabla_\parallel \delta T = 0$ everywhere. However, if the computational mesh is not aligned, as in Figure 2.4b, the perpendicular profile is different at various parallel locations and $\nabla_\parallel \delta T \neq 0$.

2.5   Results and discussion

As discussed in Section 2.3.1, in a problem like TP3, but with the Gaussian peak centered in the domain, the peak temperature is observed to rise in some cases. Although this unusual finding is not a primary result of this research on modeling anisotropy, it warrants a brief discussion. For a case with $np = 3$ and $h = 0.125$, Figure 2.5 shows temperature plotted as a function of distance, $x_\perp$, perpendicular to the principal direction of anisotropy at $y = 1.5$ for a TP3 run [panel (a)] and for a similar run with the Gaussian peak centered in the 3×3 domain [panel (b)]. The magnitude of the temperature increase seen in panel (b) is approximately 10 times greater than the temperature reduction in panel (a). An obvious difference between the runs is that, where temperature gradients are high, the curvature of the anisotropy in the run with the centered Gaussian is small compared to the TP3 run. Apparently, poor resolution of this high curvature causes the unexpected rise in peak temperature, which could be related to failure to preserve positivity as discussed by,
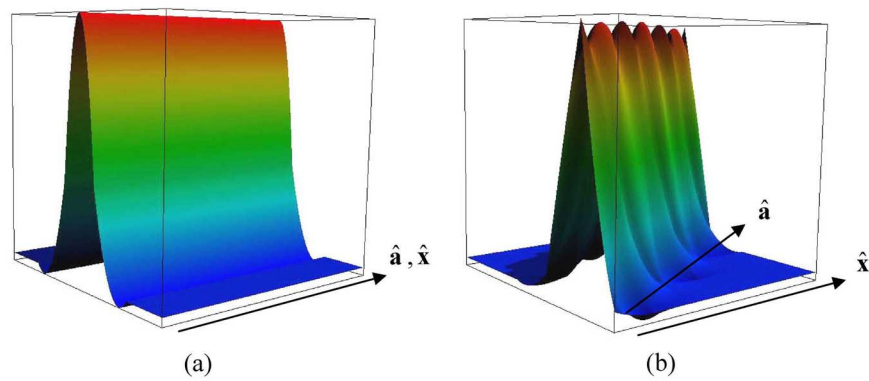
Figure 2.4: Surface plot of initial Gaussian temperature profiles illustrating error due to grid misalignment. In (a) and (b), the initial Gaussian temperature profile is poorly resolved with $h = 0.4$, and $np = 2$. $\hat{\mathbf{x}}$ indicates the Cartesian direction of grid orientation and $\hat{\mathbf{a}}$ is the principal direction of anisotropy. When the grid is aligned as in (a), the profile does not vary in the parallel direction. In (b), the grid is misaligned by $\phi = 30°$, the temperature profile varies in the parallel direction, and numerical perpendicular diffusion occurs.
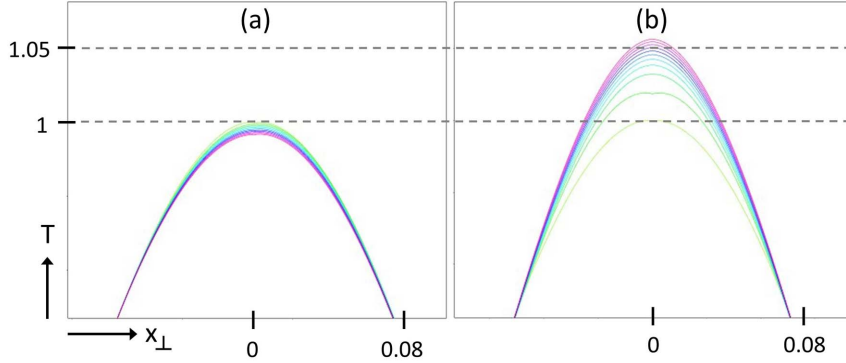
Figure 2.5: Plots of temperature vs. distance from the Gaussian temperature peak ($x_\perp$) at $y = 1.5$ for 2D test problems with curved anisotropy. Traces vary in color from yellow at early times to magenta at late times. In the TP3 simulation with $np = 3$ and $h = 0.125$ shown in panel (a), peak temperature decreases as expected. Results in panel (b) are for a similar case except that the Gaussian profile is centered in the domain. The maximum temperature *increases* in this case. The unexpected rise seems to be related to poor resolution of the highly curved anisotropy near the domain center, where temperature gradients are high. With higher resolution, the expected peak temperature decrease is observed.

for example, Sharma [34]. With higher resolution (e.g., $np = 6$ and $h = 0.1$), the peak temperature decreases as expected.

Numerical error in the three test problems is evaluated by evolving the solution for a fixed total time, and then comparing the final maximum temperature in the domain (T_{final}) to the initial maximum temperature (T_0). All simulations are resolved in time to within 2.5% relative error in $T_0 - T_{final}$. Temporal resolution error is largest in the highest resolution runs. For example, the error is 2.5% for the TP1 run with $np = 6$ and $h = 0.2$. (Error is found by running simulations with successively smaller time step sizes and establishing a converged value for $T_0 - T_{final}$.)

Parallel diffusion is unity for all results. To relate $\Delta T_{num.} \equiv T_0 - T_{final}$ to actual perpendicular diffusion, $\Delta \mathrm{T}_{real}$ is computed for a range of non-zero $D_\perp$ values. These
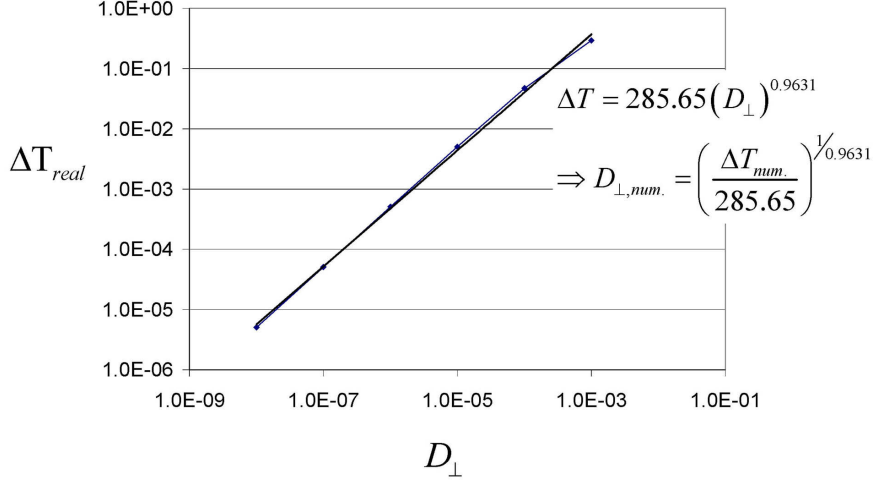
Figure 2.6: Plot showing correlation between change in peak temperature and real perpendicular diffusion. $\Delta\mathrm{T}_{real}$, the initial maximum temperature minus final maximum temperature due to non-zero simulated transverse diffusion, is plotted vs. $D_\perp$. Results are from fully resolved simulations (in space and time). This data is used to define numerical perpendicular diffusion, $D_{\perp,num.}$, given a $\Delta\mathrm{T}_{num.}$ found in simulations with $D_\perp = 0$. The data shown is for TP1. A similar approach is used to define $D_{\perp,num.}$ for all three test problems.

calculations are spatially resolved to within 1% relative error. Figure 2.6 shows $\Delta\mathrm{T}_{real}$ vs. $D_\perp$ for TP1. In simulations with $D_\perp = 0$, numerical perpendicular diffusion error can cause a non-zero $\Delta\mathrm{T}_{num.}$. A power fit equation relating $D_\perp$ to $\Delta\mathrm{T}_{real}$ is found and used to convert $\Delta\mathrm{T}_{num.}$ to an effective numerical diffusion, $D_{\perp,num.}$. Note that parallel diffusion is unity for all results. This approach is used to determine effective numerical diffusion, $D_{\perp,num.}$, as a function of $\Delta\mathrm{T}_{num.}$ for all three test problems.

Figure 2.7 shows results from TP1. $D_{\perp,num.}$ is plotted for $\phi = 5°$ to $60°$ for $dof = 24$. Equivalent plots for $dof = 18$ and 30 are omitted, but show similar trends. As shown, $D_{\perp,num.} \to 0$ as $\phi \to 0°$.

The dip in $D_{\perp,num.}$ near $\phi = 45°$ indicates an enhanced accuracy when the principal direction of anisotropy approaches alignment with one of the two diagonals of each cell.
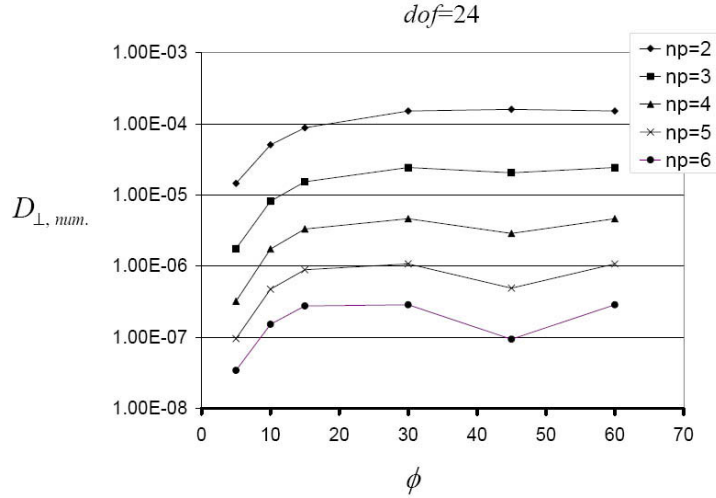
Figure 2.7: TP1 (2D straight anisotropy): Numerical perpendicular diffusion versus ϕ for $np = 2$ to 6 with total degrees of freedom (dof) fixed at $dof = 24$. (At $\phi = 0°$, $D_{\perp,num.}$ is exactly zero and cannot be plotted on the log scale.) Increasing np at a given dof provides the expected exponential reduction of error.

This enhancement could be related to the symmetry across the diagonals.

Grid alignment is fixed to $\phi = 30°$ in Figure 2.8 and the effect of element size on $D_{\perp,num.}$ is presented for $np = 2$ to 6. Results for other grid alignment angles show similar trends. Refining polynomial degree at fixed element size results in an exponential reduction in $D_{\perp,num.}$. Theoretical predictions outlined in Section 2.4, also shown in Figure 2.8, predict slightly slower convergence rates than seen in the simulation results, especially for high np. In Figures 2.9 and 2.10, similar results are shown for TP2 and TP3, respectively. Grid alignment is $\phi = 30°$ for the TP2 results and there is, of course, no alignment in the TP3 results which involve curved anisotropy.

As illustrated by the three test problems, cases with high np achieve a given accuracy with significantly fewer total degrees of freedom than lower np cases. This result is valid not only for 2D problems with straight anisotropy as shown in Figure 2.8, but also for 3D problems and for curved anisotropy, as shown in Figures 2.9 and 2.10. For example, in
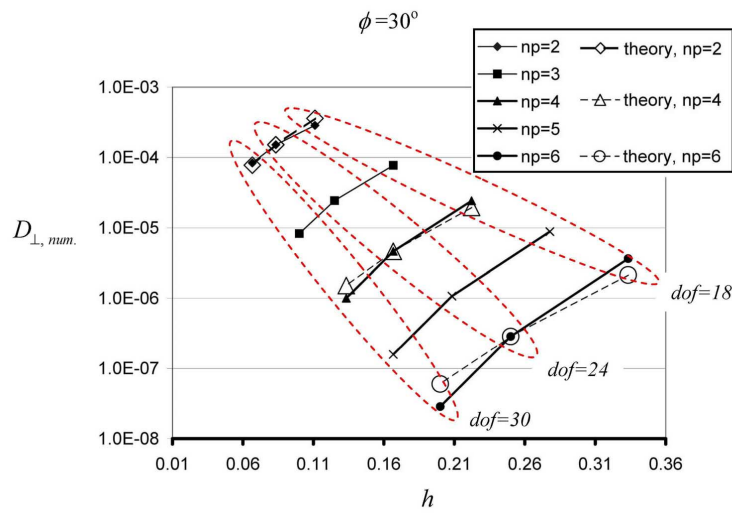
Figure 2.8: TP1 (2D straight anisotropy): Numerical perpendicular diffusion vs. h for various np at $\phi = 30°$. Data points corresponding to $dof = 18$, 24, and 30 are indicated by the dashed ellipses. The effect of np can be seen for constant h: at $h = 0.17$, increasing np from 3 to 5 reduces $D_{\perp,num.}$ by two orders of magnitude. Theoretical predictions based on $O(h^{np+1})$ scaling are provided for $np = 2$, 4, and 6. The theoretical predictions are scaled to match the simulation data for $dof = 24$.
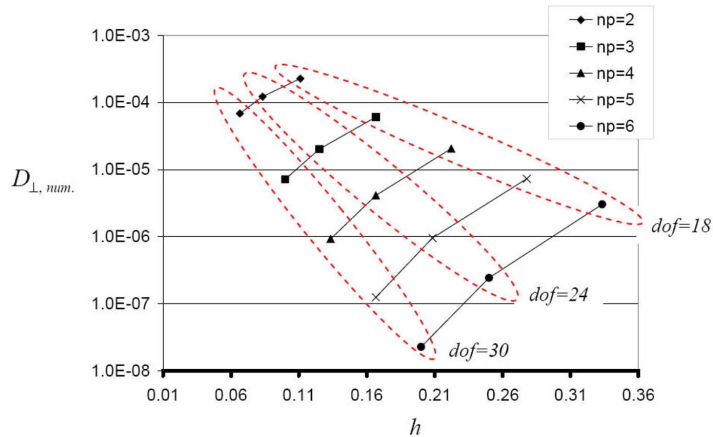
Figure 2.9: TP2 (3D straight anisotropy): Numerical perpendicular diffusion vs. h for various np. Data points corresponding to $dof = 18$, 24, and 30 are indicated by the dashed ellipses. Convergence trends are very similar to trends for TP1.
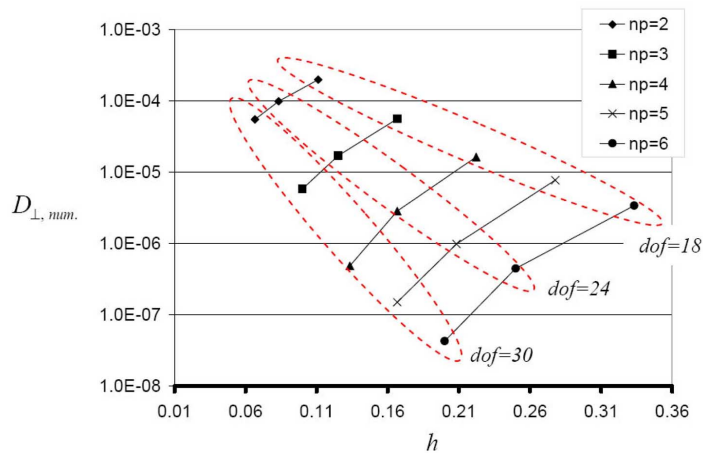
Figure 2.10: TP3 (2D curved anisotropy): Numerical perpendicular diffusion vs. h for various np. Data points corresponding to $dof = 18$, 24, and 30 are indicated by the dashed ellipses. Convergence trends are very similar to trends for TP1.

Figure 2.8, with $np = 5$ and $dof = 18$, $D_{\perp,num.} = 10^{-5}$ while with $np = 3$, $dof = 30$ is required to reach the same accuracy. By reducing the total number of degrees of freedom, high-order accuracy methods offer reduced memory requirements. Overall computational efficiency is also improved in many applications — for example, in [30] it is shown that computational efficiency is improved for long-time simulations of unsteady flows.

Chapter 3

OPEN BOUNDARY CONDITIONS FOR DISSIPATIVE MHD

In a variety of numerical problems, the computational domain must be a truncated approximation of the physical domain, allowing concentration of limited computational resources. An early example of such domain truncation is seen in the work of Charney, Fjörtoft, and von Neumann [36]; in their numerical model of North American weather, the domain is cropped around North America and special attention is paid to boundary treatment.

One type of boundary truncation is a "passive" boundary that simply lets the solution evolve as if the domain were not truncated at all. Boundary truncation can also be "active" in the sense that it drives behavior. For example, an active boundary might simulate a rise in ambient pressure that drives inflow. Boundary conditions (BC) that achieve domain truncation are variously referred to as artificial BC, non-reflecting BC, radiation BC, etc. In this dissertation, the term "open BC" will be used. This terminology suggests that the BC can be either passive or active.

The primary objective of the research presented in this chapter is to develop open BC methods for modeling the nonlinear dissipative magnetohydrodynamic (MHD) equations (see Section 1.4) with a high-order finite (spectral) element approach. Although particular emphasis is placed on dissipative MHD simulation, the methods developed are generally applicable to hyperbolic and mixed hyperbolic-parabolic systems. In fluid dynamics, open BC are necessary for problems such as pipe flow [37], propulsion [38], and weather modeling [39]. Some relevant dissipative MHD problems are plasma propulsion [40, 41], solar coronal physics [42], and some magnetic confinement schemes [43, 44]. A discussion of pertinent background information about previous open BC research is presented in Section 3.1.

Four open BC methods for dissipative MHD are implemented in HiFi: approximate

Riemann BC (ARBC), Thompson open BC (TBC), lacuna-based open BC (LOBC), and zero normal derivative BC (ZND BC). ARBC are directly based on characteristic analysis of the hyperbolic part of a mixed hyperbolic-parabolic equation system. TBC are also based on characteristic analysis, and are an extension to MHD of the work done by Thompson [45, 46] on gas dynamics. Building on the work of Ryaben'kii, Tsynkov, and Turchaninov [47], LOBC are derived from the concept of surface potentials and Calderón projections. LOBC, in the sense discussed below, control both the hyperbolic and parabolic aspects of mixed hyperbolic-parabolic systems. ZND BC impose zero normal derivative on each variable at the open boundary. Each technique is described in Section 3.2.

These open BC are applied to several test problems as discussed in Chapter 4

3.1   *Prior and foundational work*

Systematic studies that directly address the problem of open BC for linear or nonlinear dissipative MHD are notably absent. There is, however, a substantial amount of literature describing applications of open BC to hyperbolic systems, including ideal MHD, and some mixed hyperbolic-parabolic systems (e.g., Navier-Stokes). Such literature provides a starting point for work related to dissipative MHD. A paper by Tsynkov [48] provides an extensive review of open BC work. Two review papers by Givoli [49, 50] present a thorough overview of the research progress on open BC for linear problems. A review paper on open BC relevant to computational fluid dynamics (CFD) by Colonius [51], briefly covers open BC for linear wave problems and focuses on nonlinear wave problems. Hu [52] also reviews open BC techniques relevant to CFD, and focuses on the perfectly matched layer (PML) technique. The background material presented here is intended to acquaint readers with the ideas and sources from which this research is drawn. For an exhaustive summary of open BC techniques, see the review papers cited above and references therein.

For wave problems in which disturbances at the boundary are sufficiently small and smooth, linear open BC are appropriate. Linear open BC are, however, frequently used for nonlinear wave problems [51], sometimes with absorbing layers near the boundary to smooth errors. Thompson [45, 46] presents a method based on characteristics that attempts to provide an accurate nonlinear open BC for 2D hyperbolic problems. Colonius [51] points

out that Thompson's BC are not well-posed, but that they work remarkably well in practice.

LeVeque [53], in his book on finite volume methods for hyperbolic problems, describes a technique for specifying non-reflecting BC based on zero-order extrapolation. Information from interior cells is copied to ghost cells located just outside the boundary. Zero-order extrapolation has been successfully employed in past research [54, 55], but non-reflection is a consequence of the uniform representation of dependent variables within cells. The technique is not applicable to high-order elements. LeVeque [53] also describes approximate Riemann techniques for treating the characteristics of hyperbolic systems, which form the basis for the approximate Riemann BC (ARBC) technique described in Section 3.2.1. ARBC are naturally used in finite volume codes that use the approximate Riemann approach at each cell boundary. Discontinuous Galerkin methods, which combine the discontinuous approximate solutions of finite volume methods with finite element representation within cells, also employ ARBC [56]. To the author's knowledge, application of ARBC for high-order finite (spectral) element methods, as presented in this research, has not been previously described.

For hyperbolic systems, well-posedness requires that the incoming waves be constrained at domain boundaries [57]. One BC is required for each incoming characteristic. Because it is variation that constitutes a wave, for non-reflection, incoming wave strength should be constant in time and outgoing waves should be unconstrained. In mixed hyperbolic-parabolic systems, BC requirements differ from the purely hyperbolic case [58]. Hesthaven and Gottlieb [59] develop open BC for the Navier-Stokes equations (which are a mixed hyperbolic-parabolic system), aiming to ensure well-posedness. They use an energy analysis technique (described in Gustafsson et al. [57], Chapter 4) to develop BC requirements for the continuous problem, and then employ a penalty method to apply the BC in the discrete problem. Nordström and Svärd [60] present a more structured procedure for determining well-posed BC for the Navier-Stokes equations, but do not address discretization. Rahunanthan and Stanescu [61] use the same energy analysis approach to formulate stable interface/boundary conditions for a discontinuous Galerkin method applied to the Navier-Stokes equations, creating what they call a "viscous" Riemann solver. No previous work seems to address analytical techniques for proving well-posedness of (ideal or dissipative)

MHD BC; the main obstacle to using an energy analysis technique to address well-posedness and to construct an open BC is the required simultaneous symmetrization of MHD. In Appendix C, the energy analysis technique is summarized and the challenge of simultaneous symmetrization of dissipative MHD is discussed. For the present research, the difficulty of simultaneous symmetrization motivates a search for other options.

Tsynkov [48] describes an open BC approach called the difference potentials method (DPM). An infinite domain is decomposed into an interior region, where the interesting physics is happening, and an exterior region which is ignorable. The essential idea of DPM is that the exterior solution can be condensed to a potential on the surface of the interior domain. A Calderón-type projection [62] relates the surface potential to the exterior solution. DPM is designed for steady-state problems. Later work by Ryaben'kii, Tsynkov, and Turchaninov [47] adapts the DPM approach for time-dependent wave problems by using a lacuna-based approach, which will be described in detail in Section 3.2.3.

There are publications that address open BC for MHD. Dedner et al. [63] discuss an open BC for linear ideal MHD. Their non-local open BC is designed specifically for a gravitationally stratified plasma atmosphere. Faganello et al. [64] use a nonlinear open BC following Thompson [45] to minimize boundary effects while studying the effects of magnetic reconnection on the Kelvin-Helmholtz instability. While dissipation and even Hall physics is included in their MHD simulations, they assume that these non-ideal effects are negligible at the simulation boundaries. Forbes and Priest [65] discuss the difficulties of properly specifying open BC in the context of numerical models of magnetic reconnection. None of this work provides clear direction or general prescriptions for setting open BC when the boundary physics is nonlinear and dissipative.

It is important to note that past research [55, 54] has found that hyperbolic-based BC are adequate when using finite volume techniques to model mixed hyperbolic-parabolic problems. The need for refined open BC techniques for spectral element methods applied to mixed hyperbolic-parabolic problems is driven by high sensitivity of spectral element methods (and high-order methods in general) to boundary conditions.

3.2 Open BC formulations

Here, each open BC formulation is presented generically for application to any set of interior partial differential equations (PDEs) in conservation or flux-source form. In places, however, specific reference is made to dissipative MHD (see Section 1.4).

3.2.1 Approximate Riemann BC

Approximate Riemann BC (ARBC) are a type of characteristic-based BC (CBC). CBC offer a mathematical basis for specifying boundary conditions. A hyperbolic system is composed of a family of waves, governed by an eigensystem with real eigenvalues corresponding to the wave speeds. CBC identify and appropriately treat the different waves. Hyperbolic systems can be written in quasi-linear form, allowing manipulation of the eigensystem:

$$\frac{\partial \mathbf{q}}{\partial t} + \mathbb{A}_n \frac{\partial}{\partial \hat{n}} \mathbf{q} + \mathbb{A}_t \frac{\partial}{\partial \hat{t}} \mathbf{q} = 0. \tag{3.1}$$

A 2D system is considered, and $\hat{n}$ and $\hat{t}$ refer to the normal and (in-plane) tangential directions at the boundary. The matrices $\mathbb{A}_n$ and $\mathbb{A}_t$ are the flux Jacobians, $\mathbb{A}_n = \frac{\partial \mathbf{F}_n}{\partial \mathbf{q}}$ and $\mathbb{A}_t = \frac{\partial \mathbf{F}_t}{\partial \mathbf{q}}$, and $\mathbf{F}_n$ where $\mathbf{F}_t$ are the normal and tangential flux vectors, respectively. The normal flux Jacobian contains an eigensystem which can be exploited to control the incoming and outgoing waves. $\mathbb{A}_n = \mathbb{R}\mathbb{D}\mathbb{L}$, where $\mathbb{R}$ and $\mathbb{L}$ are matrices of right and left eigenvectors, respectively, and $\mathbb{D}$ is a diagonal matrix of eigenvalues.

Eigensystem decomposition is a challenge, especially for MHD. For this research, both analytical approaches (see Powell [66]) and numerical approaches have been used for decomposing flux Jacobians. The numerical approach is easier to implement — a variety of suitable numerical solver libraries such as PETSc [15] and LAPACK [67] are available.

An upwinding technique from finite volume work (see LeVeque [53]) is used for ARBC. The approach involves "approximately" solving a Riemann problem at the open boundary to determine the normal flux vector. The importance of specifying the normal flux is clarified by considering the integration of a hyperbolic system, written in conservation form, over the entire domain volume:

$$\int_V \left(\frac{\partial \mathbf{q}}{\partial t} + \nabla \cdot \mathbb{F} \right) dV = 0. \tag{3.2}$$

Using the divergence theorem,

$$\int_V \frac{\partial \mathbf{q}}{\partial t} dV + \oint_S \mathbb{F} \cdot \hat{\mathbf{n}} \, dS = 0. \tag{3.3}$$

This shows that boundary conditions must specify the normal flux at the boundary, $\mathbf{F}_n \equiv \mathbb{F} \cdot \hat{\mathbf{n}}$. By convention, the normal unit vector, $\hat{\mathbf{n}}$, points out of the domain.

In ARBC, fluxes corresponding to outgoing waves are determined by the interior solution values. Fluxes corresponding to incoming waves are determined by user-specified ambient conditions just outside of the open boundary. The spectral element code used for this research, HiFi, solves PDEs in the weak form, and a surface term like the one shown in Eqn. (3.3) is explicitly computed for each element.

Roe's Method [68] is employed to specify the flux in ARBC. In this technique, the normal flux vector at the open boundary is defined as

$$\mathbf{F}_{bnd} = \frac{1}{2} \left(\mathbf{F}_{int} + \mathbf{F}_{ext} \right) - \frac{1}{2} \left| \hat{\mathbb{A}}_n \right| (\mathbf{q}_{ext} - \mathbf{q}_{int}), \tag{3.4}$$

where $\hat{\mathbb{A}}_n$ is the approximate flux Jacobian (for the normal direction), and $\left| \hat{\mathbb{A}}_n \right| \equiv \hat{\mathbb{R}} \left| \hat{\mathbb{D}} \right| \hat{\mathbb{L}}$, where $\left| \hat{\mathbb{D}} \right|$ is a diagonal matrix of absolute values of the eigenvalues. $\mathbf{F}_{int}$ and $\mathbf{F}_{ext}$ are the fluxes computed using internal and external values, $\mathbf{q}_{int}$ and $\mathbf{q}_{ext}$. Just as the flux Jacobian, $\mathbb{A}_n$, is calculated as a function of the variables, $\mathbf{q}$, $\hat{\mathbb{A}}_n$ is calculated as a function of some average of the variables, $\hat{\mathbf{q}}$. If $\hat{\mathbf{q}}$ is chosen well, $\hat{\mathbb{A}}_n \mathbf{q}_{ext}$ and $\hat{\mathbb{A}}_n \mathbf{q}_{int}$ are approximately, if not exactly, equal to $\mathbf{F}_{ext}$ and $\mathbf{F}_{int}$, respectively. Commonly, a simple average of interior and exterior variables is used to find $\hat{\mathbf{q}}$ (i.e., $\hat{\mathbf{q}} = \frac{\mathbf{q}_{int} + \mathbf{q}_{ext}}{2}$), although more sophisticated approaches have been studied. For MHD, a simple average is arguably the best option [55].

ARBC allow incoming wave strengths to be determined by exterior conditions ($\mathbf{q}_{ext}$), which are user-specified, and outgoing wave strengths to be determined by interior conditions ($\mathbf{q}_{int}$), which are given by the interior solution values. For instance, if all of the characteristics are outgoing, $\left| \hat{\mathbb{A}}_n \right| = \hat{\mathbb{A}}_n$, and $\mathbf{F}_{bnd}$ is simply

$$\mathbf{F}_{bnd} = \frac{1}{2}\left(\mathbf{F}_{int} + \mathbf{F}_{ext}\right) - \frac{1}{2}\hat{\mathbb{A}}_n\left(\mathbf{q}_{ext} - \mathbf{q}_{int}\right), \tag{3.5}$$

which, after using the approximations $\hat{\mathbb{A}}_n\mathbf{q}_{int} \approx \mathbf{F}_{int}$ and $\hat{\mathbb{A}}_n\mathbf{q}_{ext} \approx \mathbf{F}_{ext}$, reduces to

$$\mathbf{F}_{bnd} \approx \mathbf{F}_{int}. \tag{3.6}$$

Similarly, if all characteristics are incoming, $\mathbf{F}_{bnd} \approx \mathbf{F}_{ext}$. Effectively, $\mathbf{F}_{bnd} = \mathbf{F}_{int}^{+} + \mathbf{F}_{ext}^{-}$, where the superscript "+" denotes outgoing waves and the superscript "−" denotes incoming waves.

Because ARBC are applied by specifying the flux, the equation system must be in conservation form such that no source terms are present. In the dissipative MHD equations presented in Section 1.4, total energy is the evolved variable in the energy equation, Eqn. (1.11). The equation is conservative. If Eqn. (1.11) is replaced, for example, with a pressure evolution equation, source terms would be present. Thus, the equation for total energy is necessary for ARBC. An exception to this rule is made for magnetic field ($\mathbf{B}$), which is the conserved variable. Formulation with magnetic vector potential ($\mathbf{A}$), where $\mathbf{B} = \nabla \times \mathbf{A}$, is often preferred to ensure $\nabla \cdot \mathbf{B} = 0$. Consider the evolution of $\mathbf{A}$ and $\mathbf{B}$ in ideal MHD,

$$\frac{\partial \mathbf{A}}{\partial t} = \mathbf{v} \times \mathbf{B}, \tag{3.7}$$

and

$$\frac{\partial \mathbf{B}}{\partial t} + \nabla \cdot \left(\mathbf{v}\mathbf{B} - \mathbf{B}\mathbf{v}\right) = 0. \tag{3.8}$$

The quantity to be specified using ARBC is $\hat{\mathbf{n}} \cdot \left(\mathbf{v}\mathbf{B} - \mathbf{B}\mathbf{v}\right) = \mathbf{F}_{bnd}$. Crossing $\hat{\mathbf{n}}$ into Eqn. (3.7),

$$\hat{\mathbf{n}} \times \frac{\partial \mathbf{A}}{\partial t} = \hat{\mathbf{n}} \times \left(\mathbf{v} \times \mathbf{B}\right), \tag{3.9}$$

which reduces to an equation describing the evolution of the tangential components of $\mathbf{A}$ ($\mathbf{A}_{tang}$) in terms of the boundary flux,

$$\frac{\partial \mathbf{A}_{tang}}{\partial t} = -\hat{\mathbf{n}} \cdot \left(\mathbf{v}\mathbf{B} - \mathbf{B}\mathbf{v}\right) = -\mathbf{F}_{bnd}. \tag{3.10}$$

As a boundary condition for the tangential components of $\mathbf{A}$, the time rate of change is specified according to Eqn. (3.10).

3.2.2 Thompson open BC

A pair of papers by Thompson [45, 46] describe an open BC approach based on an intuitive concept of non-reflection laid out by Hedstrom [69] for 1D non-linear problems. Consider the 1D scalar wave equation, $\frac{\partial u}{\partial t} + c\frac{\partial u}{\partial x} = 0$ with $c > 0$, where the domain has a "left" boundary at $x = 0$ and a "right" boundary at $x = 1$. Non-reflection requires that the amplitude of u at the left boundary be constant. That is, $\frac{\partial u}{\partial t} = c\frac{\partial u}{\partial x} = 0$. Now consider the 2D hyperbolic system previously given in Eqn. (3.1) (restated here for convenience),

$$\frac{\partial \mathbf{q}}{\partial t} + \mathbb{A}_n \frac{\partial}{\partial \hat{n}}\mathbf{q} + \mathbb{A}_t \frac{\partial}{\partial \hat{t}}\mathbf{q} = 0.$$

As before, $\hat{n}$ and $\hat{t}$ refer to the normal and (in-plane) tangential directions at the boundary, and the matrices $\mathbb{A}_n$ and $\mathbb{A}_t$ are the flux Jacobians. Again, the normal flux Jacobian is decomposed as $\mathbb{A}_n = \mathbb{R}\mathbb{D}\mathbb{L}$. The system can be rewritten in terms of scalar equations,

$$\mathbf{l}_i \frac{\partial}{\partial t}\mathbf{q} + \lambda_i \mathbf{l}_i \frac{\partial}{\partial \hat{n}}\mathbf{q} + \mathbf{l}_i \left(\mathbb{A}_t \frac{\partial}{\partial \hat{t}}\mathbf{q} \right) = 0, \tag{3.11}$$

where $\mathbf{l}_i$ is the ith component of $\mathbb{L}$ and λ_i is the ith component of $\mathbb{D}$. Considering wave propagation only normal to the boundary (i.e., ignoring the tangential part of the system), Hedstrom [69] shows that the condition

$$\mathbf{l}_i \frac{\partial}{\partial t}\mathbf{q} = 0 \tag{3.12}$$

assures non-reflection if only simple waves are going out.[1] For shocks of strength ϵ, the reflection strength will be of order $O(\epsilon^3)$ [69]. The condition given by Eqn. 3.12 is equivalent to $\lambda_i \mathbf{l}_i \frac{\partial}{\partial \hat{n}}\mathbf{q} = 0$. Now reintroducing the tangential part of the system, boundary equations enforcing (approximate) non-reflection can be written as

---

[1]For unqualified non-reflection, the condition is $\frac{\partial}{\partial t}(\mathbf{l}_i\mathbf{q}) = 0$; see, e.g., LeVeque [53] for a discussion of simple waves.

$$\frac{\partial \mathbf{q}}{\partial t} + \mathbb{A}_n{}^+ \frac{\partial}{\partial \hat{n}} \mathbf{q} + \mathbb{A}_t \frac{\partial}{\partial \hat{t}} \mathbf{q} = 0, \tag{3.13}$$

where $\mathbb{A}_n^+ = \mathbb{R}\mathbb{D}^+\mathbb{L}$ and $\mathbb{D}^+ = \frac{\mathbb{D}+|\mathbb{D}|}{2}$ such that only the positive eigenvalues (associated with outgoing waves) are selected. These equations represent the Thompson BC (TBC). In HiFi, TBC are enforced at the open boundary with the explicit local BC. Note that TBC are not non-reflecting if waves are traveling at oblique incidence (i.e., not normal incidence) with respect to the boundary. Also notice that this is actually a non-reflecting BC (NRBC) and cannot be used to actively drive behavior at the boundary. Thompson's first paper [45] presents the NRBC while the second paper [46] describes how non-zero incoming wave amplitudes can be used to achieve an active BC. In the research for this dissertation, only the NRBC has been studied.

As for the ARBC presented in Section 3.2.1, numerical decomposition is used for the decomposition required by TBC. The decomposition requires that the equations be written in quasi-linear form as in Eqn. 3.1. MHD can be written in quasi-linear form in terms of the magnetic field, but not in terms the magnetic vector potential. Eqn. (3.13) provides evolution equations for the normal and tangential components of $\mathbf{B}$ while the dissipative MHD equations in HiFi are formulated in terms of magnetic vector potential ($\mathbf{A}$). Using the definition of magnetic vector potential, $\mathbf{B} = \nabla \times \mathbf{A}$, and assuming uniform $\hat{n}$,

$$\nabla \times \frac{\partial(\hat{\mathbf{n}} \cdot \mathbf{A})}{\partial t} = \hat{\mathbf{n}} \cdot \frac{\partial \mathbf{B}}{\partial t}, \tag{3.14}$$

and

$$\nabla \times \frac{\partial(\hat{\mathbf{n}} \times \mathbf{A})}{\partial t} = \hat{\mathbf{n}} \times \frac{\partial \mathbf{B}}{\partial t}. \tag{3.15}$$

These equations for evolution of the spatial derivatives of $\mathbf{A}$ in terms of the evolution of normal and tangential components of $\mathbf{B}$ are enforced at the boundaries using HiFi's explicit local BC.

3.2.3 Lacuna-based open BC

Ryaben'kii et al. [47] present an open BC approach that takes advantage of lacunae in the solution of hyperbolic problems — lacuna-based open BC (LOBC). The term "lacuna" here refers to a still region behind an aft wave front. Instead of imposing some condition at the boundary, the idea of LOBC is to generate an auxiliary solution that is allowed to propagate into an exterior region appended to the interior domain. The open BC is achieved by constraining the interior solution to match the auxiliary solution at the interface of the interior and exterior regions. A conventional BC is applied at the boundary of the exterior region.

Figure 3.1 shows a schematic for LOBC. Consider a wave problem initialized with non-zero values well inside the domain and zero values near the interior-exterior interface. The auxiliary solution, which is defined only in the exterior and a near-boundary "transition region", together called the auxiliary domain, is also set to zero initially. Source terms, which drive the auxiliary solution, are generated in the near-boundary transition region such that $\mathbf{w} = \mu\mathbf{q}$, where $\mathbf{w}$ is the auxiliary solution, $\mathbf{q}$ is the interior solution, and μ is the transition function.

For an arbitrary set of PDEs in flux-source form, consider the interior problem,

$$\frac{\partial \mathbf{q}}{\partial t} + \nabla \cdot \mathbb{F}\left(\mathbf{q}, \nabla\mathbf{q}\right) = \mathbf{S}\left(\mathbf{q}, \nabla\mathbf{q}\right) \tag{3.16}$$

where $\mathbb{F}$ is the flux, and $\mathbf{S}$ is the source. The auxiliary problem is

$$\frac{\partial \mathbf{w}}{\partial t} + \nabla \cdot \mathbb{F}\left(\mathbf{w}, \nabla\mathbf{w}\right) = \mathbf{S}\left(\mathbf{w}, \nabla\mathbf{w}\right) + \mathbf{\Omega}\left(\mathbf{q}, \nabla\mathbf{q}\right). \tag{3.17}$$

Note that the flux and source terms, $\mathbb{F}$ and $\mathbf{S}$, can be functions of either $\mathbf{q}$ and $\nabla\mathbf{q}$ or $\mathbf{w}$ and $\nabla\mathbf{w}$. $\mathbf{\Omega}$ is the near-boundary source term that drives the auxiliary problem, and is a function of $\mathbf{q}$ and $\nabla\mathbf{q}$. To determine $\mathbf{\Omega}$, the substitutions $\mathbf{w} = \mu\mathbf{q}$ and $\nabla\mathbf{w} = \nabla(\mu\mathbf{q})$ are made in Eqn. (3.17), and the equation is solved for $\mathbf{\Omega}$. Noting that μ is constant in time such that $\frac{\partial \mu\mathbf{q}}{\partial t} = \mu\frac{\partial \mathbf{q}}{\partial t}$, and using Eqn. (3.16),

$$\mathbf{\Omega}(\mathbf{q}) = \nabla \cdot \mathbb{F}[\mu\mathbf{q}, \nabla(\mu\mathbf{q})] - \mathbf{S}[\mu\mathbf{q}, \nabla(\mu\mathbf{q})] - \mu\nabla \cdot \mathbb{F}(\mathbf{q}, \nabla\mathbf{q}) + \mu\mathbf{S}(\mathbf{q}, \nabla\mathbf{q}). \tag{3.18}$$
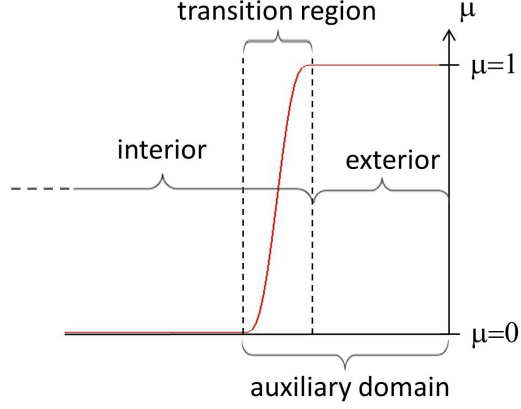
Figure 3.1: Schematic for lacuna-based open BC (LOBC). In the transition region, the transition function μ increases from 0 to 1. The auxiliary domain contains the transition region and the exterior domain.

In some cases, Eqn. (3.18) can be simplified. If $\mathbb{F}$ and $\mathbf{S}$ are functions of only $\mathbf{q}$ or $\mu\mathbf{q}$ and $\mathbb{F}$ and $\mathbf{S}$ are homogeneous functions of degree 1 in their arguments, Eqn. (3.18) simplifies to

$$\boldsymbol{\Omega}(\mathbf{q}) = \mathbb{F}(\mathbf{q}) \cdot \nabla\mu. \tag{3.19}$$

In the dissipative MHD implementation presented in Section 1.4, $\mathbb{F}$ and $\mathbf{S}$ involve derivatives of the primary variables, so the general form of Eqn. (3.18) is appropriate.[2]

The following scenario helps illustrate the basic concept of LOBC. Simulation begins at $t = 0$ and the first time step, $n = 1$, generates source term $\boldsymbol{\Omega}_1$. The problem is stepped forward (or "integrated") in time, and at each time step, a corresponding $\boldsymbol{\Omega}_n$ is generated. The wavelet generated by $\boldsymbol{\Omega}_1$ reaches the exterior boundary at $t = T_{ext}$ and $n = N_{ext}$. Assuming, for the moment, a single wave speed, the time required for a wavelet to travel from the interface to the boundary of the exterior domain is $T_{ext} = L_{ext}/c$, where L_{ext} is the length of the exterior domain and c is the wave speed. The time steps taken are $n = 1, 2, \cdots, N_{ext}$.

---

[2]In ideal MHD in conservation form, there are no source terms, but the fluxes are not homogeneous functions of degree 1. However, the fluxes for the Euler equations of gasdynamics are homogeneous of degree 1 and the simplified expression for Ω of Eqn. (3.19) is applicable.

To prevent the wavelet generated by $\mathbf{\Omega}_1$ from interacting with the exterior boundary (where a conventional BC is applied), the auxiliary problem is reintegrated, excluding the source term at $n = 1$. Thus, $\mathbf{w}|_{n=N_{ext}}$ is computed as

$$\mathbf{w}|_{n=N_{ext}} = \mathbf{w}|_{t=0} + \sum_{n=2}^{n=N_{ext}} \left[-\nabla \cdot \mathbb{F}\left(\mathbf{w}\right) + \mathbf{S}\left(\mathbf{w}\right) + \mathbf{\Omega}_n \right] \Delta t, \tag{3.20}$$

where Δt is the time step size. This truncation damps the wave before it reaches the exterior boundary. (Theoretically, it is possible to wait until $t = 2T_{ext}$, at which point the reflections from the exterior boundary will actually return and influence the interior, but in this research, the earlier reintegration is used.) After reintegration, the step $n = N_{ext} + 1$ would be taken as usual. All reflections could be prevented by repeating this procedure of reintegration, then stepping. The next reintegration, for example, would be from $n = 3$ to $n = N_{ext}+1$. However, it is more efficient to take multiple steps between reintegrations. For example, instead of reintegrating from $n = 2$ to N_{ext}, consider reintegration from $N_{ext}/3$ to N_{ext}.[3] If the wavelets corresponding to eliminated source terms have exited the transition region by the final time step of the reintegration, $\mathbf{w}$ will match $\mathbf{q}$ at the interior-exterior interface. An illustration of the time-stepping procedure is given in Figure 3.2, where $N_{ext} = 9$ and three steps are taken between reintegrations.

A slight complication can arise in practice if the choice $\mathbf{w} = \mu\mathbf{q}$ is made to compute $\mathbf{\Omega}$ as in Eqn. (3.18). If $\mathbf{q}$ has nonzero initial values in the auxiliary domain, the corresponding initial values for $\mathbf{w}$ will have steep gradients in the transition region, potentially introducing noise immediately in the simulation. This noise can be avoided by choosing $\mathbf{w} = \mu\tilde{\mathbf{q}} + \mathbf{q_0}$, where $\tilde{\mathbf{q}}$ is the variation of the solution from initial values, $\mathbf{q_0}$. The associated source terms drive the auxiliary solution to be $\mathbf{w} = \mu\tilde{\mathbf{q}} + \mathbf{q_0}$. If there is no variation of $\mathbf{q}$ (i.e., $\tilde{\mathbf{q}} = 0$) initially in the transition region, the auxiliary solution will have a uniform initial state.

In the ideal scenario just described, LOBC are theoretically reflectionless. In practice, however, lacuna-based truncation is often imperfect due to several subtleties:

Subtlety #1: True lacunae exist only when the physics under consideration is odd-dimensional. (This fact is related to Huygens' principle; see Courant and Hilbert [70].)

---

[3] For the purposes of this illustration, it may be assumed that N_{ext} is a multiple of 3.
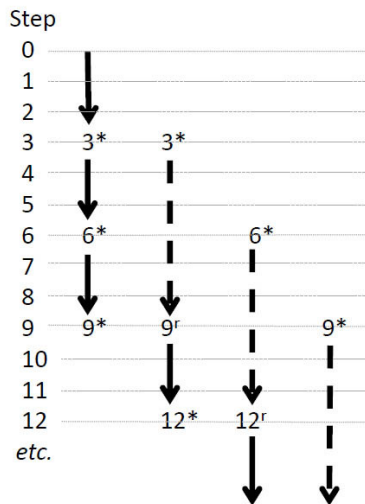
Figure 3.2: Time stepping procedure for LOBC. The main time integration is shown by solid arrows. Dashed arrows show reintegration. Nine steps are taken before the first reintegration. Three steps are taken between reintegrations. Reintegrations begin with stored solutions indicated by asterisks and results in reintegrated solutions indicated by r superscripts.

In 2D, while true lacunae do not exist, they do exist in an approximate sense. A decaying "wake" exists behind 2D waves. As more decay is allowed, lacuna-based truncation becomes more accurate. As decay is allowed, time elapses, and the leading front of the wave travels unimpeded. The exterior domain must be large enough to prevent reflection from the leading front of a wave while the wake is allowed to decay.

Subtlety #2: Lacunae are hyperbolic phenomena and exist only in purely hyperbolic systems; dissipation modifies lacunae by allowing the waves to diffuse into the lacunae. If the dissipative length scales are comparable to the transition region length, error is introduced. If, on the other hand, dissipative scales are much shorter or much longer than the transition length, error will be minimal.

Subtlety #3: Lacunae exist behind each wave in a hyperbolic system. LOBC can be exact only when the slowest wave is allowed to exit the transition region before truncation.

For example, the 1D Euler equations have three speeds: u, $u + c$, and $u - c$. In the case of slow outflow, it may be problematic to wait for all waves to pass through the transition region prior to temporal truncation of the sources — the necessary size of the exterior region could be prohibitively large. The approach taken here is to perform temporal truncation based on the fastest wave speed. By using an exterior region that extends beyond the interior domain by a distance of at least twice the transition length, most slow-moving (or obliquely-moving) wavelets are allowed to pass through the transition region prior to temporal truncation. Despite premature truncation of some wavelets, LOBC perform well if slow-moving (or obliquely-moving) wavelets have small amplitudes such that the truncation leads to small errors. In some cases, like a vortex that is moving with a slow background outflow, the required conditions for LOBC will not be satisfied. In fact, part of the slowly exiting vortex might have significant inward velocity which would obviously violate the premises of LOBC.

Subtlety #4: In the transition region, the auxiliary solution wave speeds should match those of the interior solution as closely as possible. Mismatched speeds cause disagreement between the auxiliary and interior solutions at the interior-exterior interface, and reflections result. For example, consider the sound speed, which depends on temperature. If the auxiliary pressure is given by $p^a = \mu\tilde{p} + p_0$ and auxiliary density by $\rho^a = \mu\tilde{\rho} + \rho_0$, the auxiliary temperature is

$$T^a \propto \frac{\mu\tilde{p} + p_0}{\mu\tilde{\rho} + \rho_0}. \tag{3.21}$$

For a linear problem, $\frac{p_0}{\rho_0} \propto T^a \approx T$. In the nonlinear extreme where $\tilde{p} \gg p_0$ and $\tilde{\rho} \gg \rho_0$, again $T^a \approx T$. If variations ($\tilde{p}$ and $\tilde{\rho}$) are near the background values (p_0 and ρ_0), $T^a \neq T$. For this case, lower background values can sometimes be used so that the extreme nonlinear case is approached. Similarly, when using an internal energy formulation for gas dynamics or MHD, care should be taken to ensure that $p^a = \mu\tilde{p} + p_0$. Auxiliary pressure is defined as

$$p^a = (\gamma - 1)(e^a - KE^a - ME^a), \tag{3.22}$$

where e^a is the auxiliary total energy, $e^a = \mu\tilde{e} + e_0$, KE^a is the auxiliary kinetic energy,

$KE^a = (\mathbf{m}^a)^2/(2\rho^a)$, where $\mathbf{m}$ is momentum, and ME^a is the auxiliary magnetic energy, $ME^a = (\mathbf{B}^a)^2/2$, where $\mathbf{B}$ is magnetic field. Assuming that the background flow speed is zero, $\mathbf{m}^a = \mu\tilde{\mathbf{m}}$. As usual, $\rho^a = \mu\tilde{\rho} + \rho_0$. If $\mathbf{B}^a = \mu\tilde{\mathbf{B}} + \mathbf{B}_0$, auxiliary pressure is

$$p^a = (\gamma - 1)\left(\mu\tilde{e} + e_0 - \frac{(\mu\tilde{\mathbf{m}})^2}{\mu\tilde{\rho} + \rho_0} - \frac{(\mu\tilde{\mathbf{B}} + \mathbf{B}_0)^2}{2}\right). \tag{3.23}$$

Here, $e_0 = p_0/(\gamma - 1) + \mathbf{B}_0^2/2$. In the linear case, Eqn. (3.23) yields $p^a \approx p_0$, resulting in $T^a \approx T_0$. In the nonlinear case with background values small relative to variations, $e^a \approx \mu e$, and $KE^a \approx \mu KE$, but $ME^a = \mu^2 ME$. Thus, $p^a \neq \mu p$, and $T^a \neq T$. This problem is corrected by generating the source term for the magnetic evolution equation with $\sqrt{\mu}\mathbf{B}$. Then, $ME^a = \mu ME$ and the auxiliary solution temperature matches the interior solution.

A goal of this research has been to explore these subtle complications related to lacuna-based truncation and determine whether LOBC can be useful despite them. As shown in Chapter 4, results indicate that LOBC are indeed useful for dissipative MHD simulation.

Smoothness requirements of the transition function depend on the physical system being modeled. For the Euler equations, for example, continuous first derivatives are needed — if the auxiliary pressure has a discontinuous derivative, the associated discontinuous force (∇p^a) would be problematic. For magnetic-vector-potential-based MHD, continuous second derivatives are required to ensure a smooth representation of auxiliary current. The transition function, μ, used here is based on a quintic polynomial. For a transition of length L_{trans}, between points x_0 and x_1, that polynomial is

$$P_5 = \Delta^3(10 - 15\Delta + 6\Delta^2), \tag{3.24}$$

where $\Delta = (x - x_0)/L_{trans}$. For LOBC, a function is sought which has C^2-continuity and which has a C^2-continuous square root. P_5 is C^2-continuous, but $P_5^{1/2}$ is not. However, $P_5^{3/2}$ and $P_5^{3/4}$ are C^2-continuous. The transition function $\mu = P_5^{3/2}$ is used, along with its square root for magnetic variables. To minimize noise in the spatial representation of μ, the transition region is designed so that its limits correspond to cell boundaries. Generally, two or more cells are used in the transition region.

Direct replacement of $\mathbf{q}$ with $\mathbf{w}$ in the exterior after reintegration could introduce discontinuities if the solutions do not perfectly match. This problem is alleviated by gradual

replacement — $\mathbf{q}$ is unmodified at the interior-exterior interface, and smoothly transitions to $\mathbf{w}$ at a distance of one transition length from the interface into the exterior region using the quintic polynomial transition given by Eqn. 3.24. The

When lacuna-based truncation is imperfect, $\mathbf{w}$ can be nonzero inside the transition region. The approach taken in the HiFi implementation is to force $\mathbf{w}$ to zero at a distance of two transition lengths inside the interior region boundary. The quintic polynomial transition given by Eqn. 3.24 is used to smoothly force $\mathbf{w}$ to zero after each time step.

The present LOBC implementation in HiFi is not optimized. $\mathbf{q}$ is computed everywhere, as is $\mathbf{w}$. Since $\mathbf{w}$ is zero in most of the interior, an improvement would be to compute it only where it is nontrivial. Furthermore, the reintegration is carried out for both $\mathbf{q}$ and $\mathbf{w}$. With some specialization, $\mathbf{\Omega}$ could be stored and reintegration could be conducted only for $\mathbf{w}$.

3.2.4 Zero normal derivative BC

Zero normal derivative boundary conditions (ZND BC) enforce zero normal derivative for each dependent variable at the open boundary. As shown in Chapter 4, ZND BC allow significant reflections, but are stable for dissipative MHD and provide a good point of comparison for more sophisticated open BC.

Chapter 4

OPEN BOUNDARY CONDITION TEST PROBLEMS

The capabilities and performance of the open BC options presented in Chapter 3 are qualitatively and quantitatively explored in several problems, each of which involves solving dissipative MHD (see Section 1.4) or the gasdynamics subset of dissipative MHD. A channel flow problem qualitatively demonstrates the ability of ARBC to serve as an active BC, driving the interior dynamics; error is not rigorously studied. In four other test problems, performance of the open BC is quantified in terms of the proximity of their associated solutions to a reference solution. Reference solutions are obtained by solving the problems on greatly extended domains to prevent boundary effects. Performance is measured in terms of the L_∞-norm of the pressure error (i.e., the maximum error) in the simulation. In plotted results, L_∞ error is normalized by the maximum pressure during the reference simulation. The four test problems for which boundary reflection error is quantified include 1D and 2D pressure pulse problems, an FRC translation problem in which the FRC exits an open boundary, and a cyclic coaxial plasma acceleration problem.

As discussed in Section 1.4, equations in HiFi are cast in normalized form. In this chapter, problem details and results are presented in terms of normalized variables.

4.1 Channel flow

ARBC have been applied in simulations of gas dynamic flow through a converging-diverging channel, shown in Figure 4.1(a). The channel is infinitely long in the out-of-plane direction. Inflow is dictated at the inlet (left boundary) by an ARBC there. The flow through the channel becomes supersonic and drives a shock through the outlet (right boundary) which is truncated with an ARBC. After steady supersonic flow is established, outlet pressure is raised and a shock reenters the channel and eventually reaches a steady state standing position in the expansion section.

In the following description of the computational setup and results, physical values are presented in normalized units.

4.1.1   Computational setup

Geometry and initial condition

Initial pressure and density are $p = 0.01$ and $\rho = 0.1$, respectively. The throat gap is 2.0, the inlet size is 2.8, and the outlet size is 5.0. The axial distance from inlet to throat is 2.0 and the axial distance from the throat to the junction of the open boundary and the channel wall termination is 7.0. Downstream of the wall termination, the open boundary bulges an additional distance of 1.0. At the outlet, the open boundary is curved to demonstrate that ARBC can accommodate curvature.

Note that the ratio of specific heats, γ, is 1.4 for this problem.

Dissipation

The simulation essentially uses Euler equations with small dissipation values to facilitate the numerics. The dissipation coefficients are $D_\rho = \xi = \kappa = 5 \times 10^{-3}$. Thermal conduction is isotropic. See Section 1.4 for details about the dissipation coefficients.

Boundary conditions

ARBC are used at the inlet (left) and outlet (right). Figure 4.1(b) shows the ambient values used for the ARBC. The ambient values begin at background levels. Early in time, inlet values of pressure and density are smoothly increased. Later, the ambient pressure at the outlet is increased. In terms of the dependent variables and the boundary normal ($\hat{\mathbf{n}}$), BC at the top and bottom walls are: $\hat{\mathbf{n}} \cdot \mathbf{v} = 0$ (zero normal flow); $\hat{\mathbf{n}} \cdot \nabla(\hat{\mathbf{n}} \times \mathbf{v}) = 0$ (perfect slip); $\hat{\mathbf{n}} \cdot \nabla T = 0$ (insulating); and zero density flux, which, given $\hat{\mathbf{n}} \cdot \mathbf{v} = 0$, essentially enforces $\hat{\mathbf{n}} \cdot \nabla \rho = 0$ because of the artificial density diffusion term in Eqn. (1.12).
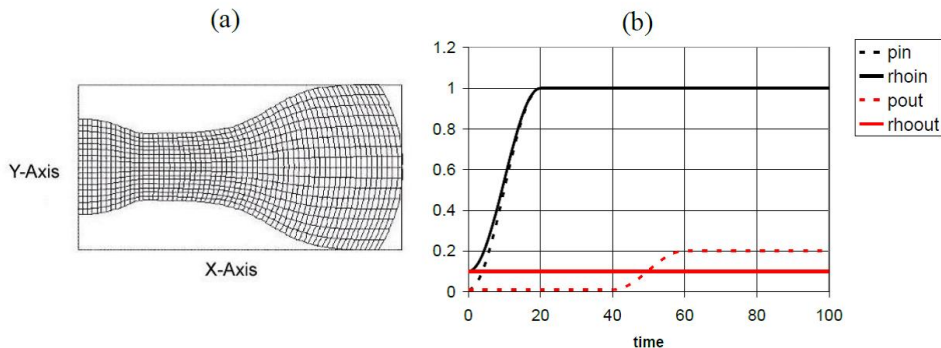
Figure 4.1: Converging-diverging channel simulation setup. Panel (a) shows a representative mesh and the problem geometry. Note that the channel is infinitely long in the z-direction, and z-direction variations are assumed to be zero. Panel (b) shows the exterior values for the inlet and outlet as a function of time. (Units of space, time, density and pressure are all normalized.)

Spatial resolution and time advance

The computational grid has 16 cells in the vertical direction, and 64 cells in the axial direction. Each cell has 6th-degree polynomial representation in each direction. The grid is stretched as shown in 4.1(a). An adaptive time step is used. The time step size is initialized at $dt = 5 \times 10^{-2}$, and increases during the first five steps to the maximum allowed value of $dt = 0.1$, where it remains for the duration of the simulation.

4.1.2   Results

As the ambient pressure and density at the inlet are increased with time, the flow in the converging part of the channel is accelerated to sonic conditions at the throat. Supersonic flow develops in the diverging part of the channel and exits the right boundary where the ambient values are held fixed at the initial values. After the flow has reached steady state, ambient outlet pressure is raised, and a shock is pushed back into the channel. A new steady state develops and the shock stands in the diverging part of the channel. The progression from startup to standing shock is shown in Figure 4.2.
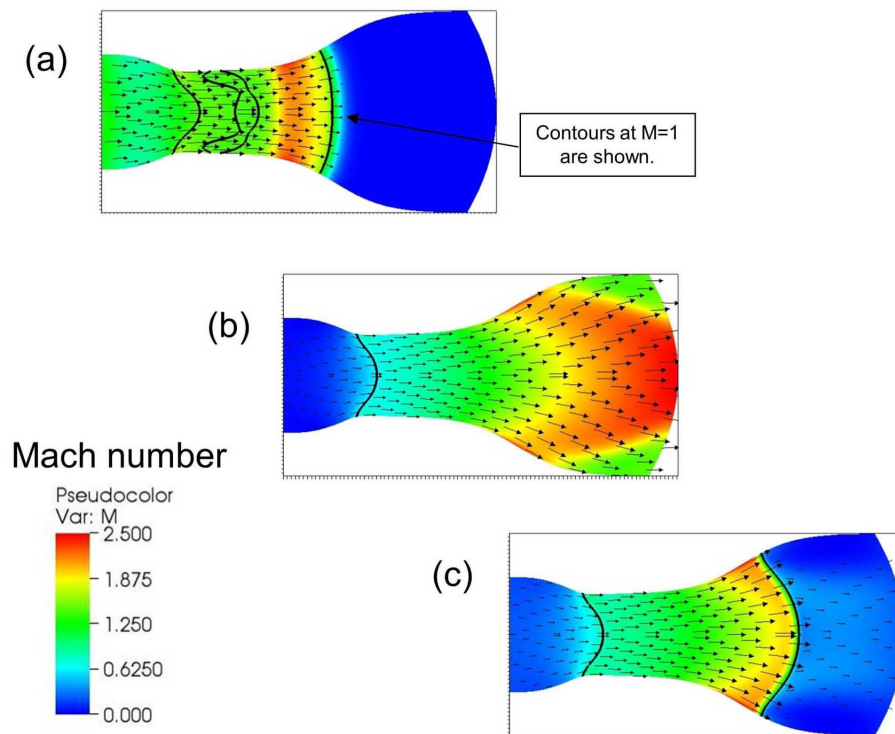
Figure 4.2: Progression of events in converging-diverging channel simulation. Arrows indicate velocity direction. Mach number is shown in pseudocolor. (a) Inlet pressure is ramped up and choked flow develops at throat. A shock moves toward the outlet. (b) Flow becomes supersonic and steady and is supersonic at outlet. (c) Outlet pressure rises and shock forms in channel. Simulated location agrees with analytical calculation.

The shock location is predicted analytically by assuming steady state 1D compressible flow, and allowing for variable area as a function of position. Following Fox and McDonald [71], the stagnation pressure is computed for the steady state HiFi solution (which occurs by time = 80) using the following formula: $p_0 = p(1 + (\gamma - 1)M^2/2)^{\gamma/(\gamma-1)}$. The stagnation pressure at the inlet is $p_{0,in} = 0.582$ and at the outlet is $p_{0,out} = 0.408$, measured at the channel centerline[1]. Using the table of normal shock flow functions in Fox and McDonald [71], the upstream and downstream Mach numbers, can be found as $M_{up} = 2.195$ and $M_{down} = 0.548$. The area ratio A/A^*, where A is the channel area at the shock and A^* is the area at the channel throat, can be found according to

$$\frac{A}{A^*} = \frac{1}{M} \left[\frac{1 + \frac{\gamma-1}{2}M^2}{1 + \frac{\gamma-1}{2}} \right]^{\frac{\gamma+1}{2(\gamma-1)}} . \tag{4.1}$$

Inserting the upstream Mach number yields $A/A^* = 1.996$. The distance across the diverging part of the channel as a function of the distance, x, from the throat is $d = 2 + 1.5[\tanh(0.8x - 3) - 0.995]$. The distance across the channel at the throat is $d^* = 2$. Solving for the position x that satisfies $d(x)/d^* = A/A^* = 1.996$, the analytical shock location is found to be $x_s = 4.18$. In the steady state HiFi solution [see Figure 4.2(c)], the location of the standing shock (indicated by the M=1 contour) extends axially from $x = 4.20$ (at the channel wall) to $x = 5.13$ (at the channel centerline). The HiFi result agrees well with the analytical result at the channel wall. Presumably, 2D effects cause the deviation at the centerline.

4.2 1D and 2D pressure pulse propagation

These pressure pulse propagation problems provide a simple gasdynamics test for comparing the performance of the four open boundary conditions presented in Section 3.2.

In the following description of the computational setup and results, physical values are presented in normalized units.

---

[1]One might expect that the stagnation pressures would be dictated by the ARBC ambient conditions. At the inlet, for example, the ambient pressure at late times is p=1 [see Figure 4.1(b)], and the ambient velocity is zero. In accordance with the formula given above, the ambient stagnation pressure is 1. This is different than the measured value of $p_{0,in} = 0.582$. ARBC do not exactly dictate conditions in the interior domain.

4.2.1 Computational setup

Geometry and initial condition

Figure 4.3 depicts the setup for the 2D pressure pulse problem with boundaries at $x = 1$ and $y = 1$. The 1D pressure pulse problem is the restriction of the 2D problem to $y = 0$. A pressure pulse is initialized at the center of the domain. The fluid is initially at rest and has uniform temperature. Background pressure and density are $p_0 = \rho_0 = 1$.

A localized perturbation with peak pressure $p_{max} = p_0 + \delta$ and peak density $\rho_{max} = \rho_0 + \delta$ is initialized at the center of the domain, as shown in Figure 4.3. The pressure/density perturbation varies radially from $x = 0$, $y = 0$ as a "bump" function, $\exp[1 - 1/[1 - (r/\lambda)^2]$, where $r = \sqrt{x^2 + y^2}$, and $\lambda = 0.3$, resulting in a perturbation that is isolated within $r = 0.3$.[2] Small and large perturbations, $\delta = 10^{-3}$ and $\delta = 0.5$, are used to test linear and nonlinear regimes.

Dissipation

In all cases, the dissipation coefficients are $\xi = \kappa = 10^{-3}$. Thermal conductivity is isotropic. $D_\rho = 0$ for these runs.

Boundary conditions

Symmetry BC are used at the bottom and left boundaries, and open BC are applied at the top and right boundaries. The wave speed used to dictate the LOBC truncation is the sound speed in the background fluid, $c_s = \sqrt{\gamma p_0/\rho_0}$, where $\gamma = 5/3$ is the ratio of specific heats.

Spatial resolution and time advance

The computational grids have eight cells per unit length, each with 4th-degree polynomials. The time step size is fixed as $dt = 10^{-2}$.

---

[2]An advantage of the bump function is that the transition between the bump function and the uniform solution at $r = \lambda$ is perfectly smooth, i.e., infinitely differentiable.
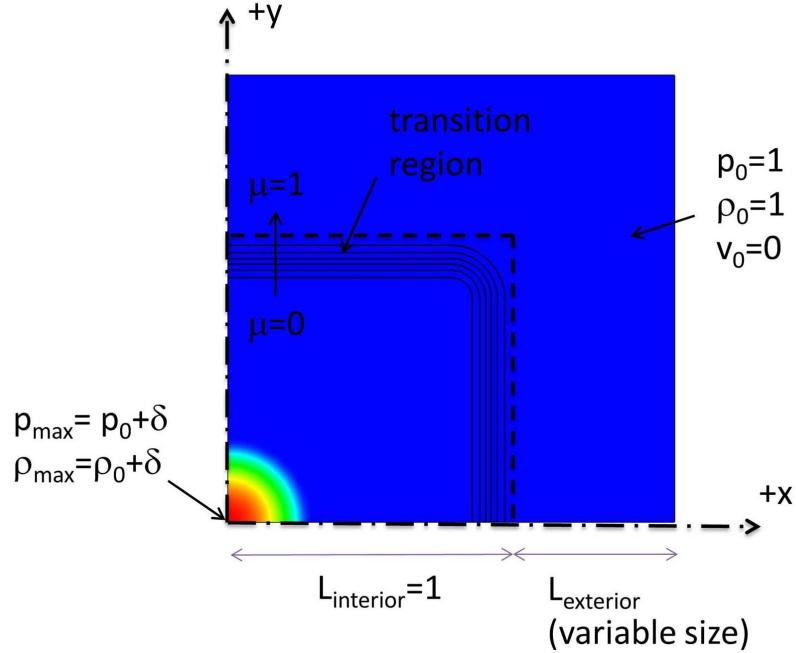
Figure 4.3: Computational domain and initialization for 2D pressure pulse propagation. The 1D pressure pulse problem is the restriction of the 2D problem to $y = 0$. Symmetry BC are used at $x = 0$ and $y = 0$. Open BC are used at the $x = 1$ and $y = 1$. Initial pressure is shown in pseudocolor. For ARBC, ZND BC, and TBC tests, only the interior (i.e., the region inside the heavy dashed line) is modeled. For the LOBC, the interior and exterior are modeled. The LOBC transition region is at the edge of the interior region, where $0.75 < x < 1$ and $0.75 < y < 1$. Solid contours indicate the value of the transition function, μ. Simulations with $L_{ext} = 0.5$ and 2.0 are run.

4.2.2   Results

Open BC performance is measured in terms of the L_∞-norm of the pressure error (i.e., the maximum error) in the simulations. The normalized L_∞ error is

$$L_\infty(t) = \frac{\max[p(x, y, t) - p_0(x, y, t)]}{p_{max}}, \tag{4.2}$$

where $p_0(x, y, t)$ is the reference solution, which is computed on an extended domain to prevent boundary effects, and p_{max} is the maximum pressure in the reference simulation. For these results, p_{max} is the maximum initial pressure: $p_{max} = 1 + \delta$.

Figure 4.4 shows a series of snapshots of the absolute value of the perturbed pressure $(p - p_0)$ for the pulse case with ARBC domain truncation. The nonlinear case $(\delta = 0.5)$ is depicted. The reason for plotting the absolute value of the perturbed pressure is that a logarithmic scale can be used to help reveal small reflections. The pressure pulse expands, leaving a qualitatively uniform solution in its wake. As the pulse passes through the boundaries, no reflection is readily observable. Late in time, small pressure deviations caused by reflections are seen in the domain. Qualitatively, results are similar for TBC and LOBC. Figure 4.5 shows snapshots for the same run except with ZND BC, and more significant pressure deviations are seen.

Figure 4.6 presents 1D results for linear $(\delta = 10^{-3})$ and nonlinear $(\delta = 0.5)$ cases. In 1D, errors for ARBC, TBC, and LOBC are higher in the nonlinear case. ARBC and TBC are, as discussed in Sections 3.2.1 and 3.2.2, based on linearization of the problem, and lose effectiveness for nonlinear waves (except for simple waves), as shown by results in Figure 4.6. As discussed in Section 3.2.3, the accuracy of LOBC is reduced in the regime between linear $(\delta \ll 1)$ and highly nonlinear $(\delta \gg 1)$ extremes. This reduced accuracy explains the higher error for LOBC in the nonlinear case. The linear and nonlinear results in 2D are presented in Figure 4.7. The fact that the results are nearly identical implies that the main source of error is not the nonlinearity for any of the open BC in 2D. For LOBC, the higher error seen in the 2D results is presumably because of the lack of true lacunae in 2D. For ARBC and TBC, higher error is also seen in 2D, possibly because of the oblique nature of the waves interacting with the boundary — both ARBC and TBC are designed to treat only waves traveling in the normal direction. Oblique waves can cause reflections. For ZND BC, higher error is seen in the 1D results than in the 2D results. In two dimensions, the wave strength diminishes as the wave spreads radially, but the strength remains constant in one dimension. In 2D, a weaker wave interacts with the BC, and less reflection occurs.

The following conclusions can be drawn from the pressure pulse propagation results. ZND BC results show high L_∞ error in 1D and 2D as compared to the other two open
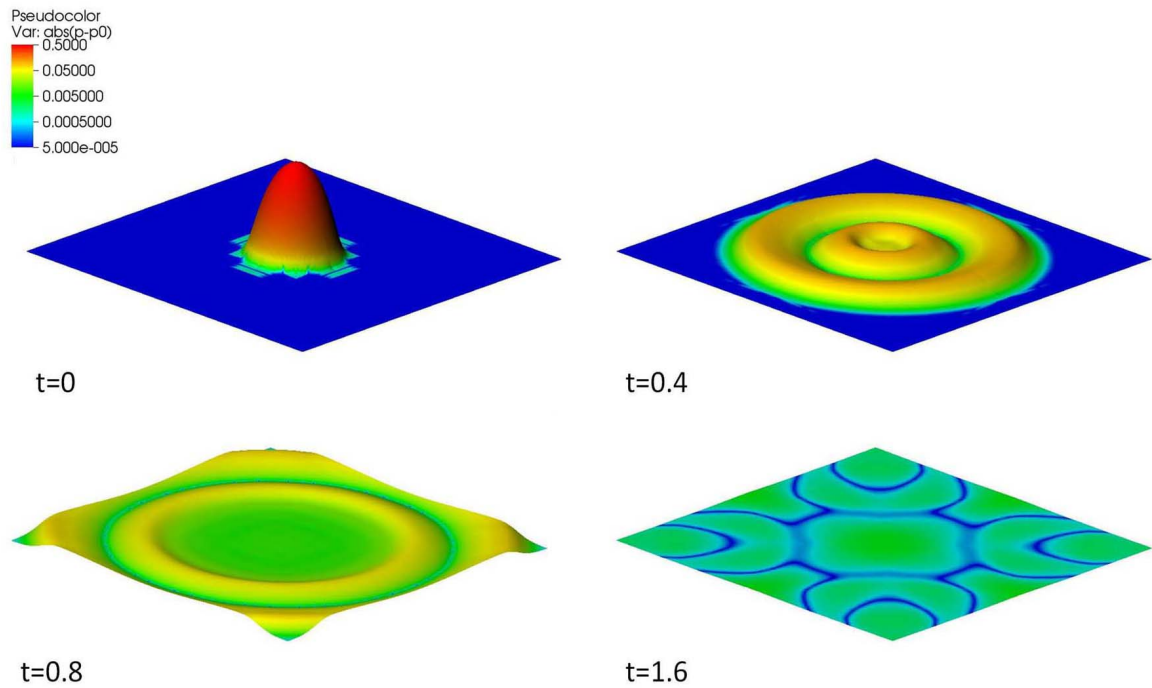
Figure 4.4: Snapshots of the absolute value of the perturbed pressure $(p - p_0)$ for the nonlinear pressure pulse problem with ARBC domain truncation. At time $t = 0$, the initial condition is seen in the 1×1 square domain. At $t = 0.4$ and $t = 0.8$, a pressure wave expands and passes through the open boundary. The ARBC produces no observable reflection until late in time. At $t = 1.6$, small perturbations are observed to persist in the domain.
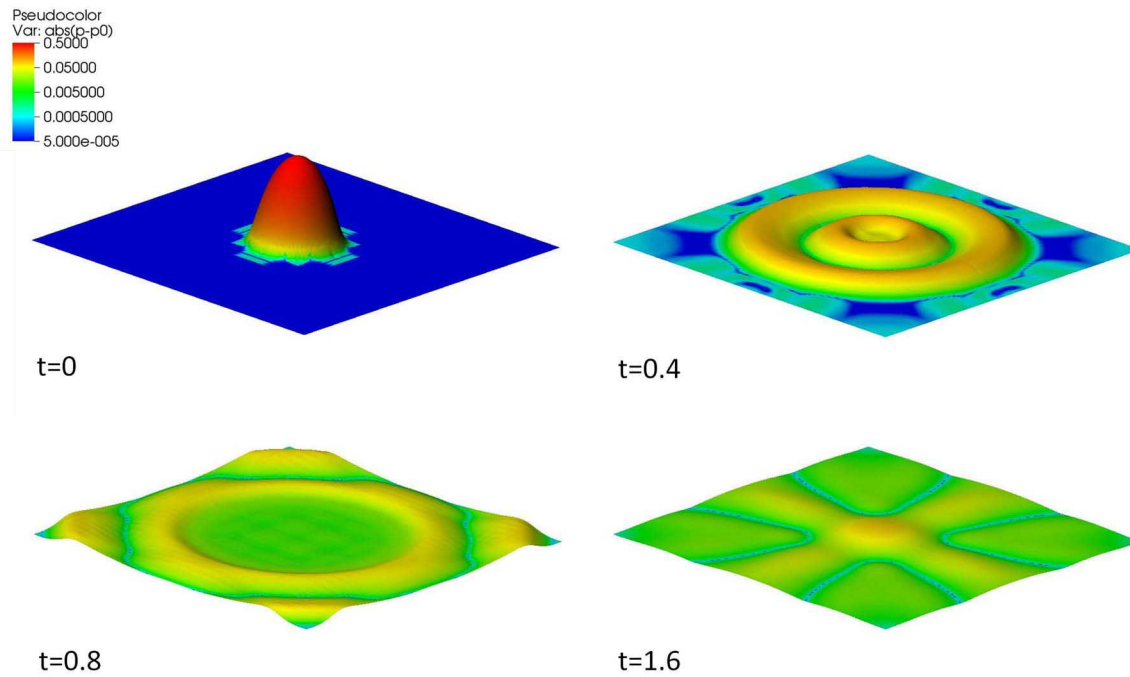
Figure 4.5: Snapshots of the absolute value of the perturbed pressure $(p - p_0)$ for the nonlinear pressure pulse problem with ZND BC domain truncation. As the pressure wave passes through the open boundary at $t = 0.8$, spurious boundary effects are observable. At $t = 1.8$, reflections from the ZND BC are much more pronounced than in the other open BC cases. Relatively small reflections are seen in the ARBC case shown in Figure 4.4.
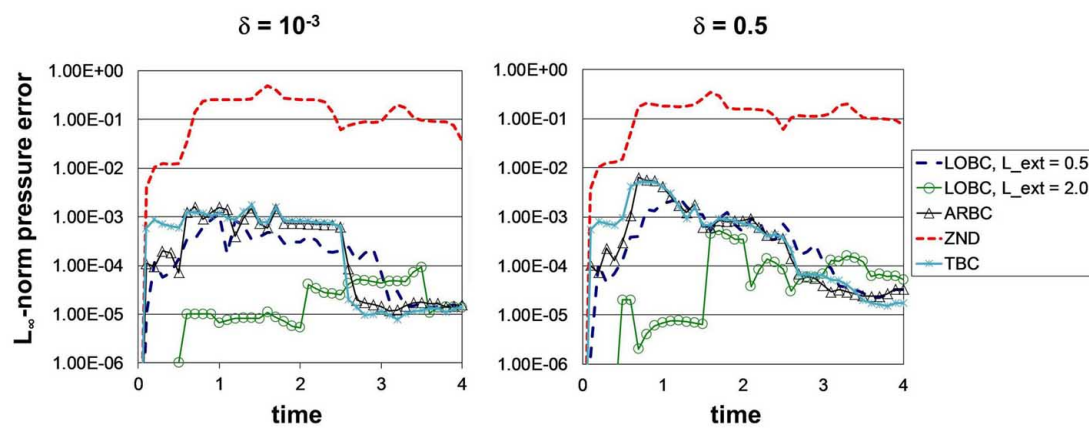
Figure 4.6: 1D pulse problem results for linear ($\delta = 10^{-3}$) and nonlinear ($\delta = 0.5$) cases. L_∞ error, measured with respect to reference cases, is plotted vs. normalized time. For ARBC, TBC, and LOBC, error increases in the nonlinear case, but remains below 1%. Errors for ZND BC are over an order of magnitude higher than all other open BC options. LOBC with $L_{ext} = 2.0$ performs best for both cases with error less than 0.1%.
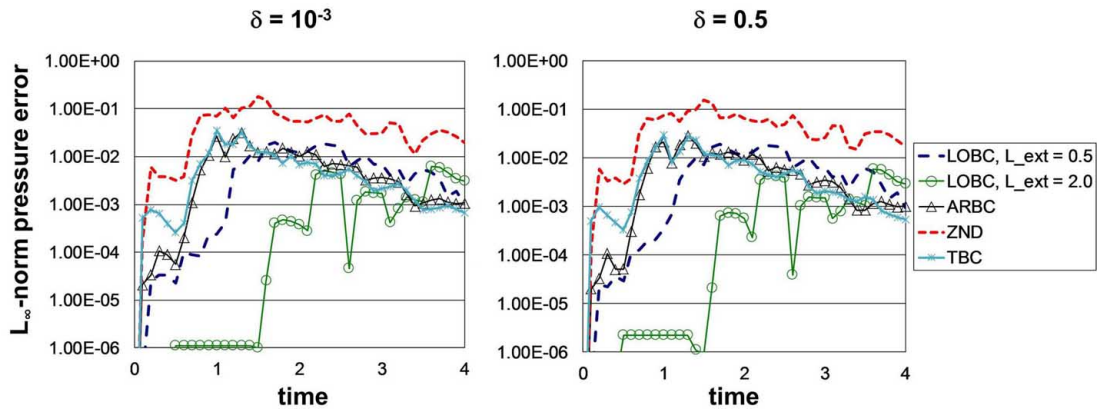
Figure 4.7: 2D pulse problem results for linear ($\delta = 10^{-3}$) and nonlinear ($\delta = 0.5$) cases. L_∞ error, measured with respect to reference cases, is plotted vs. normalized time. Errors are nearly identical for linear and nonlinear cases, suggesting that the nonlinearity is not the main source of error for any of the open BC in 2D (see discussion in text). ZND BC produce errors an order of magnitude higher than the other open BC. LOBC with $L_{ext} = 2.0$ performs best for both cases with error less than 1%.

BC considered. ARBC and TBC performance is similar, and is comparable to LOBC with $L_{ext} = 0.5$. The LOBC with $L_{ext} = 2.0$ consistently performs best for 1D, 2D, linear, and nonlinear cases.

4.3   Field-reversed configuration translation

An overview of the field-reversed configuration (FRC) is presented in Section 1.5. FRC translation is important for various experiments including the electrodeless Lorentz-force (ELF) thruster program [72], which is presented in detail in Section 6.4.[3] The ELF thruster concept generates thrust by repeated FRC formation, high-speed translation, and ejection. An open BC is appropriate for ELF modeling. This problem addresses the challenge of allowing an FRC plasma to exit an open boundary.

In the following description of the computational setup and results, physical values are presented in normalized units.

4.3.1   Computational setup

Geometry and initial condition

The FRC translation problem is depicted in Figure 4.8. The initial condition for this problem is generated using a numerical equilibrium solver developed by Marklin [73], which is described in Section 1.5. The open-field-line equilibrium pressure is truncated, as discussed in Section 1.5, so that the FRC is isolated. The peak density and pressure of the FRC are $\rho_{max} = 1$ and $p_{max} = 1$. Density is initialized as the square root of pressure. The background pressure and density are $p_0 = 5 \times 10^{-3}$ and $\rho_0 = 0.071$. The magnetic field strength at the ends of the interior domain, where the field has no axial variation, is $B_{end} = 0.6$. The initial velocity of the FRC and background plasma is $v_0 = 1$, which is the peak thermal speed.

---

[3]Simulations in Section 6.4 focus on application of the plasma-neutral model derived in Chapter 5. To minimize the complexity of the simulation and focus attention on the plasma-neutral interaction, periodic BC are used at the axial ends instead of the open BC as discussed in the present section.
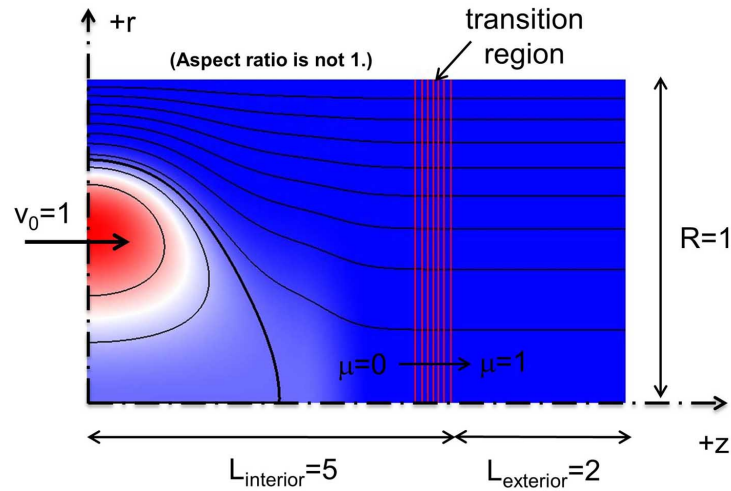
Figure 4.8: FRC translation simulation setup. The right half of the computational domain is shown. The initial condition has left-right symmetry. Pressure is shown in pseudocolor. Black contour lines show the poloidal magnetic flux. A single bold black contour indicates the separatrix. Uniform axial velocity, $v_0 = 1$, is given to the FRC and the low-density background plasma. ARBC, TBC, and ZND BC simulations use only the interior domain. For the LOBC, the interior and exterior are modeled. The LOBC transition region is at the edge of the interior region, where $4 < x < 5$. Red vertical contour lines show the transition function, μ.

Dissipation

Values for dissipation coefficients are $D_\rho = 5 \times 10^{-3}$, $\kappa_\parallel = 1$, $\kappa_\perp^m = 0.01$, $\xi = 0.01$, and $\eta = 2 \times 10^{-3}$. The parallel thermal conduction is relatively high, as physically expected in magnetized plasma.

Boundary conditions

The open BC options are applied at the left and right ends of the cylindrical domain. The wave speed used to dictate the LOBC truncation is the fast MHD wave speed in the background fluid, c_f, found by the relation $c_f^2 = \left(\gamma p_0 + B_{end}^2/2\right)/\rho_0$, where $\gamma = 5/3$ is the ratio of specific heats.

    In terms of the dependent variables and the boundary normal ($\hat{\mathbf{n}}$), the radial wall BC are: $\hat{\mathbf{n}} \cdot \mathbf{v} = 0$ (hard wall); $(\hat{\mathbf{n}} \cdot \nabla)(\hat{\mathbf{n}} \times \mathbf{v}) = 0$ (perfect slip); $\hat{\mathbf{n}} \times \partial \mathbf{A}/\partial t = 0$ (perfectly conducting); $\hat{\mathbf{n}} \cdot \left[\kappa_\parallel \hat{\mathbf{b}}\hat{\mathbf{b}} + \kappa_\perp \left(\mathbb{I} - \hat{\mathbf{b}}\hat{\mathbf{b}}\right)\right] \cdot \nabla T = 0$ (thermally insulating); and zero density flux, which, given $\hat{\mathbf{n}} \cdot \mathbf{v} = 0$, essentially enforces $\hat{\mathbf{n}} \cdot \nabla \rho = 0$ because of the artificial density diffusion term in Eqn. (1.12).

    As mentioned in Section 3.2.3, for LOBC, ideally, the external region size (L_{ext}) should not match the dissipation scale length. In the pressure pulse problems shown, the dissipative scales are much smaller than L_{ext}, but here, parallel thermal conduction is high. The relevant dissipation scale length can be estimated as $L_\kappa \approx (T_{ext}\kappa_\parallel)^{1/2}$, where T_{ext} is the time that source terms are kept in the LOBC, in this case, $T_{ext} = L_{ext}/c_f \approx 0.39$. Therefore, $L_\kappa \approx 0.62$, while $L_{ext} = 2.0$.

Spatial resolution and time advance

The computational grids have two cells per axial unit axial length, and eight cells per unit radial length, and each cell has 6th-order polynomials. The time step is fixed as $dt = 10^{-2}$.

4.3.2   Results

Open BC performance is measured in terms of the L_∞-norm of the pressure error (i.e., the maximum error) in the simulations. The normalized L_∞ error is

$$L_\infty(t) = \frac{\max[p(x,y,t) - p_0(x,y,t)]}{p_{max}}, \qquad\qquad (4.3)$$

where $p_0(x,y,t)$ is the reference solution, which is computed on an extended domain to prevent boundary effects, and p_{max} is the maximum pressure in the reference simulation. For these results, p_{max} is the maximum initial pressure: $p_{max} = 1$.

The qualitative solution behavior is seen in Figure 4.9, which shows a series of snapshots of pressure for the run with LOBC domain truncation alongside snapshots from the reference case. The LOBC damps the solution effectively, and no reflection is observable in these snapshots. Snapshots for ARBC and TBC cases, which fail early in the simulation as discussed below, are not shown. Snapshots for the ZND BC case are qualitatively similar to the LOBC case.

Quantitative results for FRC translation are given in Figure 4.10. The ARBC and TBC runs fail quickly; strong thermal conduction parallel to magnetic field lines interacts non-physically with these hyperbolic-based open BC and numerical instabilities result. Although the $L_\kappa \ll L_{ext}$ condition is not satisfied, the maximum LOBC error is only 2%. While strong dissipation can cause reflection error, perhaps the dissipation significantly smoothes that error. The ZND BC run is numerically stable, and the maximum L_∞ error is 3%.

4.4 Coaxial-electrode plasma acceleration

Coaxial-electrode plasma acceleration is a process common to a variety of plasma experiments and applications including plasma formation in the ZaP flow Z-pinch experiment [43], magnetoplasmadynamic (MPD) thrusters [6, 74], and plasma gun spheromak formation [75, 76] to name a few.

In the following description of the computational setup and results, physical values are presented in normalized units.
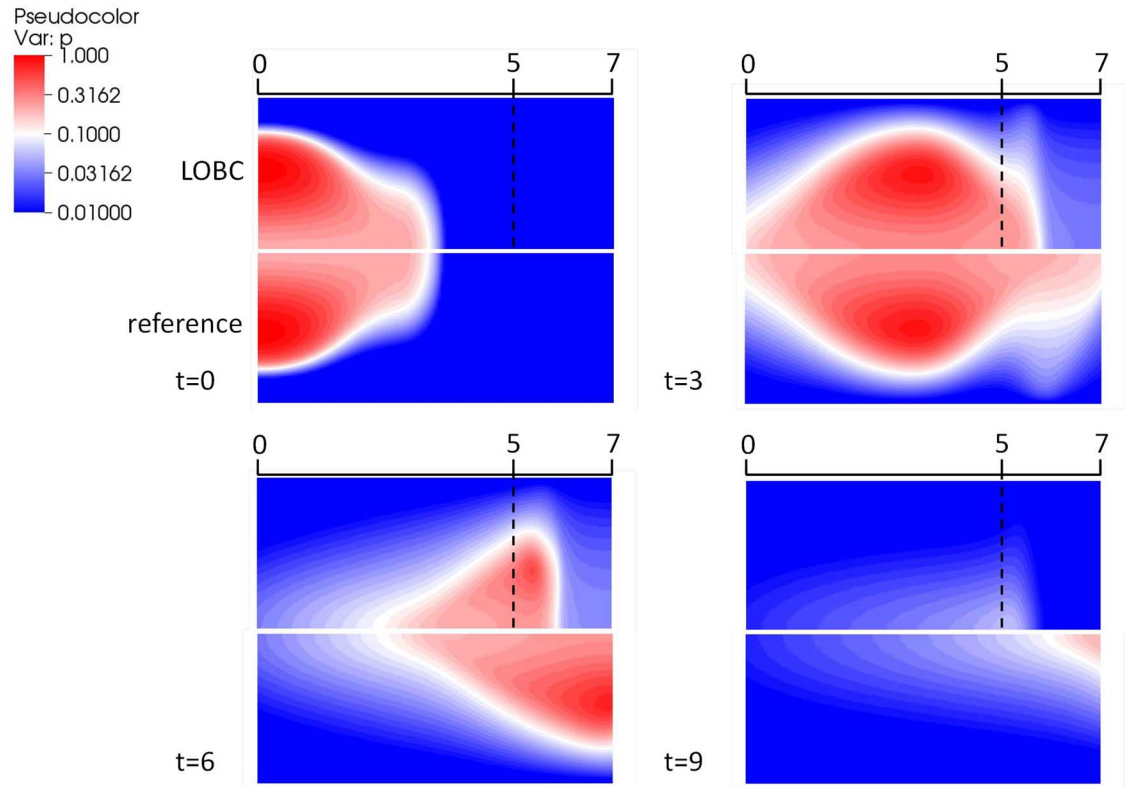
Figure 4.9: Snapshots of pressure in the FRC problem comparing LOBC to reference case. Only the right half of the computational domain is shown — the portion with $z > 0$. The solution for the LOBC case is shown in the upper part of each snapshot, and the reference case is shown in the lower part with the domain reflected across the cylindrical axis. (The reference domain actually extends to $z = 14$.) The interior region is between $z = 0$ and $z = 5$, and the interior-exterior boundary is indicated with a dashed line. By time $t = 3$, the FRC edge reaches the interior-exterior boundary. The LOBC has significantly damped the solution at $t = 6$. The solution is nearly completely damped by $t = 9$.
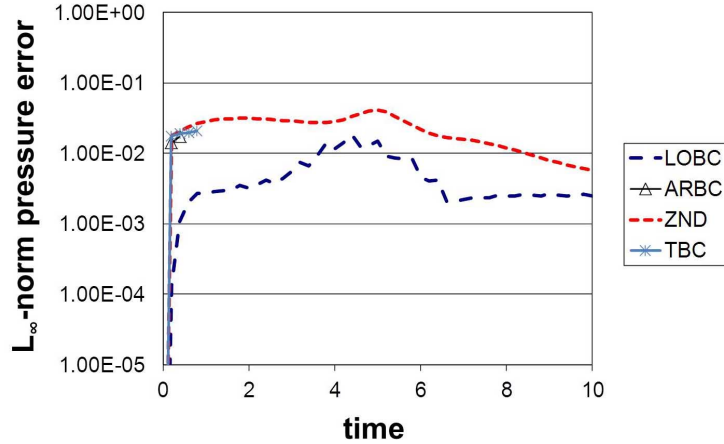
Figure 4.10: Results for FRC translation simulation. L_∞ error, measured with respect to a reference case, is plotted vs. normalized time. Only a few data points are shown for ARBC and TBC which quickly fail due to dissipative effects. LOBC error is 2% vs. 3% for ZND BC.

4.4.1 Computational setup

Geometry and initial condition

The plasma acceleration problem setup is shown in Figure 4.11. The geometry and plasma acceleration parameters are similar to those present in the ZaP acceleration region. The background pressure and density are $p_0 = 10^{-3}$ and $\rho_0 = 0.1$. A density concentration with peak density $\rho = 5$ is centered at a distance of 0.2 from the left boundary. A bump function, $\exp[1 - 1/[1 - (z'/\lambda)^2]]$, where $z' = z - 0.2$ and $\lambda = 0.1$, is used to isolate the density concentration between $z = 0.1$ and $z = 0.3$.

Dissipation

Dissipation coefficients are $D_\rho = 2 \times 10^{-3}$, $\kappa = 0.04$ (isotropic thermal conduction), $\eta = 2 \times 10^{-3}$, and $\xi = 0.04$.
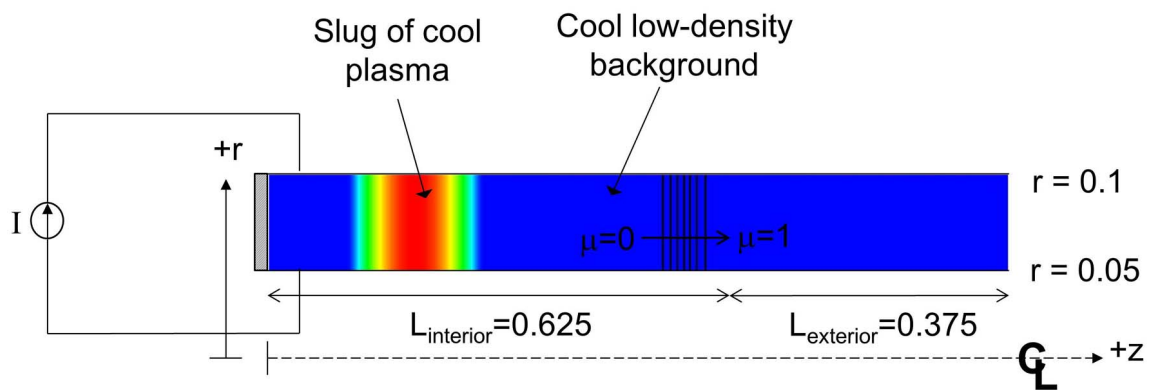
Figure 4.11: Coaxial plasma acceleration simulation setup. As shown in pseudocolor, density is concentrated in a "slug" with near the left boundary. The peak density is $\rho = 5$. A current supply drives flux injection through an insulating boundary at the left end. A current sheet forms, and the plasma slug is heated and driven axially toward the open boundary at the right end. For ARBC, TBC, and ZND BC tests, only the interior is modeled. For the LOBC, the interior and exterior are modeled. The LOBC transition region is at the edge of the interior region, where $0.5 < z < 0.625$. Black vertical contour lines show the transition function, μ.

Boundary conditions

Flux injection is achieved by specifying the azimuthal magnetic field on the left boundary with an inverse radial dependence, $B_\theta(r,t) = B_0(t)\frac{a}{r}$, where a is the radius of the inner electrode. In this way, the total current driven between the electrodes is specified as $I = 2\pi a B_0(t)$. Additional BC at the left boundary are $\hat{\mathbf{n}} \cdot \mathbf{v} = 0$ (hard wall), $\hat{\mathbf{n}} \times \mathbf{v} = 0$ (no-slip), $\rho = \rho_0$ (fixed density), and $\hat{\mathbf{n}} \cdot \nabla p = 0$ (zero normal derivative of pressure). A resistive layer is present near the left boundary, facilitating the diffusion of magnetic flux into the domain. From an axial distance of 0.1 from the left boundary, η rises from 2×10^{-3} to 0.1 at the left boundary. The functional form of the rise is a half-period (trough to crest) of a sinusoid.

Open BC are used at the right boundary. The plasma accelerates to a maximum speed of approximately 6.67 times the background sound speed, c_s. Therefore, the speed used to dictate LOBC truncation is $6.67c_s$.

At the inner and outer electrodes, the BC are identical to those applied for the FRC problem described in Section 4.3 — hard wall, perfect slip, perfectly conducting, thermally insulating, and zero density flux.

Spatial resolution and time advance

The computational grids have 64 cells per unit axial length (i.e., 40 cells in the interior domain, which has a length of 0.625), and 4 cells across the radial extent of 0.05. Each cell has 6th-degree polynomials. A fixed time step size of 5×10^{-4} is used.

Special conditions

A cyclic simulation is performed. Current is cycled up and down, and a cyclic density source, approximating gas injection and ionization, is used to replenish the plasma. The density source has the same spatial profile as the original slug, and the total density added in each cycle is equal to the original density. The current and density source profiles are shown in Figure 4.12. The maximum enclosed current is $I_{max} = 1.9$. In this scenario, without an open BC, after many cycles, a prohibitively large computational domain would be required to prevent the influence of reflections from the downstream boundary on the solution in the
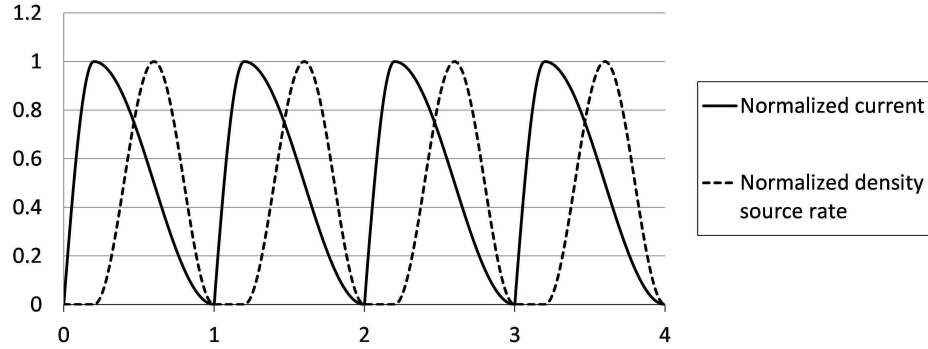
Figure 4.12: Profiles of the cyclic current and density source rates (normalized by their respective maximum values) for the coaxial plasma acceleration problem. Over each normalized time unit, current is sinusoidally ramped up and down. After the current has swept downstream, the density source replenishes the plasma at the location of original concentration.

"interior" region shown in Figure 4.11.

4.4.2 Results

Open BC performance is measured in terms of the L_∞-norm of the pressure error (i.e., the maximum error) in the simulations. The normalized L_∞ error is

$$L_\infty(t) = \frac{\max[p(x,y,t) - p_0(x,y,t)]}{p_{max}}, \tag{4.4}$$

where $p_0(x,y,t)$ is the reference solution, which is computed on an extended domain to prevent boundary effects, and p_{max} is the maximum pressure in the reference simulation. For these results, the maximum pressure, $p_{max} = 4.27$, occurs at $t = 0.24$.

The solution behavior is seen in Figure 4.13, which shows snapshots of pressure during the first acceleration cycle for case with the LOBC alongside snapshots from the reference case. The LOBC damps the solution effectively. There is no observable reflection in these snapshots. Snapshots for the ARBC and TBC cases, which fail early in the simulation as discussed below, are not shown. Snapshots for the ZND BC are qualitatively similar to the

LOBC case.

The L_∞ results during four plasma acceleration cycles (per Figure 4.12) are shown in Figure 4.14. As in the FRC translation problem, in the presence of significant dissipation, the ARBC and TBC fail. Again, LOBC outperform ZND BC. In the first acceleration event, which has peak kinetic energy at $t \approx 0.4$, error for the LOBC is 0.7% and 6% for the ZND BC. For later acceleration events at $t \approx 1.4$, 2.4, and 3.4, reflection is higher for LOBC and ZND BC. This can be explained by the fact that current sheet propagation speed is sensitive to the low-density plasma wake left behind the previously accelerated sheet. The ZND BC allows the low-density plasma to deviate from the reference case, causing L_∞ error near 100% for the second, third, and fourth acceleration events. The LOBC gives current sheet wake properties closer to the reference case, and error for the second, third, and fourth acceleration events ranges from 2% to 17%.

The reference case for the four-cycle coaxial plasma acceleration run required a domain length of 8. The total computational time required for the reference case and the LOBC case is similar — two hours on 64 processors. The ZND BC case requires 20 minutes on 64 processors. If the LOBC technique is optimized to avoid the inefficiencies described in Section 3.2.3, the computational effort for the optimized LOBC can be estimated. In this case, the auxiliary domain is 80% the size of the interior domain. Optimized LOBC time stepping (including integration and reintegration) should require only twice the effort of normal integration (see Figure 3.2). Estimating the additional effort as $80\% \times 2 = 160\%$ and total effort as $160\% + 100\% = 260\%$ of the ZND BC case, the approximate computational time on 64 processors is 20 minutes $\times$ 2.6 = 52 minutes — a significant savings compared to the four cycle reference run.
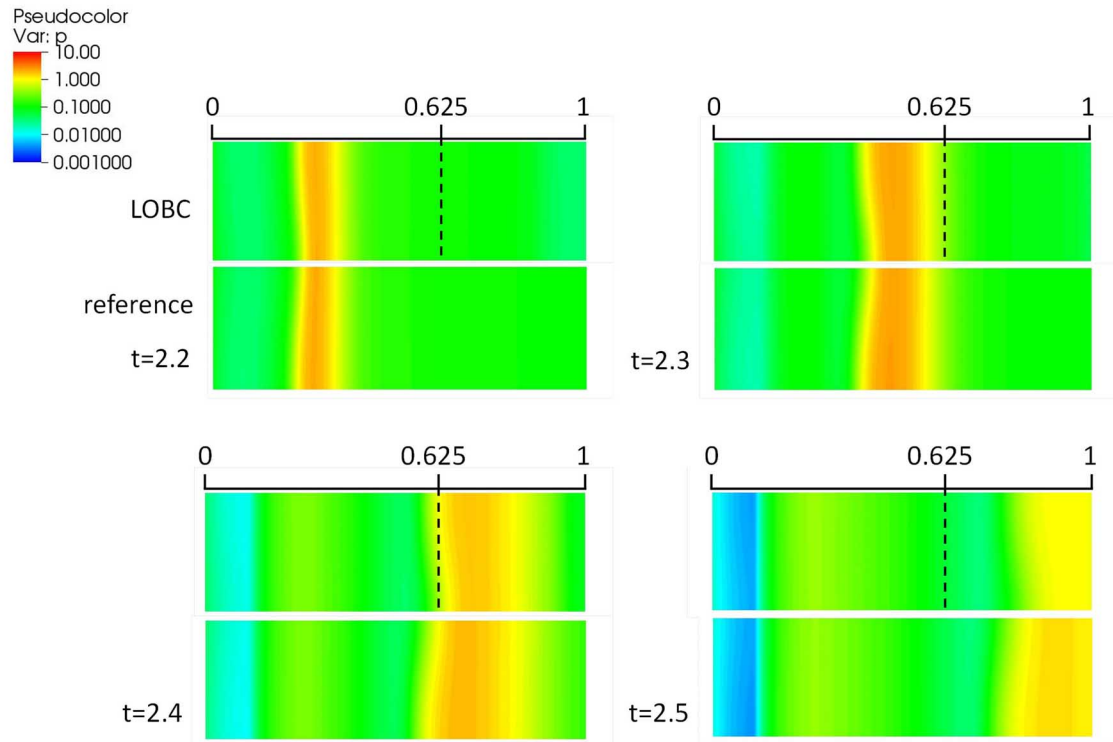
Figure 4.13: Snapshots of pressure in the coaxial-electrode plasma acceleration problem comparing LOBC to reference case. The interior region is between $z = 0$ and $z = 0.625$, and the interior-exterior boundary is indicated with a dashed line. The solution for the LOBC case is shown in the upper part of each snapshot, and the reference case is shown in the lower part with the domain reflected across the cylindrical axis. (The reference domain actually extends to $z = 8$.) At $t = 2.2$, the third cycle is beginning. By $t = 2.4$, the high-pressure accelerated plasma has passed through the interior-exterior interface. At $t = 2.5$, the accelerated plasma pressure has been significantly damped by the LOBC, and will be almost completely damped before affecting the interior solution.
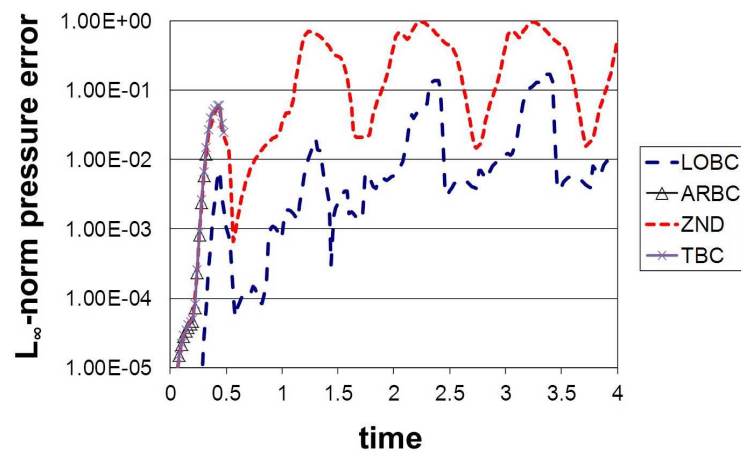
Figure 4.14: Results for four cycles of coaxial-electrode plasma acceleration. L_∞ error, measured with respect to a reference case, is plotted vs. normalized time. Dissipation causes numerical instability of ARBC and TBC around $t = 0.5$. ZND BC and LOBC are stable with maximum L_∞ errors near 100% and 10%, respectively.

Chapter 5

MODELING NEUTRAL FLUID EFFECTS IN COLLISIONAL PLASMAS

In the edge region of magnetically confined fusion plasma, where the neutral particle population is high, the role of neutrals can be crucial [77, 78, 79]. Neutrals can penetrate the hot plasma core and affect energy confinement in a variety of ways. For example, if a relatively cool (low-energy) neutral penetrates deep into the plasma and charge exchanges with a hot (high-energy) ion, the newly created hot neutral could travel across the confining magnetic fields and deposit its energy on the vacuum vessel wall. Also, penetrating neutrals are eventually ionized, in general, requiring an energy investment from the plasma. The textbook by Goldston and Rutherford [80] provides an insightful discussion of neutral penetration in plasmas. In some cases, neutral penetration is desirable. For instance, supersonic jets of neutral gas have been (and are being) explored on the spherical tokamaks NSTX [81] and MAST [82] as a possible mechanism for fueling burning plasmas. The presence of neutral gas can also have important effects on space plasmas such as cometary ionospheres [83], the heliopause [84, 85], and the solar corona [86]. Section 5.1 discusses past plasma-neutral modeling research.

A reacting plasma-neutral model has been developed that combines a single-fluid MHD approach for the plasma with a gasdynamic fluid treatment for the neutrals. This approach was first presented by Shumlak [87]. The model accounts for electron-impact ionization, radiative recombination, and resonant charge exchange (CX):

$$
\begin{aligned}
e^- + n &\rightarrow i^+ + 2e^- - \phi_{ion} \\
e^- + i^+ &\rightarrow n + h\nu \\
i^+ + n &\rightarrow n + i^+
\end{aligned}
\tag{5.1}
$$
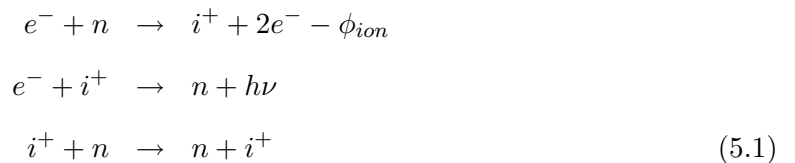
Single ionization and overall charge neutrality are assumed, and electron mass is neglected.

Only one type of atom, along with its daughter ions, is considered. The model allows separate densities, temperatures, and velocities for the plasma and neutral fluids. An optically thin plasma is assumed so that radiation energy due to atomic physics effects, such as de-excitation energy associated with radiative recombination, is lost from the system. To simplify the model, excited states are not tracked. Instead, an effective ionization potential, ϕ_{ion}, is assumed. This potential approximately includes the electron binding energy plus the excitation energy that is expended (on average) for each ionization event.

The model derivation is given in Section 5.2. Implementation of the model in 2D HiFi is discussed in Section 5.3. Several applications of the model are presented in Chapter 6.

5.1 Prior and foundational work

A seminal 1965 paper by Braginskii [11] describes derivation of plasma fluid equations by taking moments of the Boltzmann equation. This technique is the basis of the plasma-neutral model presented in this chapter. A model that allows reactions (charge exchange, recombination, and ionization), but assumes a cold, static neutral gas has been developed in previous research by this author [88]. Braginskii's 1965 paper includes a model for partially ionized gas; his model treats the plasma and neutral as a combined fluid, and does allow for reactions between species and associated species conversion. A linear two-fluid plasma-neutral model, but again without reactions and associated species conversion, is presented by Zaqarashvili et al. [86].

A variety of simulation tools have been developed to understand and predict behavior of edge plasmas in tokamaks and other fusion-grade plasmas. Two leading examples are UEDGE [89, 90] and B2 [91, 92]. These codes are based on a fluid description and are often coupled to Monte Carlo neutral transport codes such as DEGAS 2 [93], and Eirene [94]. Also, to determine turbulent transport, these codes, all 2D, are often coupled to 3D fluid codes. For example, UEDGE has been coupled to the turbulent transport code, BOUT [95]. Furthermore, these codes have been developed to treat impurity effects. Izzo et al. [96, 97] have developed an extension of the 3D NIMROD code called NIMRAD to model massive injection of impurity gas, which is used to quench dangerous disruptions in tokamaks. 0D and 1D models have been developed by You [82] to model refueling physics in tokamak-like

devices.

A model proposed by Helander et al. [98] uses a fluid moment approach similar to Braginskii, and shows detailed a derivation of neutral fluid transport coefficients assuming the neutral distribution function is CX-dominated. In deriving transport coefficients, the neutral viscosity and thermal conductivity coefficients have components that are inversely proportional to the CX frequency, whereas if neutral-neutral scattering collisions are assumed dominant, viscosity and thermal conductivity coefficients are inversely proportional to the scattering frequency. The principal result of Helander et al. is a combined-fluid ion-neutral model[1] that employs CX-related neutral transport coefficients. Section 5.3 and Appendix G contain additional discussion of transport.

Several models have been developed to simulate the interaction of the solar wind with the local interstellar medium (see review by Zank [99]). Pauls et al. [84] develop a fluid model that includes charge exchange effects, neglects ionization and recombination, neglects transport, and assumes that no electromagnetic fields are present. Baranov and Malama [100] present a steady state model that uses a Monte Carlo approach for handling collision integrals.

The development of models for partially ionized gas has primarily focused on specific problems like tokamak edge physics or the interaction of the solar wind with the heliopause. A model or code suitable for capturing the primary fluid effects of ionization, recombination, and charge exchange in a variety of plasma science problems is not described in literature. This fact motivates the model and code development research presented in this chapter. In Table 5.1, the features of several models are compared. As seen, the plasma-neutral model implemented in HiFi lacks the specialized magnetic fusion edge plasma (especially tokamak-related) features of B2 and UEDGE, but has generality that makes it unique. In Section 5.3, where the HiFi plasma-neutral implementation is presented, differences between the HiFi plasma-neutral implementation and the alternative models are highlighted.

---

[1]The electron fluid is not included in the analysis by Helander. In an implementation of this model, an electron fluid equation would be either solved separately or included with the ion fluid.

Table 5.1: Comparison of models for partially ionized gas. For a variety of models, the presence or absence of several general features is indicated by "Y" if the feature is present and "N" if it is not. The models by Pauls, Zaqarashvili, and Helander have full neutral momentum equations as does the HiFi plasma-neutral implementation described in this chapter. The models used in UEDGE and B2 have a variety of sophisticated features relevant in the magnetized edge of tokamak (and similar) plasmas, including tokamak-like drift transport. The models by Braginskii and Zaqarashvili do not allow for reactions and associated species conversion. The Pauls and Zaqarashvili models do not address transport. UEDGE and B2 have transport models suited for tokamak-like edge plasmas. The transport model used in the HiFi plasma-neutral model is discussed in detail in this chapter and is compared to the Braginskii and Helander transport models.

	UEDGE [89, 90] and B2 [91, 92]	Pauls [84]	Braginskii [12]	Zaqarashvili [86]	Helander [98]	HiFi plasma-neutral
full neutral momentum	N[1]	Y	N	Y	N	Y
tokamak drift transport	Y[2]	N	N	N	N	N
species conversion	Y	Y	N	N	Y	Y
transport	Y[3]	N	Y[4]	N[5]	Y[6]	Y

1. These codes have "inertialess" models for plasma and neutral perpendicular momentum. Details are available in cited works.

2. These codes take into account convective transport due to particle drifts. Details are available in cited works.

3. These codes use either specialized fluid models for diffusion of neutral density, or Monte Carlo calculations to determine transport.

4. Braginskii makes suggestions, but does not write explicit expressions for transport coefficients for his combined plasma-neutral model.

5. The Zaqarashvili model is linearized and does not address transport.

6. The Helander model uses neutral transport coefficients derived assuming a CX-dominated neutral distribution.

5.2   Model derivation

This derivation is separated into three parts: in Section 5.2.1, the required integrals of the collision operators are detailed; in Section 5.2.2, the three-component electron-ion-neutral model is described; finally, in Section 5.2.3, the reduction of the three-component model to the two-component plasma-neutral model is shown. Implementation of this two-component plasma-neutral model in HiFi and associated validity limits are discussed in Section 5.3.

The Boltzmann equation for species α is

$$\frac{\partial f_\alpha}{\partial t} + \mathbf{v} \cdot \nabla_\mathbf{x} f_\alpha + \frac{q_\alpha}{m_\alpha}(\mathbf{E} + \mathbf{v} \times \mathbf{B}) \cdot \nabla_\mathbf{v} f_\alpha = \left.\frac{\partial f_\alpha}{\partial t}\right|_{collisions} = C_\alpha^{scat.,react.}, \qquad (5.2)$$

where the subscript of the collision operators, $C_\alpha^{scat.,react.}$, refers to the species affected by the term, and the superscript refers to the scattering or reacting collision type. The scattering collisions are elastic collisions. The reactions can be thought of as inelastic collisions (except for resonant CX, in which case the initial and final quantum states are degenerate). All of the relevant reactions may be summarized as

$$\sum_{\alpha=i,e,n} \left(\sum_{scat.=ii,ie,in,ee,en,nn} C_\alpha^{scat.} + \sum_{react.=ion,rec,cx} C_\alpha^{react.} \right), \qquad (5.3)$$

where contributions are to ion, electron, and neutral (i, e, and n) species due to scattering collisions — ion-ion, ion-electron, ion-neutral, electron-electron, electron-neutral, and neutral-neutral (ii, ie, in, ee, en, nn) — and reacting collisions — ionization, recombination, and CX (ion, rec, cx). The plasma-neutral model is derived from Eqn. (5.2) using the same basic approach as Braginskii [11], except that a neutral species is included, species conversion (due to ionization, recombination, and CX) is allowed, and related effects on mass, momentum, and energy equations are captured. Closure of the model is achieved by expanding the ion, electron, and neutral distribution functions using Chapman-Enskog-type [11, 101], which involves specifying an ordering of important terms in the Boltzmann equations. The lowest order term in the Boltzmann equation for each species is assumed to be the self-scattering collisions for the species. This has important implications for transport as discussed in Section 5.3 and Appendix G.

In addition to the physical model derived from the Boltzmann equation, a phenomeno-logical model to capture critical ionization velocity (CIV) effects is presented in Section 5.2.4.

5.2.1 Collision operator integrals

For the purposes of this derivation, specific forms of the scattering collision operators are not needed. The electron-impact ionization, radiative recombination, and resonant CX collision operators are

$$C_n^{ion} = -f_n \int f_e \sigma_{ion} v_{rel} d\mathbf{v}, \tag{5.4}$$

$$C_e^{ion} = C_i^{ion} = f_n \int f_e \sigma_{ion} v_{rel} d\mathbf{v}, \tag{5.5}$$

$$C_e^{rec} = -f_e \int f_i \sigma_{rec} v_{rel} d\mathbf{v}, \tag{5.6}$$

$$C_i^{rec} = -f_i \int f_e \sigma_{rec} v_{rel} d\mathbf{v}, \tag{5.7}$$

$$C_n^{rec} = \frac{m_e}{m_n} f_e \int f_i \sigma_{rec} v_{rel} d\mathbf{v} + \frac{m_i}{m_n} f_i \int f_e \sigma_{rec} v_{rel} d\mathbf{v}, \tag{5.8}$$

$$C_i^{cx} = f_n \int \sigma_{cx} v_{rel} f_i d\mathbf{v} - f_i \int \sigma_{cx} v_{rel} f_n d\mathbf{v}, \tag{5.9}$$

and

$$C_n^{cx} = \frac{m_i}{m_n} f_i \int \sigma_{cx} v_{rel} f_n d\mathbf{v} - \frac{m_i}{m_n} f_n \int \sigma_{cx} v_{rel} f_i d\mathbf{v}. \tag{5.10}$$

Here, v_{rel} is the relative speed of the colliding particles. The ionization and recombination cross-sections are assumed to be functions of only the random component of the electron particle velocity. As discussed by Ripken and Fahr [102], the form of the resonant CX colli-sion operator is attributable to the resonance, i.e., the initial and final quantum mechanical

states have identical energy. The CX cross section is assumed to be a function of a representative collision velocity as discussed below. See Appendix D for specific cross-section and rate formulas for ionization, recombination, and CX used for this research.

A Maxwellian form for f_α is assumed — $f_\alpha = n_\alpha \left(\pi v_{T\alpha}^2\right)^{-3/2} e^{-(\mathbf{v}-\mathbf{v}_\alpha)^2/v_{T\alpha}^2}$, where n_α is the species number density, $v_{T\alpha} \equiv \sqrt{\frac{2kT_\alpha}{m_\alpha}}$ is the species thermal speed, $\mathbf{v}$ is the velocity, and $\mathbf{v}_\alpha$ is the bulk velocity. The random velocity is defined as $\mathbf{w} \equiv \mathbf{v} - \mathbf{v}_\alpha$.

0th, 1st, and 2nd moments of the reaction collision operators are derived next. A summary of results is provided following the moment derivations.

As noted in Section 5.1, Pauls et al. [84] describe these moments for resonant CX, but not for electron-impact ionization and radiative recombination. In the model proposed by Helander et al. [98], moments of the ionization and recombination collision operators are shown without supporting details. Moments of the CX operator are not necessary in the Helander combined-fluid formulation. (See detailed discussion of the model by Helander et al. in Appendix G.) The UEDGE [89, 90] and B2 [91, 92] codes apparently rely on Monte Carlo codes to compute moments of the collision operators, although some approximations of CX moments are optionally included (such as the direct transfer of momentum between ion and neutral fluids due to CX, as discussed below).

0th *moments* — $\int C_\alpha^{scat.,react.} d\mathbf{v}$

Scattering has no 0th moment effect.

For the 0th moment effect of ionization on the neutral species, the required integral of Eqn. (5.4) is

$$\int C_n^{ion} d\mathbf{v} = -\int f_n(\mathbf{v}') \int f_e(\mathbf{v}) \sigma_{ion}(v_{rel}) v_{rel} d\mathbf{v} d\mathbf{v}'. \tag{5.11}$$

Consider the inner integral over electron particle velocity space. The Maxwellian electron distribution is a function of the random velocity, $\mathbf{w} \equiv \mathbf{v} - \mathbf{v}_e$. The relative velocity is $v_{rel} = |\mathbf{v} - \mathbf{v}'|$. Assuming that the electron thermal speed is high compared to either the bulk flow speed of the neutral fluid or the neutral thermal speed, the relative velocity in the ionizing collisions is $v_{rel} \approx w$, where $w \equiv |\mathbf{w}|$. The inner integral is then

$$\int f_e(\mathbf{v})\sigma_{ion}(v_{rel})v_{rel}d\mathbf{v} \approx \int f_e(\mathbf{w})\sigma_{ion}(w)wd\mathbf{w} = n_e\langle\sigma_{ion}v_e\rangle, \qquad (5.12)$$

where $\langle\cdot\rangle$ refers to the statistical average over velocity space, and $\langle\sigma_{ion}v_e\rangle$ is called the ionization rate parameter and has units of volume per time. This rate is given for a variety of atoms in Appendix D. The entire integral is now

$$\int C_n^{ion}d\mathbf{v} \approx \Gamma_n^{ion} \equiv -\int f_n(\mathbf{v}')n_e\langle\sigma_{ion}v_e\rangle d\mathbf{v}' = -n_e n_n\langle\sigma_{ion}v_e\rangle, \qquad (5.13)$$

where the notation, $\Gamma_\alpha^{react.}$, is introduced for source rates due to a given reaction collision (react.) affecting species α. Using a similar procedure, the ionization contribution to the ion species is found to be $\int C_i^{ion}d\mathbf{v} \approx \Gamma_i^{ion} = -\Gamma_n^{ion}$. The ionization contribution to the electron species is identical, $\int C_e^{ion}d\mathbf{v} \approx \Gamma_e^{ion} = \Gamma_i^{ion}$. Only Γ_i^{ion} will be used to refer to ionization source rates for the ion, neutral, and electron species. Appropriate substitutions will be made based on $\Gamma_e^{ion} = -\Gamma_n^{ion} = \Gamma_i^{ion}$.

For recombination,

$$\int C_i^{rec}d\mathbf{v} \approx \Gamma_i^{rec} \equiv -n_i n_e\langle\sigma_{rec}v_e\rangle. \qquad (5.14)$$

The quantity $\langle\sigma_{rec}v_e\rangle$ is the recombination rate. Appendix D discusses the recombination rate formula used in this work. The 0th moment recombination contribution to the electron and neutral species are $\int C_e^{rec}d\mathbf{v} \approx \Gamma_e^{rec} = \Gamma_i^{rec}$ and $\int C_n^{rec}d\mathbf{v} \approx \Gamma_n^{rec} = -\Gamma_i^{rec}$. Appropriate substitutions will be made so that only Γ_n^{rec} will be used to refer to recombination source rates.

It is intuitively obvious that CX does not result in a net change of total electron, ion, or neutral populations. However, understanding the details of the CX collision term is important for higher moments and so the 0th moment is examined now. Following Paul et al. [84], C_i^{cx}, given by Eqn. (5.9), can be accurately approximated as

$$C_i^{cx} \approx \sigma_{cx}\left(v_i^* n_i f_n - v_n^* n_n f_i\right), \qquad (5.15)$$

where $v_\alpha^* \equiv v_{T\alpha}\sqrt{4/\pi + x^2}$. Here, $x \equiv |\mathbf{v} - \mathbf{v}_\alpha|/v_{T\alpha}$. The steps required to arrive at Eqn. (5.15) are shown in Appendix E.1. The 0th moment integration is detailed in Appendix E.2.

As discussed, after additional approximation (resulting in a total worst-case approximation error on the order of a few percent),

$$\int \sigma_{cx} v_i^* n_i f_n d\mathbf{v} \approx \sigma_{cx}(V_{cx}) n_i n_n V_{cx}, \tag{5.16}$$

where a representative speed for the CX interaction, V_{cx}, is defined as

$$V_{cx} \equiv \sqrt{\frac{4}{\pi} v_{Ti}^2 + \frac{4}{\pi} v_{Tn}^2 + v_{in}^2}, \tag{5.17}$$

where $v_{in}^2 \equiv |\mathbf{v}_i - \mathbf{v}_n|^2$. Note that σ_{cx} is evaluated at V_{cx}. Formulas for the dependence of σ_{cx} on velocity are given in Appendix D. It is useful to define the quantity

$$\Gamma^{cx} \equiv \sigma_{cx}(V_{cx}) n_i n_n V_{cx}. \tag{5.18}$$

Now it is clear that $\int C_i^{cx} d\mathbf{v} \approx \Gamma^{cx} - \Gamma^{cx} = 0$ and $\int C_n^{cx} d\mathbf{v} \approx \frac{m_i}{m_n}(\Gamma^{cx} - \Gamma^{cx}) = 0$.

1st *moments* — $\int m_\alpha \mathbf{v} C_\alpha^{scat.,react.} d\mathbf{v}$

For scattering collisions between species α and β, 1st moments are $\int m_\alpha \mathbf{v} C_\alpha^{\alpha\beta} d\mathbf{v}$. Splitting the particle velocity into bulk and random components, $\mathbf{v} = \mathbf{v}_\alpha + \mathbf{w}$,

$$\int m_\alpha \mathbf{v} C_\alpha^{\alpha\beta} d\mathbf{v} = m_\alpha \mathbf{v}_\alpha \int C_\alpha^{\alpha\beta} d\mathbf{v} + m_\alpha \int \mathbf{w} C_\alpha^{\alpha\beta} d\mathbf{v}. \tag{5.19}$$

The first term on the right is zero. The second term is the frictional force,

$$\mathbf{R}_\alpha^{\alpha\beta} = m_\alpha \int \mathbf{w} C_\alpha^{\alpha\beta} d\mathbf{v}. \tag{5.20}$$

Approximations of frictional forces between ions and electrons are presented by Braginskii [11]. Frictional forces between charged species (ions and electrons) and the neutral species are presented in the three-component and two-component models of Sections 5.2.2 and 5.2.3, but in the HiFi implementation given in Section 5.3 of the two-component model, these terms are assumed to be negligible. Section 5.3 contains discussion and justification of this assumption.

The effect of ionization on the ion species is found by taking the 1st moment of Eqn. (5.5),

$$\int m_i \mathbf{v} C_i^{ion} d\mathbf{v} = \int m_i \mathbf{v} f_n(\mathbf{v}) \int f_e(\mathbf{v}') \sigma_{ion} v_{rel} d\mathbf{v}' d\mathbf{v}. \tag{5.21}$$

Using the earlier result of Eqn. (5.12) for the inner integral, and splitting the neutral particle velocity into bulk and random components, $\mathbf{v} = \mathbf{v}_n + \mathbf{w}$,

$$\int m_i \mathbf{v} C_i^{ion} d\mathbf{v} = m_i n_e \langle \sigma_{ion} v_e \rangle \left(\mathbf{v}_n \int f_n d\mathbf{v} + \int \mathbf{w} f_n d\mathbf{v} \right). \tag{5.22}$$

The first term on the right is simply $m_i \mathbf{v}_n \Gamma_i^{ion}$. The second term involves an odd integral and goes to zero. Therefore,

$$\int m_i \mathbf{v} C_i^{ion} d\mathbf{v} = m_i \mathbf{v}_n \Gamma_i^{ion}. \tag{5.23}$$

Similarly, the 1st moment contributions of ionization to the electron and neutral species are $\int m_e \mathbf{v} C_e^{ion} d\mathbf{v} = m_e \mathbf{v}_n \Gamma_i^{ion}$, and $\int m_n \mathbf{v} C_n^{ion} d\mathbf{v} = -m_n \mathbf{v}_n \Gamma_i^{ion}$.

1st moment contributions of recombination to the ion, electron, and neutral species are $\int m_i \mathbf{v} C_i^{rec} d\mathbf{v} = -m_i \mathbf{v}_i \Gamma_n^{rec}$, $\int m_e \mathbf{v} C_e^{rec} d\mathbf{v} = -m_e \mathbf{v}_e \Gamma_n^{rec}$, and $\int m_n \mathbf{v} C_n^{rec} d\mathbf{v} = (m_i \mathbf{v}_i + m_e \mathbf{v}_e) \Gamma_n^{rec}$.

For CX, the 1st moment contribution to the ion species is

$$
\begin{aligned}
\int m_i \mathbf{v} C_i^{cx} d\mathbf{v} &\approx m_i \sigma_{cx} \int \mathbf{v} \left(n_i v_i^* f_n - n_n v_n^* f_i \right) d\mathbf{v} \\
&= m_i \sigma_{cx} \left(n_i \mathbf{v}_n \int v_i^* f_n d\mathbf{v} + n_i \int \mathbf{w} v_i^* f_n d\mathbf{v} \right. \\
&\qquad \left. - n_n \mathbf{v}_i \int v_n^* f_i d\mathbf{v} - n_n \int \mathbf{w} v_n^* f_i d\mathbf{v} \right) \\
&= m_i (\mathbf{v}_n - \mathbf{v}_i) \Gamma^{cx} \\
&\qquad + m_i \sigma_{cx} \left(n_i \int \mathbf{w} v_i^* f_n d\mathbf{v} - n_n \int \mathbf{w} v_n^* f_i d\mathbf{v} \right).
\end{aligned}
\tag{5.24}
$$

The two terms in the last line of Eqn. (5.24) represent the frictional transfer of momentum, $\mathbf{R}_{in}^{cx} \equiv m_i \sigma_{cx} n_i \int \mathbf{w} v_i^* f_n d\mathbf{v}$ and $\mathbf{R}_{ni}^{cx} \equiv m_i \sigma_{cx} n_n \int \mathbf{w} v_n^* f_i d\mathbf{v}$. The integrations required

to specify $\mathbf{R}_{in}^{cx}$ and $\mathbf{R}_{ni}^{cx}$ are described in Appendix E.3. As found by Pauls et al. [84], appropriate approximations are

$$\mathbf{R}_{in}^{cx} \approx -m_i \sigma_{cx}(V_{cx}) n_i n_n \mathbf{v}_{in} v_{Tn}^2 \left[4\left(\frac{4}{\pi} v_{Ti}^2 + v_{in}^2 \right) + \frac{9\pi}{4} v_{Tn}^2 \right]^{-1/2}, \qquad (5.25)$$

and

$$\mathbf{R}_{ni}^{cx} \approx m_i \sigma_{cx}(V_{cx}) n_i n_n \mathbf{v}_{in} v_{Ti}^2 \left[4\left(\frac{4}{\pi} v_{Tn}^2 + v_{in}^2 \right) + \frac{9\pi}{4} v_{Ti}^2 \right]^{-1/2}. \qquad (5.26)$$

Thus, the 1st moment CX contribution to the ion species is

$$\int m_i \mathbf{v} C_i^{cx} d\mathbf{v} \approx m_i(\mathbf{v}_n - \mathbf{v}_i)\Gamma^{cx} + \mathbf{R}_{in}^{cx} - \mathbf{R}_{ni}^{cx}. \qquad (5.27)$$

The neutral species CX contribution has the same magnitude, but the opposite sign, $\int m_n \mathbf{v} C_n^{cx} d\mathbf{v} = -\int m_i \mathbf{v} C_i^{cx} d\mathbf{v} \approx m_i \left(\mathbf{v}_i - \mathbf{v}_n \right) \Gamma^{cx} + \mathbf{R}_{ni}^{cx} - \mathbf{R}_{in}^{cx}.$

2nd moments $-$ $\int \frac{1}{2} m_\alpha \mathbf{v}^2 C_\alpha^{scat.,react.} d\mathbf{v}$

For scattering collisions between species α and β, 2nd moments are $\int \frac{1}{2} m_\alpha \mathbf{v}^2 C_\alpha^{\alpha\beta} d\mathbf{v}$. Splitting the particle velocity into bulk and random components, $\mathbf{v} = \mathbf{v}_\alpha + \mathbf{w}$,

$$\int \frac{1}{2} m_\alpha \mathbf{v}^2 C_\alpha^{\alpha\beta} d\mathbf{v} = m_\alpha \mathbf{v}_\alpha \mathbf{R}_\alpha^{\alpha\beta} + \frac{1}{2} m_\alpha \int \mathbf{w}^2 C_\alpha^{\alpha\beta} d\mathbf{v}, \qquad (5.28)$$

where the first term is related to the frictional force (already discussed), and the second term is the frictional heating,

$$\mathbf{Q}_\alpha^{\alpha\beta} = \frac{1}{2} m_\alpha \int \mathbf{w}^2 C_\alpha^{\alpha\beta} d\mathbf{v}. \qquad (5.29)$$

The approach of Braginskii [11] is followed for the ion-electron scattering frictional terms. Frictional force terms and frictional heating terms related to the scattering interaction of charged species (ions and electrons) and the neutral species are presented in the three-component and two-component models of Sections 5.2.2 and 5.2.3, but in the HiFi implementation given in Section 5.3 of the two-component model, these terms are assumed to be negligible. Section 5.3 contains discussion and justification of this assumption.

The 2nd moment of C_i^{ion}, after again using Eqn. (5.12) for the integral over electron velocity space, is

$$\int \frac{1}{2}m_i\mathbf{v}^2 C_i^{ion}d\mathbf{v} \approx m_i n_e \langle \sigma_{ion}v_e \rangle \left(\frac{1}{2}\mathbf{v}_n^2 \int f_n d\mathbf{v} + \mathbf{v}_n \cdot \int \mathbf{w}f_n d\mathbf{v} + \frac{1}{2}\int \mathbf{w}^2 f_n d\mathbf{v} \right). \quad (5.30)$$

The first term on the right is related to the 0th moment. The middle term is an odd integral and vanishes as before. The final term is an even integral that is easily evaluated in spherical coordinates. Inserting the Maxwellian form for f_n, the integral is

$$\begin{aligned}
\int \mathbf{w}^2 f_n d\mathbf{v} &= \int \mathbf{w}^2 n_n \left(\pi v_{Tn}^2\right)^{-3/2} e^{-\mathbf{w}^2/v_{Tn}^2} d\mathbf{v} \\
&= \frac{4}{v_{Tn}^3 \sqrt{\pi}} n_n \int_0^\infty w^4 e^{-w^2/v_{Tn}^2} dw \\
&= \frac{3}{2}n_n v_{Tn}^2, \quad (5.31)
\end{aligned}$$

where $w^2 = \mathbf{w} \cdot \mathbf{w}$ has been used. Eqn. (5.30) is now

$$\int \frac{1}{2}m_i\mathbf{v}^2 C_i^{ion}d\mathbf{v} \approx \frac{m_i}{m_n}\frac{\Gamma_i^{ion}}{2}\left(m_n\mathbf{v}_n^2 + \frac{3}{2}m_n v_{Tn}^2 \right). \quad (5.32)$$

Using the definition of v_{Tn}, the two terms on the right can be identified as transfer of kinetic energy and internal energy. Defining $Q_i^{ion} \equiv \Gamma_i^{ion}\frac{3}{2}kT_n$, the finished equation for the 2nd moment of C_i^{ion} is

$$\int \frac{1}{2}m_i\mathbf{v}^2 C_i^{ion}d\mathbf{v} \approx \frac{m_i}{m_n}\left(\Gamma_i^{ion}\frac{1}{2}m_n\mathbf{v}_n^2 + Q_i^{ion} \right). \quad (5.33)$$

Similarly,

$$\int \frac{1}{2}m_e\mathbf{v}^2 C_e^{ion}d\mathbf{v} \approx \frac{m_e}{m_n}\left(\Gamma_i^{ion}\frac{1}{2}m_n\mathbf{v}_n^2 + Q_i^{ion} \right) - \Gamma_i^{ion}\phi_{ion}, \quad (5.34)$$

where the effective ionization energy is extracted, and

$$\int \frac{1}{2}m_n\mathbf{v}^2 C_n^{ion}d\mathbf{v} \approx -\left(\Gamma_i^{ion}\frac{1}{2}m_n\mathbf{v}_n^2 + Q_i^{ion} \right). \quad (5.35)$$

The 2nd moment of C_i^{rec} is

$$\int \frac{1}{2} m_i \mathbf{v}^2 C_i^{rec} d\mathbf{v} \approx - \left(\Gamma_n^{rec} \frac{1}{2} m_i \mathbf{v}_i^2 + Q_n^{rec} \right), \tag{5.36}$$

where $Q_n^{rec} \equiv \Gamma_n^{rec} \frac{3}{2} k T_i$. The 2nd moment of C_e^{rec} is

$$\int \frac{1}{2} m_e \mathbf{v}^2 C_e^{rec} d\mathbf{v} = -\frac{1}{2} m_e n_i \left(\mathbf{v}_e^2 \int f_e \sigma_{rec} v d\mathbf{v} \right.$$
$$\left. + \mathbf{v}_e \cdot \int \mathbf{w} f_e \sigma_{rec} v d\mathbf{v} + \int \mathbf{v}^2 f_e \sigma_{rec} v d\mathbf{v} \right). \tag{5.37}$$

The first term on the right represents transfer of kinetic energy. The second term is an odd integral and goes to zero. There is no readily available closed form for the last term, which is like a transfer of internal energy, but is modified by the presence of $\sigma_{rec} v$. If recombination is expected to play an important role, this term should be addressed. In this work, recombination effects are expected to be unimportant, so it is ignored, leaving

$$\int \frac{1}{2} m_e \mathbf{v}^2 C_e^{rec} d\mathbf{v} = -\Gamma_n^{rec} \frac{1}{2} m_e \mathbf{v}_e^2. \tag{5.38}$$

The 2nd moment of C_n^{rec} is

$$\int \frac{1}{2} m_n \mathbf{v}^2 C_n^{rec} d\mathbf{v} = \Gamma_n^{rec} \left(\frac{1}{2} m_i \mathbf{v}_i^2 + \frac{1}{2} m_e \mathbf{v}_e^2 \right) + Q_n^{rec}. \tag{5.39}$$

The 2nd moment contribution of CX to the ion species is

$$\int \frac{1}{2} m_i \mathbf{v}^2 C_i^{cx} d\mathbf{v} = \frac{1}{2} m_i \sigma_{cx} \int \mathbf{v}^2 \left(v_i^* n_i f_n - v_n^* n_n f_i \right) d\mathbf{v}, \tag{5.40}$$

which, after expanding the velocities into fluid and random velocities, is

$$\int \frac{1}{2} m_i \mathbf{v}^2 C_i^{cx} d\mathbf{v} = m_i \sigma_{cx} \left(\frac{1}{2} n_i \mathbf{v}_n^2 \int v_i^* f_n d\mathbf{v} - \frac{1}{2} n_n \mathbf{v}_i^2 \int v_n^* f_i d\mathbf{v} + n_i \mathbf{v}_n \cdot \int \mathbf{w} v_i^* f_n d\mathbf{v} \right.$$
$$\left. - n_n \mathbf{v}_i \cdot \int \mathbf{w} v_n^* f_i d\mathbf{v} + \frac{1}{2} \int \mathbf{w}^2 \left(n_i v_i^* f_n - n_n v_n^* f_i \right) d\mathbf{v} \right)$$
$$= \Gamma^{cx} \frac{1}{2} m_i (\mathbf{v}_n^2 - \mathbf{v}_i^2) + \mathbf{v}_n \cdot \mathbf{R}_{in}^{cx} - \mathbf{v}_i \cdot \mathbf{R}_{ni}^{cx}$$
$$+ \frac{1}{2} \sigma_{cx} m_i \int \mathbf{w}^2 \left(n_i v_i^* f_n - n_n v_n^* f_i \right) d\mathbf{v}. \tag{5.41}$$

The integral terms in the last line of Eqn. (5.41) represent the transfer of random thermal energy, $Q_{in}^{cx} \equiv \frac{1}{2}\sigma_{cx}m_i \int \mathbf{w}^2 n_i v_i^* f_n d\mathbf{v}$ and $Q_{ni}^{cx} \equiv \frac{1}{2}\sigma_{cx}m_i \int \mathbf{w}^2 n_n v_n^* f_i d\mathbf{v}$. The integrations required to specify Q_{in}^{cx} and Q_{ni}^{cx} are described in Appendix E.4. As found by Pauls et al. [84], appropriate approximations are

$$Q_{in}^{cx} \approx \sigma_{cx}m_i n_i n_n \frac{3}{4}v_{Tn}^2\sqrt{\frac{4}{\pi}v_{Ti}^2 + \frac{64}{9\pi}v_{Tn}^2 + v_{in}^2}, \qquad (5.42)$$

and

$$Q_{ni}^{cx} \approx \sigma_{cx}m_i n_i n_n \frac{3}{4}v_{Ti}^2\sqrt{\frac{4}{\pi}v_{Tn}^2 + \frac{64}{9\pi}v_{Ti}^2 + v_{in}^2}. \qquad (5.43)$$

Eqn. 5.40 can now be written

$$\int \frac{1}{2}m_i\mathbf{v}^2 C_i^{cx}d\mathbf{v} = \Gamma^{cx}\frac{1}{2}m_i(\mathbf{v}_n^2 - \mathbf{v}_i^2) + \mathbf{v}_n \cdot \mathbf{R}_{in}^{cx} - \mathbf{v}_i \cdot \mathbf{R}_{ni}^{cx} + Q_{in}^{cx} - Q_{ni}^{cx}. \qquad (5.44)$$

The 2nd moment of C_n^{cx} is

$$\int \frac{1}{2}m_n\mathbf{v}^2 C_n^{cx}d\mathbf{v} = \Gamma^{cx}\frac{1}{2}m_i(\mathbf{v}_i^2 - \mathbf{v}_n^2) - \mathbf{v}_n \cdot \mathbf{R}_{in}^{cx} + \mathbf{v}_i \cdot \mathbf{R}_{ni}^{cx} - Q_{in}^{cx} + Q_{ni}^{cx}. \qquad (5.45)$$

Summary of reaction collision operator integrals

Summarizing for the 0th moment,

$$\int C_e^{ion} d\mathbf{v} \approx \Gamma_i^{ion}$$

$$\int C_i^{ion} d\mathbf{v} \approx \Gamma_i^{ion}$$

$$\int C_n^{ion} d\mathbf{v} \approx -\Gamma_i^{ion}$$

$$\int C_e^{rec} d\mathbf{v} \approx -\Gamma_n^{rec}$$

$$\int C_i^{rec} d\mathbf{v} \approx -\Gamma_n^{rec}$$

$$\int C_n^{rec} d\mathbf{v} \approx \Gamma_n^{rec}$$

$$\int C_i^{cx} d\mathbf{v} \approx \Gamma^{cx} - \Gamma^{cx} = 0$$

$$\int C_n^{cx} d\mathbf{v} \approx \Gamma^{cx} - \Gamma^{cx} = 0. \tag{5.46}$$

Summarizing for the 1st moment,

$$\int m_e \mathbf{v} C_e^{ion} d\mathbf{v} \approx m_e \mathbf{v}_n \Gamma_i^{ion}$$

$$\int m_i \mathbf{v} C_i^{ion} d\mathbf{v} \approx m_i \mathbf{v}_n \Gamma_i^{ion}$$

$$\int m_n \mathbf{v} C_n^{ion} d\mathbf{v} \approx -m_n \mathbf{v}_n \Gamma_i^{ion}$$

$$\int m_e \mathbf{v} C_e^{rec} d\mathbf{v} \approx -m_e \mathbf{v}_e \Gamma_n^{rec}$$

$$\int m_i \mathbf{v} C_i^{rec} d\mathbf{v} \approx -m_i \mathbf{v}_i \Gamma_n^{rec}$$

$$\int m_n \mathbf{v} C_n^{ion} d\mathbf{v} \approx (m_i \mathbf{v}_i + m_e \mathbf{v}_e) \Gamma_n^{rec}$$

$$\int m_i \mathbf{v} C_i^{cx} d\mathbf{v} \approx m_i (\mathbf{v}_n - \mathbf{v}_i) \Gamma^{cx} + \mathbf{R}_{in}^{cx} - \mathbf{R}_{ni}^{cx}$$

$$\int m_n \mathbf{v} C_n^{cx} d\mathbf{v} \approx m_i (\mathbf{v}_i - \mathbf{v}_n) \Gamma^{cx} + \mathbf{R}_{ni}^{cx} - \mathbf{R}_{in}^{cx}. \tag{5.47}$$

Summarizing for the 2nd moment,

$$
\int \frac{1}{2} m_e \mathbf{v}^2 C_e^{ion} d\mathbf{v} \quad \approx \quad \frac{m_e}{m_n} \left(\Gamma_i^{ion} \frac{1}{2} m_n \mathbf{v}_n^2 + Q_i^{ion} \right) - \Gamma_i^{ion} \phi_{ion}
$$

$$
\int \frac{1}{2} m_i \mathbf{v}^2 C_i^{ion} d\mathbf{v} \quad \approx \quad \frac{m_i}{m_n} \left(\Gamma_i^{ion} \frac{1}{2} m_n \mathbf{v}_n^2 + Q_i^{ion} \right)
$$

$$
\int \frac{1}{2} m_n \mathbf{v}^2 C_n^{ion} d\mathbf{v} \quad \approx \quad - \left(\Gamma_i^{ion} \frac{1}{2} m_n \mathbf{v}_n^2 + Q_i^{ion} \right)
$$

$$
\int \frac{1}{2} m_e \mathbf{v}^2 C_e^{rec} d\mathbf{v} \quad \approx \quad -\Gamma_n^{rec} \frac{1}{2} m_e \mathbf{v}_e^2
$$

$$
\int \frac{1}{2} m_i \mathbf{v}^2 C_i^{rec} d\mathbf{v} \quad \approx \quad - \left(\Gamma_n^{rec} \frac{1}{2} m_i \mathbf{v}_i^2 + Q_n^{rec} \right)
$$

$$
\int \frac{1}{2} m_n \mathbf{v}^2 C_n^{rec} d\mathbf{v} \quad \approx \quad \Gamma_n^{rec} \left(\frac{1}{2} m_i \mathbf{v}_i^2 + \frac{1}{2} m_e \mathbf{v}_e^2 \right) + Q_n^{rec}
$$

$$
\int \frac{1}{2} m_i \mathbf{v}^2 C_i^{cx} d\mathbf{v} \quad \approx \quad \Gamma^{cx} \frac{1}{2} m_i \left(\mathbf{v}_n^2 - \mathbf{v}_i^2 \right) + \mathbf{v}_n \cdot \mathbf{R}_{in}^{cx} - \mathbf{v}_i \cdot \mathbf{R}_{ni}^{cx} + Q_{in}^{cx} - Q_{ni}^{cx}
$$

$$
\int \frac{1}{2} m_n \mathbf{v}^2 C_n^{cx} d\mathbf{v} \quad \approx \quad \Gamma^{cx} \frac{1}{2} m_i \left(\mathbf{v}_i^2 - \mathbf{v}_n^2 \right) + \mathbf{v}_i \cdot \mathbf{R}_{ni}^{cx} - \mathbf{v}_n \cdot \mathbf{R}_{in}^{cx} + Q_{ni}^{cx} - Q_{in}^{cx}. \quad (5.48)
$$

5.2.2 Electron-ion-neutral three-component model

The next step toward the two-component plasma-neutral model is to compose the three-fluid electron-ion-neutral equations. Using the expressions for moments of the reaction collision operators summarized in Section 5.2.1, and taking moments of Eqn. (5.2) (closely following the approach of Braginskii [11]), the following continuity, momentum, and energy equations are derived for the ion, electron, and neutral species.

Continuity

$$
\frac{\partial n_i}{\partial t} + \nabla \cdot (n_i \mathbf{v}_i) = \Gamma_i^{ion} - \Gamma_n^{rec}, \tag{5.49}
$$

$$
\frac{\partial n_e}{\partial t} + \nabla \cdot (n_e \mathbf{v}_e) = \Gamma_i^{ion} - \Gamma_n^{rec}, \tag{5.50}
$$

$$
\frac{\partial n_n}{\partial t} + \nabla \cdot (n_n \mathbf{v}_n) = \Gamma_n^{rec} - \Gamma_i^{ion}. \tag{5.51}
$$

Momentum

$$\frac{\partial}{\partial t}(m_i n_i \mathbf{v}_i) + \nabla \cdot (m_i n_i \mathbf{v}_i \mathbf{v}_i + \mathbb{P}_i) = q_i n_i (\mathbf{E} + \mathbf{v}_i \times \mathbf{B})$$

$$+ \mathbf{R}_i^{ie} + \mathbf{R}_i^{in} + \Gamma_i^{ion} m_i \mathbf{v}_n - \Gamma_n^{rec} m_i \mathbf{v}_i + \Gamma^{cx} m_i (\mathbf{v}_n - \mathbf{v}_i) + \mathbf{R}_{in}^{cx} - \mathbf{R}_{ni}^{cx}, \quad (5.52)$$

$$\frac{\partial}{\partial t}(m_e n_e \mathbf{v}_e) + \nabla \cdot (m_e n_e \mathbf{v}_e \mathbf{v}_e + \mathbb{P}_e) = -q_e n_e (\mathbf{E} + \mathbf{v}_e \times \mathbf{B})$$

$$- \mathbf{R}_i^{ie} + \mathbf{R}_e^{en} + \Gamma_i^{ion} m_e \mathbf{v}_n - \Gamma_n^{rec} m_e \mathbf{v}_e, \quad (5.53)$$

$$\frac{\partial}{\partial t}(m_n n_n \mathbf{v}_n) + \nabla \cdot (m_n n_n \mathbf{v}_n \mathbf{v}_n + \mathbb{P}_n) =$$

$$- \mathbf{R}_i^{in} - \mathbf{R}_e^{en} + \Gamma_n^{rec}(m_i \mathbf{v}_i + m_e \mathbf{v}_e) - \Gamma_i^{ion} m_n \mathbf{v}_n + \Gamma^{cx} m_i (\mathbf{v}_i - \mathbf{v}_n)$$

$$- \mathbf{R}_{in}^{cx} + \mathbf{R}_{ni}^{cx}, \quad (5.54)$$

where q_i and q_e are the ion and electron charge magnitudes, respectively, and $\mathbf{R}_i^{ie}$ is the usual scattering collisional transfer of momentum to the ion species presented by Braginskii [11] as $\mathbf{R}_{ie}$. $\mathbf{R}_i^{in}$ is a similar scattering collisional momentum transfer to the ion species, but for ion-neutral collisions. $\mathbf{R}_e^{en}$ is a similar momentum transfer for electron-neutral collisions. The species pressure tensor, $\mathbb{P}_\alpha$, can be decomposed as $\mathbb{P}_\alpha = p_\alpha \mathbb{I} + \pi_\alpha$, where p_α is the scalar pressure and π_α is the stress tensor.

Energy

$$\frac{\partial \varepsilon_i}{\partial t} + \nabla \cdot (\varepsilon_i \mathbf{v}_i + \mathbf{v}_i \cdot \mathbb{P}_i + \mathbf{h}_i) = \mathbf{v}_i \cdot (q_i n_i \mathbf{E} + \mathbf{R}_i^{ie} + \mathbf{R}_i^{in})$$

$$+ Q_i^{ie} + Q_i^{in} + \frac{m_i}{m_n}(\Gamma_i^{ion} \frac{1}{2} m_n \mathbf{v}_n^2 + Q_i^{ion}) - \Gamma_n^{rec} \frac{1}{2} m_i \mathbf{v}_i^2 - Q_n^{rec}$$

$$+ \Gamma^{cx} \frac{1}{2} m_i \left(\mathbf{v}_n^2 - \mathbf{v}_i^2 \right) + \mathbf{v}_n \cdot \mathbf{R}_{in}^{cx} - \mathbf{v}_i \cdot \mathbf{R}_{ni}^{cx} + Q_{in}^{cx} - Q_{ni}^{cx}, \quad (5.55)$$

$$\frac{\partial \varepsilon_e}{\partial t} + \nabla \cdot (\varepsilon_e \mathbf{v}_e + \mathbf{v}_e \cdot \mathbb{P}_e + \mathbf{h}_e) = \mathbf{v}_e \cdot (-q_e n_e \mathbf{E} - \mathbf{R}_i^{ie} + \mathbf{R}_e^{en})$$

$$+ Q_e^{ie} + Q_e^{en} + \frac{m_e}{m_n}(\Gamma_i^{ion}\frac{1}{2}m_n\mathbf{v}_n^2 + Q_i^{ion}) - \Gamma_i^{ion}\phi_{ion} - \Gamma_n^{rec}\frac{1}{2}m_e\mathbf{v}_e^2, \qquad (5.56)$$

$$\frac{\partial \varepsilon_n}{\partial t} + \nabla \cdot (\varepsilon_n \mathbf{v}_n + \mathbf{v}_n \cdot \mathbb{P}_n + \mathbf{h}_n) = -\mathbf{v}_n \cdot (\mathbf{R}_i^{in} + \mathbf{R}_e^{en})$$

$$+ Q_n^{in} + Q_n^{en} + \Gamma_n^{rec}(\frac{1}{2}m_i\mathbf{v}_i^2 + \frac{1}{2}m_e\mathbf{v}_e^2) + Q_n^{rec} - (\Gamma_i^{ion}\frac{1}{2}m_n\mathbf{v}_n^2 + Q_i^{ion})$$

$$+ \Gamma^{cx}\frac{1}{2}m_i(\mathbf{v}_i^2 - \mathbf{v}_n^2) + \mathbf{v}_i \cdot \mathbf{R}_{ni}^{cx} - \mathbf{v}_n \cdot \mathbf{R}_{in}^{cx} + Q_{ni}^{cx} - Q_{in}^{cx}, \qquad (5.57)$$

where $\varepsilon_\alpha \equiv m_\alpha \mathbf{v}_\alpha^2/2 + p_\alpha/(\gamma - 1)$ is the total fluid energy density, and Q_i^{ie} and Q_e^{ie} are the usual scattering collisional heat generation presented by Braginskii [11] as Q_{ie} and Q_{ei}, respectively. $Q_{i/n}^{in}$ and $Q_{e/n}^{en}$ represent the same type of heat generation due to ion-neutral and electron-neutral collisions, respectively. The species heat fluxes are represented by $\mathbf{h}_\alpha$. Maxwell's equations couple the fluid dynamics to the electric and magnetic field evolution. The heat fluxes ($\mathbf{h}_\alpha$), and the stress tensors (π_α) must be specified to close the model. This closure is often accomplished by using a Chapman-Enskog-like expansion of the distribution function. These terms are further addressed in Section 5.3.

5.2.3   Plasma-neutral two-component model

To reach a two-component model that is a simple extension of the dissipative MHD model shown in Section 1.4, the electron and ion fluids are treated as a single fluid. The MHD approximations are made, such that $n = n_i = n_e$, $m_e \to 0$, and $\mathbf{v} = \mathbf{v}_i$. It is further assumed that $q_i = q_e$ and $m_i = m_n$. Current density, $\mathbf{j} = q_e n(\mathbf{v}_i - \mathbf{v}_e)$ is introduced.

In this section, some comments are made on the assumptions made, and the physical meaning of terms, but the comments are mostly limited to those terms related to typical dissipative MHD. Additional interpretation of the physical meaning of the terms related to plasma-neutral reaction physics is reserved for Section 5.3, which describes implementation of the plasma-neutral model in HiFi. Section 5.3 also highlights the differences between the HiFi plasma-neutral implementation and the alternative models presented in Section 5.1.

Continuity

Along with the neutral continuity equation, only a single plasma continuity equation is needed.

$$\frac{\partial n}{\partial t} + \nabla \cdot (n\mathbf{v}) = \Gamma_i^{ion} - \Gamma_n^{rec}, \tag{5.58}$$

$$\frac{\partial n_n}{\partial t} + \nabla \cdot (n_n\mathbf{v}_n) = \Gamma_n^{rec} - \Gamma_i^{ion}. \tag{5.59}$$

Momentum

The ion and electron momentum equations are summed to yield the plasma momentum equation.

$$\frac{\partial}{\partial t}(m_i n\mathbf{v}) + \nabla \cdot (m_i n\mathbf{v}\mathbf{v} + p\mathbb{I} + \pi) = \mathbf{j} \times \mathbf{B}$$
$$+\mathbf{R}_i^{in} + \mathbf{R}_e^{en} + \Gamma_i^{ion} m_i \mathbf{v}_n - \Gamma_n^{rec} m_i \mathbf{v} + \Gamma^{cx} m_i(\mathbf{v}_n - \mathbf{v}) + \mathbf{R}_{in}^{cx} - \mathbf{R}_{ni}^{cx}, \tag{5.60}$$

$$\frac{\partial}{\partial t}(m_i n_n\mathbf{v}_n) + \nabla \cdot (m_i n_n\mathbf{v}_n\mathbf{v}_n + p_n\mathbb{I} + \pi_n) =$$
$$-\mathbf{R}_i^{in} - \mathbf{R}_e^{en} + \Gamma_n^{rec} m_i \mathbf{v} - \Gamma_i^{ion} m_i \mathbf{v}_n + \Gamma^{cx} m_i(\mathbf{v} - \mathbf{v}_n) + \mathbf{R}_{ni}^{cx} - \mathbf{R}_{in}^{cx}. \tag{5.61}$$

To arrive at Eqn. (5.60) for plasma momentum evolution, the relationship [11, 103, 104]

$$m_i n\mathbf{v}\mathbf{v} + \mathbb{P} = \sum_{\alpha=i,e} (m_\alpha n\mathbf{v}_\alpha\mathbf{v}_\alpha + \mathbb{P}_\alpha)$$

is used. The total scalar plasma pressure is $p = p_i + p_e$, and the total plasma stress tensor is $\pi = \pi_i + \pi_e$. Assuming the same density and temperature for ions and electrons, for magnetized or unmagnetized plasma, the components of the electron stress tensor, π_e, are all much smaller than the corresponding components in the ion stress tensor, π_i, essentially because of the much larger momentum carried by ions [11]. Components of π_e are smaller by a factor of $\sqrt{m_i/m_e}$ or greater than the corresponding components of π_i. The

factor $\sqrt{m_i/m_e}$ is approximately 43 for protons and is larger for species with higher atomic numbers, so the approximation $\pi \approx \pi_i$ is appropriate.

Generalized Ohm's law

The generalized Ohm's law is found from the electron momentum equation after letting $m_e \to 0$, and using $\mathbf{v}_e = \mathbf{v}_i - \mathbf{j}/en$.

$$\mathbf{E} + \mathbf{v} \times \mathbf{B} = \frac{1}{en} \left(\mathbf{j} \times \mathbf{B} - \nabla \cdot \mathbb{P}_e - \mathbf{R}_i^{ie} + \mathbf{R}_e^{en} \right). \tag{5.62}$$

Energy

Again adding the electron and ion equations and letting $m_e \to 0$,

$$\frac{\partial \varepsilon}{\partial t} + \nabla \cdot \left(\varepsilon \mathbf{v} + \mathbf{v} \cdot (p\mathbb{I} + \pi) + \mathbf{h} \right) =$$
$$\mathbf{j} \cdot \mathbf{E} + \mathbf{v} \cdot \mathbf{R}_i^{in} + \mathbf{v} \cdot \mathbf{R}_e^{en} + Q_i^{in} + Q_e^{en}$$
$$+ \Gamma_i^{ion} \left(\frac{1}{2} m_i \mathbf{v}_n^2 - \phi_{ion} \right) + Q_i^{ion} - \Gamma_n^{rec} \frac{1}{2} m_i \mathbf{v}^2 - Q_n^{rec}$$
$$+ \Gamma^{cx} \frac{1}{2} m_i \left(\mathbf{v}_n^2 - \mathbf{v}^2 \right) + \mathbf{v}_n \cdot \mathbf{R}_{in}^{cx} - \mathbf{v} \cdot \mathbf{R}_{ni}^{cx} + Q_{in}^{cx} - Q_{ni}^{cx}, \tag{5.63}$$

$$\frac{\partial \varepsilon_n}{\partial t} + \nabla \cdot \left(\varepsilon_n \mathbf{v}_n + \mathbf{v}_n \cdot (p_n \mathbb{I} + \pi_n) + \mathbf{h}_n \right) = -\mathbf{v}_n \cdot \left(\mathbf{R}_i^{in} + \mathbf{R}_e^{en} \right)$$
$$+ Q_n^{in} + Q_n^{en} + \Gamma_n^{rec} \frac{1}{2} m_i \mathbf{v}^2 + Q_n^{rec} - \Gamma_i^{ion} \frac{1}{2} m_i \mathbf{v}_n^2 - Q_i^{ion}$$
$$+ \Gamma^{cx} \frac{1}{2} m_i (\mathbf{v}^2 - \mathbf{v}_n^2) + \mathbf{v} \cdot \mathbf{R}_{ni}^{cx} - \mathbf{v}_n \cdot \mathbf{R}_{in}^{cx} + Q_{ni}^{cx} - Q_{in}^{cx}. \tag{5.64}$$

To arrive at Eqn. (5.63) for plasma fluid energy evolution, $\mathbf{R}_i^{ie} \cdot (\mathbf{v} - \mathbf{v}_e)$ has cancelled with $Q_i^{ie} + Q_e^{ie}$ as discussed by Braginskii [11]. Note that, when taking the second moment of C_e^{en}, the plasma-electron bulk fluid reference frame is used so that the term $\mathbf{v} \cdot \mathbf{R}_e^{en}$ arises instead of the $\mathbf{v}_e \cdot \mathbf{R}_e^{en}$ term seen in the electron energy equation. Also, the relationship [11, 103, 104]

$$\varepsilon \mathbf{v} + \mathbf{v} \cdot \mathbb{P} + \mathbf{h} = \sum_{\alpha=i,e} \left(\varepsilon_\alpha \mathbf{v}_\alpha + \mathbf{v}_\alpha \cdot \mathbb{P}_\alpha + \mathbf{h}_\alpha \right)$$

is used in adding the ion and electron flux terms. Here, $\varepsilon = (p_i + p_e)/(\gamma - 1) + \rho \mathbf{v}^2/2$, and $\mathbf{h} = \mathbf{h}_i + \mathbf{h}_e - \gamma p_e \mathbf{j}/[ne(\gamma - 1)]$. (The electron stress tensor is neglected in the defining $\mathbf{h}$.)

To arrive at equations for plasma pressure evolution, the plasma kinetic energy is subtracted from Eqn. 5.63. For details, see Appendix F. The neutral pressure equation is derived in analogous fashion. The resulting pressure evolution equations for plasma and neutral species are

$$\frac{1}{\gamma - 1}\frac{\partial p}{\partial t} + \nabla \cdot (\frac{\gamma}{\gamma - 1}p\mathbf{v} + \mathbf{v} \cdot \pi + \mathbf{h}) = \mathbf{v} \cdot \left[\nabla \cdot (p\mathbb{I} + \pi)\right] + \mathbf{j} \cdot \mathbf{E} - \mathbf{v} \cdot (\mathbf{j} \times \mathbf{B})$$
$$+ Q_i^{in} + Q_e^{en} + (\Gamma_i^{ion} + \Gamma^{cx})\frac{1}{2}m_i(\mathbf{v} - \mathbf{v}_n)^2 - \Gamma_i^{ion}\phi_{ion} + Q_i^{ion} - Q_n^{rec}$$
$$+ \mathbf{R}_{in}^{cx} \cdot (\mathbf{v}_n - \mathbf{v}) + Q_{in}^{cx} - Q_{ni}^{cx}. \tag{5.65}$$

$$\frac{1}{\gamma - 1}\frac{\partial p_n}{\partial t} + \nabla \cdot (\frac{\gamma}{\gamma - 1}p_n\mathbf{v}_n + \mathbf{v}_n \cdot \pi_n + \mathbf{h}_n) = \mathbf{v}_n \cdot \left[\nabla \cdot (p_n\mathbb{I} + \pi_n)\right]$$
$$+ Q_n^{in} + Q_n^{en} + (\Gamma_n^{rec} + \Gamma^{cx})\frac{1}{2}m_i(\mathbf{v} - \mathbf{v}_n)^2 - Q_i^{ion} + Q_n^{rec}$$
$$+ \mathbf{R}_{ni}^{cx} \cdot (\mathbf{v} - \mathbf{v}_n) + Q_{ni}^{cx} - Q_{in}^{cx}. \tag{5.66}$$

The fluid evolution equations are coupled to Faraday's law and the low-frequency Ampère's law. The transport terms $(\pi, \pi_n, \mathbf{h}, \mathbf{h}_n, \mathbf{R}_i^{ie}, \mathbf{R}_i^{in}, \mathbf{R}_e^{in}, \mathbf{R}_e^{en}, \mathbf{R}_n^{in}, \text{and } \mathbf{R}_n^{en})$ must be defined to close the model. This closure is discussed in Section 5.3, in which implementation of the model in HiFi is discussed.

5.2.4 Critical ionization velocity (CIV)

CIV was originally conceived in 1954 by Hannes Alfvén as a mechanism for coalescence of planets from interstellar neutral gas [105]. He predicted that when neutral gas falls toward a central stellar object, if the kinetic energy of the gas particles exceeds a critical velocity such that the kinetic energy surpasses the ionization energy for that particle, ionization would take place. The critical velocity is

$$v_{crit} \equiv \sqrt{2\phi_{ion}/m_n}. \tag{5.67}$$

There is now consensus among astrophysicists that planet formation is explained by the nebular hypothesis [106], in which CIV does not play a significant role. However, after Alfvén's original hypothesis, CIV has been observed in numerous laboratory and space experiments as discussed in the review by Brenning [107]. Theoretical understanding of CIV is reviewed by Lai [108]. Generally, CIV ionization is attributed to transfer of kinetic energy from the neutral particles to the electrons, creating a population of energetic electrons that proceed to ionize more neutrals which then excite more electrons in a reinforcing cycle. The mechanism for the energy conversion is thought to be a plasma instability - perhaps a lower hybrid drift instability or a modified two-stream instability.

The plasma-neutral model described above cannot capture the energy transfer mechanism which involves a non-Maxwellian electron population. The model can, however, approximate the effect by simply increasing ionization when v_{crit} is exceeded. Without CIV, the ionization source rate, Γ_i^{ion} in this model is due only to electron-impact ionization, as derived in Section 5.2.1. However, CIV ionization can be included by redefining Γ_i^{ion} as

$$\Gamma_i^{ion} \equiv \Gamma_i^{e-impact} + \Gamma_i^{CIV}, \tag{5.68}$$

where $\Gamma_i^{e-impact} = n_e n_n \langle \sigma_{ion} v_e \rangle$. Where the relative speed of the neutral gas to the plasma, v_{rel}, exceeds the critical velocity, Γ_i^{CIV} is assumed to proportional to the peak impact ionization rate, which occurs at T_{peak}:

$$
\begin{aligned}
v_{rel} &< v_{crit} \Rightarrow \Gamma_i^{CIV} = 0 \\
v_{rel} &\geq v_{crit} \Rightarrow \Gamma_i^{CIV} = f_{CIV} \Gamma_i^{e-impact}(T_{peak}).
\end{aligned}
\tag{5.69}
$$

f_{CIV} is an arbitrary parameter that can be calibrated based on comparison of simulation results with experimental data. This form for Γ_i^{CIV} is crude and could likely be improved in future development of this phenomenological model for CIV.

5.3   HiFi implementation

The two-component plasma-neutral model of Section 5.2.3 has been implemented in the 2D HiFi code (see Section 1.3), in the physics module pn.f. Appendix D describes the cross-

sections and reaction rates used in the HiFi implementation. Appendix A contains specific information about using the pn.f HiFi module including a description of the normalizations used, and sample input deck options.

The implemented equations are as follows. Interpretation of the plasma-neutral reaction terms is provided in the discussion of the equations, and comparisons are drawn between this model and other models for partially ionized gas (see Section 5.1).

Continuity

$$\frac{\partial \rho}{\partial t} + \nabla \cdot (\rho \mathbf{v} - D_\rho \nabla \rho) = m_i (\Gamma_i^{ion} - \Gamma_n^{rec}), \tag{5.70}$$

$$\frac{\partial \rho_n}{\partial t} + \nabla \cdot (\rho_n \mathbf{v}_n - D_\rho \nabla \rho_n) = m_i (\Gamma_n^{rec} - \Gamma_i^{ion} - \lambda \Gamma^{cx}). \tag{5.71}$$

The source terms in the plasma continuity equation represent the gain of ions due to ionization (Γ_i^{ion}) and the loss of ions due to recombination ($-\Gamma_n^{rec}$). Similar terms for ionization and recombination are present as sources for the neutral continuity equation in addition to a third term, $-\lambda \Gamma^{cx}$, which represents an *ad hoc* term to allow for the loss of the neutral products of CX collisions (called CX neutrals). If short mean free paths of CX neutrals are expected, the factor λ should be set to zero. If large mean free paths are expected for CX neutrals, the factor can be set to a value between zero and one to allow CX neutrals to leave the system along with their momentum and energy. (Non-zero λ is used in only one of the applications — the RMF-driven FRC spin-up presented in Section 6.3.)

The codes UEDGE [89, 90] and B2 [91, 92], discussed in Section 5.1, employ separate ion, electron, and neutral continuity equations. They can optionally use source terms similar to those given above in the continuity equations, or they can account for the use Monte Carlo codes to determine the neutral distribution function. The model proposed by Braginskii [11] uses a combined plasma-neutral continuity equation and does not include reaction effects. Zaqarashvili et al. [86] allow separate plasma and neutral continuity equations, but do not allow reactions. Pauls et al. [84] do not include ionization and recombination reactions.

Momentum

$$\frac{\partial}{\partial t}(\rho\mathbf{v}) + \nabla \cdot \left\{ \rho\mathbf{v}\mathbf{v} + p\mathbb{I} - \xi[\nabla\mathbf{v} + (\nabla\mathbf{v})^{\intercal}] - 2\xi_a\mathbb{I} \circ (|\nabla\mathbf{v}| \circ \nabla\mathbf{v}) \right\} =$$
$$\mathbf{j} \times \mathbf{B} + \Gamma_i^{ion}m_i\mathbf{v}_n - \Gamma_n^{rec}m_i\mathbf{v} + \Gamma^{cx}m_i(\mathbf{v}_n - \mathbf{v}) + \mathbf{R}_{in}^{cx} - \mathbf{R}_{ni}^{cx}, \qquad (5.72)$$

$$\frac{\partial}{\partial t}(\rho_n\mathbf{v}_n) + \nabla \cdot \left\{ \rho_n\mathbf{v}_n\mathbf{v}_n + p_n\mathbb{I} - \xi_n[\nabla\mathbf{v}_n + (\nabla\mathbf{v}_n)^{\intercal}] \right\} =$$
$$\Gamma_n^{rec}m_i\mathbf{v} - \Gamma_i^{ion}m_i\mathbf{v}_n + \Gamma^{cx}m_i[(1-\lambda)\mathbf{v} - \mathbf{v}_n] + (1-\lambda)\mathbf{R}_{ni}^{cx} - \mathbf{R}_{in}^{cx}. \qquad (5.73)$$

The stress tensors π and π_n from Eqns. (5.60) – (5.61) have been replaced with standard approximations. The plasma stress tensor approximation, $-\xi[\nabla\mathbf{v} + (\nabla\mathbf{v})^{\intercal}]$, is the same as presented in Section 1.4. The neutral fluid stress tensor, $-\xi_n[\nabla\mathbf{v}_n + (\nabla\mathbf{v}_n)^{\intercal}]$, is identical in form. The dynamic viscosity coefficients, ξ and ξ_n, are either set as uniform values, or determined as functions of other variables. For example, the plasma viscosity can be calculated using the formula for unmagnetized viscosity given by Braginskii [11]. The neutral viscosity can be calculated using a rigid elastic sphere model (see, e.g., Chapman and Cowling [101]). In each application problem of Chapter 6, specific choices for viscosity coefficients are stated. See also the discussion in Appendix G related to determining transport coefficients when reactions are present. In the plasma momentum equation, ξ_a is the same uniform artificial viscosity coefficient discussed for the dissipative MHD model of Section 1.4. Appendix B contains additional discussion of artificial viscosity.

Notice that the terms $\mathbf{R}_i^{in}$ and $\mathbf{R}_e^{en}$ have been dropped. In Goldston [80] (p. 163), neutral-charged particle collisions are shown to be relatively unimportant compared to coulomb collisions for plasmas that are "even a few percent ionized". In the research presented in this dissertation, simulations focus on plasmas with significant ionization fractions. If the model is applied to a problem in which interesting physics occurs in regions of very low ionization, these terms should be addressed and included. Schunk and Nagy [83] propose treating neutral-charged particle interactions as Maxwell molecule collisions. The terms involving reaction rates (Γ^{rxn}) times velocities represent the direct transfer of momentum

due to bulk fluid effects. The terms $\mathbf{R}_{in}^{cx}$ and $\mathbf{R}_{ni}^{cx}$ represent the "frictional" drag forces due to charge exchange, and are analogous to the frictional drag force acting on electrons and represented by $\eta\mathbf{j}$ in the generalized Ohm's law. When the ion and neutral distribution functions interact, if the bulk fluid velocities are identical, the distribution functions overlap, the CX reaction rate is symmetric in the velocity space, and there are no inter-species frictional forces. If the bulk fluid velocities differ, the distribution functions do not overlap, the CX reaction rate is no longer symmetric in the velocity space, and frictional forces arise. Note that similar terms for ionization and recombination integrate to zero as shown in Section 5.2.1. There is no asymmetry of the reaction rates of ionization and recombination in velocity space because the rates depend only on the electron velocity distribution function. The related integrals are odd in velocity, and no frictional terms related to ionization and recombination arise.

As in the neutral continuity equation, the factor λ can be set to a value between zero and one to represent the partial or complete escape of CX neutrals. The terms in the neutral momentum equation affected by the loss of CX neutrals are direct momentum transfer, and frictional momentum transfer terms; these terms are multiplied by $(1 - \lambda)$.

Momentum equations in the codes UEDGE [89, 90] and B2 [91, 92], discussed in Section 5.1, are highly specialized. Parallel momentum for separate ion and electron fluids is treated with attention to physics present in the tokamak edge. Perpendicular plasma momentum in these codes is determined with an inertialess approach taking into account effects relevant in the tokamak edge physics, including particle drifts, and possibly incorporating turbulent transport. Perpendicular neutral momentum is either determined by an intertialess diffusion approximation, or by Monte Carlo codes. The model proposed by Braginskii [11] has a combined plasma-neutral momentum without reaction effects. Zaqarashvili et al. [86] allow separate plasma and neutral momentum equations, but do not allow reactions or transport. The momentum equations of Pauls et al. [84] include identical CX terms[2], but do not include ionization and recombination reactions, and neglect the plasma and neutral stress tensors. Helander et al. [98] derive a combined ion-neutral momentum equation. The individual

---

[2]As noted in the derivation, the approach of Pauls et al. [84] for moments of CX is adopted in this work.

(ion and neutral) momentum are found using relations determined by Chapman-Enskog-like solution of the relevant Boltzmann equations assuming a CX-dominated neutral distribution function.

Generalized Ohm's law

$$\frac{\partial \mathbf{A}}{\partial t} = \mathbf{v} \times \mathbf{B} - \eta \mathbf{j}. \tag{5.74}$$

It is in this equation that Faraday's law and the low-frequency Ampère's law are incorporated. The magnetic vector potential, $\mathbf{A}$, determines the magnetic field via $\mathbf{B} = \nabla \times \mathbf{A}$. Faraday's law states that $\nabla \times \mathbf{E} = -\partial \mathbf{B}/\partial t$. Substituting the expression for $\mathbf{B}$ in terms of $\mathbf{A}$ yields $\nabla \times \mathbf{E} = \nabla \times (-\partial \mathbf{A}/\partial t)$. This is the basis for replacing $\mathbf{E}$ in Eqn. (5.62) with $-\partial \mathbf{A}/\partial t$. The low-frequency Ampère's law is used to determine the current density as $\mathbf{j} = \nabla \times \mathbf{B}/\mu_0$.

In addition to neglecting the electron-neutral scattering term $\mathbf{R}_e^{en}$ (see discussion in the previous section on the momentum equations), two other terms in the generalized Ohm's law shown in Eqn. (5.62) are assumed to be negligibly small: $\mathbf{j} \times \mathbf{B}/(en)$ (the Hall term) and $\nabla \cdot \mathbb{P}_e/(en)$ (the diamagnetic term). Several sources [11, 16, 17] provide detailed discussion of the range of validity for these assumptions. A particularly important requirement is that length scales of interest should be much larger than the ion gyroradius.

The frictional drag term, $-\mathbf{R}_i^{ie}/(en)$, of Eqn. (5.62) is generally anisotropic with drag forces perpendicular to the magnetic field being a factor of two stronger than those parallel to the field. For this research, isotropic resistive drag, $\eta \mathbf{j}$, is assumed. The magnitude of the resistivity value is either taken to be constant, or is set equal to the sum of two resistive contributions. The first contribution is a typical Spitzer resistivity caused by Coulomb drag between the electrons and ions. If the ion charge is unity,

$$\eta_{sp} = \frac{5 \times 10^{-5} \ln(\Lambda)}{T_e^{3/2}} \text{Ohm-m}, \tag{5.75}$$

where $\ln(\Lambda)$ is specified (hard-coded) for a given simulation, and T_e is the electron temperature in eV. The second contribution is the so-called "Chodura" resistivity [109], which is

a phenomenological resistivity designed to capture anomalous electron drag that occurs at low density and high current. Chodura resistivity is calculated as

$$\eta_C = \nu_C \frac{m_e}{ne^2}\text{Ohm-m},\tag{5.76}$$

where ν_C is a frequency,

$$\nu_C = C_C \omega_{pi}\left[1 - e^{-\frac{v_e}{f v_s}}\right]\text{s}^{-1},\tag{5.77}$$

where C_C is the Chodura constant, typically set as $C_C \approx 0.1$, the electron drift speed is $v_e = |\mathbf{j}|/(en)$, the sound speed is $v_s = \sqrt{\gamma p/\rho}$. The parameter f is typically $f \approx 3$. ω_{pi} is the ion plasma frequency. As v_e exceeds v_s significantly, η_C becomes large. This rise in resistivity is intended to capture the effect of microinstabilities in the electron fluid. In investigations using the 5-moment two-fluid (electron and ion) model, Loverich and Shumlak [110] and Hakim and Shumlak [111] observed an anomalous resistivity of this type in a nonlinear five-moment two-fluid model. The additive combination of these two resistivities is called Spitzer-Chodura resistivity,

$$\eta_{SC} = \eta_{sp} + \eta_C.\tag{5.78}$$

In the codes UEDGE [89, 90] and B2 [91, 92], discussed in Section 5.1, electric fields are determined using a Poisson solver rather than an Ohm's law. The model proposed by Braginskii [11] uses an Ohm's law similar to that given by Eqn. 5.74, except that special attention is given to electron-neutral scattering collisions which are neglected in Eqn. 5.74. Zaqarashvili et al. [86] use an Ohm's law similar to that of Braginskii. The model used by Pauls et al. [84] assumes that no electromagnetic fields are present.

Pressure

$$\frac{1}{\gamma - 1}\frac{\partial p}{\partial t} + \nabla \cdot \left(\frac{\gamma}{\gamma - 1}p\mathbf{v} + \mathbf{h}\right) = \mathbf{v} \cdot \nabla p + \eta\mathbf{j}^2 + \xi\nabla\mathbf{v} : [\nabla\mathbf{v} + (\nabla\mathbf{v})^{\mathsf{T}}]$$

$$+ \xi_a \{\mathbb{I} \circ [|\nabla\mathbf{v}| \circ \nabla\mathbf{v} + |\nabla\mathbf{v}^{\mathsf{T}}| \circ \nabla\mathbf{v}^{\mathsf{T}}]\} : \nabla\mathbf{v}$$

$$+ (\Gamma_i^{ion} + \Gamma^{cx})\frac{1}{2}m_i(\mathbf{v} - \mathbf{v}_n)^2 - \Gamma_i^{ion}\phi_{ion} + Q_i^{ion} - Q_n^{rec}$$

$$+ \mathbf{R}_{in}^{cx} \cdot (\mathbf{v}_n - \mathbf{v}) + Q_{in}^{cx} - Q_{ni}^{cx}, \tag{5.79}$$

$$\frac{1}{\gamma - 1}\frac{\partial p_n}{\partial t} + \nabla \cdot \left(\frac{\gamma}{\gamma - 1}p_n\mathbf{v}_n + \mathbf{h}_n\right) = \mathbf{v}_n \cdot \nabla p_n + \xi_n\nabla\mathbf{v}_n : [\nabla\mathbf{v}_n + (\nabla\mathbf{v}_n)^{\mathsf{T}}]$$

$$+ [\Gamma_n^{rec} + (1 - \lambda)\Gamma^{cx}]\frac{1}{2}m_i(\mathbf{v} - \mathbf{v}_n)^2 - Q_i^{ion} + Q_n^{rec}$$

$$+ (1 - \lambda)\mathbf{R}_{ni}^{cx} \cdot (\mathbf{v} - \mathbf{v}_n) + (1 - \lambda)Q_{ni}^{cx} - Q_{in}^{cx}. \tag{5.80}$$

Using the resistive MHD generalized Ohm's law of Eqn. 5.74, the terms $\mathbf{j} \cdot \mathbf{E} - \mathbf{v} \cdot (\mathbf{j} \times \mathbf{B})$ can be written as $\mathbf{E}^* \cdot \mathbf{j}$, where $\mathbf{E}^* = \mathbf{E} + \mathbf{v} \times \mathbf{B}$ [104]. Using Eqn. (5.3) for $\mathbf{E}$, $\mathbf{E}^* \cdot \mathbf{j}$ reduces to the term $\eta\mathbf{j}^2$ in the plasma pressure equation above. The charged-neutral particle scattering terms, Q_i^{in} and Q_e^{en}, are dropped for the same reasons cited for dropping the similar scattering terms in the momentum equations. The term $\mathbf{R}_{in}^{cx} \cdot (\mathbf{v}_n - \mathbf{v})$ in the plasma pressure equation represents the work done by the frictional force $\mathbf{R}_{in}^{cx}$, which acts on the plasma fluid with the relative velocity $(\mathbf{v}_n - \mathbf{v})$. A similar term in the neutral pressure equation represents the frictional work done by the plasma fluid on the neutral fluid. As discussed in Section 5.2.1, the terms Q_i^{ion} and Q_n^{rec} are associated with the gain/loss of thermal energy due to ionization and recombination. The terms Q_{ni}^{cx} and Q_{in}^{cx} are thermal energy transfer terms related to CX.

The stress tensors, π and π_n, have been approximated as discussed for the momentum equations. The plasma heat flux is approximated as

$$\mathbf{h} = -\left[\kappa_{\parallel}\hat{\mathbf{b}}\hat{\mathbf{b}} + \kappa_{\perp}\left(\mathbb{I} - \hat{\mathbf{b}}\hat{\mathbf{b}}\right)\right] \cdot \nabla T - \gamma p_e\mathbf{j}/[ne(\gamma - 1)],$$

where the $\kappa_{\parallel}$ and $\kappa_{\perp}$ account for the effects of ion and electron thermal diffusion parallel and perpendicular, respectively, to the magnetic field direction which is given by the unit

vector $\hat{\mathbf{b}}$ (*cf.* Section 1.4). The part of the plasma heat flux proportional to the electron pressure, p_e, accounts for the convection of electron thermal energy. (In all of the simulations presented, temperature variation is ignorable in the direction of the current, so this term is zero.) The neutral heat flux is calculated as $\mathbf{h}_n = -\kappa_n \nabla T_n$, where κ_n is the neutral thermal conductivity, as discussed in detail below. Each viscosity and thermal conduction coefficient can be uniform or variable. For example, a non-uniform plasma thermal conductivity can be calculated using formulas given by Braginskii [11]. The neutral thermal conduction can be calculated using a rigid elastic sphere model (see, e.g., Chapman and Cowling [101]) or using an *ad hoc* expression that can be applied, as discussed below, for a neutral distribution function in which CX and scattering effects are on the same order. In each application problem of Chapter 6, specific choices for thermal conductivity coefficients are stated. See also the discussion in Appendix G related to determining transport coefficients when reactions are present.

As mentioned above, neutral thermal conductivity can be uniform or variable. One option for neutral thermal conductivity in the HiFi implementation is the hard sphere model derived assuming that the neutral-neutral elastic collision term is the lowest-order term in the neutral Boltzmann equation when applying Chapman-Enskog expansion. Using a hard sphere model, the neutral thermal conductivity is

$$\kappa_{n,hs} = \frac{5}{2} \frac{k_b}{m_n} \frac{n_n k_b T_n}{\nu_{hs}} \;\; \frac{\text{W}}{\text{m eV}}, \tag{5.81}$$

where $k_b = 1.602 \times 10^{-19}$ J/eV is Boltzmann's constant. ν_{hs} is the neutral-neutral scattering frequency, defined as $\nu_{hs} \equiv \bar{C} \pi d^2 n_n$, where $\bar{C}$ is the mean neutral velocity defined by $(\bar{C})^2 \equiv 8 k_b T_n / (\pi m_n)$, and d is the diameter of a hard sphere representing the desired atom. This conductivity is implemented two atoms: deuterium, and neon. The hard sphere diameters for these atoms are taken to be $d_d = 0.240$ nm and $d_{ne} = 0.308$ nm. Another option has been implemented that approximates the neutral thermal conductivity found when CX collisions are assumed to enter the expanded neutral Boltzmann equation at the same order as neutral-neutral elastic collisions. This approximate thermal conductivity is

$$\kappa_{n,cx-hs} = \frac{5}{2} \frac{k_b}{m_n} \frac{n_n k_b T_n}{\nu_{cx-hs}} \ \frac{\text{W}}{\text{m eV}}, \tag{5.82}$$

where $\nu_{cx-hs} \equiv \nu_{cx} + \nu_{hs}$. The CX frequency is defined as $\nu_{cx} \equiv \bar{C} n \sigma_{cx}$, where n is the plasma number density and σ_{cx} is the CX cross section. (See Appendix D for CX cross sections.) While this approximation is *ad hoc*, it approximates the perpendicular thermal transport intuitively expected in the edge of a magnetically confined plasma. For example, in a region with low neutral density, ν_{hs} may be small, resulting in high $\kappa_{n,hs}$. However, if $\nu_{cx} \gg \nu_{cx}$ is high, CX limits the step size of the neutrals, and thermal conductivity is computed as $\kappa_{n,cx-hs} \approx \frac{5}{2} \frac{k_b}{m_n} \frac{n_n k_b T_n}{\nu_{cx}}$. Appendix G provides further discussion of reaction effects on transport, including comparison of the *ad hoc* neutral thermal conductivity given in Eqn. (5.82) to a similar term formally derived by Helander et al. [98] assuming a CX-dominated neutral distribution.

As in the neutral continuity and momentum equations, the factor λ can be set to a value between zero and one to represent the partial or complete escape of CX neutrals. In the neutral pressure equation, the terms affected by the loss of CX neutrals are the direct conversion of kinetic energy to thermal energy, frictional work, and thermal energy transfer terms; these terms are multiplied by $(1 - \lambda)$.

In the codes UEDGE [89, 90] and B2 [91, 92], discussed in Section 5.1, ion and electron fluid energy evolution is determined using fluid equations and closures similar to those proposed by Braginskii [11]. Neutral energy evolution is either modeled using a simple neutral diffusion fluid model or by full Monte Carlo calculation. The model proposed by Braginskii [11] uses a combined plasma-neutral energy equation without reaction effects. Zaqarashvili et al. [86] have separate plasma and neutral energy evolution, but do not allow reactions or transport. The energy equations of Pauls et al. [84] include identical CX terms, but do not include ionization and recombination reactions, and neglect the plasma and neutral stress tensors and heat fluxes. Helander et al. [98] derive a combined ion-neutral energy equation. The individual (ion and neutral) energies are found using relations determined by Chapman-Enskog-like solution of the relevant Boltzmann equations assuming a CX-dominated neutral distribution function.

Chapter 6

PLASMA-NEUTRAL MODEL APPLICATIONS

Several studies have been conducted using the HiFi implementation of the two-component plasma-neutral model presented in Section 5.3:

- Plasma acceleration with parallel-plate electrodes. Particular attention is given to critical ionization velocity (CIV) effects.

- Plasma acceleration with coaxial electrodes. Effects of neutral gas on the canting angle of the snowplow plasma front seen in coaxial-electrode plasma acceleration are identified.

- RMF-driven FRC ion spin-up. The damping effect of charge exchange from the rotating ions and a slow neutral population is observed.

- The Electrodeless Lorentz-Force (ELF) thruster [112] is modeled. These simulations are intended to provide guidance for development and operation of the ELF thruster and to validate the plasma-neutral model.

The above applications are described in detail in Sections 6.1 – 6.4. The first three are qualitative applications; in the final application (to ELF), results are thoroughly quantified, and preliminary experimental results are compared to the modeling results.

6.1 Plasma acceleration with parallel-plate electrodes

The plasma-neutral model has been applied to study plasma acceleration with parallel-plate electrodes as shown in Figure 6.1.1. A power supply is modeled as a current source, which injects flux at the left boundary, driving a specified amount of total current between the electrodes. The strength of the injected out-of-plane magnetic field is uniform in the
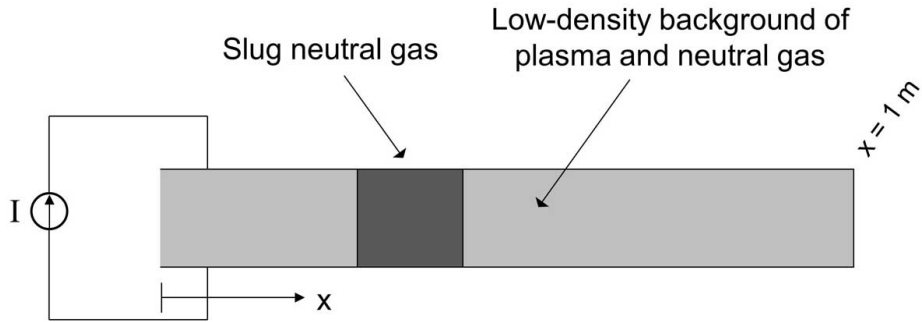
Figure 6.1: Parallel-plate-electrode plasma acceleration test for CIV effects in plasma-neutral model. In this geometry, the dynamics are 1D — variations exist only in the x-direction. A current sheet drives a snowplow plasma front as the plasma between the plates is accelerated. This accelerated plasma interacts with the downstream slug of neutral gas. The plasma and neutral gas density and applied voltage varied. CIV effects are turned on and off to determine the importance of the effects. The factor f_{CIV} shown in Eqn. (5.69) is set to either 0 or 10.

y-direction, and the behavior captured by the plasma-neutral model is one-dimensional. As the plasma is accelerated, a snowplow plasma front forms. The primary goal of this application is to explore the possibility of capturing critical ionization velocity (CIV) effects using the implementation discussed in Section 5.2.4.

6.1.1 Computational setup

Three pairs of simulations are run: CIV-1a/b, CIV-2a/b, and CIV-3a/b. The setup for the first pair of simulations, CIV-1a/b, is based loosely on an experiment by Chang et al. [113] designed to measure CIV effects in cometary neutral gas. In the second pair of simulations, CIV-2a and -2b, densities are increased. In the third pair of runs, the driven current is increased. Full details follow.

The varied parameters are f_{CIV}, which controls the magnitude of CIV effects, the plasma and neutral densities, and the applied voltage. In runs with the label "a", CIV effects are

Table 6.1: Characteristic quantities for parallel-plate plasma acceleration simulations. The normalization basis is given in terms of length (L_0), density (n_0), and magnetic field (B_0). Characteristic pressure, velocity, and time are derived from this basis.

Sim. name	L_0(m)	n_0 (m^{-3})	B_0 (T)	p_0 (Pa)	v_0 (m/s)	t_0 (s)
CIV-1a/b	1	10^{18}	0.01	79.6	1.54×10^5	6.48×10^{-6}
CIV-2a/b	1	10^{20}	0.01	79.6	1.54×10^4	6.48×10^{-5}
CIV-3a/b	1	10^{20}	0.4	1.27×10^5	6.17×10^5	1.62×10^{-6}

activated by setting the factor f_{CIV} shown in Eqn. (5.69) to 10. In runs with the label "b", $f_{CIV} = 0$.

Deuterium plasma and neutral gas are assumed. The mass taken for deuterium atoms and ions is 3.345×10^{-27} kg. The effective ionization potential for deuterium (taking into account ionization from the diatomic configuration) is $\phi_{ion} = 33$ eV [114].

Characteristic quantities

A normalization basis is chosen in terms of characteristic length (L_0), density (n_0), and magnetic field (B_0). Characteristic pressure, velocity, and time are defined in terms of this basis as $p_0 = \frac{B_0^2}{\mu_0}$, $v_0 = \sqrt{\frac{p_0}{n_0 m_i}}$, and $t_0 = \sqrt{\frac{L_0}{v_0}}$. In normalized terms, the setup for each of the six simulations is identical. By choosing different characteristic quantities in the simulations, different behaviors are observed. Table 6.1 shows these characteristic quantities for each simulation.

Geometry and initial condition

The 1D domain for all of the simulations is shown in Figure 6.1. The domain length is 1 m. The initial condition in terms of the characteristic quantities given in Table 6.1 are as follows. The background (plasma and neutral) density and (plasma and neutral) pressure are $\rho_{min} = 0.1$ and $p_{min} = 0.001$. Between $0.35 < x < 0.45$ m, the neutral density is 1.7. The neutral density smoothly transitions (using a half-period of a sinusoid) from the

background value to 1.7 at the edges of this region, i.e., in the ranges $0.3 < x < 0.35$ m and $0.45 < x < 0.5$ m. The neutral gas has the background pressure everywhere. The plasma has the background density and pressure everywhere.

Dissipation

Normalized dissipation coefficients are now given.[1](Characteristic quantities for normalizations are given above.) These coefficients are identical for all of the six simulations. Viscosity coefficients are $\xi = 5 \times 10^{-3}$ and $\xi_n = 10^{-2}$. Thermal conduction coefficients are $\kappa_\perp^m = 5 \times 10^{-3}$ for the plasma, and $\kappa_n = 10^{-2}$ for the neutral fluid. Magnetic field in this problem is out-of-plane. Out-of-plane temperature gradients are ignorable, so parallel thermal conduction is irrelevant. Resistivity is $\eta = 10^{-3}$. Density diffusion is $D_\rho = 5 \times 10^{-4}$. These dissipation coefficients are not meant to accurately represent physical dissipation. Actual physical dissipation mechanisms in the problem are assumed to be small. Strong gradients and shocks are expected in a physical system of the type modeled here. The values are chosen because they provide sufficient dissipation for numerically smooth solutions that approximate the expected physical solutions.

Boundary conditions

The top and bottom boundaries are periodic. At the left boundary a current source is modeled by specifying the out-of-plane magnetic field (B_z). Initially, $B_z = 0$. For $0 < t < 0.5$, $\partial B_z/\partial t = 0.5$. Thus, at $t = 0.5$, $B_z = 0.25$. Using Ampère's law, the total current driven (per unit out-of-plane length, L_z) between the electrodes is $I/L_z = B_z/\mu_0$. In physical units, when $B_0 = 0.01$ T, $I/L_z = 1.99$ kA, and when $B_0 = 0.4$, $I/L_z = 79.6$ kA. Zero normal derivative BC are enforced for plasma and neutral density, (x-direction) plasma and neutral momenta, and plasma and neutral pressures. At the right boundary, the boundary conditions are the same except that zero normal derivative is enforced for B_z, and plasma momentum is set to zero.

---

[1]For the relation of normalized dissipation coefficients to dimensionless numbers, see the discussion in Section 1.4.

Spatial resolution and time advance

Each simulation is run from $t = 0$ to $t = 2$ using a fixed timestep size of 2×10^{-3}. The grid used for these simulations has 48 cells, each with 6th-degree polynomials.

6.1.2   Results

In the absence of reactions, the simulation results would be identical. That is, the normalized dissipations are uniform and constant, implying identical dimensionless numbers (Reynolds number, magnetic Reynolds number, etc.) for all simulations. The plasma-neutral reaction physics depends on the physical values present in the simulations. For example, for a normalized velocity of 1 in CIV-1a, the actual velocity would be 1.54×10^5 m/s. The critical ionization velocity for deuterium is $v_{crit} = 3.61 \times 10^4$ m/s, so CIV ionization would be significant. In CIV-2a, however, the same normalized velocity implies an actual velocity of only 1.54×10^4, so CIV ionization would be insignificant. Also, ionization, recombination, and charge exchange depend strongly on the actual densities, temperatures, and velocities.

Results from simulations CIV-1a and -1b are presented in Figure 6.2. In CIV-1a, CIV effects are included in the model (by using $f_{CIV} = 10$), and CIV ionization has a significant effect on the observed velocity and density profiles, as compared to the results for CIV-1b, in which CIV effects are excluded from the model (by using $f_{CIV} = 0$). In CIV-1a, the neutral accumulation due to CIV ionization slows the plasma motion until the relative plasma-neutral velocity is less than v_{crit}. In CIV-1b, the plasma acceleration is almost completely uninhibited by the slug of neutral gas. Although CIV ionization is set to zero, the other plasma-neutral interactions have effects observable in the neutral density plotted in the lower-right panel of Figure 6.2. The neutral density profile is observed to diffuse and evolve over time. Factors contributing to neutral density evolution include charge exchange (CX) heating (which creates a neutral pressure gradient), CX momentum transfer, electron-impact ionization, and also the artificial neutral density diffusion term.

Results from CIV-2a and -2b, in which densities are 100 times greater than in the CIV-1 simulations, are shown in Figure 6.3. The current source does not deliver enough energy to accelerate the plasma to v_{crit}, so CIV effects are irrelevant.
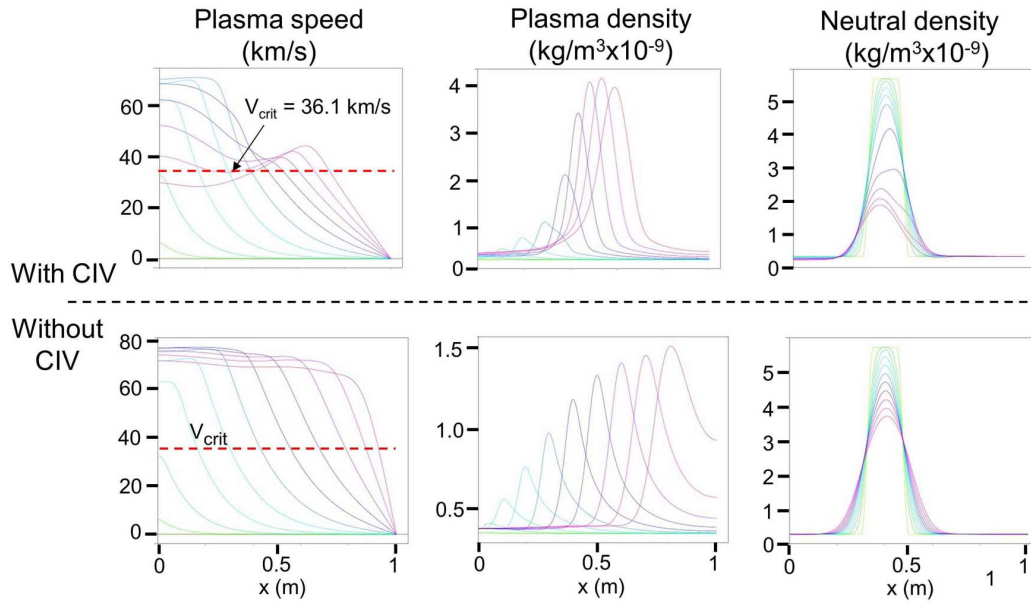
Figure 6.2: Results from parallel-plate-electrode simulations CIV-1a/b in which CIV is significant. Plasma speed, plasma density, and neutral density are shown for runs CIV-1a (top) and CIV-1b (bottom). When CIV effects are included (as in CIV-1a), mass accumulation caused by CIV ionization slows the plasma. The critical velocity (v_{crit}) for deuterium is 36.1 km/s as shown in the figure. The neutral density in CIV-1b (without CIV) is observed to diffuse and evolve over time. The non-CIV plasma-neutral interactions (charge exchange, electron-impact ionization, and radiative recombination) are factors in neutral density evolution, along with the artificial neutral density diffusion. (Trace color varies from yellow at early times to magenta at late times.)
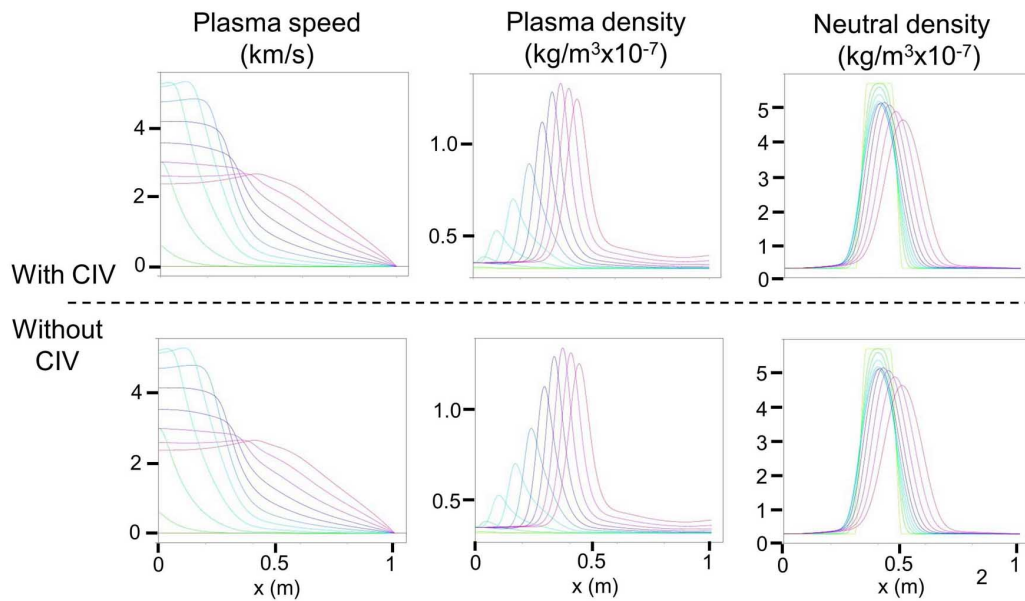
Figure 6.3: Results from parallel-plate-electrode simulations CIV-2a/b in which CIV is shown to be insignificant. Plasma speed, plasma density, and neutral density are shown for runs CIV-2a (top) and CIV-2b (bottom). Results with and without CIV effects are identical because the plasma speed never exceeds v_{crit}. (Trace color varies from yellow at early times to magenta at late times.)

As seen in Figure 6.4, in simulations CIV-3a and -3b, the current source drives the plasma to speeds greater than v_{crit}, and the energy of this dense, high-speed flow is large enough that the slug of neutral gas is easily ionized with or without CIV effects. Figure 6.5 shows plasma, neutral, and total masses per unit out-of-plane length as a function of time. Note that total mass varies in the CIV-3a simulation because of the inflow that occurs at the $x = 0$ boundary. (Total momentum and energy are variable for the same reason. Conservation properties of the plasma-neutral HiFi implementation are verified in the ELF simulations presented in Section 6.4.) Also plotted in Figure 6.5 are cumulative total ionization (i.e., CIV plus electron-impact ionization) and CIV ionization per unit out-of-plane length during the simulation. As shown, although CIV is present in CIV-3a, electron-impact ionization plays a dominant role. CIV ionization accounts for only 14% of total ionization. The CIV-3b results seen in Figure 6.4 are qualitatively similar although no CIV ionization is present.

6.2   Plasma acceleration with coaxial electrodes

Plasma acceleration in a coaxial-electrode configuration, as shown in Figure 6.6, has also been modeled. A current source, like the one described in Section 6.1, drives a specified current between the inner and outer electrodes. When current is driven, azimuthal magnetic flux is injected. A current sheet forms in low-density background plasma, and encounters either a plasma or a neutral slug, which has been initialized downstream. If the slug is neutral, the injected magnetic energy heats and ionizes the neutrals as acceleration occurs. The injected magnetic field is stronger near the inner electrode, so the inner plasma (whether pre-existing or created by ionization) is driven faster than the outer plasma, creating a canted snowplow plasma front. Differences in the current sheet propagation speed and canting angle are observed.

6.2.1   Computational setup

The computational setup details are similar to those presented for the 1D parallel-plate acceleration problem in Section 6.1.1. Note that CIV ionization is not included in this problem or any others except the one presented in Section 6.1.
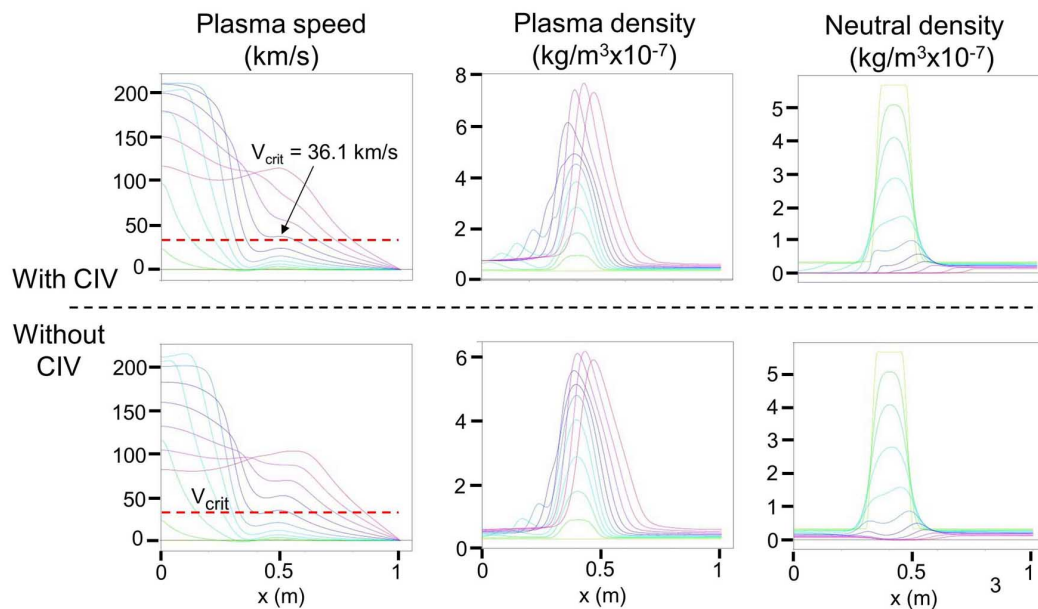
Figure 6.4: Results from parallel-plate-electrode simulations CIV-3a/b in which CIV is shown to be insignificant. Plasma speed, plasma density, and neutral density are shown for runs CIV-3a (top) and CIV-3b (bottom). Results with and without CIV effects are qualitatively similar because the accelerated plasma has enough energy to rapidly ionize the slug of neutral gas with typical electron-impact ionization. (Trace color varies from yellow at early times to magenta at late times.)
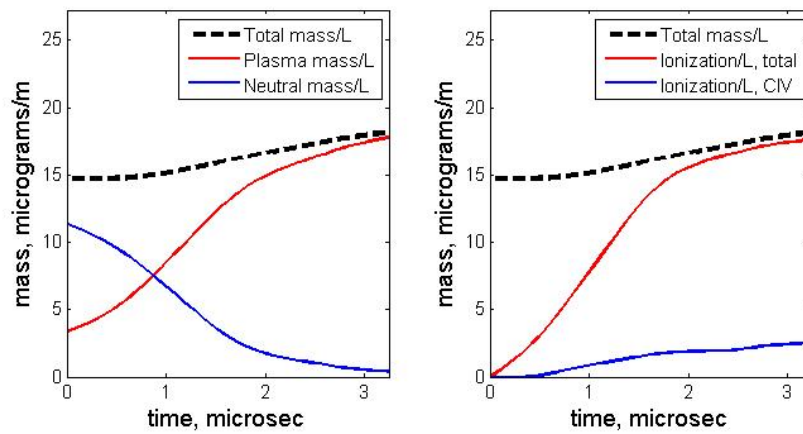
Figure 6.5: Time traces of mass-related quantities for the parallel-plate-electrode simulations CIV-3a/b, in which electron-impact ionization is found to be dominant. Masses per unit out-of-plane length are shown. The left panel shows plasma, neutral, and total mass. On the right, cumulative total ionization mass and CIV ionization mass are shown. The total mass varies because of the inflow at the $x = 0$ boundary. During the simulation, the ionization fraction increases from 26.7% to 96.5%. Of the total cumulative ionization during the simulation, only 14% is due to CIV ionization.
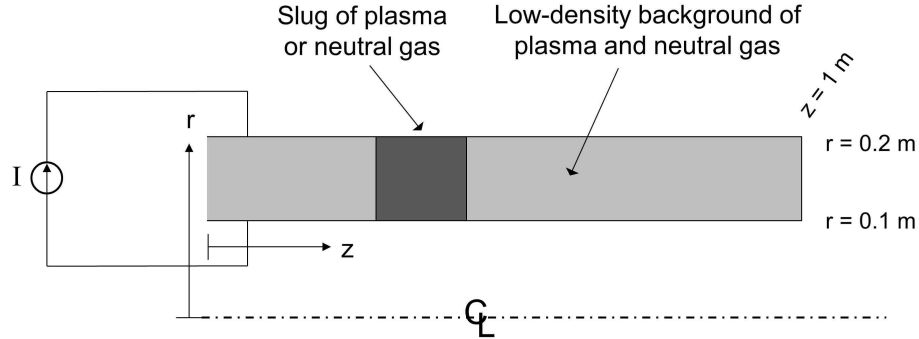
Figure 6.6: Coaxial-electrode plasma acceleration setup. In this geometry, the dynamics are 2D — there are variations in the r-z plane. Azimuthal flux is injected at the left boundary. The injected flux encounters either a high-density slug of plasma, which is accelerated, or neutral gas, which is ionized and accelerated. A "snowplow" plasma front forms because the magnetic pressure is greater near the central electrode and the plasma at smaller radii is accelerated more strongly.

Deuterium plasma and neutral gas are assumed. The mass taken for deuterium atoms and ions is 3.345×10^{-27} kg. The effective ionization potential for deuterium (taking into account ionization from the diatomic configuration) is $\phi_{ion} = 33$ eV [114].

Characteristic quantities

A normalization basis is chosen in terms of characteristic length (L_0), density (n_0), and magnetic field (B_0). Characteristic pressure, velocity, and time are defined in terms of this basis as $p_0 = \frac{B_0^2}{\mu_0}$, $v_0 = \sqrt{\frac{p_0}{n_0 m_i}}$, and $t_0 = \sqrt{\frac{L_0}{v_0}}$. The normalization basis for this 2D coaxial acceleration problem is $L_0 = 1$ m, $n_0 = 10^{20}$ m^{-3}, and $B_0 = 0.2$ T. This basis gives the following characteristic pressure, velocity, and time: $p_0 = 3.18 \times 10^4$ Pa, $v_0 = 3.08 \times 10^5$ m/s, and $t_0 = 3.24 \times 10^{-6}$ s.

Geometry and initial condition

The cylindrical domain for these simulations is shown in Figure 6.6. The domain length is 1 m. The radius of the inner electrode is $r_{inner} = 0.1$ m, and the outer electrode radius is $r_{outer} = 0.2$ m. The initial condition in terms of normalized variables are as follows. The background (plasma and neutral) density and (plasma and neutral) pressure are $\rho_{min} = 0.1$ and $p_{min} = 0.001$. Between $0.35 < x < 0.45$ m, the slug (either plasma or neutral) density is 1.7. The slug density smoothly transitions (using a half-period of a sinusoid) from the background value to 1.7 at the edges of this region, i.e., in the ranges $0.3 < x < 0.35$ m and $0.45 < x < 0.5$ m. The plasma and neutral gas have the background pressure everywhere.

Dissipation

Normalized dissipation coefficients are identical to those presented in Section 6.1.1. Characteristic quantities for normalizations are given above.

Boundary conditions

At the left boundary a current source is modeled by specifying the azimuthal magnetic field as a function of r and t. Initially, $B_\theta(r) = 0$. For $0 < t < 0.5$, $\partial B_\theta(r, t)/\partial t = 0.5/r$. Thus, at $t = 0.5$, $B_\theta(r_{inner}) = 2.5$ or 0.5 T in SI units. Using Ampère's law, the maximum total current driven between the electrodes is $I = 2\pi r_{inner} B_\theta/\mu_0 = 250$ kA. At the left boundary, zero normal derivative BC are enforced for plasma and neutral densities, plasma and neutral momenta, and plasma and neutral pressures. At the right boundary, the boundary conditions are the same except that zero normal derivative is enforced for B_θ, and the axial plasma momentum is set to zero. At the inner and outer radial boundaries, in terms of the dependent variables and the boundary normal ($\hat{\mathbf{n}}$), the BC for the plasma components are: $\hat{\mathbf{n}} \cdot \mathbf{v} = 0$ (hard wall); $\hat{\mathbf{n}} \times \mathbf{v} = 0$ (no-slip); $\hat{\mathbf{n}} \times \mathbf{E} = 0$ (perfectly conducting); $\hat{\mathbf{n}} \cdot \nabla \rho = 0$; and $\hat{\mathbf{n}} \cdot \nabla T = 0$ (thermally insulating). Radial boundary conditions for the neutral fluid are similar: hard wall; no-slip; and thermally insulating.

Spatial resolution and time advance

The two simulations are run from $t = 0$ to $t = 0.7$ (or $t = 2.27$ μs) using a fixed timestep size $dt = 2 \times 10^{-3}$ (or $dt = 6.48$ ns). The grid used for these simulations has 48 cells axially and 6 cells radially, each with 6th-degree polynomials.

6.2.2   Results

Figure 6.7 shows snapshots of the two simulations at the same time, $t = 2.07$ μs. In both cases, the current sheet forms a "snowplow" which drives plasma axially. The magnetic field in the coaxial geometry is stronger near the inner electrode, and a stronger acceleration force is applied to the inner plasma. The snowplow becomes canted, and generally the canting becomes greater as the snowplow continues to accelerate. When neutral gas is present, the current sheet snowplow is delayed in comparison to the pure plasma case. The primary cause of this slowing is that energy from the current source is spent ionizing the neutrals instead of accelerating the plasma in the current sheet. Comparing the axial location of current sheet attachment (defined as the location of maximum total current) to the inner electrode, in the PS case, the point of attachment is 10 cm ahead of the attachment point for the NS case. Another observed effect is that the canting angle is over $7°$ steeper in the plasma slug case — $22.7°$ vs. $15.4°$. At $t = 2.27$ μs, the attachment point in the neutral slug case reaches the same location as the plasma slug case in Figure 6.7 (≈ 0.87 m), and the canting angle steepens to $17.0°$ — still not as steep as the plasma slug case.

6.3   RMF-driven FRC spin-up

The field-reversed configuration (FRC) is presented in Section 1.5, and rotating magnetic field (RMF) current drive is briefly described. See Figure 1.3 for a schematic of RMF current drive. RMF is usually operated at a frequency much lower than the electron cyclotron frequency and much higher than the ion cyclotron frequency. In this way, electron coupling is much more effective than ion coupling, and electrons are preferentially driven azimuthally in the FRC, providing the desired azimuthal current drive. RMF-driven azimuthal current can be used to create FRCs or to sustain the confining magnetic flux. However, ions are dragged
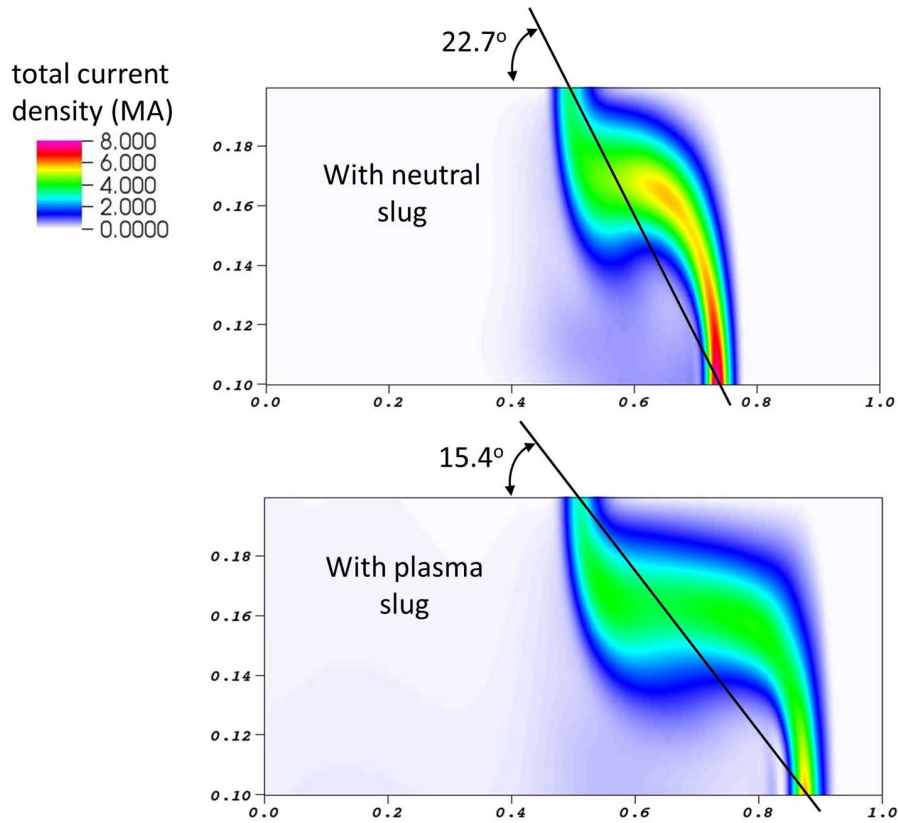
Figure 6.7: Plots of current density in coaxial-electrode plasma acceleration simulations. In the simulation depicted in the upper frame, a neutral slug (NS) is initialized. In the lower frame, a plasma slug (PS) is initialized. Both snapshots are taken at $t = 2.07$ μs. In the NS case, reaction effects slow the progress of the "snowplow" formed by the annular current sheet. Also, the canting angle of the snowplow is modified. The angles are indicated in the figure. (Note that the actual angles are given, not the apparent angles in the stretched aspect ratio depiction.) The canting in the PS case is significantly steeper.

along with the electron species to some extent because of ion-electron collisions. If drag causes ion rotation near the electron rotation rate, the current drive would be eliminated. Furthermore, fast ion rotation can result in an instability[2] that ruins plasma confinement. Experimental evidence [115, 116] from the TCSU experiment [117] indicates that a damping mechanism is present and prevents excessive ion rotation speed. The damping is not perfectly understood, but the most likely contributors are ion viscosity and resonant charge exchange (CX) drag. Ion viscosity could damp rotation by simply viscously connecting the ions to the stationary radial wall. CX allows rotating ions to become rotating neutrals, which either contribute their momentum and kinetic energy to the neutral gas species or escape the plasma entirely. Thoroughly understanding the damping mechanism is important for designing new, larger machines. There is some concern that larger machines will have inadequate damping [115]. This test problem is based loosely on the TCSU experiment as presented in the dissertation by Peter [115], but the results are not intended to be used for quantitative comparison with the experiment. See Chapter 7 for a discussion of possible changes to the problem that would be appropriate if quantitative comparison to TCSU is pursued by future researchers.

The HiFi plasma-neutral model implementation described in Section 5.3 is employed to model the TCSU experiment. The factor λ is set to 1, allowing the neutral products of CX (CX neutrals) to escape the plasma with their momentum and kinetic energy. The mean free path of a typical CX neutral (moving at the ion thermal velocity, $v_{th,i}$) can be estimated as

$$\lambda_{mfp,\ CX\ neutral} = \frac{v_{th,i}}{n_i \left\langle \sigma_{cx} v_{rel} \right\rangle} \approx \left(n_i \sigma_{cx} \right)^{-1}, \tag{6.1}$$

where the approximation is reasonable only if certain conditions are met. The dominant collisions for CX neutrals should be CX collisions. Assuming a high ionization fraction, neutral-neutral collisions are unimportant, and this condition is met. Also, σ_{cx} should be relatively velocity independent (which it is) and the averaged ion-neutral relative velocity, $\left\langle v_{rel} \right\rangle$ should be near the ion thermal speed, $v_{th,i}$. If rotation speeds do not exceed $v_{th,i}$,

---

[2]The rotational instability is something like what happens when a soft clay pot on a potter's wheel becomes asymmetric and spins out of control.

and the neutral temperature is not higher than the ion temperature, $\langle v_{rel} \rangle \approx v_{th,i}$. The CX cross section (for hydrogenic plasmas) is approximately 3×10^{-19} m^2. For TCSU, the average ion density is 5×10^{18} m^{-3}, so the CX neutral mean free path is 0.7 m. This is larger than the machine radius of 0.4 m. Therefore, assuming that CX neutrals are lost is reasonable.

6.3.1 Computational setup

Deuterium plasma and neutral gas are assumed. The mass taken for deuterium atoms and ions is 3.345×10^{-27} kg. The effective ionization potential for deuterium (taking into account ionization from the diatomic configuration) is $\phi_{ion} = 33$ eV [114].

Characteristic quantities

A normalization basis is chosen in terms of characteristic length (L_0), density (n_0), and magnetic field (B_0). Characteristic pressure, velocity, and time are defined in terms of this basis as $p_0 = \frac{B_0^2}{\mu_0}$, $v_0 = \sqrt{\frac{p_0}{n_0 m_i}}$, and $t_0 = \sqrt{\frac{L_0}{v_0}}$. The normalization basis for TCSU simulations is $L_0 = 0.4$ m, $n_0 = 10^{19}$ m^{-3}, and $B_0 = 0.0125$ T. This basis gives the following characteristic pressure, velocity, and time: $p_0 = 124$ Pa, $v_0 = 6.10 \times 10^4$ m/s, and $t_0 = 6.56 \times 10^{-6}$ s.

Geometry and initial condition

The maximum radius of the cylindrical domain is 0.4 m. The total axial length is 3 m. The initial condition is computed with the MHD equilibrium code developed by G. Marklin [22], as discussed in Section 1.5. The FRC is centered in the 3-m axial extent of the domain. The separatrix touches the axis ($r = 0$) at +/- 1.00 m axially from the center of the domain. The initial FRC flux and plasma pressure are shown in Figure 6.8. Open-field-line pressure is not truncated axially. The maximum initial plasma density is 10^{19} m^{-3} and the maximum initial total plasma temperature is 78 eV. Plasma pressure is assumed to be split evenly between the ions and electrons. Plasma density is initialized as the square root of plasma pressure. The background (minimum) plasma and neutral densities are both 10^{18} m^{-3}.
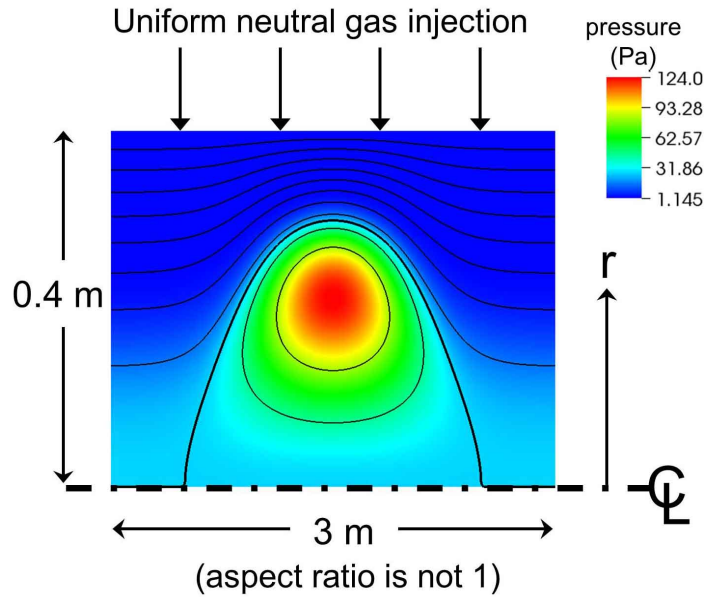
Figure 6.8: RMF-driven FRC spin-up problem initial condition. Black contours are of flux; the dark black line is the separatrix. The FRC pressure is shown in color.

The background plasma and neutral pressures are 1.24 Pa and 1.24×10^{-3} Pa, respectively, corresponding to background temperatures of 7.8 eV and 7.8×10^{-3} eV.

Dissipation

Resistivity is calculated using the Spitzer-Chodura composite model shown in Section 5.3, Eqns. (5.75) – (5.78). Plasma thermal conduction is calculated using formulas from Braginskii [11]. Plasma viscosity is uniform, with normalized viscosity coefficient $\xi = 0.1$. (Characteristic quantities for normalizations are given above.) Neutral viscosity and thermal conduction are also uniform, with coefficients $\xi_n = 0.1$ and $\kappa_n = 10^{-2}$. The normalized density diffusion coefficient is $D_n = 5 \times 10^{-4}$.

Boundary conditions

The domain is periodic axially. In terms of the dependent variables and the boundary normal ($\hat{\mathbf{n}}$), the radial wall BC for the plasma components are: $v_r = 0$ (hard wall); $v_z = 0$ (no-slip on axial velocity); $\hat{\mathbf{n}} \times \mathbf{E} = 0$ (perfectly conducting); $p/\rho = p_0/\rho_0$ (fixed temperature); $\hat{\mathbf{n}} \cdot \nabla\rho = 0$; $\partial v_\phi/\partial r = 0$. The BC on v_ϕ is not a perfect slip BC. The normal viscous flux for azimuthal momentum evolution is $\hat{\mathbf{n}} \cdot \xi(\nabla\mathbf{v} + \nabla\mathbf{v}^\mathsf{T}) = \xi(\partial v_\phi/\partial r + v_\phi/r)$. By setting $\partial v_\phi/\partial r = 0$, viscous flux proportional to v_ϕ/r is present. As will be seen in the results, this viscous connection to the radial wall limits the azimuthal spin-up so that a steady state is reached.

For the neutral fluid, the radial momentum density is specified as $\rho v_r = -2 \times 10^{-4}$ kg/(m^{2}s). This causes a uniform influx of neutral gas at the radial wall. Integrating over the entire surface, $S \approx 7.5$ m^2, of the cylindrical domain gives the total rate of neutral gas influx, $\partial M_n/\partial t \approx 1.5$ μg/μsec. Over the duration of the 20 μs simulation, the total amount of neutral gas injection is ≈ 30 μg. This amount of gas injection does not correspond to a particular experimental fueling or recycling rate; the injection was chosen arbitrarily for this qualitative test problem. For comparison, the total initial plasma mass is ≈ 14 μg. The other neutral fluid radial wall BC are similar to the plasma conditions: no-slip on axial velocity; fixed temperature; $\hat{\mathbf{n}} \cdot \nabla\rho_n = 0$; and $\partial v_{n,\phi}/\partial r = 0$.

Spatial resolution and time advance

The spatial resolution is 32 cells axially by 16 cells radially, each with 4th-degree polynomials. The total simulated time is 20 μsec. A fixed time step of $dt = 6.6$ ns is used.

Special conditions

A radius-dependent azimuthal body force of F_b N/m^3 is applied. F_b is defined as $F_b = \beta r$, where β is a constant parameter, chosen to be 75. Assuming constant, uniform density and no other forces, the azimuthal plasma momentum equation is

$$\rho\frac{\partial v_\theta}{\partial t} = F_b. \tag{6.2}$$

The azimuthal acceleration is $a_\theta = F_b/\rho$. The angular acceleration is $\alpha = a_\theta/r = F_b/(r\rho)$. Because $F_b \propto r$, if density is uniform, angular acceleration is uniform.

The total applied torque can be calculated as $T = \int_V F_b r dV$. For a total domain length L and maximum radius R, $T = \pi L R^4 \beta/2$. Inserting $L = 3$ m and $R = 0.4$ m, $T \approx 9$ Nm. This torque is within 25% of the peak analytic torque computed by Peter [115] for his high-torque condition.

The final azimuthal velocity at radius r after accelerating for time t_{tot} is $v_{\theta,final} = \beta r t_{tot}/\rho$. For a point of reference, this formula for $v_{\theta,final}$, with $t_{tot} = 20$ μs, $\rho = 3.345 \times 10^{-8}$ kg/m^3, and $r = 0.2$ m, yields $v_{\theta,final} \approx 10^4$ m/s. This is a significant fraction of the characteristic thermal speed ($v_0 = 6.10 \times 10^4$ m/s). Of course, low density regions of the plasma are accelerated more aggressively.

Neutral products of charge exchange are allowed to leave the system (with associated mass, momentum, and energy). That is, the factor, λ, in the plasma-neutral model of Section 5.3 is set to 1.

6.3.2   Results

The TCSU simulation results presented in Figure 6.9 demonstrate that the plasma-neutral model can capture the effect of charge exchange drag. Notice that in both cases — with and without plasma-neutral interaction — the plasma rotation rate reaches a relatively steady state. The azimuthal velocity is limited by the viscous connection of the plasma and neutral azimuthal momenta as discussed under boundary condition setup in Section 6.3.1. Neutral effects cause a 33% reduction in maximum rotation speed. Figure 6.10 shows plasma, neutral, and total masses as a function of time. Total mass increases because of the neutral gas injection. Also plotted in Figure 6.10 are plasma, neutral, and total azimuthal momenta vs. time.

6.4   Electrodeless Lorentz Force thruster

The Electrodeless Lorentz Force thruster (ELF) program [112] is developing a new type of electric propulsion (EP) device based on the formation and acceleration of FRC plasmas. The modeling research presented here focuses on a particular ELF-related program called
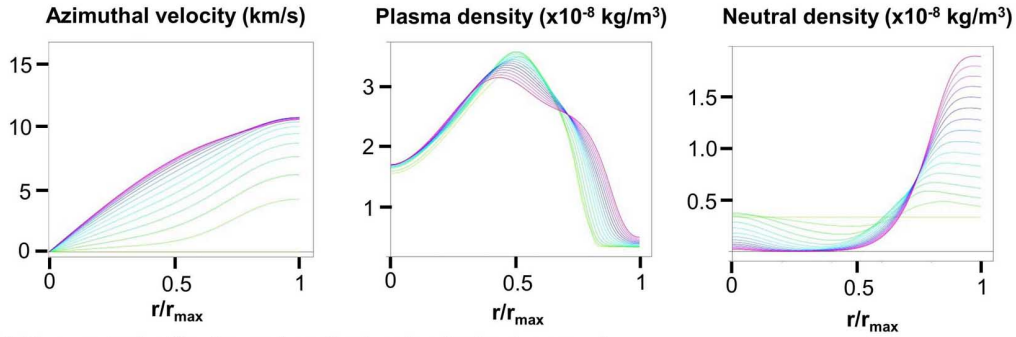
Figure 6.9: Slice plots of rotating FRC with and without neutral effects. Variables are plotted at a slice along the axial midplane. Reaction rates are set to zero in the case without neutral effects. In the case with neutral effects, peak plasma density is maintained by ionization, and the maximum ion rotation speed is reduced by approximately 25%. (Trace color varies from yellow at early times to magenta at late times.)
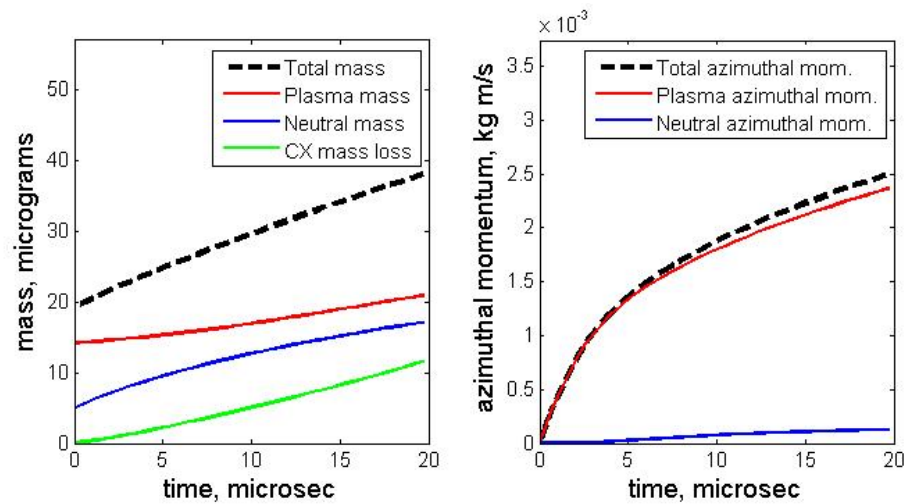
Figure 6.10: Time traces of mass- and momentum-related quantities for the rotating FRC simulation with neutral effects. Plasma mass, neutral mass, total mass, and cumulative mass lost via escaping CX neutrals are shown in the left panel. On the right, azimuthal plasma momentum, neutral momentum, and total momentum are plotted. A total of 30 μg of neutral gas is injected during the simulation. Some of this mass is lost via CX neutrals, but total mass steadily rises. Late in time, the total azimuthal momentum rises at approximately the same rate as the total mass, and azimuthal velocity reaches steady state. (See Figure 6.9).

neutral entrainment, which extends the original ELF work [20] to include entrainment of neutral target gas with the accelerated FRC. ELF is intended to provide an EP option with high power, high efficiency, and a long operational lifetime. In the ELF experimental apparatus, depicted in Figure 6.11, an FRC is generated in a conical formation section using rotating magnetic field (RMF). (See Section 1.5 for an overview of FRCs and RMF.) As the FRC current increases, the magnetic field is compressed near the conical flux conserving wall. The wall exerts an axial force, accelerating the FRC into a cylindrical vessel, where it encounters a neutral gas field that has been injected immediately prior to the FRC formation and acceleration. The region of the cylinder in which the plasma-neutral interaction primarily occurs is called the neutral entrainment section (NES). Discrete copper theta-pinch coils are located at several axial positions along the NES. The coils are connected to a circuit that controls the flux in the vessel. If the circuit is closed in a simple loop around the vessel (i.e., "crowbarred"), flux is conserved in the vessel. If current is driven through the coils, axial flux is injected. The dissertation by Weber [20] provides many details about the ELF experiment omitted here for simplicity.

For the purposes of this research, the progression of an ELF experimental discharge may be thought of as follows. First, neutral neon gas is introduced in two different ways. Feed gas for the FRC is injected as an undirected puff that is intended to approximately fill the RMF formation region. Gas intended for neutral entrainment is injected with a Laval nozzle designed to create a collimated "beam" of gas on the cylindrical axis. A valve is rapidly opened and closed to limit the axial extent of the beam. RMF is applied with timing such that the accelerated FRC encounters the neutral beam in the NES. The theta-pinch coils are sequentially fired to "squeeze" the FRC and impart additional axial momentum while the FRC interacts with the neutral gas.

High power and long operational lifetime characteristics are often mutually exclusive. High power frequently means rapid damage to the electrodes of an EP device, but this issue is alleviated by the absence of an electrode in ELF.

Efficiency in a propulsion device is generally calculated as the ratio of directed kinetic energy to the total input energy. The input energy that is not converted to directed kinetic energy is considered "lost" since it does not contribute to thrust. In ELF, neutral en-

theta-pinch coils

Drift chamber with
0.4-m radius

+r

RMF
formation section

Neutral Entrainment
Section (NES)

0.14 m

0.45 m

0.50 m

+z
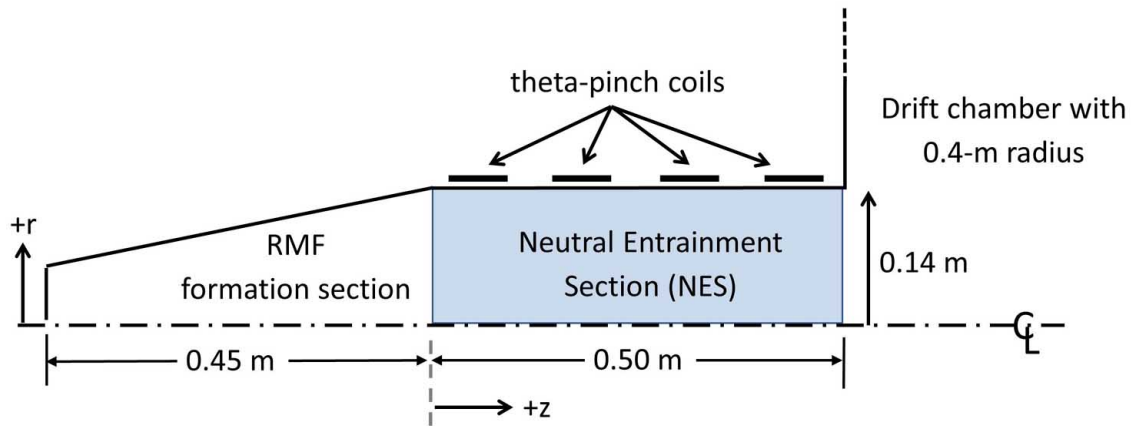
Figure 6.11: Schematic of ELF thruster. An FRC is formed in the conical section. The magnetic pressure associated with the FRC accelerates it axially into the Neutral Entrainment Section (NES). In the NES, the FRC encounters a field of neutral gas which is ionized and entrained. The FRC and neutral gas exhaust into a large drift chamber. Approximate locations of theta-pinch coils are shown. For most of the work presented, including the initial experimental results of Section 6.4.5, the coils are not energized — they simply act as flux-conserving straps. In Section 6.4.4, these coils are modeled. In a functional ELF thruster, the coils would be sequentially fired to accelerate the FRC axially.

trainment is intended to improve efficiency as compared to conventional EP devices, which ionize and then accelerate gas. In conventional devices, the ratio of accelerated particles (ions or neutrals) to ionization events is approximately $R_{accel/ion} = 1 : 1$. That is, for each accelerated particle, the full ionization energy is invested. Efficiency can be improved by entraining neutrals while accelerating ions. For example, if the ion-neutral coupling is good during the entrainment, and if significant additional axial momentum is delivered by the theta-pinch coils, ratios of $R_{accel/ion} = 2 : 1$ or higher are possible. A goal of the ELF program is to quantify and maximize this ion-neutral coupling, thus increasing the amount of input energy that is converted to directed kinetic energy.

As the FRC plasma interacts with the neutral gas, there is frictional coupling between the ions and neutrals, caused primarily by charge exchange (CX). In the ELF NES, an axial force is applied to the FRC via the sequentially fired theta-pinch coils, which counteract the frictional drag force as the neutral gas is accelerated/entrained, maintaining a roughly constant FRC speed. In this way, energy input through the theta-pinch coils is efficiently converted to axial kinetic energy. Ideally, ionization should be minimized (relative to CX) because it removes thermal energy from the system (which might be converted to directed energy by a nozzle), and acts to reduce the charge exchange coupling because CX is temperature dependent.

A goal of ELF is functionality with virtually any gas, including, for example, hydrogen, xenon, neon, and air. The research presented here focuses on pure neon gas.

The two-component plasma-neutral model implemented in HiFi (see Section 5.3) is used to simulate the ELF thruster. The goals of this effort are to improve the physics understanding of the plasma-neutral interaction in the NES, to establish a model that can be applied in continuing ELF studies, and begin validation of the plasma-neutral model. The majority of the modeling effort has focused on the interaction of the FRC with the neutral gas field as described in Sections 6.4.1 and 6.4.2. The physics of the interaction is examined with respect several variables: neutral gas field profile, neutral gas density, initial FRC density, initial FRC speed, and initial FRC temperature. Simulations of ELF FRC acceleration with a series of external theta-pinch coils have been conducted. Net momentum input from the coils is demonstrated. These simulations show the applicability of the HiFi plasma-neutral

implementation for continued numerical study of the ELF thruster, including momentum input via coils, which is expected to be crucial for success with ELF.

Because future ELF studies will require understanding the physics related to flux injection with the theta-pinch coils, proof-of-concept simulations with theta-pinch coils are run as described in Section 6.4.3. In one of these flux injection simulations, reaction effects are included. In the other, reactions are not included. The results are presented and compared in Section 6.4.4.

In Section 6.4.5, experimental results for ELF operating without coils are presented and compared with simulation results.

6.4.1 Computational setup for ELF simulations (without coils)

Neon plasma and neutral gas are assumed. The mass taken for neon atoms and ions is 3.351×10^{-26} kg. The effective ionization potential for neon is $\phi_{ion} = 25$ eV [114].

Characteristic quantities

A normalization basis is chosen in terms of characteristic length (L_0), density (n_0), and magnetic field (B_0). Characteristic pressure, velocity, and time are defined in terms of this basis as $p_0 = \frac{B_0^2}{\mu_0}$, $v_0 = \sqrt{\frac{p_0}{n_0 m_i}}$, and $t_0 = \sqrt{\frac{L_0}{v_0}}$. The normalization basis for ELF simulations is $L_0 = 0.141$ m, $n_0 = 7 \times 10^{19}$ m^{-3}, and $B_0 = 0.012$ T. This basis gives the following characteristic pressure, velocity, and time: $p_0 = 115$ Pa, $v_0 = 6.99 \times 10^3$ m/s, and $t_0 = 2.02 \times 10^{-5}$ s.

Geometry and initial condition

The computational domain for the HiFi ELF simulations is shown in Figure 6.12. The figure also shows the experimental geometry with the neutral entrainment sections aligned. The cylindrical simulation domain has a maximum radius of 0.141 m and a total length of 2.25 m. As shown, a moving plasma is initialized in a 1.25-m region at the left side of the domain. On the right is a section containing the 0.5 m neutral entrainment section (NES) and a 0.5-m buffer zone to minimize the interaction that occurs through the periodic

boundary conditions that are used at the ends of the domain. There is no drift chamber in the simulated domain since the focus is on the physics within the NES. The magnetic topology, temperature, and density of the RMF-formed ELF FRC is approximated by the equilibrium FRC initial condition shown. Before entering the NES, the RMF-formed FRC can not take the full shape of the equilibrium HiFi FRC — the required physical space is not available in the conical RMF formation region. Instead, it is assumed that the RMF-formed FRC emerges from the conical region and enters the NES with roughly the same magnetic topology, temperature, and density as the HiFi FRC as it enters the simulated NES. The discrete theta-pinch coils shown in the diagram are used in the simulation described in Sections 6.4.3 and 6.4.4.

The initial condition is generated with a Grad-Shafranov (G-S) solver by Marklin [22]. The initial peak FRC pressure and density are varied as discussed in Section 6.4.2. Plasma pressure is assumed to be split evenly between ions and electrons. The initial plasma density is proportional to the square root of plasma pressure. As discussed in Section 1.5, the open-field-line pressure is ramped down from the usual G-S solution to the background pressure value. In this case, the ramp-down is between 0.39 and 0.54 m from the axial center of the FRC using a smooth sinusoidal function of axial distance. As shown in Figure 6.12, the separatrix radius is approximately R_s =0.09 m. The separatrix length is $L_s = 0.62$ m, so the separatrix elongation is $E \equiv L_s/2R_s$ =3.4. This magnetic topology approximately matches the experimentally generated ELF FRCs. Background (minimum) pressure and density are set to 6×10^{-3} Pa and 3.5×10^{17} m^{-3} for both plasma and neutral species. (The implied minimum total temperature is 0.1 eV.)

One of two different neutral gas profiles is initialized in the 0.5-m-long NES: a profile which varies as a Gaussian radially, and a profile with uniform density across the entire radius. These will be referred to as "Gaussian" and "block" profiles. The Gaussian profile has the form $\rho_n = \rho_{n,max}\exp(-(r/\lambda)^2)$, where $\lambda = R/3(= 0.047)$ m. The full Gaussian or block profiles are axially truncated with a smooth sinusoidal function of axial position to the minimum density value at both ends of the NES, between 0.2 and 0.25 m from its axial center.

In addition to the neutral gas profile, four other parameters are varied: total initial
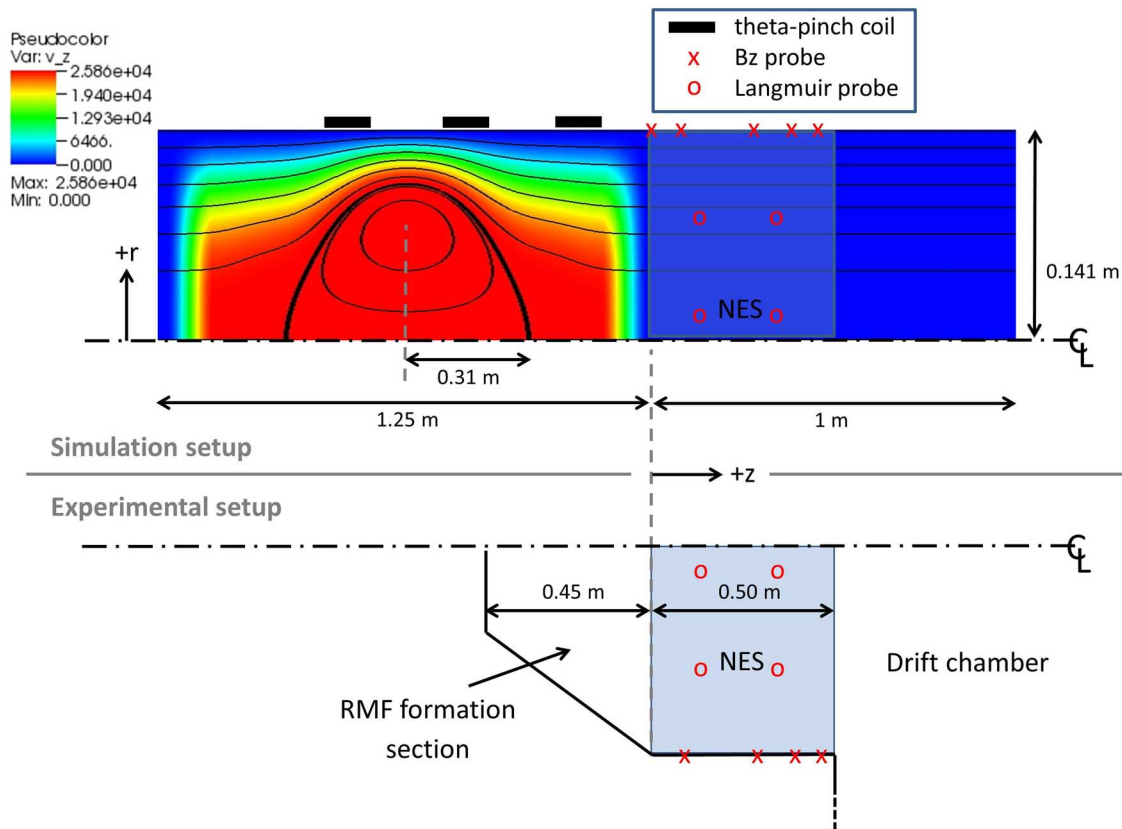
Figure 6.12: ELF simulation setup is shown in the upper half of the diagram. In the lower half, the experimental dimensions are shown. (Figure 6.11 presents the experimental setup alone.) The radial dimension is exaggerated. $z = 0$ is defined to be at the entrance of the Neutral Entrainment Section (NES) in both the simulation and experiment. The FRC initialized in the simulation is significantly larger than the entire experimental RMF formation section; the dimensions of the simulated FRC initial condition are intended to approximately match the experimental FRC observed at $z = 0$. FRC axial speed is indicated in color with a scale in m/s. Simulations are conducted with several different maximum initial axial speeds — the case shown has maximum speed of 25.9 km/s. In other cases, speed is scaled uniformly up or down. Contour lines show poloidal magnetic flux. The bold contour indicates the separatrix, where the flux is zero. The three discrete theta-pinch coils used for flux injection simulations are indicated. The synthetic diagnostics and corresponding experimental diagnostics are also shown.

neutral mass (M_{n0}); initial plasma mass (M_{p0}); initial maximum FRC speed (v_{init}); and initial FRC total (ion plus electron) temperature (T_0). "Baseline" values of these parameters are $M_{n0} = 7.27 \times 10^{-8}$ kg, $M_{p0} = 3.43 \times 10^{-8}$ kg, $v_{init} = 25.9$ km/s, and $T_0 = 10.2$ eV.

As shown in Figure 6.12, the plasma is given an initial axial speed profile. Within the FRC separatrix, the plasma has the maximum FRC speed, v_{init}. Outside the separatrix, the velocity is reduced by multiplying by two screening functions. The first is a function of flux, ψ. From the separatrix, where $\psi = 0$, to the wall, where the flux increases to $\psi = \psi_{wall}$, the flux function transitions from 1 to 0 as a half period of a sinusoid. An axial truncation, which is symmetric about the center of the FRC, is also applied. Within 0.5 m of the center, the value is 1. Between 0.5 m and 0.625 m, the function of axial distance transitions smoothly to 0, again, as a half period of a sinusoid.

Dissipation

The plasma viscosity coefficient (ξ) is computed using the formula derived by Braginskii [11] for isotropic ion viscosity. As discussed in Section 5.2.3, viscosity is dominated by ion viscosity. As seen in Table 6.2, the ion magnetization is low, so an isotropic ion viscosity is an appropriate approximation. Thermal conductivity coefficients ($\kappa_\parallel$ and $\kappa_\perp$) are also computed using Braginskii formulas. Neutral viscosity (ξ_n) and thermal conductivity (κ_n) are computed using hard sphere approximations as discussed in Chapman and Cowling [101].

The neutral viscosity and thermal conduction are high enough everywhere in the domain (even where the neutral gas is coolest) that numerical noise is not a problem. However, charged particle collisions have much higher cross sections, causing high collisionality in the plasma. As a result, viscous and thermal dissipations are very weak (especially where the plasma is coolest). To avoid the noise that can be associated with weak dissipation, floor values for plasma viscosity and thermal conduction are implemented. The minimum normalized viscosity is $\xi_{min} = 5 \times 10^{-3}$. The minimum thermal conductivity (parallel and perpendicular) is $\kappa_{min} = 10^{-2}$. For comparison, at the characteristic magnetic field ($B_0 = 0.012$ T), characteristic plasma density ($n_0 = 7 \times 10^{19}$ m^{-3}), and characteristic total plasma temperature ($p_0/(n_0 q_e) = 10$ eV), these viscosity and thermal conductivity coefficients are

$\xi = 3.5 \times 10^{-2}$, $\kappa_\| = 16$, and $\kappa_\perp = 0.3$. At the characteristic magnetic field and density, but with a total plasma temperature of 0.1 eV, $\xi = 3.5 \times 10^{-7}$, $\kappa_\| = \kappa_\perp = 1.5 \times 10^{-4}$.

A small density diffusion, $D_n = 2 \times 10^{-3}$, is used to eliminate noise in the plasma and neutral density fields. An artificial viscosity, $\xi_a = 1 \times 10^{-3}$, is used to prevent unphysical oscillations where shock conditions are approached in the simulations.

Boundary conditions

As mentioned above, periodic BC are used at the axial ends. In terms of the dependent variables and the boundary normal ($\hat{\mathbf{n}}$), the radial wall BC are: $\hat{\mathbf{n}} \cdot \mathbf{v} = 0$ (hard wall); $(\hat{\mathbf{n}} \cdot \nabla)(\hat{\mathbf{n}} \times \mathbf{v}) = 0$ (perfect slip); $\hat{\mathbf{n}} \times \partial \mathbf{A}/\partial t = 0$ (perfectly conducting); $\hat{\mathbf{n}} \cdot \left[\kappa_\| \hat{\mathbf{b}}\hat{\mathbf{b}} + \kappa_\perp \left(\mathbb{I} - \hat{\mathbf{b}}\hat{\mathbf{b}} \right) \right] \cdot \nabla T = 0$ (thermally insulating); and zero density flux, which, given $\hat{\mathbf{n}} \cdot \mathbf{v} = 0$, essentially enforces $\hat{\mathbf{n}} \cdot \nabla \rho = 0$ because of the artificial density diffusion term in Eqn. (5.70). Corresponding gasdynamics BC are used for the neutral fluid — hard wall, perfect slip, thermally insulating, and zero density flux.

A series of trial simulations have been used to establish the radial wall BC. If no-slip BC are applied, sharp boundary layers develop at the wall, causing numerical difficulties. Physically, of course, the fluid (plasma or neutral) at the wall does not "slip". The important question is whether the wall friction is significant. If thin boundary layers with minimal associated drag are assumed, a perfect-slip boundary condition is appropriate, and the difficulties associated with thin viscous boundary layers is avoided. These assumptions are made and the perfect-slip BC is adopted for the simulations presented here. Another question is whether to fix the temperature at the wall or to assume an insulating wall. In trial simulations with fixed temperature, sharp temperature gradients develop at the radial wall, and the thermal energy of the FRC is quickly transported out of the domain through the boundary. Unlike conventional FRC plasmas with strong magnetic fields and good thermal confinement, the FRCs in the ELF experiment have relatively weak magnetic fields and poor confinement properties. As seen in the plasma parameter summary for ELF presented in Table 6.2, the ion magnetization is low, so thermal energy is rapidly lost to the wall if the wall temperature is fixed to the background value of 0.1 eV. It is assumed that

Table 6.2: ELF plasma parameters. The plasma properties used to compute the parameters are given in the top section of the table. The next section gives the general plasma parameters, and the lower two sections give and electron- and ion-specific parameters. The ions are unmagnetized ($x_i < 1$), so viscosity (which is ion-dominated) and ion thermal conduction are isotropic. The electrons are well magnetized ($x_e \gg 1$), leading to (electron-dominated) anisotropic thermal conduction. Electron and ion mean free paths are much less than the device radius of 0.141 m, so the fluid approximation is reasonable.

Quantity	Description	ELF value
m_i	Neon ion mass	3.35×10^{-26} kg
T_i and T_e	Ion and electron temperature	5 eV
B	Characteristic magnetic field	0.012 T
n	Characteristic plasma density	7×10^{19} m^{-3}
l_d	Debye length	1.99×10^{-6} m
$\ln(\Lambda)$	Natural log of the plasma parameter	9.94
Ω_{ce}	Electron gyrofrequency	2.11×10^{9} s^{-1}
τ_e	Electron collision frequency	5.49×10^{-9} s
x_e	Electron magnetization ($\Omega_{ce}\tau_e$)	11.6
v_{Te}	Electron thermal speed	1.33×10^{6} m/s
r_{Le}	Electron Larmor radius	6.28×10^{-4} m
λ_e	Electron mean free path	7.29×10^{-3} m
Ω_{ci}	Ion gyrofrequency	5.74×10^{4} s^{-1}
τ_i	Ion collision frequency	1.49×10^{-6} s
x_i	Ion magnetization ($\Omega_{ci}\tau_i$)	0.0857
v_{Ti}	Ion thermal speed	6.91×10^{6} m/s
r_{Li}	Ion Larmor radius	1.21×10^{-1} m
λ_i	Ion mean free path	1.03×10^{-2} m

there is a mechanism in the ELF experiment at the radial wall, such as a plasma sheath, which prevents rapid thermal energy loss. A thermally insulating BC is used.

Another noteworthy quantity in Table 6.2 is the ion Larmor radius. It is 0.121 m — nearly as large as the device radius of 0.141 m. This means that the assumptions made in eliminating the Hall and diamagnetic terms from the generalized Ohm's law of Section 5.3 are not justified. More exact results can be expected from ELF simulations if these terms are included.

During the first 1 μs of some of the ELF simulations, especially high-temperature runs (see Section 6.4.2), numerical noise can cause convergence failure in the HiFi nonlinear solver. The noise seems to predominantly affect the current density and momentum fields. As discussed in Section 1.5, when the open-field-line pressure is axially truncated, as it is for the ELF initial condition, the plasma is out of equilibrium. Axial flows develop where the truncated pressure profile has gradients that are not balanced by $\mathbf{j} \times \mathbf{B}$ forces. The noise seems to develop over the first few time steps as these axial flows develop. To avoid nonlinear solver convergence failure, a short "smoothing" period is conducted during the first 1 μs of each simulation. In the smoothing period, dissipation coefficients are uniform and the time step is held constant at $dt = 10$ ns for 100 time steps (which amounts to 1 μs). The plasma and neutral density diffusions during the smoothing period are 2×10^{-3} (which are the same values used after the smoothing period). Viscosities for plasma and neutral fluids are set to 10^{-2}. Parallel and perpendicular plasma thermal conductivities are $\kappa_{\parallel} = 1$ and $\kappa_{\perp}^m = 10^{-3}$. Neutral thermal conduction is set to 10^{-3}. Uniform electrical resistivity, $\eta = 2 \times 10^{-3}$, is used. This short smoothing period eliminates convergence difficulties.

Spatial resolution and time advance

The computational grid for these simulations is split into 72 cells axially, 8 cells radially. 8th-degree polynomials are used in each cell. Simulations are each run for a total of 100 μs. In 100 μs, an object traveling at 25 km/s will move 2.5 m, which is approximately the length of the ELF domain shown in Figure 6.12.

6.4.2   Results of ELF simulations (without coils)

The simulation results are quantified in terms of three metrics:

- f_{mom}: The fraction of momentum transferred from the plasma to the neutrals at the end of the run.

  - Initially, of course, all of the momentum is in the plasma species, so the percentage transferred is simply a comparison of the momentum present in the remaining neutrals (those which have not been ionized).

- f_{conv}: The fraction of original neutral gas that is converted to plasma.

  - It is important to know the neutral conversion fraction to better understand the momentum transfer. For example, if the conversion fraction is near 100%, the momentum present in the neutral species might be small simply because most of the original neutrals have been converted to high-momentum plasma.

- $p_{max,wall}$: The maximum total ion plus neutral pressure at the radial wall during the simulation.

  - This metric provides a measure of the damage that could be done to the radial wall in the ELF experiment. To have a high lifetime propulsion device, damage will need to be sufficiently low.

To compare the Gaussian neutral gas profile to the block profile, baseline cases are run for each profile. Figures 6.13 and 6.14 present pseudocolor snapshots of neutral density and total ion plus neutral pressure, respectively, for the block neutral profile baseline run at several times. Figures 6.15 and 6.16 present the same pseudocolor snapshots for the Gaussian neutral profile baseline run. Black and white arrows indicate the direction and magnitude of plasma and neutral momentum, respectively. (Note that although the radial dimension is expanded in the figures, the arrows indicate true direction.) Two of the metrics, f_{mom} and f_{conv}, are similar for the block and Gaussian baseline runs: f_{mom} =56.4% for both
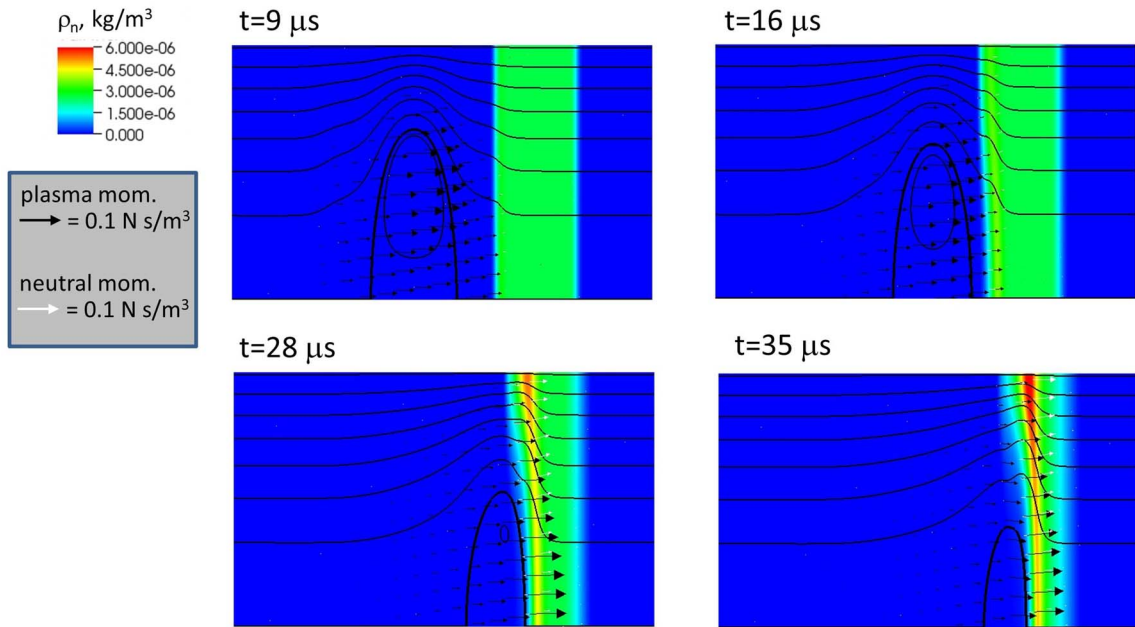
Figure 6.13: Neutral density pseudocolor plots for baseline ELF simulation with "block" neutral gas profile. Black and white arrows indicate the direction and magnitude of plasma and neutral momentum density, respectively. A thin layer of high neutral density forms as the FRC impinges on the neutral gas field. Neutral gas is pushed radially by the concentration of FRC density and energy near the cylinder centerline.

the block and Gaussian profiles; f_{conv}=44% for the block run and 43% for the Gaussian profile. The maximum pressure at the radial wall, however, is significantly different: for the block profile, $p_{max,wall}$=211 Pa vs. 77 Pa for the Gaussian profile. The difference in the total pressure can be seen by comparing Figures 6.14 and 6.16. The last snapshots in each figure are taken at approximately the same time that the maximum total pressure occurs at the radial wall. As seen in the snapshots, in the Gaussian profile case, the magnetic field lines stretch and absorb the energy of the strong radial jet that is generated when the FRC impinges on the neutral gas. In the block profile case, the neutral gas is radially continuous, and apparently the magnetic field is not able to play the same role in preventing the transmission of high pressure to the radial wall.
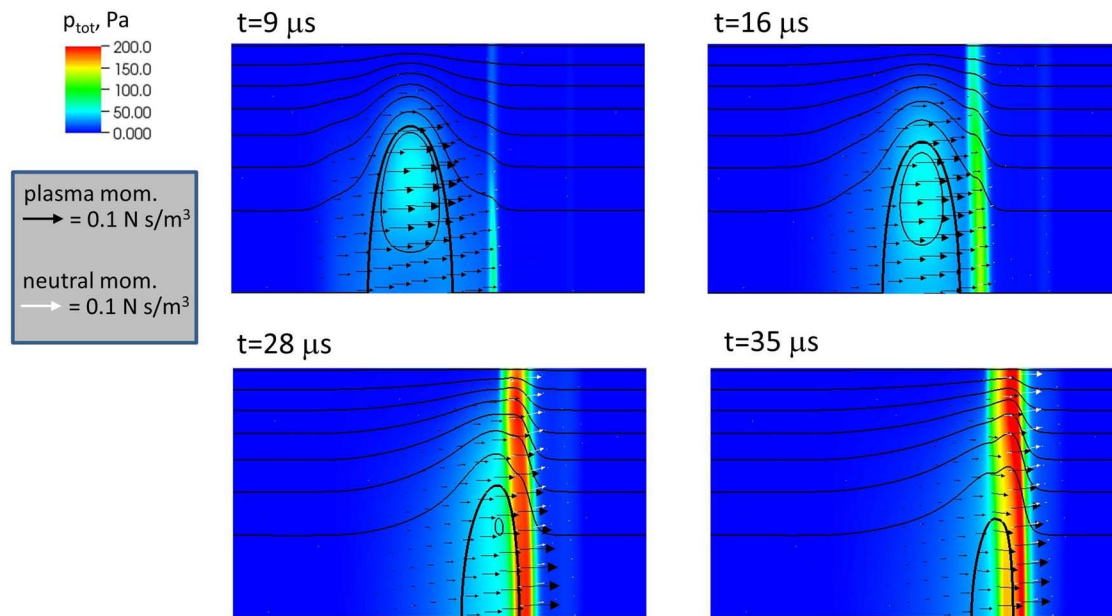
Figure 6.14: Total ion plus neutral pressure pseudocolor plots for baseline ELF simulation with "block" neutral gas profile. Black and white arrows indicate the direction and magnitude of plasma and neutral momentum density, respectively. A thin layer of high pressure forms where the FRC impinges on the neutral gas. At $t = 35$ μs, the pressure reaches 211 Pa at the radial wall.
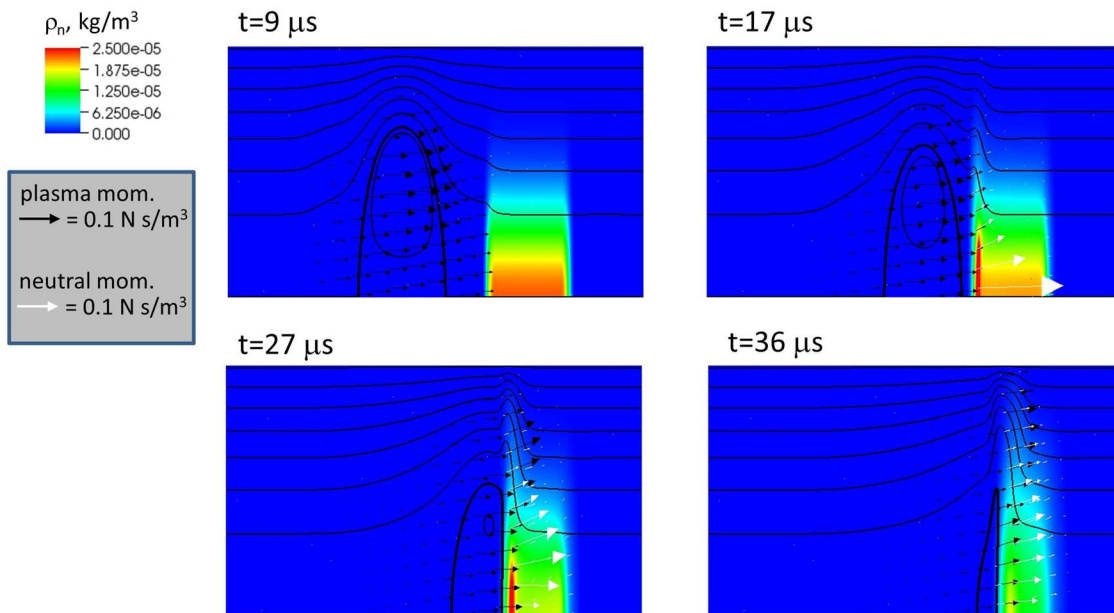
Figure 6.15: Neutral density pseudocolor plots for baseline ELF simulation with "Gaussian" neutral gas profile. Black and white arrows indicate the direction and magnitude of plasma and neutral momentum density, respectively. Note that the neutral density scale in this figure has a maximum value over four times higher than in Figure 6.13. Higher initial density is required for the Gaussian profile to have the same total mass as the block profile case. Peak neutral density in the Gaussian case is also significantly higher than in the block case. The relatively high density is limited to the region within 7 cm of the cylindrical axis, whereas in the block case, density is highest at the radial wall.
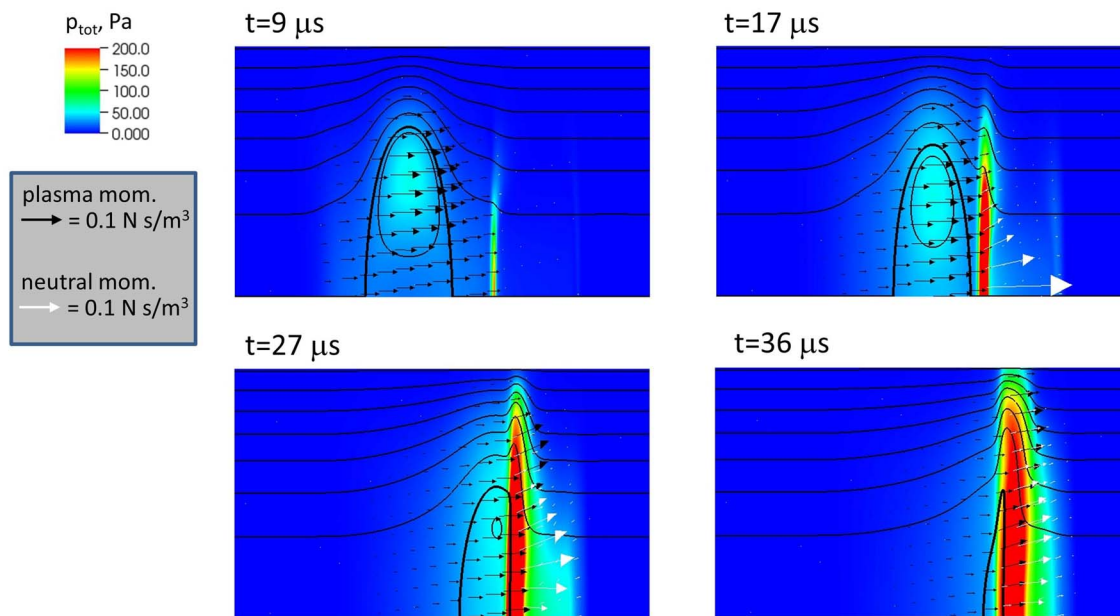
Figure 6.16: Total ion plus neutral pressure pseudocolor plots for baseline ELF simulation with "Gaussian" neutral gas profile. Black and white arrows indicate the direction and magnitude of plasma and neutral momentum density, respectively. At $t = 36$ μs, the pressure reaches 77 Pa at the radial wall — much less than the 211 Pa seen in the block case.

Table 6.3: ELF simulations and results. The varied parameters are total initial neutral mass (M_{n0}), initial FRC temperature (T_0), initial FRC speed (v_0), and initial plasma mass (M_{p0}). The values of these parameters shown in the table are normalized by the baseline values, which are $M_{n0} = 7.27 \times 10^{-8}$ kg, $M_{p0} = 3.43 \times 10^{-8}$ kg, $v_{init} = 25.9$ km/s, and $T_0 = 10.2$ eV. The block and Gaussian "baseline" runs are indicated. Results are tabulated for the three metrics, f_{conv}, f_{mom}, and $p_{max,wall}$. Subsequent figures display plots of these results.

	run #	profile	$\tilde{M}_{n0}$	$\tilde{T}_0$	$\tilde{v}_0$	$\tilde{M}_{p0}$	f_{mom}	$p_{max,wall}$	f_{conv}
block baseline →	b1	block	1	1	1	1	56.4	211.2	44.4
	1	gauss	0.2	1	1	1	13.3	29.7	68.6
	2	"	0.5	"	"	"	29.0	54.6	61.6
Gaussian baseline →	3	"	1	"	"	"	56.0	76.9	42.8
	4	"	1.5	"	"	"	73.8	90.5	30.4
	5	"	2	"	"	"	84.8	106.8	22.8
	6	"	0.5	2	"	"	16.3	35.6	80.8
	7	"	1	"	"	"	49.4	84.5	58.3
	8	"	1.5	"	"	"	75.5	135.2	42.3
	9	"	0.5	4	"	"	2.4	17.2	96.7
	10	"	1	"	"	"	23.3	46.3	82.0
	11	"	1.5	"	"	"	54.2	89.6	63.2
	12	"	1	1	1	0.75	70.8	64.3	33.2
	13	"	"	"	1.333	1	25.4	119.7	77.0
	14	"	"	"	1	1.333	41.6	91.5	53.1
	15	"	"	"	0.75	1	75.0	62.7	20.7

The lower maximum pressure at the radial wall seen in the baseline case for the Gaussian neutral gas profile suggests that the Gaussian profile is more suitable for ELF because less damage is expected to the radial wall. All of the non-baseline runs described next use the Gaussian profile. Table 6.3 presents the test runs along with results for the three metrics.

For the test runs with the Gaussian neutral gas profile, the three metrics are plotted in Figure 6.17. In cases with higher initial plasma energy in the form of additional plasma mass at a given temperature, additional initial FRC speed, or higher temperature for a given plasma mass, f_{conv} is higher, and f_{mom} is lower. The lower values of f_{mom} can be at

least partly explained by the reduced amount neutral gas of neutral gas due to the higher f_{conv}. A key conclusion drawn from Figure 6.17 is that, as seen in the plots of the metrics vs. M_{n0}, for $f_{mom} > 60\%$, the 5 eV initial FRC has lower wall impact in terms of $p_{max,wall}$ than the hotter FRCs.

It is also useful to look at time traces key quantities throughout a simulation. Figure 6.18 shows peak ion temperature, trapped magnetic flux, and plasma, neutral, background, and total masses, and the total amount of ionized, recombined, and charge exchanged mass as a function of time during the 100 μs baseline simulation for the Gaussian neutral gas profile. The final cumulative CX mass transfer exceeds ionization transfer by a factor of 10. This is encouraging since, as discussed at the outset of Section 6.4, CX coupling is preferred to ionization, because CX maximizes frictional plasma-neutral coupling without reducing the thermal energy of the plasma.

Figure 6.19 shows momentum-related quantities. Plasma, neutral, and total momentum are plotted. Also shown are the terms related to direct and frictional CX, ionization, and recombination momentum transfer to the plasma, which are appear as reaction source terms in Eqn. (5.72). Whereas the final cumulative CX mass transfer exceeds ionization transfer by a factor of 10, the final cumulative CX momentum transfer is only a factor of two higher than ionization momentum transfer. The explanation for this difference is that, on average, the plasma-neutral relative speed is higher during the ionization mass transfer events than in the CX mass transfer events.

Figure 6.20 shows a variety of energy-related quantities. Kinetic and thermal energies are shown for the plasma and neutral species. Magnetic energy is shown. Total energy is shown, along with total energy with ionization losses removed. Ionization, recombination, and CX give rise to several energy transfer terms that appear in Eqn. (5.79). Thermal energy transfer due to CX is the most significant of these terms, as shown.

These results do not precisely indicate the best "settings" for ELF. Instead, they provide insight into the important physics related to energy and momentum transfer, and wall damage. The plasma-neutral HiFi module has been passed on to the ELF program team, and will be used and further developed to help guide ELF experimentation.
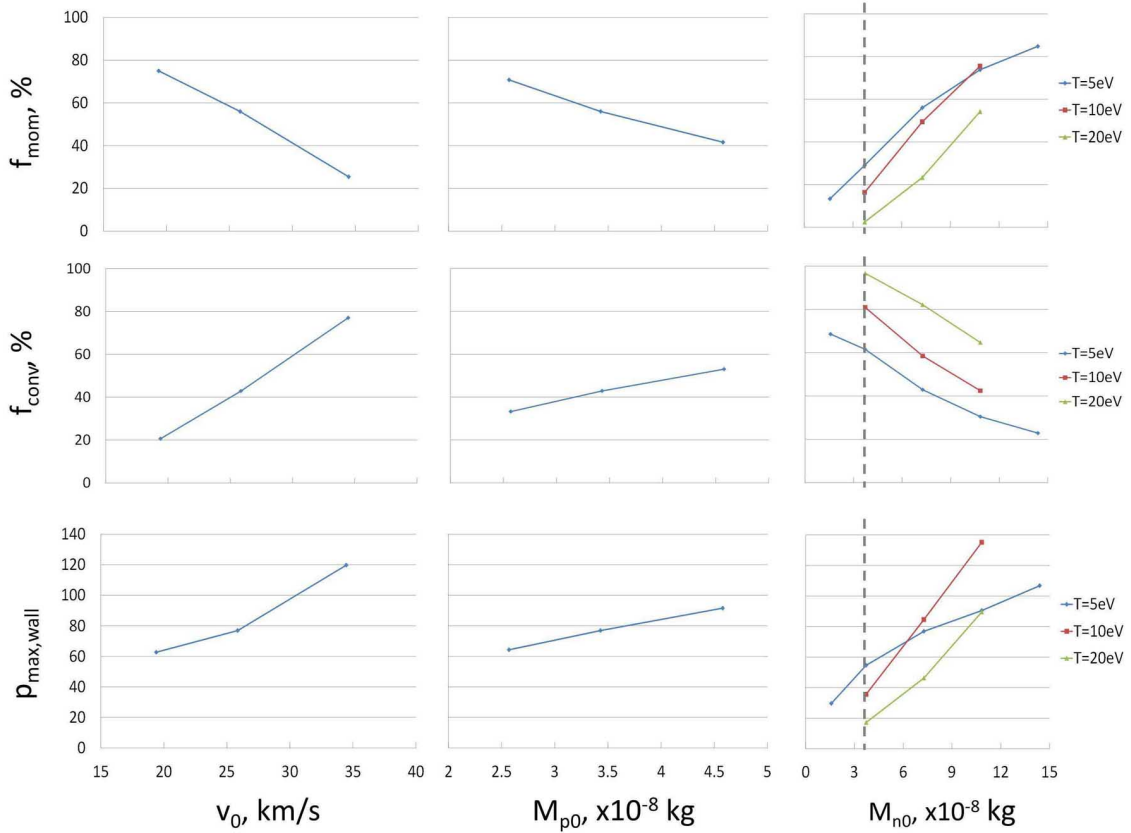
Figure 6.17: Metrics for ELF simulations with Gaussian neutral gas profile. Variations in the three metrics — the fraction of momentum transferred (f_{mom}), the ionization fraction (f_{ioniz}), and the maximum total ion plus neutral pressure at the radial wall ($p_{max,wall}$) — are shown with respect to the ELF parameter space — initial FRC axial speed (v_0), initial plasma mass (M_{p0}), initial neutral mass (M_{n0}), and initial FRC temperature (T_0). In the right column, v_0 and M_{p0} are set to their baseline (median) values. In the left and center columns, only results for $T_0 = 5$ are shown, and all other metrics but v_0 and M_{p0}, respectively, are set to baseline (median) values. In the plots of the metrics vs. M_{n0}, the vertical dashed lines indicate M_{p0}. An interesting result is seen in the plots of the metrics vs. M_{n0}: for $f_{mom} > 60\%$, the 5 eV initial FRC has lower wall impact in terms of $p_{max,wall}$ than the hotter FRCs.
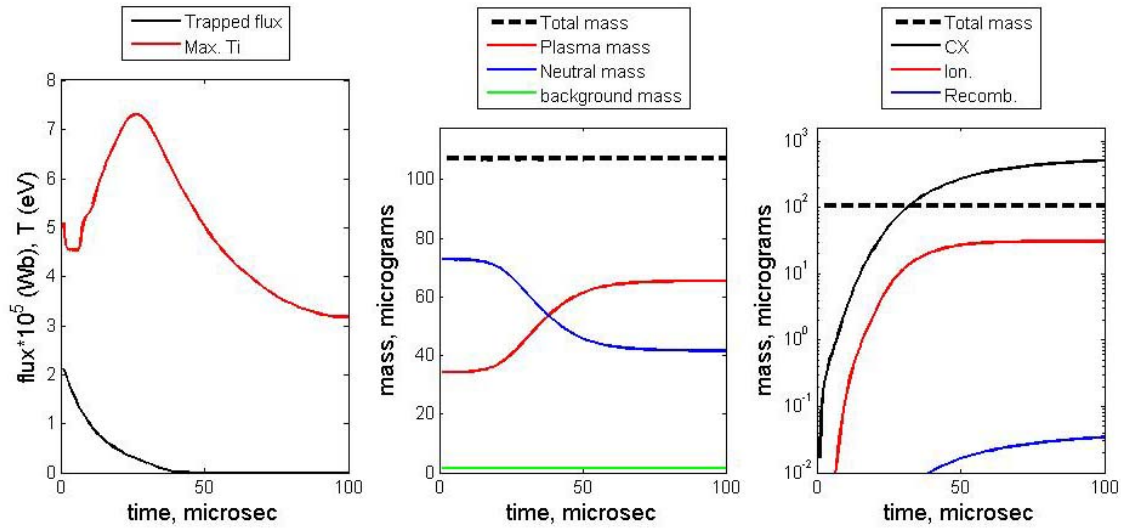
Figure 6.18: Time traces of peak ion temperature, magnetic flux, and mass-related quantities for ELF baseline simulation. Peak ion temperature (Max. Ti) and trapped magnetic flux are shown in the left panel. The FRC flux dissipates by 40 μs. Ion temperature peaks at 7.3 eV after the FRC encounters the neutral target gas. Plasma, neutral, and total mass are shown in the middle panel. The total plasma mass nearly doubles as the FRC interacts with the neutral target gas. The right panel shows cumulative charge exchange mass transfer (CX), ionization transfer (Ion.), and recombination transfer (Recomb.). The final cumulative CX transfer exceeds ionization transfer by more than an order of magnitude.
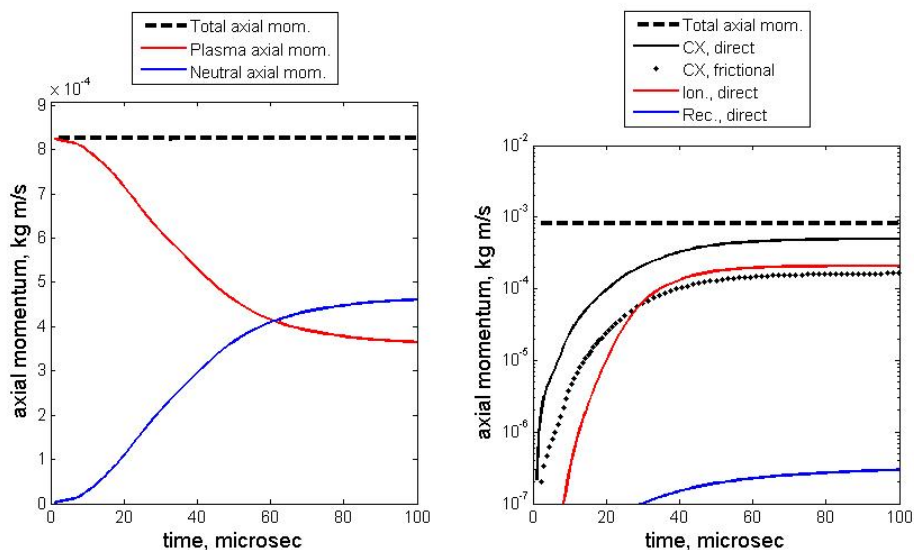
Figure 6.19: Time traces of momentum-related quantities for ELF baseline simulation with Gaussian profile. In the left panel, plasma, neutral, and total momentum are shown. In the right panel, the cumulative transfer of momentum is shown for direct CX transfer (CX, direct), frictional CX transfer (CX, frictional), direct ionization transfer (Ion., direct), and direct recombination transfer (Rec., direct). (Magnitudes of these cumulative quantities are shown.) The cumulative direct CX momentum transfer is more than twice the ionization transfer, and the frictional CX momentum transfer is nearly equal to the ionization transfer. Recombination effects are negligible.
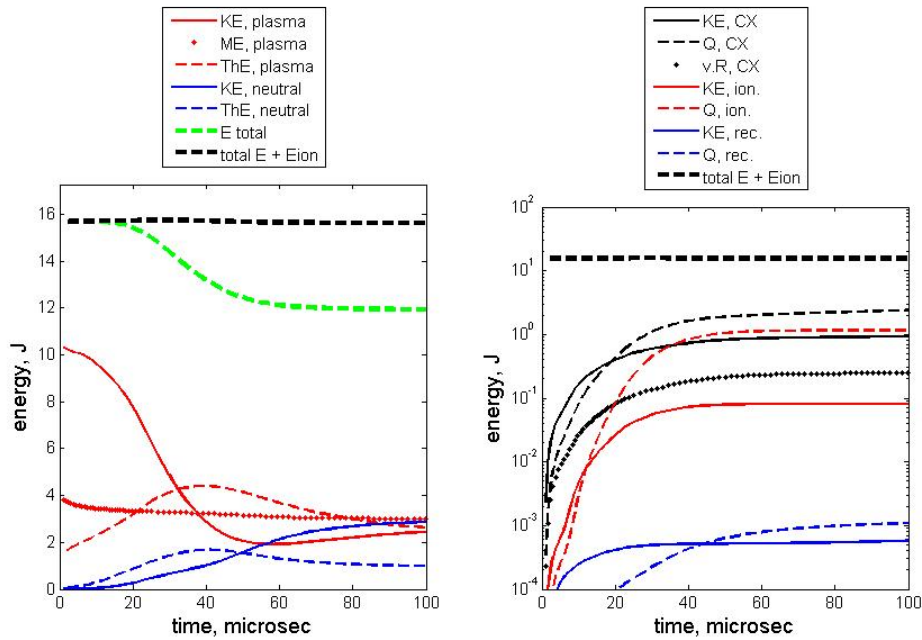
Figure 6.20: Time traces of energy-related quantities for ELF baseline simulation. In the left panel, plasma and neutral kinetic energy (KE), magnetic energy (ME), plasma and neutral thermal energy (ThE), total energy (E total), and total energy plus the cumulative ionization energy (total E + Eion) are shown. The fact that "total E + Eion" is flat verifies that, as expected, ionization is the only energy sink in the simulation. The right panel shows cumulative heating of the plasma fluid due to a variety of mechanisms: kinetic and thermal energy transfer due to CX (KE, CX and Q, CX), frictional CX drag transfer (v.R, CX), and kinetic and thermal energy transfer due to ionization and recombination (KE, ion., Q, ion., KE, rec., and Q, rec.). (Magnitudes of these cumulative quantities are shown.) Direct thermal energy transfer due to ionization is much less than that due to CX. Recombination effects are negligible.

6.4.3   Computational setup for ELF proof-of-concept simulation with coils

Two simulations similar to the baseline simulation with the Gaussian neutral gas profile are run. These simulation are proof-of-concept simulations that demonstrate the capability of using coils to squeeze/accelerate the FRC in a HiFi plasma-neutral simulation. In one flux injection simulation, reaction effects are included, and in the other, they are eliminated (leaving only the dissipative MHD system).

The computational setup is similar to that presented in Section 6.4.1. The geometry of the simulation, including the theta-pinch coils is shown in Figure 6.12. Changes to the simulation details are presented below. Dissipation and boundary conditions are different. A special condition allowing radiation in low-density regions is introduced.

Dissipation

To smooth the numerical noise that arises due to the flux injection, dissipation is increased. The minimum normalized viscosity coefficient is increased to $\xi = 5 \times 10^{-2}$ (vs. $\xi = 5 \times 10^{-3}$ in the simulations without flux injection). The density dissipation is increased to $D_n = 5 \times 10^{-3}$ (vs. $D_n = 2 \times 10^{-3}$ in the simulations without flux injection).

Boundary conditions

As for the simulations without coils, periodic boundaries are used at the ends of the cylindrical domain. The neutral fluid radial wall BC are unchanged. Radial wall BC for the plasma components are as follows.

Voltage is applied at the radial wall with three coils that each specify voltage over an axial extent of 0.1 m. The three coils are centered at $z = -0.15$ m, $z = 0.15$ m, and $z = -0.15$ m. Each coil has a peak voltage of 400 V, and a quarter-cycle time of 10 μs. When a coil is fired, it is set to maximum voltage. The voltage then varies sinusoidally through zero (after one quarter-cycle) and to the negative maximum voltage at which point the voltage returns to zero and remains zero for the duration of the simulation. After a half-cycle, the total injected flux is zero.

The loop voltage applied by the coils drives axial flux according to $V = -d\psi/dt$. The

flux is $\psi = \int \mathbf{B} \cdot d\mathbf{S}$, where $d\mathbf{S}$ is an area element of the cylinder cross-section. Inserting $\mathbf{B} = \nabla \times \mathbf{A}$ and reducing the area integral to a contour integral produces the expression $\psi = 2\pi R A_\phi$, where R is the cylinder radius, and A_ϕ is the azimuthal component of the vector potential. The boundary condition for A_ϕ is then $\partial A_\phi / \partial t = -V/(2\pi R)$.

The radial velocity boundary condition is $v_r = (\mathbf{E} \times \mathbf{B})_r / \mathbf{B}^2$. The azimuthal electric field is $E_\phi = V/(2\pi R)$. B_r and B_z are computed from A_ϕ at the boundary. The normal flux in the axial momentum equation is set to zero, ensuring that no axial force is imparted to the plasma by the wall.

The boundary condition for density depends on the direction of the radial flow at the wall. If the flow is inward, i.e., if flux is being increased/injected, the normal flux is set to $\rho_{min} v_r$, where $\rho_{min} = 1.17 \times 10^{-8}$ kg m^{-3}. (The background density is 3.5×10^{17} m^{-3}.) If the flow is outward, the normal flux is set to ρv_r, where ρ is the computed density at the boundary.

For the simulations done without coils, zero normal plasma heat flux is imposed at the wall. In trial runs using coils to inject flux, with zero normal heat flux at the wall, the temperature rises to hundreds of eV near the wall. This heating is due to the viscous and ohmic heating generated in the low-density background plasma during flux injection. Such high temperatures are not physically realistic, and cause numerical noise and numerical stiffness associated with the high wave speeds present in the hot plasma. To prevent these numerical difficulties, a heat sink is provided by fixing plasma temperature at the radial wall to the initial (minimum) temperature.

Special conditions

In regions of low-density plasma, dissipated heat is allowed to escape from the system. This may be thought of as radiative heat loss from the plasma. The term Q_{diss}^0 is used to represent all of the dissipative heating in the plasma pressure equation, Eqn. (5.79), including the terms multiplied by η, ξ, and ξ_a, which correspond to Ohmic heating, viscous heating, and artificial viscous heating, respectively. In regions with density less than $0.2 n_0 = 1.4 \times 10^{19}$ m^{-3}, this heating is multiplied by a factor, f_{rad}, which is between 0 and 1. The formula

applied in the low-density region is

$$
\begin{aligned}
Q_{diss} &= f_{rad}Q^0_{diss} \\
&= \frac{1}{2}\Big(1 + \cos\big[\pi(0.2n_0 - n)/(0.2n_0)\big]\Big)Q^0_{diss}.
\end{aligned}
\tag{6.3}
$$

6.4.4 Results of proof-of-concept ELF simulation with coils

Two proof-of-concept simulations are conducted: one simulation includes reactions, and the other does not. Three theta-pinch coils inject flux, compressing and accelerating the FRC. These results are strictly preliminary, and are not meant to provide a basis for conclusions about coil interaction with the ELF FRC. The flux injection parameters — that is, the quarter-cycle time, voltage, and exact coil locations — are not made to match the ELF experiment. In particular, the quarter-cycle time and the voltage are not representative of the expected ELF parameters. The expected quarter-cycle time is shorter (by a factor of approximately two) and the voltage is higher (by a factor approximately five). The planned experimental ELF coil parameters are more numerically challenging because the total flux injection is greater and occurs over a shorter time.

Figures 6.21 and 6.22 show snapshots of neutral density and total ion plus neutral pressure, respectively, for the simulation with reactions. Comparisons can be drawn between these plots and corresponding plots in Figures 6.15 and 6.16 for the baseline case without flux injection. High peak neutral gas density and momentum are seen in Figure 6.15 between 15 and 30 μs at the interface of the FRC and neutral gas. Similar concentrations of neutral gas density and momentum are not seen in Figure 6.21. Flux injection compresses the FRC, increasing its temperature. Ionization is then more active than CX, and the neutral gas is ionized before significant momentum is transferred from the plasma to the neutral gas. The high pressure caused by flux injection is observable in Figure 6.22.

Figure 6.23 show snapshots of ion pressure for the simulation without reactions. Results at 9 and 16 μs are similar to the results seen in Figure 6.22. No reactions are included, so at 27 and 35 μs, the axial motion of the FRC is unimpeded by the neutral gas.

Figures 6.24, 6.25, and 6.26 show time traces of key quantities for the simulation with
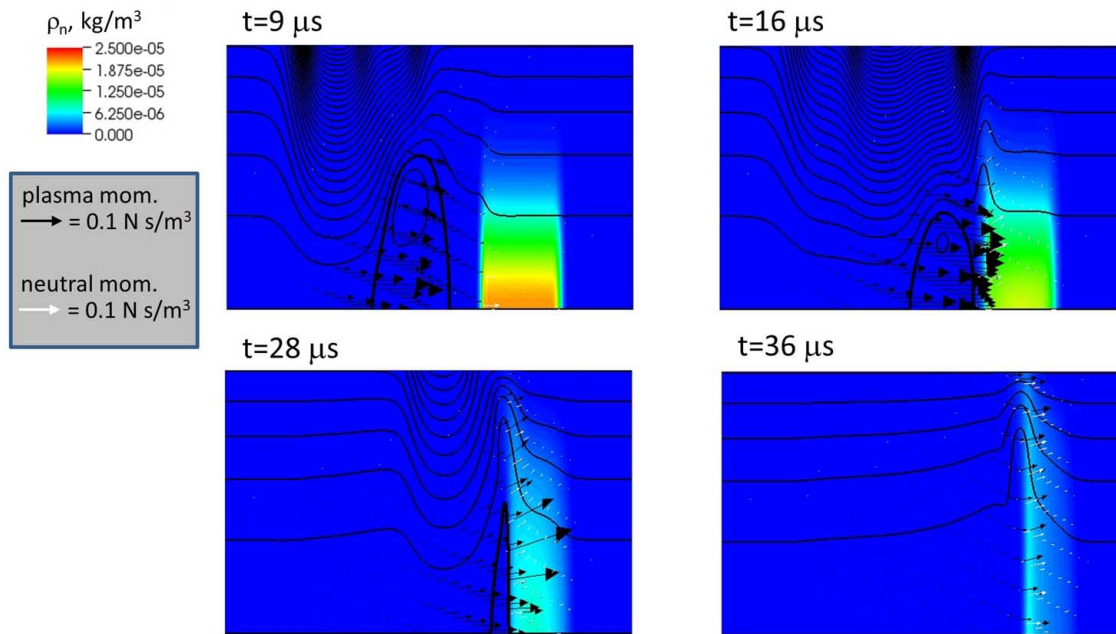
Figure 6.21: Neutral density pseudocolor plots for ELF flux injection simulation with reactions included. Black and white arrows indicate the direction and magnitude of plasma and neutral momentum density, respectively. As compared to similar plots for the case without flux injection shown in Figure 6.15, at 16, 28, and 36 μs, the neutral gas is ionized quickly and the disk-like density concentration seen in Figure 6.15 where the FRC meets the neutral gas, is not present. As a result of the rapid ionization, less momentum transfer to the neutral gas occurs as suggested by the smaller neutral momentum arrows in this figure.
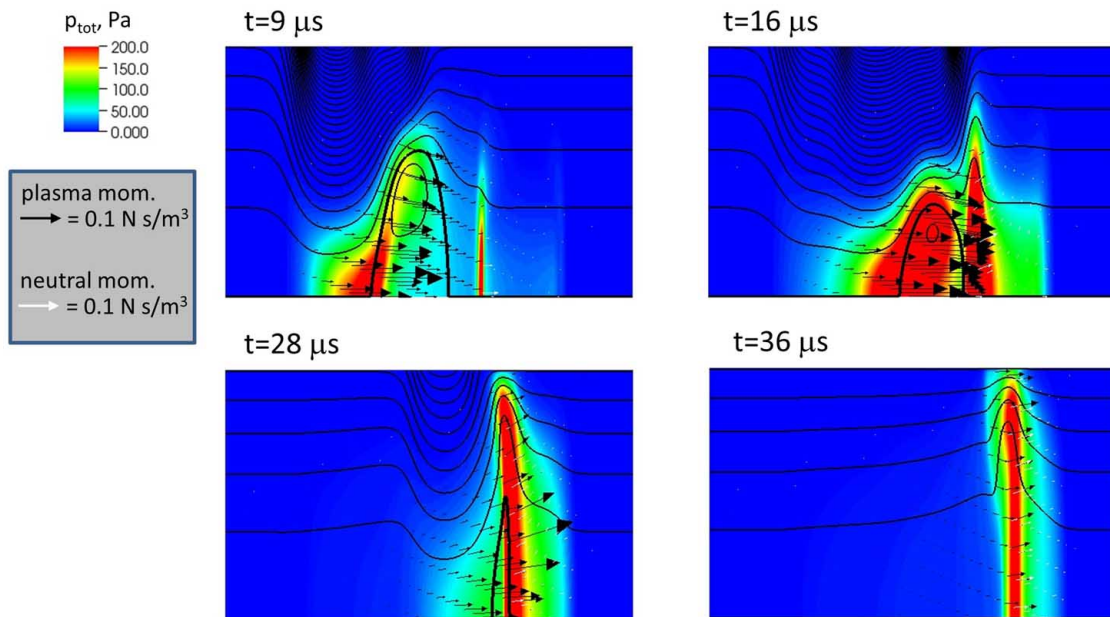
Figure 6.22: Total ion plus neutral pressure pseudocolor plots for ELF flux injection simulation with reactions included. Black and white arrows indicate the direction and magnitude of plasma and neutral momentum density, respectively. As compared to similar plots for the case without flux injection shown in Figure 6.16, significantly higher pressure is observed in the first two snapshots due to the flux injection and associated FRC compression. Also, less momentum transfer to the neutral gas has occurred as suggested by the smaller neutral momentum arrows in this figure.
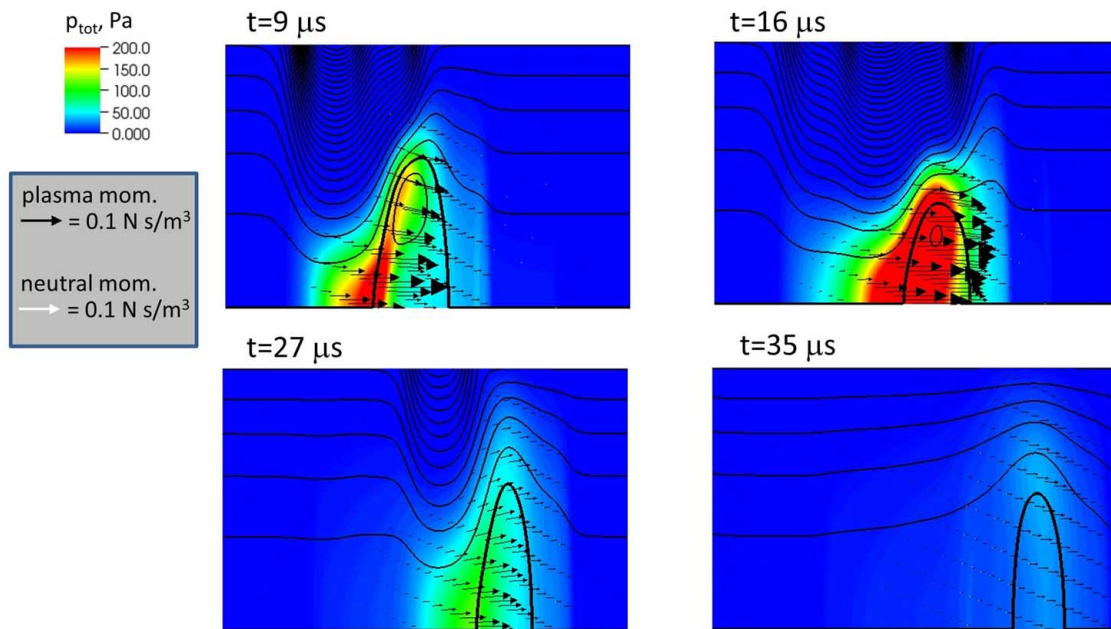
Figure 6.23: Total ion plus neutral pressure pseudocolor plots for ELF flux injection simulation without reactions. Black and white arrows indicate the direction and magnitude of plasma and neutral momentum density, respectively. As compared to the results shown in Figure 6.22 for a similar flux injection simulation with reactions included, the snapshots at 9 and 16 μs are similar. At late times, interaction with the neutral gas causes dramatically different pressure evolution in Figure 6.22.

flux injection. Comparisons can be drawn between these plots and corresponding plots in Figures 6.18, 6.19, and 6.20 for the baseline case without flux injection. The validity of comparisons is reduced because of the differences in simulation parameters discussed in Section 6.4.3. Figure 6.24 shows that the total temperature increases to 11 eV as the compressed FRC interacts with the neutral gas as compared to 7 eV in the case without flux injection shown in Figure 6.18. As in the case without flux injection, CX transfer exceeds ionization transfer by more than an order of magnitude. Figure 6.25 shows an increase in total axial momentum of 5.6%. Figure 6.26 shows that the total energy begins at 15 J, increases during the flux injection to 45 J, then falls to 12 J by the end of the simulation. The net loss of energy is largely due to thermal conduction to the radial wall.

In the flux injection simulation without reactions, total axial momentum increases by only 2.4% as compared to 5.6% when reactions are included. This indicates that the presence of the neutral target gas can result in improved coupling of the coils to the plasma and neutral gas in ELF.

6.4.5   Comparison of experimental results to simulation results

The diagnostics (synthetic and experimental) shown in Figure 6.12 are used to collect data for comparisons of experimental and simulation results. Diagnostics include magnetic field probes and Langmuir probes. The magnetic field probes are "B-dot" probes that yield the total change in magnetic field. The B-dot probes are located at the NES wall, 0.141 m from the ELF centerline, at four different axial locations: $z =$ 0.095, 0.28, 0.38, and 0.46 m. Langmuir probe arrays at $z = 0.13$ and $z = 0.33$ m each include nine individual probes with 0.01- to 0.02-m spacing. Data is presented from only the probes indicated in Figure 6.12 at 0.02-m and 0.08-m radial locations. The Langmuir probes are double probes that measure the ion density. Weber [20] provides details about the experimental diagnostics. For each Langmuir probe data point, results from three to five ELF discharges (shots) are averaged. For each B-dot probe data point, five to ten shots are averaged. The estimated shot-to-shot variability of both Langmuir probe and B-dot probe data is ≈25%. The absolute error for the Langmuir and B-dot probes are ≈50 % and ≈5 %, respectively.
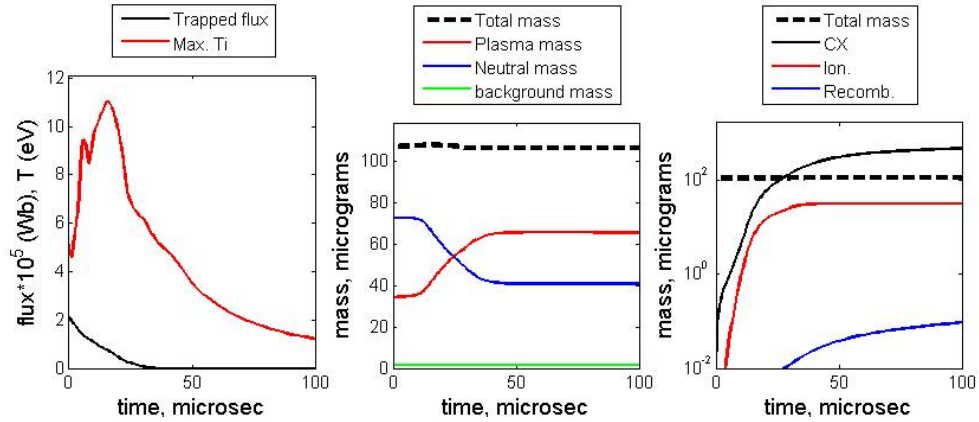
Figure 6.24: Time traces of peak ion temperature, magnetic flux, and mass-related quantities for ELF flux injection simulation with reactions. Peak ion temperature (Max. Ti) and trapped magnetic flux are shown in the left panel. The FRC flux dissipates by 30 μs. Plasma, neutral, and total mass are shown in the center panel. A slight increase in total mass is seen due to the background density that flows into the volume as flux is injected. The right panel shows cumulative charge exchange mass transfer (CX), ionization transfer (Ion.), and recombination transfer (Recomb.). CX transfer exceeds ionization transfer by more than an order of magnitude.

Results from preliminary experimental results are shown for two cases — with and without neutral beam injection. In a run designated ELF-NB, the translating FRC encounters a neutral beam in the NES. Run ELF-0 is a control case without the neutral beam. Two HiFi simulations, designed for direct comparison to these experimental cases (unlike the simulations presented in Section 6.4.2), have been conducted. These are designated HiFi-NB and HiFi-0, corresponding to ELF-NB and ELF-0, respectively.

The FRC total mass initially expected by the ELF neutral entrainment program was $\approx$30 μg. In the preliminary experimental work, difficulty has been encountered in generating FRCs with total masses near $\approx$30 μg. Using density measurements from Langmuir probe arrays, and estimates of the magnetic topology, the mass of the experimental FRCs is estimated to be approximately 2 μg. A possible explanation for the the lower mass is that
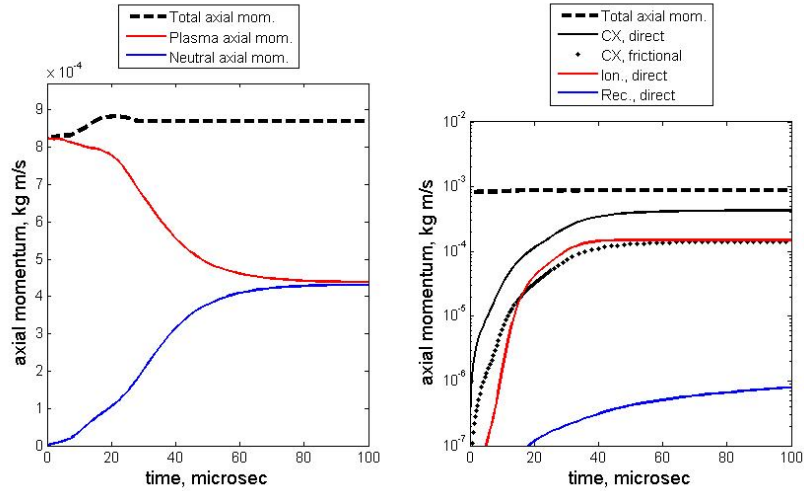
Figure 6.25: Time traces of momentum-related quantities for ELF flux injection simulation with reactions. In the left panel, plasma, neutral, and total momentum are shown. In the right panel, the cumulative transfer of momentum is shown for direct CX transfer (CX, direct), frictional CX transfer (CX, frictional), direct ionization transfer (Ion., direct), and direct recombination transfer (Rec., direct). (Magnitudes of these cumulative quantities are shown.) The results are not dramatically different than those for the similar case without flux injection shown in Figure 6.19. A 5.6 % increase in total momentum is observed.

the fill gas from which the FRC is formed by RMF is less than expected in the preliminary work. Because the same RMF energy is used to form the lower FRC mass, the FRC temperature is higher. The total ion plus electron temperature is estimated to be 30 eV.

In many respects, HiFi-NB and HiFi-0 are similar to the baseline simulation described in Section 6.4.1. However, the neutral gas profile and the initial FRC mass are modified with the goal of matching the experimental conditions as closely as possible. The neutral beam properties are measured by a fast ion gauge. The total neutral beam mass is estimated to be ≈ 30 μg. The axial profile of the beam is approximately Gaussian with a characteristic width of 0.2 m ($\propto e^{-(z/0.2)^2}$). The radial profile is also close to Gaussian with a characteristic width of 0.1 m ($\propto e^{-(r/0.1)^2}$). The maximum neutral beam density is at $z =$0.23 m when
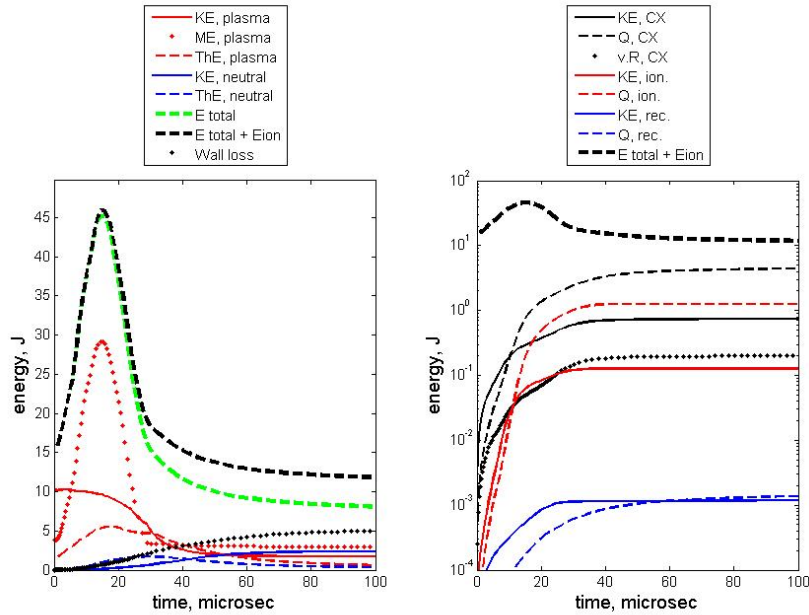
Figure 6.26: Time traces of energy-related quantities for ELF simulation with flux injection. In the left panel, plasma and neutral kinetic energy (KE), magnetic energy (ME), plasma and neutral thermal energy (ThE), total energy (E total), and total energy plus the cumulative ionization energy (total E + Eion) are shown. Thermal energy conducted to the wall (wall loss) is also shown. As flux is injected, the magnetic energy increases to a maximum of approximately 30 J, causing a factor of three increase in total energy. The wall loss over the 100-μs simulation is 5 J. The right panel shows cumulative heating of the plasma due to a variety of mechanisms: kinetic and thermal energy transfer due to CX (KE, CX and Q, CX), frictional CX drag transfer (v.R, CX), and kinetic and thermal energy transfer due to ionization and recombination (KE, ion., Q, ion., KE, rec., and Q, rec.). (Magnitudes of these cumulative quantities are shown.)

the RMF is applied. The neutral beam speed is $\approx$800 m/s. Only $\approx$ 40 μs elapses during FRC formation, acceleration, and translation to $z = 0.23$ m. The movement of the neutral beam during this time is $\approx$ 0.03 m. Therefore, the static initial neutral gas profile in the

HiFi-NB run is axially centered at $z = 0.26$ m. The peak simulated neutral density is 2.35 $\times 10^{-6}$ kg/m^3 (7×10^{19} m^{-3}). Using the Gaussian radial and axial profiles described above, the total neutral mass is 26 μg. The FRCs in HiFi-NB and HiFi-0 are similar to the baseline FRC described in Section 6.4.1 in magnetic topology. That is, the separatrix radius is 0.09 m, and the separatrix length is 0.62 m. However, the FRC mass is reduced to 1.7 μg to match the experimentally generated FRCs, and the total ion plus electron temperature is increased to 30.6 eV.

For the plots presented next, the time is shifted: in the HiFi plots, $t = 0$ corresponds to the time at which the maximum magnetic field is measured by the magnetic probe at $z = 0$ for the HiFi-0 case; similarly, in the experimental plots, $t = 0$ corresponds to the time at which the maximum magnetic field is expected at $z = 0$. (The experimental magnetic probe at $z = 0$ does not provide a good signal, so an estimate is made based on the other probe data.)

Before examining comparisons of experimental and synthetic diagnostic data, it is useful to study the simulation results to develop an intuitive picture of the plasma-neutral behavior. Snapshots of the HiFi-NB simulation are shown in Figure 6.27. As shown, the FRC dissipates by $t = 13$ μs. Energy is delivered, apparently by thermal conduction, to the region of high neutral density, ionizing a significant amount of neutral gas by $t = 0$ μs. The plasma expands and continues to drift axially as seen at $t = 27$ and 50 μs. Comparing these results to those presented in Section 6.4.2, the qualitative behavior is much different. The FRC in the simulation depicted in Figure 6.15 is more massive by a factor of 20, and strong interaction with the neutral beam compresses the FRC plasma and causes magnetic field lines to bend as high pressure and strong radial flows develop. In contrast, the results shown in Figure 6.27 show no observable compression of the FRC, and no corresponding bending of magnetic field. As a result, the magnetic signature of the event as detected by the B-dot probes is expected to be small. The plasma mass increases by 50.2% during the HiFi-NB simulation.

In Figure 6.28, synthetic and experimental Langmuir probe measurements are compared for experimental and simulation results. Figure 6.29 compares synthetic and experimental magnetic probe data for experimental and simulation results. To compare with the change
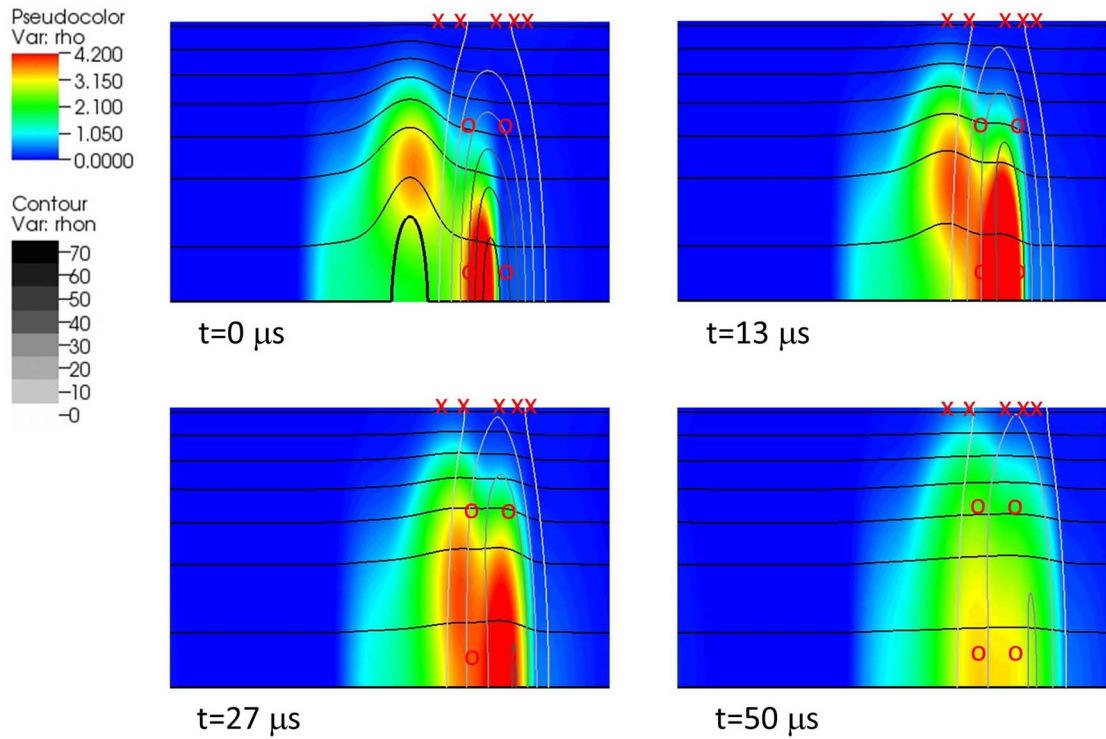
Figure 6.27: Snapshots from HiFi-ELF comparison simulation with neutral beam. Plasma density is shown in pseudocolor, and neutral density is shown in grayscale contours. Magnetic flux is indicated by black contours. The position of synthetic B-dot and Langmuir probes are marked with red x's, and o's, respectively. The FRC trapped flux rapidly dissipates. Where the neutral gas density is high, prior to the arrival of the bulk of the FRC, ionization creates a significant amount of new plasma. There is not a recognizable FRC compression event that causes high pressure and bends field lines as observed in cases with higher FRC mass shown in Section 6.4.2.

in axial magnetic field found using the B-dot probes, the magnetic field measurements indicated for HiFi are adjusted to indicate the change in axial magnetic field instead of the actual axial magnetic field.

The comparison of experimental and modeling results shows some similarities. For both experimental and simulation results, the presence of the neutral beam causes a significant rise in density, and broadens and delays time traces of both density and magnetic field. Several aspects of the comparison should be improved in future work to further validate the HiFi simulations. Additional fidelity is necessary in matching the simulated initial conditions with experimental conditions. For instance, the total FRC mass, temperature, and magnetic topology should be more thoroughly studied experimentally and properly modeled in HiFi. The profile of the neutral gas should be more accurately understood experimentally and properly represented in HiFi. A ballistic pendulum thrust measurement device described by Weber [20] could be used to measure the total momentum in the experiment, and would provide an interesting point for comparison with HiFi results. Also, if the FRC mass in the experiment were increased to a level closer to the neutral beam mass, more distinctive features might be observable in the diagnostic data.
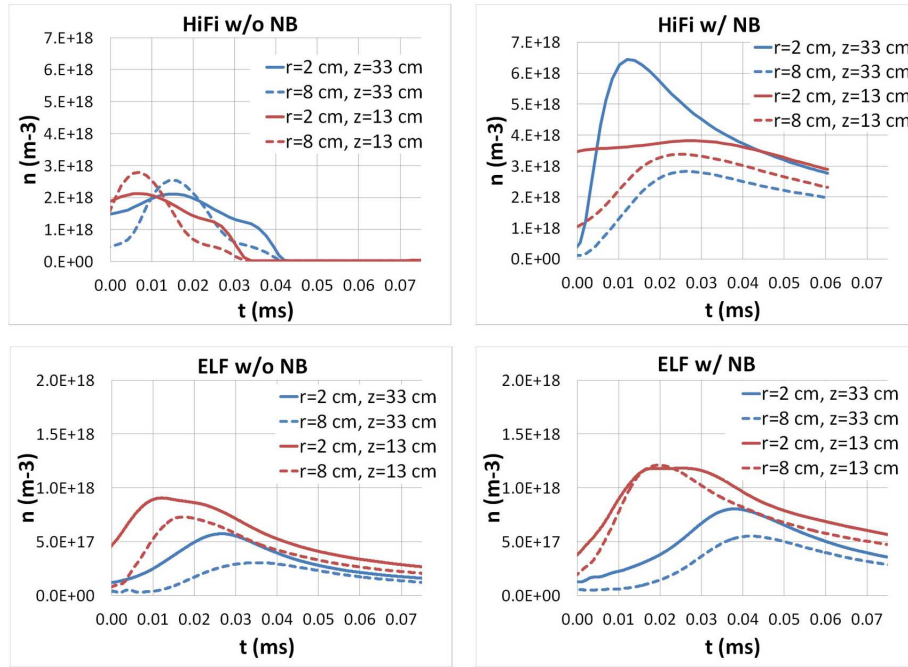
Figure 6.28: Comparison of experimental and synthetic plasma density diagnostic data. In the results for HiFi-0 (HiFi w/o NB), the density traces show an intact FRC passing by the Langmuir probes. The results for HiFi-NB (HiFi w/ NB) show that the density rises dramatically at $r = 2$ cm as expected based on the snapshots in Figure 6.27. Generally, the peak densities of the traces occur at later times when the neutral beam is present. In HiFi-NB, the density traces are broader than the HiFi-0 traces, indicating the expansion seen in Figure 6.27. The experimental results show some similar trends. The ELF-0 (ELF w/o NB) results are more peaked than the ELF-NB (ELF w/ NB) results, suggesting that the plasma-neutral interaction causes plasma expansion. As seen in the simulation density traces, the peaks of the experimental density traces are delayed when the neutral beam is present.
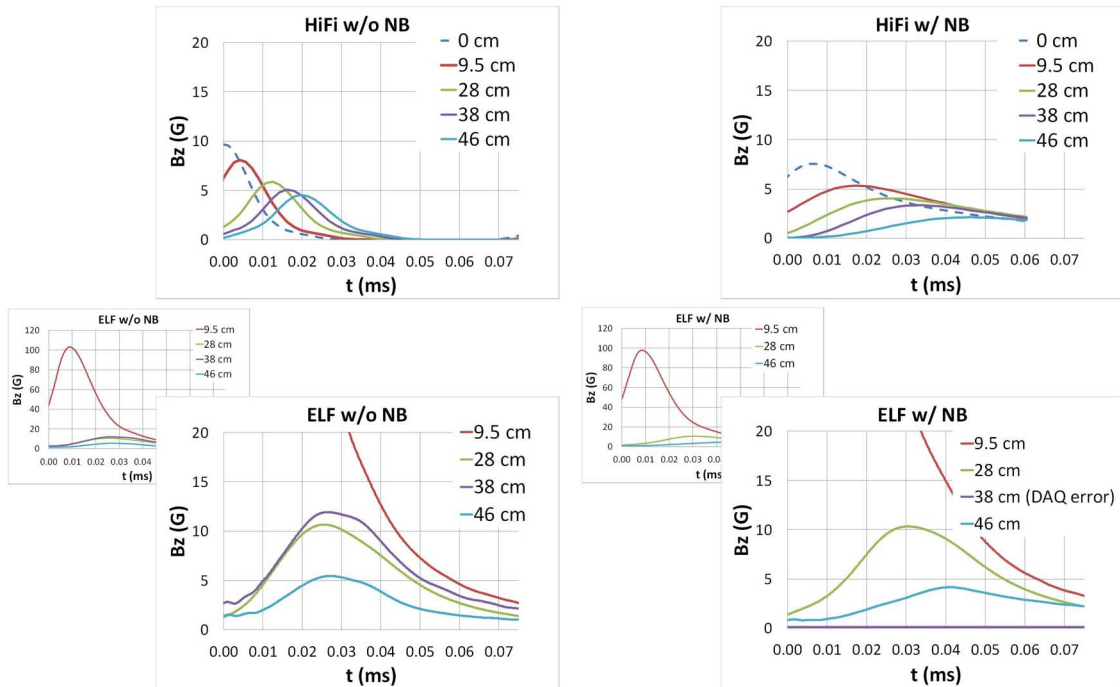
Figure 6.29: Comparison of experimental and synthetic axial magnetic field diagnostic data. The magnetic field traces seen for HiFi-0 (HiFi w/o NB) show an intact FRC passing by the magnetic probes. In the results for HiFi-NB (HiFi w/ NB), the magnetic field traces are delayed and broadened. In the experimental results, as shown in the small, inset plots, the peak magnetic field measured at $z = 9.5$ cm is near 100 G. This high field is a feature of the RMF-formed FRC that is not present in the equilibrium FRC simulated with HiFi. The ELF-0 (ELF w/o NB) results show relatively peaked profiles as compared to the broader traces seen in the ELF-NB (ELF w/ NB) results, which show spreading comparable to the HiFi-NB results. Note that data is not available from the probe at $z = 38$ cm, which had a data acquisition problem in the ELF-NB discharge.

Chapter 7

CONCLUSIONS

Three main contributions have been made to computational plasma science, with particular focus on improving and extending magnetohydrodynamic (MHD) modeling capability. The first is that the accuracy of spectral element spatial representation for modeling strong anisotropy has been quantitatively explored with attention to grid alignment, and the total number of degrees of freedom needed to achieve a certain accuracy. Second, a novel open boundary condition (BC) suitable for dissipative MHD problems has been developed and compared with several alternative open BC. Third, a simple but useful fluid model for capturing neutral effects in plasmas has been developed, implemented, and applied. This model essentially combines the typical single MHD plasma fluid with an additional neutral fluid, while accounting for charge exchange, ionization, and recombination. The HiFi implicit spectral element code has been used for the computational implementation and testing required for each contribution.

Research related to each contribution is summarized below.

7.1 Summary of modeling anisotropic heat conduction with high-order spectral elements

By modeling anisotropic heat conduction with a spectral element technique, it has been shown that high-order elements yield a given accuracy with less total degrees of freedom than lower-order elements. Similar results are found for problems in 2D and 3D and for straight and curved anisotropy. Convergence with grid alignment has been explored, and results show that even small grid misalignment cause significant numerical error. This error can be efficiently controlled by using high-order spectral spatial representation.

In the study of grid alignment error, a subtlety has been found in which accuracy improves near a 45° alignment angle. Some grid adaptation schemes (like the one implemented in HiFi) use grid refinement algorithms based on error minimization, and the fact that there

is a local minimum in numerical error due to grid misalignment should be noted.

Theoretical predictions of numerical diffusion error are presented and, for a given grid alignment, these predictions are in good agreement with computed results. Error estimates that take grid alignment into account have not been made.

While high-order spectral elements clearly have advantages when modeling anisotropic heat conduction in numerically difficult problems like fusion plasmas, as discussed in Section 2.1, there associated challenges that are not solved simply by using high-order representations. Two of these challenges are preserving positivity (i.e., ensuring flow of heat from hot to cold), and properly specifying non-local closures associated with low collisionality. Work is ongoing to establish practical solutions to these problems.

Employing spectral element representations may be beneficial in fields as diverse as fusion science, image processing, and medical imaging. For example, high-order finite element techniques are gaining favor in electromagnetic wave modeling where direction-dependent numerical dispersion error must be controlled [27] [118]. The present research provides a basis for quantifying the benefits of the spectral element approach when modeling anisotropic behavior.

7.2   Summary of modeling open boundary conditions for dissipative MHD

Three methods for modeling open BC have been described. The first method, approximate Riemann boundary conditions (ARBC), locally computes fluxes using an approximate Riemann technique to specify incoming wave strengths. In the second method, lacuna-based open boundary conditions (LOBC), an exterior region is attached to the interior domain where hyperbolic effects are damped before reaching the exterior region boundary where the remaining parabolic effects are bounded using conventional BC. The third method, zero normal derivative BC (ZND BC), enforce zero normal derivative on each dependent variable at the open boundary.

Three test problems conducted with a spectral element code, HiFi, demonstrate the open BC. Boundary reflection is quantified for ARBC, LOBC, and ZND BC by comparing associated solutions to a reference solution computed in a domain large enough to prevent undesired boundary effects. 1D and 2D pressure pulse problems test linear and nonlinear

regimes. In the pressure pulse problems, ARBC and LOBC outperform ZND BC, giving normalized L_∞-norm pressure errors less than 5%. LOBC performance is found to improve as the exterior region size is increased.

An FRC translation problem with strong thermal conduction, and a coaxial plasma acceleration problem with high-speed, high-gradient flow, are more challenging for the open BC. In both of these problems, LOBC excel where ARBC fail due to the presence of strong dissipation.

ZND BC are by far the easiest to implement of the three open BC. However, for problems that are sensitive to boundary effects, ZND BC could be inadequate.

In the pressure pulse problems of Section 4.2, which are dominantly hyperbolic, ARBC consistently outperform ZND BC. Other advantages and disadvantages of ARBC are:

- ARBC implementation is more complicated than ZND BC, but significantly less involved than LOBC.

- In the FRC translation and coaxial acceleration problems of Sections 4.3 and 4.4, parabolic effects are significant at the open boundaries, and ARBC do not properly bound the system behavior, allowing numerical instability.

- Oblique-moving waves are not properly treated in this technique, which is designed for waves moving normal to the open boundary.

When ARBC fail in the presence of dissipation, LOBC provide an open BC option that generates significantly less reflection than ZND BC, as demonstrated in the test problems. Other advantages and disadvantages of LOBC are:

- Implementation of LOBC is complicated and problem-dependent.

- As discussed in detail in Section 3.2.3, exact non-reflection with LOBC can be lost for a variety of reasons: in 2D problems, true lacunae do not exist; dissipation modifies lacunae; auxiliary solution components associated with slow-moving or obliquely moving waves must often be prematurely truncated; nonlinearity can cause a mismatch of the wave speeds of the auxiliary solution with the interior solution.

- Even when exact non-reflection is not possible, the test problems show that significantly lower reflection error is achievable with LOBC than with either ARBC or ZND BC.

- As discussed in Section 3.2.3, the present LOBC implementation in HiFi is not optimized, and could be improved in future work. Computational effort could be reduced by performing reintegration only for the auxiliary solution. Also, memory requirements could be reduced by computing the auxiliary solution only where it is non-trivial. Computational effort of the LOBC simulation with and without these optimizations is discussed in Section 4.4.2 for the four-cycle coaxial-electrode plasma acceleration problem. As discussed there, computational effort is approximately six times greater than for the ZND BC case, but is comparable to the reference simulation. With optimizations, it is estimated that the effort could be reduced to approximately three times the effort for the ZND BC simulation.

The challenges of implementing LOBC as an open BC for dissipative MHD have been explored. While known alternatives either produce undesirable reflections or are numerically unstable, LOBC have proven to be effective.

An open BC that is able to drive interior dynamics in dissipative MHD problems is a worthy future goal. Although the ARBC meets this need in the nozzle flow problem presented, it is inapplicable to problems with strong dissipation. Unless the ARBC can be modified to accommodate dissipation, another approach is needed. Perhaps the LOBC can be adapted for this purpose.

7.3   Summary of modeling neutral fluid effects in collisional plasmas

A reacting and interacting three-fluid electron-ion-neutral model has been derived from the Boltzmann equation with elastic collisions and three inelastic collisions: resonant charge exchange; electron-impact ionization; and radiative recombination. The required moments of the reaction collision terms are described in detail. A three-fluid model is derived and then reduced to a two-fluid plasma-neutral model which is implemented in the HiFi code.

In addition to the reaction physics, a model for critical ionization velocity (CIV) effects is developed and implemented.

In future work, the plasma-neutral model could be improved in a variety of ways: Multiple plasma and neutral species could be accommodated; multiple ionization could be allowed; excited states could be tracked; radiation effects could be included; as discussed in Appendix G, the transport coefficients could be improved to more accurately close the plasma-neutral model; electron physics could be added to the Ohm's law by including the Hall term and diamagnetic term; charged-neutral elastic collisions could be included, and should be included in problems where the ionization fraction is low; the approach taken to include CIV effects could be refined, for example, by taking into account the dependence of CIV on the strength and orientation of magnetic field; and additional reactions could be included such as non-resonant charge, three-body recombination, polarization ionization, etc. With so many possible areas for improvement, future code development efforts should target the improvements that are most important and useful for the anticipated applications.

The plasma-neutral model is applied to four different problems:

- Plasma acceleration with parallel-plate electrodes. CIV effects are modeled.

- Plasma acceleration with coaxial electrodes. The canting angle of the snowplow plasma front is observed.

- Ion spin-up in FRCs with rotating magnetic field (RMF) current drive. Drag due to the presence of neutral gas is studied.

- The Electrodeless Lorentz-Force (ELF) thruster. The effectiveness of neutral entrainment by the accelerated FRC is quantified.

In the first three problems, the applicability of the plasma-neutral HiFi implementation is qualitatively demonstrated. In the final problem, the modeling results are compared quantitatively to experimental results.

In MHD, if a resistive or ideal Ohm's law is used, parallel-plate plasma acceleration is driven by magnetic field injected uniformly between the plates, the plasma behavior is

one-dimensional. The Ohm's law used in the plasma-neutral model is of this type, and the behavior in the plasma-neutral model solutions are also one-dimensional. The study of parallel-plate plasma acceleration focuses on modeling CIV effects in the 1D problem. The CIV model presented in Section 5.2.4 is successfully applied. It is found that CIV effects are important only in the limited regime where the flow is fast enough that speeds exceed the critical velocity for CIV, but not so hot that neutral gas is easily ionized with or without CIV effects. Experimentally, a wealth of interesting two-dimensional phenomena are seen in parallel-plate accelerators (see, e.g., the dissertation by Berkery [119]). An interesting line of future research would be to study the two-dimensional physics that would result if Hall effect physics were included in the Ohm's law of the plasma-neutral model.

In coaxial plasma acceleration simulations, it is found that neutral fluid effects can significantly change the observed behavior in terms of the snowplow plasma front axial propagation speed and the canting angle of the snowplow. Additional physics not presently captured by the plasma-neutral is known to be important in accelerating snowplow current sheets — specifically, Hall effect physics can strongly affect snowplow canting behavior [119, 6]. A particularly interesting future application would be to model the coaxial acceleration region of the ZaP flow Z-pinch experiment [43].

The simulations of RMF-driven FRCs in TCSU presented in Section 6.3 qualitatively demonstrate the applicability of the plasma-neutral model to this problem. To achieve quantitative agreement with the TCSU experiment, and to make a significant contribution to understanding the important physics involved with the ion rotation damping, additional fidelity would be necessary in the simulations. Viscosity is thought to be critical [115], so the viscosity model used in the simulations of Section 6.3 should be refined. (A uniform isotropic viscosity is used.) Radial wall BCs on neutral and plasma density and pressure are not physically meaningful and should be improved. For example, the rate and location of neutral density injection/recycling in TCSU should be matched as well as possible. Also, short of including the electron-fluid physics needed to exactly model the RMF current drive, the applied torque profile should be modified to be more realistic. It is known, for example, that the RMF does not easily penetrate the conductive core plasma and RMF torque is reduced near the center of the FRC [120].

The ELF simulations presented in Section 6.4 verify the HiFi plasma-neutral model in the sense that mass, momentum, and energy are conserved in a complicated, highly non-linear simulation. The ELF results have already proven useful to the experimental effort. Simply observing the rate of flux decay in the simulations has been a useful insight — it may prove difficult to use theta-pinch coils to accelerate an FRC which has lost most or all of its trapped flux. The pressure observed at the radial wall when the block neutral gas profile is used is high when compared to the pressure observed in simulations with the Gaussian profile. High pressure is probably associated with wall damage, which could limit the operational lifetime of the thruster. To avoid operating conditions that damage the wall, the program will focus on neutral gas profiles more like the Gaussuian profile, in which neutral gas is concentrated near the cylindrical axis. Furthermore, the simulations provide information about the appropriate FRC temperature and density, and neutral gas density for ideal neutral entrainment while, again, minimizing damage to the radial wall of the thruster.

The ELF program has plans to continue using the HiFi plasma-neutral implementation to model neutral gas entrainment in ELF, including the application of theta-pinch coils to inject flux, compress, and accelerate the coupled plasma-neutral gas. For this reason, a proof-of-concept simulation has been conducted to demonstrate plasma-neutral interaction in an ELF simulation with flux injection. Only a small increase in total momentum, 5.6%, is observed. As discussed in Section 6.4.4, the proof-of-concept simulation parameters do not closely match ELF parameters. Significantly higher momentum transfer is expected when flux injection is modeled more accurately in future work.

The comparisons presented in Section 6.4.5 are a preliminary step toward validating the plasma-neutral model. To continue the validation, a significant coordinated effort with the experiment would be required. Experimental conditions including neutral gas profile and FRC magnetic topology, temperature, and total mass should be accurately recreated in the simulated initial conditions. Another possible improvement would be to implement the RMF formation, which is a 3D phenomenon, in 3D HiFi. Also, by generating higher-mass FRCs in the ELF experiment, distinctive magnetic field and density evolution might be more easily observed and compared in the experimental and synthetic diagnostics.

BIBLIOGRAPHY

[1] A. H. Glasser and X. Z. Tang. The SEL macroscopic modeling code. *Comput. Phys. Commun.*, 164:237 – 243, 2004.

[2] V. S. Lukin. *Computational Study of the Internal Kink Mode Evolution and Associated Magnetic Reconnection Phenomena*. PhD thesis, Princeton University, 2008.

[3] V. S. Lukin, A. H. Glasser, W. Lowrie, and E. T. Meier. Overview of HiFi implicit spectral element code framework for general multi-fluid applications. *J. Comput. Phys.*, 2011. To be submitted.

[4] J. K. Hargreaves. *The Solar-Terrestrial Environment*. Cambridge, 1992.

[5] J. W. Freeman. *Storms in Space*. Cambridge, 2001.

[6] R. G. Jahn. *Physics of Electric Propulsion*. McGraw-Hill, 1968.

[7] V. D. Shafranov. The initial period in the history of nuclear fusion research at the Kurchatov Institute. *Phys.-Usp.*, 44:835 – 843, 2001.

[8] International Fusion Research Council. Status report on fusion research. *Nucl. Fusion*, 45:A1 – A28, 2005.

[9] Committee for The National Academies Summit on America's Energy Future and National Research Council. *The National Academies Summit on America's Energy Future: Summary of a Meeting*. National Academies Press, 2008.

[10] PSI-Center. www.aa.washington.edu/research/PSI/.

[11] S. I. Braginskii. Transport processes in a plasma. In M. A. Leontovitch, editor, *Rev. Plasma Phys., Vol. 1*, pages 205 – 311. Consultants Bureau, New York, NY, 1965.

[12] G. E. Karniadakis and S. J. Sherwin. *Spectral/hp Element Methods for Computational Fluid Dynamics*. Oxford Univ. Press, New York, 2005. Second edition.

[13] R. D. Henderson. Adaptive spectral element methods for turbulence and transition. In T. J. Barth and H. Deconinck, editors, *High-Order Methods for Computational Physics*, pages 225 – 324. Springer-Verlag, New York, 1999.

[14] G. Strang and G. J. Fix. *An Analysis of the Finite Element Method.* Prentice-Hall, Englewood Cliffs, N.J., 1973.

[15] Portable, Extensible Toolkit for Scientific Computation (PETSc). www.mcs.anl.gov/petsc/petsc-as/.

[16] N. Krall and A. Trivelpiece. *Principles of Plasma Physics.* McGraw-Hill, 1973.

[17] J. P. Freidberg. Ideal magnetohydrodynamic theory of magnetic fusion systems. *Rev. Modern Phys.*, 54:801 – 902, 1982.

[18] L. C. Steinhauer. Review of field-reversed configurations. *Phys. Plasmas*, 18:070501, 2011.

[19] M. J. Tuszewski. Field reversed configurations. *Nucl. Fusion*, 28:2033 – 2092, 1988.

[20] T. E. Weber. *The Electrodeless Lorentz Force Thruster Experiment.* PhD thesis, University of Washington, 2010.

[21] A. L. Hoffman, H. Y. Guo, J. T. Slough, et al. The TCS rotating magnetic field FRC current-drive experiment. *Fusion Sci. Technol.*, 41:92 – 106, 2002.

[22] G. J. Marklin. Private communication, 2008.

[23] C. R. Sovinec et al. Nonlinear magnetohydrodynamics simulation using high-order finite elements. *J. Comput. Phys.*, 195:355 – 386, 2004.

[24] R. Marchand and M. Dumberry. CARRE: a quasi-orthogonal mesh generator for 2D edge plasma modelling. *Comput. Phys. Commun.*, 96:232 – 246, 1996.

[25] E. T. Meier, V. S. Lukin, and U. Shumlak. Spectral element spatial discretization error in solving highly anisotropic heat conduction equation. *Comput. Phys. Commun.*, 181:837 – 841, 2010.

[26] P. Perona and J. Malik. Scale-space and edge detection using anisotropic diffusion. *IEEE Trans. Pattern Anal. Mach. Intell.*, 12:629 – 639, 1990.

[27] G. Sun and C. W. Trueman. Suppression of numerical anisotropy and dispersion with optimized finite-difference time-domain methods. *IEEE Trans. Antennas and Propagation*, 53:4121 – 4128, 2005.

[28] P. J. Basser and D. K. Jones. Diffusion-tensor MRI: theory, experimental design, and data analysis – a technical review. *NMR Biomed.*, 15:456 – 467, 2002.

[29] M. Saadatfar and M. Sahimi. Diffusion in disordered media with long-range correlations: Anomalous, Fickian, and superdiffusive transport and log-periodic oscillations. *Phys. Rev. B*, 65:036116, 2002.

[30] H.-O. Kreiss. *Numerical methods for solving time-dependent problems for partial differential equations.* Presses de l'Université de Montréal, Montréal, Que., 1978.

[31] S. Günter et al. Finite element and higher order difference formulations for modelling heat transport in magnetised plasma. *J. Comput. Phys.*, 226:2306 – 2316, 2007.

[32] E. D. Held et al. Nonlocal closures for fluid simulations. *Phys. Plasmas*, 11:2419 – 2426, 2004.

[33] J.-Y. Ji, E. D. Held, and C. R. Sovinec. Moment approach to deriving parallel heat flow for general collisionality. *Phys. Plasmas*, 16:022312, 2009.

[34] P. Sharma and G. W. Hammett. Preserving monotonicity in anisotropic diffusion. *J. Comput. Phys.*, 227:123 – 142, 2007.

[35] D. del-Castillo-Negrete and L. Chacón. Local and nonlocal parallel heat transport in general magnetic fields. *Phys. Rev. Letters*, 106:195004, 2011.

[36] J. G. Charney, R. Fjörtoft, and J. v. Neumann. Numerical integration of the barotropic vorticity equation. *Tellus*, 2:237 – 254, 1950.

[37] C. Hirsch. *Numerical Computation of Internal and External Flows.* Wiley, 1988. Second edition.

[38] J. A. Moríñigo and J. J. Salvá. Robust non-reflecting boundary conditions for the simulation of rocket nozzle flow. *Aero. Sci. and Tech.*, 14:429 – 441, 2010.

[39] D. R. Durran. *Numerical Methods for Wave Equations in Geophysical Fluid Dynamics.* Springer-Verlag, 1999.

[40] A. V. Ilin et al. Simulations of plasma detachment in VASIMR. *AIAA-2002-0346, Proceedings of the 40th AIAA Aerospace Sciences Meeting and Exhibit, Reno, January 2002.*

[41] B. L. England and P. G. Mikellides. Numerical simulation of a MW-class self field magnetoplasmadynamic thruster using the MACH 2 code. *IEPC-2005-206, Proceedings of the 29th International Electric Propulsion Conference, Princeton, November 2005.*

[42] S. Landi and M. Velli. Alfvén waves and shock wave formation at an X-point magnetic field configuration. *Astrophys. J.*, 624:392 – 401, 2005.

[43] U. Shumlak et al. Equilibrium, flow shear and stability measurements in the Z-pinch. *Nuc. Fusion*, 49:075039, 2009.

[44] T. Kanki. Magnetohydrodynamic simulation of dynamical behavior of a field-reversed configuration during magnetic mirror reflection. *Phys. Plasmas*, 10:3635 – 3643, 2003.

[45] K. W. Thompson. Time-dependent boundary conditions for hyperbolic systems. *J. Comput. Phys.*, 68:1 – 24, 1987.

[46] K. W. Thompson. Time-dependent boundary conditions for hyperbolic systems, II. *J. Comput. Phys.*, 89:439 – 461, 1990.

[47] V. S. Ryabenkii, S. V. Tsynkov, and V. I. Turchaninov. Global discrete artificial boundary conditions for time-dependent wave propagation. *J. Comput. Phys.*, 174:712 – 758, 2001.

[48] S. V. Tsynkov. Numerical solution of problems on unbounded domains: A review. *App. Num. Math.*, 27:465 – 532, 1998.

[49] D. Givoli. Non-reflecting boundary conditions: A review. *J. Comput. Phys.*, 94:1 – 29, 1991.

[50] D. Givoli. High-order local non-reflecting boundary conditions: a review. *Wave Motion*, 39:319 – 326, 2004.

[51] T. Colonius. Modeling artificial boundary conditions for compressible flow. *Annu. Rev. Fluid Mech.*, 36:315 – 345, 2004.

[52] F. Q. Hu. Absorbing boundary conditions. *Int. J. Comput. Fluid Dyn.*, 18:513 – 522, 2004.

[53] R. LeVeque. *Finite Volume Methods for Hyperbolic Problems*. Cambridge Univ. Press, 2002.

[54] U. Shumlak and B. Udrea. An approximate Riemann solver for MHD computations on parallel architectures. *AIAA 2001-2591*, 2001.

[55] B. Udrea. *An advanced implicit solver for MHD*. PhD thesis, University of Washington, 1999.

[56] B. Cockburn, G. E. Karniadakis, and C. W. Shu. The development of discontinuous Galerkin methods. In B. Cockburn, G. E. Karniadakis, and C. W. Shu, editors, *Discontinuous Galerkin Methods: Theory, Computation and Applications*, pages 3 – 50. Springer-Verlag, 2000.

[57] B. Gustafsson, H.-O. Kreiss, and J. Oliger. *Time Dependent Problems and Difference Methods*. Wiley, New York, 1995.

[58] J. C. Strikwerda. Initial boundary value problems for incompletely parabolic systems. *Comm. on Pure and Applied Math.*, 30:797 – 822, 1977.

[59] J. S. Hesthaven and D. Gottlieb. A stable penalty method for the compressible Navier-Stokes equations: I. Open boundary conditions. *J. Sci. Comput.*, 17:579 – 612, 1996.

[60] J. Nordström and M. Svärd. Well-posed boundary conditions for the Navier-Stokes equations. *J. Numer. Anal.*, 43:1231 – 1255, 2005.

[61] A. Rahunanthan and D. Stanescu. Stable interface conditions for discontinuous Galerkin approximations of Navier-Stokes equations. *J. Sci. Comput.*, 41:118 – 138, 2009.

[62] A. P. Calderon. Boundary-value problems for elliptic equations. In *Soviet-American Conference on Partial Differential Equations at Novosibirsk, Moscow, Fizmatgiz*, pages 303 – 304, 1963.

[63] A. Dedner et al. Transparent boundary conditions for MHD simulations in stratified atmospheres. *J. Comput. Phys.*, 171:448 – 478, 2001.

[64] M. Faganello et al. Being on time in magnetic reconnection. *New J. Phys.*, 11:1 – 25, 2009.

[65] T. G. Forbes and E. R. Priest. A comparison of analytical and numerical models for steadily driven magnetic reconnection. *Rev. Geophys.*, 25:1583 – 1607, 1987.

[66] K. G. Powell et al. An upwind scheme for magnetohydrodynamics. In K. W. Morton and M. J. Baines, editors, *Numerical Methods for Fluid Dynamics V*, pages 163 – 180, 1995.

[67] LAPACK (Linear Algebra PACKage). www.netlib.org/lapack/.

[68] P. L. Roe. Approximate Riemann solvers, parameter vectors, and difference schemes. *J. Comput. Phys.*, 43:357 – 372, 1981.

[69] G. W. Hedstrom. Nonreflecting boundary conditions for nonlinear hyperbolic systems. *J. Comput. Phys.*, 30:222 – 237, 1979.

[70] R. Courant and D. Hilbert. *Methods of Mathematical Physics, Volume II*. Wiley, 1962.

[71] R. W. Fox and A. T. McDonald. *Introduction to Fluid Mechanics*. Wiley, 1992. Fourth edition.

[72] J. Slough. Personal communication.

[73] G. J. Marklin. Personal communication.

[74] E. Choueiri. Lorentz force accelerator with an open-ended lithium heat pipe. *AIAA-96-2737, Proceedings of the 32nd AIAA Joint Propulsion Conference, Lake Buena Vista, FL, July 1996*.

[75] V. S. Lukin et al. Numerical modeling of magnetohydrodynamic activity in the Swarthmore Spheromak Experiment. *Phys. Plasmas*, 8:1600 – 1606, 2001.

[76] T. R. Jarboe. Review of spheromak research. *Plasma Phys. Control. Fusion*, 36:945 – 990, 1994.

[77] T. D. Rognlien. Understanding of edge plasmas in magnetic fusion energy devices. *Plasma Phys. Control. Fusion*, 47:A283 – A295, 2005.

[78] T. D. Rognlien and M. E. Rensink. Edge-plasma models and characteristics for magnetic fusion energy devices. *Fusion Eng. Design*, 60:497 – 514, 2002.

[79] D. E. Post. A review of recent developments in atomic processes for divertors and edge plasmas. *J. Nucl. Mater.*, 220:143 – 157, 1995.

[80] R. J. Goldston and P. H. Rutherford. *Introduction to Plasma Physics*. IOP Publishing Ltd., 1995.

[81] V. Soukhanovskii et al. Supersonic gas injector for fueling and diagnostic applications on the National Spherical Torus Experiment. *Rev. Sci. Instrum.*, 75:4320 – 4323, 2004.

[82] S. You. *Computational and Experimental Studies of Tokamak Refuelling*. PhD thesis, Imperial College, 2002.

[83] R. W. Schunk and R. W. Nagy. *Ionospheres*. Cambridge, 2000.

[84] H. L. Pauls, G. P. Zank, and L. L. Williams. Interaction of the solar wind with the local interstellar medium. *J. Geophys. Research*, 100:21,595 – 21,604, 1995.

[85] V. B. Baranov. Gasdynamics of the solar wind interaction with the interstellar medium. *Space Sci. Rev.*, 52:89 – 120, 1990.

[86] T. V. Zaqarashvili, M. L. Khodachenko, and H. O. Rucker. Magnetohydrodynamic waves in solar partially ionized plasmas: two-fluid approach. *Astron. Astrophys.*, 529:A82–1 – A82–9, 2011.

[87] U. Shumlak. Physical model for a three-component, reacting plasma (ions, electrons and neutrals). Private communication, 2009.

[88] E. T. Meier. Developing and Benchmarking MH4D, a Tetrahedral Mesh MHD Code. Master's thesis, University of Washington, 2008.

[89] T. D. Rognlien et al. A fully implicit, time dependent 2-D fluid code for modeling tokamak edge plasmas. *J. Nucl. Mater.*, 196:347 – 351, 1992.

[90] T. D. Rognlien et al. Self-consistent simulation of turbulence and transport in tokamak edge plasmas. *Contrib. Plasma Phys.*, 44:188 – 193, 2004.

[91] R. Schneider et al. B2-EIRENE simulation of ASDEX and ASDEX-upgrade scrape-off layer plasmas. *J. Nucl. Mater.*, 196:810 – 815, 1992.

[92] R. Schneider et al. Plasma edge physics with B2-Eirene. *Contrib. Plasma Phys.*, 46:3 – 191, 2006.

[93] D. Stotler and C. Karney. Neutral gas-transport modeling with DEGAS-2. *Contrib. Plasma Phys.*, 34:392 – 397, 1994.

[94] The EIRENE code, Version Jan. 92, User manual, KFS Jülich report JUEL-2599 (Mar. 1992), and www.eirene.de.

[95] X. Q. Xu et al. Low-to-high confinement transition simulations in divertor geometry. *Phys. Plasmas*, 7:1951 – 1958, 2000.

[96] V. A. Izzo et al. Magnetohydrodynamic simulations of massive gas injection into Alcator C-Mod and DIII-D plasmas. *Phys. Plasmas*, 15:056109, 2008.

[97] V. A. Izzo et al. DIII-D and ITER rapid shutdown with radially uniform deuterium delivery. *Plasma Phys. Contr. Fusion*, 51:105004, 2009.

[98] P. Helander, S. I Krasheninnikov, and P. J. Catto. Fluid equations for a partially ionized plasma. *Phys. Plasmas*, 1:3174 – 3180, 1994.

[99] G. P. Zank. Interaction of the solar wind with the local interstellar medium: A theoretical perspective. *Space Sci. Rev.*, 89:413 – 688, 1993.

[100] V. B. Baranov and Y. G. Malama. Model of the solar wind interaction with the local interstellar medium: Numerical solution of self-consistent problem. *J. Geophys. Res.*, 98:15157 – 15163, 1993.

[101] S. Chapman and T. G. Cowling. *The Mathematical Theory of Non-Uniform Gases.* Cambridge, 1970. Third edition.

[102] H. W. Ripken and H. J. Fahr. Modification of the local interstellar gas properties in the heliospheric interface. *Astron. and Astrophys.*, 122:181 – 192, 1983.

[103] J. A. Bittencourt. *Fundamentals of Plasma Physics.* Permagon, 1986.

[104] M. Goosens. *An Introduction to Plasma Astrophysics and Magnetohydrodynamics.* Kluwer, 2003.

[105] H. Alfvén. *On the Origin of the Solar System.* Oxford Univ. Press, New York, 1954.

[106] S. S. Russell. The formation of the Solar System. *J. Geol. Soc. London*, 164:481 – 492, 2007.

[107] N. Brenning. Review of the CIV phenomenon. *Space Science Reviews*, 59:200 – 314, 1992.

[108] S. T. Lai. A review of critical ionization velocity. *Rev. of Geophys.*, 39:471 – 506, 2001.

[109] A. G. Sgro and C. W. Nielson. Hybrid model studies of ion dynamics and magnetic field diffusion during pinch implosions. *Phys. Fluids*, 19:126 – 133, 1975.

[110] J. Loverich and U. Shumlak. Nonlinear full two-fluid study of m=0 sausage instabilities in an axisymmetric Z-pinch. *Phys. Plasmas*, 13:082310, 2006.

[111] A. Hakim and U. Shumlak. Two-fluid physics and field-reversed configurations. *Phys. Plasmas*, 14:055911, 2007.

[112] Electrodeless Lorentz Force Thruster program. www.aa.washington.edu/research/plasmaDynamics/elf.html.

[113] T.-F. Chang, H. U. Rahman, and R. S. White. Laboratory simulation of neutral gas ionization. *J. Geophys. Res.*, 94:5533 – 5538, 1989.

[114] U. Yusupaliev. Stoletov constant and effective ionization potential of a diatomic gas molecule. *B. Lebedev Phys. Inst.*, 34:334 – 339, 2007.

[115] A. M. Peter. *Paramagnetic spin-up of a field reversed configuration with rotating magnetic field current drive.* PhD thesis, University of Washington, 2003.

[116] C. L. Deards. *Factors affecting ion spin-up in the Translation, Confinement and Sustainment Upgrade Experiment.* PhD thesis, University of Washington, 2010.

[117] K. E. Miller et al. The TCS Upgrade: Design, construction, conditioning, and enhanced RMF FRC performance. *Fusion Sci. Tech.*, 54:946 – 961, 2008.

[118] J. Jin. *The Finite Element Method in Electromagnetics.* Wiley, 2002.

[119] J. W. Berkery. *Current Sheet Mass Leakage in a Pulsed Plasma Accelerator.* PhD thesis, Princeton University, 2005.

[120] R. D. Milroy. A numerical study of rotating magnetic fields as a current drive for field reversed configurations. *Phys. of Plasmas*, 6:2771 – 2780, 1999.

[121] C. Redwine. *Upgrading to Fortran 90.* Springer, 1995.

[122] Subversion revision control software. http://subversion.apache.org/.

[123] VisIt visualization tool. https://wci.llnl.gov/codes/visit/.

[124] S. Abarbanel and D. Gottlieb. Optimal time splitting for two- and three-dimensional Navier-Stokes equations with mixed derivatives. *J. Comput. Phys.*, 41:1 – 33, 1981.

[125] L. J. Maher and B. A. Tinsley. Atomic hydrogen escape rate due to charge exchange with hot plasmaspheric ions. *J. Geophys. Research*, 82:689 – 695, 1977.

[126] W. L. Fite, A. C. H. Smith, and R. F. Stebbings. Charge transfer in collisions involving symmetric and asymmetric resonance. *Proc. Royal Soc. London A*, 268:527 – 536, 1962.

[127] D. T. Hall. *Ultraviolet resonance radiation and the structure of the heliosphere.* PhD thesis, University of Arizona, 1992.

[128] C. F. Barnett. *Atomic Data for Fusion, Vol. 1.* Oak Ridge National Laboratory, 1990.

[129] B. M. Smirnov. *Physics of Atoms and Ions*. Springer, 2003.

[130] G. S. Voronov. A practical fit formula for ionization rate coefficients of atoms and ions by electron impact: Z=1-28. *Atomic Data Nucl. Data*, 65:1 – 35, 1997.

[131] R. W. P. McWhirter. Spectral intensities. In R. H. Huddlestone and S. L. Leonard, editors, *Plasma Diagnostic Techniques*. Academic Press, New York, 1965.

[132] J. D. Huba. NRL Plasma Formulary, 2004. http://wwwppd.nrl.navy.mil/nrlformulary/.

[133] P. J. Catto. A short mean-free path, coupled neutral-ion transport description of a tokamak edge plasma. *Phys. Plasmas*, 1:1936 – 1943, 1994.

[134] D. A. Ennis et al. New understandings and achievements from independent-injector drive experiments on HIT-SI. *Nucl. Fusion*, 50:072001, 2010.

Appendix A

USING HIFI

This appendix presents some practical details for using HiFi [1, 2, 3]. The steps necessary to acquire 2D HiFi (SEL) are given in Section A.1. Running a simulation with pn.f, the physics module containing specifications for the plasma-neutral model presented in Chapter 5.3, is described in Section A.2. Finally, post-processing, and visualizing the simulation results is explained in Section A.3. This appendix is intended to serve as a rough guide for new users of the 2D HiFi code, although it may provide some useful insight for non-users.

HiFi is written in Fortran 90/95, and users should be familiar with modern Fortran programming to use the code. An especially useful Fortran reference is the book by Redwine [121].

A.1 Acquiring HiFi

A.1.1 User agreement

The user agreement for HiFi is given in Figure A.1. The principal developers of HiFi are Dr. Vyacheslav (Slava) Lukin and Dr. Alan Glasser. By sending the signed agreement to Dr. Lukin at vlukin1(at)mailaps.org, a user name and password can be obtained for the online code repository. Note that this dissertation has focused on the 2D version of HiFi. 3D HiFi is also available from the same developers.

A.1.2 Code versions and repository structure

HiFi is stored in a Subversion [122] repository. At the time of this writing, the current repository version is 378.

The 2D HiFi (SEL) repository includes the "trunk" code (SEL/trunk)and "branches" (SEL/branches). In the research presented in this dissertation, two different branches are used: SEL/branches/obc and SEL/branches/neutrals. Within the folder SEL/trunk, mul-

SEL code development project, up to version 2.3
Copyright (c) 2002-2007, Los Alamos National Laboratory.
HiFi (also known as SEL) code development project, versions 2.3-3.1
Copyright (c) 2007-2009, University of Washington.
Copyright (c) 2010-2011, University of Washington & Naval Research Laboratory.
Written by HiFi team with Vyacheslav S. Lukin and Alan H. Glasser as principle developers.
All rights reserved.

HiFi (SEL) User Agreement Form

HiFi (SEL) is an open source code development project for solving systems of coupled non-linear PDEs on (semi-)structured logically hexahedral (rectangular) grids that abides by the following BSD-style license. The project has been supported, in part, by the U.S. Department of Energy. Before having access to the code, you must agree to the conditions of the license that serve as additional protections for the HiFi (SEL) code.

Terms of Agreement

Redistribution and use in source and binary forms, with or without modification, are permitted provided that the following conditions are met:

1) Redistributions of source code must retain the above copyright notice, this list of conditions and the following disclaimer.
2) Redistributions in binary form must reproduce the above copyright notice, this list of conditions and the following disclaimer in the documentation and/or other materials provided with the distribution.
3) Neither the name of the project nor the names of its developers may be used to endorse, promote, or publish products derived from this software without specific prior written permission by one of the principle developers.
4) Publications or figures made using results of the HiFi (SEL) code calculations will acknowledge the HiFi (SEL) code.
5) It is understood that the HiFi (SEL) code is still under development and thus may not contain all features that users may need/want for their problem of interest.
6) It is understood that the HiFi (SEL) project does not guarantee that support will always be available to users of the code. In addition, it is understood that extensive support from a HiFi (SEL) team member on a particular application generally implies that any publication derived from the application will include that team's member(s) as a co-author.

THIS SOFTWARE IS PROVIDED BY *HiFi team* "AS IS" AND ANY EXPRESS OR IMPLIED WARRANTIES, INCLUDING, BUT NOT LIMITED TO, THE IMPLIED WARRANTIES OF MERCHANTABILITY AND FITNESS FOR A PARTICULAR PURPOSE ARE
DISCLAIMED. IN NO EVENT SHALL *neither any HiFi team member, nor the University of Washington, nor the United States Government, nor any agency thereof, nor any of their employees* BE LIABLE FOR ANY DIRECT, INDIRECT, INCIDENTAL, SPECIAL, EXEMPLARY, OR CONSEQUENTIAL DAMAGES (INCLUDING, BUT NOT LIMITED TO, PROCUREMENT OF SUBSTITUTE GOODS OR SERVICES; LOSS OF USE, DATA, OR PROFITS; OR BUSINESS INTERRUPTION) HOWEVER CAUSED AND ON ANY THEORY OF LIABILITY, WHETHER IN CONTRACT, STRICT LIABILITY, OR TORT (INCLUDING NEGLIGENCE OR OTHERWISE) ARISING IN ANY WAY OUT OF THE USE OF THIS SOFTWARE, EVEN IF ADVISED OF THE POSSIBILITY OF SUCH DAMAGE.

If you agree to the above terms and would like to download and/or use the HiFi (SEL) code, please fill out this form and e-mail it to Vyacheslav Lukin at **vlukin1@mailaps.org**.

HiFi (SEL) Agreement form

Name: _____

Organization: _____

Mailing Address: _____

Mailing Address: _____

Email Address: _____

Requested username for Web access: _____

Any comments or special requests:

I agree to the above Terms of Agreement and certify that the information submitted in the form is true.

NAME: _____

DATE: _____

Figure A.1: HiFi user agreement.

tiple versions of SEL may be present, e.g., "code_3.0.0", and "code_3.1". The latest version is "code_3.1", and it is this version that is the basis for the code used for this dissertation which is present in SEL/branches/open_bc/code_3.1 and SEL/branches/neutrals/code_3.1.

As discussed in Section 1.3, the core solver routines are separate from the "physics" module where PDEs to be solved are specified. As an example of how to use HiFi, the focus of this appendix is on the file pn.f. This file is present in the directory SEL/branches/neutrals/code_3.1. The core solver code is in the directory SEL/branches/neutrals/code_3.1/solver.

In SEL/trunk, the folder "post" contains the postprocessing code which will be discussed below.

In SEL/trunk, there is a file called README which has some details about the code organization and compiling the code. Further details will be available upon receiving access to the code.

A.2 Running a plasma-neutral simulation

In this section, relevant details for running a simulation with the HiFi physics module pn.f are given, including: input deck (Section A.2.1); normalizations (Section A.2.2); grid (Section A.2.3); variables and equations (Section A.2.4); equilibrium (Section A.2.5); boundary conditions (Section A.2.6); and interpreting runtime output (Section A.2.7).

Several subroutines in pn.f will be referred to by name. Each subroutine in pn.f has some comments about its function. Also, see the file the physics module template file, physics_templ.f, in SEL/trunk/code_3.1 for additional comments on individual physics module subroutines.

A.2.1 Input deck

The following commented input deck is used to conduct the baseline ELF simulation described in Section 6.4. Note that all of the options are not listed and commented. Default values are used for those not listed. See the file README discussed in Section A.1.2 for an input deck with all options commented for `algorithm_input` and `universal_input`.

```
&algorithm_input
solve_type="condense"   ! use static condensation
step_type="theta"       ! theta method for time advance
theta=.5                ! theta=.5 --> Crank-Nicolson

adapt_dt=t              ! use adaptive time step
errtol=1.e-4            ! tolerance for nonlinear solve
ksp_restart=30
always_pc_reset=t

itmax=140               ! maximum number of newton iterations
itmax_incr=3            ! increase time step if fewer iterations
itmax_decr=7            ! decrease time step if more iterations
dt_incr=1.2             ! factor of time step increase
dt_decr=.6              ! factor of time step decrease

nodal=f                 ! use modal basis

quad_type="gl0"
grid_type="sel"
grid_inv_type="jacobi"

adapt_grid=f

monitor=t
fd_test=f
fd_bound_test=f
du_diagnose=f

outfile_type="hdf5"
parallel_write=t
parallel_read=f
/
```

```
&universal_input
dmout=10                ! write out solution every 10 steps
outdir="results/elf_BL" ! output directory

restart_flag=t          ! restart from earlier run
restart_dir="results/elf_BL_eq"
                        ! restart directory
restart_step=100        ! restart step
/

&pn_list
nx=72                   ! 72 cells in the axial direction
ny=8                    ! 8 cells in the radial direction
nbx=12                  ! split grid into 72/12=6 axial blocks;
                            ! the number of processors used must be divisible
                            ! by nbx.
np=8                    ! polynomial degree 8
nq=8                    ! 8 quadrature points (in a rectangular
                        ! grid, np=nq gives exact integration)
xperiodic=t             ! periodic in axial direction
yperiodic=f             ! not periodic in radial direction

dt=5.e-4                ! initial time step size
dtmax=5.e-3             ! maximum time step size
tmax=5.                 ! maximum time
nstep=10000             ! maximum number of time steps

init_type="trans_test"  ! run a "trans_type" simulation
cylinder=t              ! cylindrical coordinates

equilfile="frc_long.dat"! the equilibrium file name
```

```
xmin=-5.32              ! minimum axial position
lx=15.96                ! total axial extent
ly=1.                   ! total radial extent
                        ! in physical units (after multiplying by L0),
                        ! the domain extends axially from  -0.625 meters
                        ! to +1.625 meters.
                        ! the FRC is initially centered at x=0.


L0=.141                 ! length normalization
n0=7.e19                ! density normalization
b0=.012                 ! magnetic field normalization


atom="neon"             ! neon neutral gas and plasma


ddiff=2.e-3             ! density diffusion


eta_case="spitzer-chodura"
                        ! spitzer-chodura resistivity
etavac=2.               ! maximum resistivity


visc_case="braginskii"  ! braginskii (isotropic) plasma viscosity
mu_min=5.e-3            ! minimum viscosity
mu_sv=1.e-3            ! artificial viscosity


viscn_case="hard_sphere"! hard sphere neutral viscosity


kappa_case="braginskii" ! braginskii plasma thermal conduction
kappa_min=1.e-2         ! minimum plasma thermal conduction


kappan_case="hard_sphere"
                        ! hard sphere neutral thermal conduction


initv=3.7               ! initial axial speed
```

```
pmin=5.e-5                  ! minimum initial pressure
rhomin=.005                 ! minimum initial density

initrhon=10.                ! initial peak neutral density
initTn=.0025                ! initial neutral temperature

targ_type="gauss"           ! gaussian neutral gas profile

ion_fac=1.                  ! ionization factor (1 --> on; 0 --> off)
recomb_fac=1.               ! recombination factor (1 --> on; 0 --> off)
cx_fac=1.                   ! charge exchange factor (1 --> on; 0 --> off)
civ_fac=0.                  ! CIV factor (>1 --> on; 0 --> off)

te_frac=.5                  ! fraction of plasma pressure in electron species
/
```

A.2.2 Normalizations

To avoid issues related to computer round-off error, working in normalized units is recommended. PDEs implemented in HiFi are typically normalized. For the plasma-neutral module, pn.f, normalizations are given in Table A.1.

By multiplying the normalized quantity by the normalization, the value in physical units is found. For example, to determine the density in SI units, the normalized density ($\tilde{\rho}$) is multiplied by the density normalization constant: $\rho = \tilde{\rho}\rho_0$. As shown in Table A.1, $\rho_0 = n_0 m_i$. A spreadsheet is recommended to facilitate conversions and, effectively, comprehension of code input/output.

As an example of normalization, consider the plasma continuity equation,

$$\frac{\partial \rho}{\partial t} + \nabla \cdot (\rho \mathbf{v} - D_\rho \nabla \rho) = m_i(\Gamma_i^{ion} - \Gamma_n^{rec}),$$

which is Eqn. (5.70) of Section 5.3. The normalized equation is

Table A.1: Normalizations for plasma-neutral simulation. The quantities used as the normalization basis are density, magnetic field, and length (n_0, B_0, and L_0) in SI units. Normalizations are given in SI units except for temperature which is given in electron volts. The quantities q_e, μ_0, and k_B are the elementary charge, permeability of free space, and Boltzmann constant, respectively: $q_e = 1.601 \times 10^{-19}$ C, $\mu_0 = 4\pi \times 10^{-7}$ T m/A, and $k_B = 1.381 \times 10^{-23}$ J/K.

normalization	definition	units
ρ_0	$n_0 m_i$	kg / m^3
p_0	B_0^2/μ_0	Pa
T_0	$B_0^2/(\mu_0 q_e n_0)$	eV
A_0	$L_0 B_0$	T m
v_0	$B_0/\sqrt{\mu_0 n_0 m_i}$	m/s
j_0	$B_0/(L_0 \mu_0)$	A/m^2
t_0	$L_0\sqrt{\mu_0 n_0 m_i}/B_0$	s
$D_{\rho,0}$	L_0^2/t_0	m^2/s
η_0	$\mu_0 L_0^2/t_0$	Ω m
ξ_0	$\rho_0 L_0^2/t_0$	Pa s
κ_0	$n_0 k_B L_0^2/t_0$	W/(m K)

$$\frac{\partial \tilde{\rho}}{\partial \tilde{t}} + \tilde{\nabla} \cdot (\tilde{\rho}\tilde{\mathbf{v}} - \tilde{D}_\rho \tilde{\nabla} \tilde{\rho}) = \tilde{\Gamma}_i^{ion} - \tilde{\Gamma}_n^{rec}, \tag{A.1}$$

where the normalized quantities are accented with tildes. The atomic physics source rates are normalized such that, for example, $\tilde{\Gamma}_i^{ion}\Gamma_0 = \Gamma_i^{ion}m_i$, where $\Gamma_0 = \rho_0/t_0$. Source rates have units of kg/(m^{3}s). In pn.f, the variables `recomb_norm`, `ion_norm`, and `cx_norm` are defined such that the normalized quantities are computed as simple functions of normalized variables. For ionization,

$$
\begin{aligned}
\tilde{\Gamma}_i^{ion} &= \Gamma_i^{ion}m_i/\Gamma_0 \\
&= A \times 10^{-6} \frac{1 + P*(\phi_{ion}/T_e)^{1/2}}{X + \phi_{ion}/T_e} \left(\frac{\phi_{ion}}{T_e}\right)^K e^{-\phi_{ion}/T_e} n n_n \frac{m_i}{\Gamma_0} \\
&= A \times 10^{-6} \frac{1 + P*(\phi_{ion}/T_e)^{1/2}}{X + \phi_{ion}/T_e} \left(\frac{\phi_{ion}}{T_e}\right)^K e^{-\phi_{ion}/T_e} \tilde{\rho}\tilde{\rho}_n n_0 t_0 \\
&= \texttt{ion\_norm} \frac{1 + P*(\phi_{ion}/T_e)^{1/2}}{X + \phi_{ion}/T_e} \left(\frac{\phi_{ion}}{T_e}\right)^K e^{-\phi_{ion}/T_e} \tilde{\rho}\tilde{\rho}_n.
\end{aligned}
\tag{A.2}
$$

The formula used for Γ_i^{ion} involves the constants A, P, X, and K, as discussed in Appendix D. Notice that the quantity $\texttt{ion\_norm} = A \times 10^{-6} n_0 t_0$ is an accumulation of constants so that $\tilde{\Gamma}_i^{ion}$ is a simple function of the dimensionless quantity ϕ_{ion}/T_e, and the normalized variables ρ and ρ_n. Constants are similarly accumulated for viscosities, thermal conductivities, and resistivity.

A.2.3   Grid

In the subroutine physics_grid, the input arguments are `ksi` and `etag`, the logical coordinates of the quadrature points within a given cell. The output arguments are `x` and `y`, the (normalized) physical coordinates for the axial and radial directions, respectively, within the cell. The arrays of each of these arguments have two indices; the first is the axial index and the second is the radial index. For example, in a square cell, `x(1,1)=x(1,2)=x(1,3)`, etc., and `y(1,1)=y(2,1)=y(3,1)`, etc.

Simulations in cylindrical or cartesian coordinates can be run with the pn.f module. The comments in this appendix address simulations in cylindrical coordinates, where the $r - z$ plane is discretized. In pn.f, "**x**" corresponds to the axial direction, and "**y**" to the radial direction.

The physics_grid subroutine is called cell-by-cell, as are all of the other pn.f subroutines discussed in this appendix. So, for example, locally computing the maximum value of **x** will not necessarily give the maximum value of the global logical space (which is one).

A.2.4   Variables and equations

In all 2D HiFi (SEL) physics modules, the subroutine "physics_rhs" is where flux and source terms are specified for the interior equations. The module pn.f has 10 variables. As indicated in the comments there, the variables are

1. Plasma density, ρ

2. Negative phi-direction magnetic vector potential, $-A_\phi$

3. Plasma pressure, p

4. Plasma axial momentum, ρv_z

5. Plasma radial momentum, ρv_r

6. Out-of-plane current density, j_ϕ

7. Neutral density, ρ_n

8. Neutral axial momentum, $\rho_n v_{z,n}$

9. Neutral radial momentum, $\rho_n v_{r,n}$

10. Neutral pressure, p_n

In this list and in pn.f, normalized variables are implied and the tilde accents are dropped.

The variable j_ϕ is an auxiliary variable in the sense that it is not a primary variable evolved in the equations presented in Section 5.3. Fluxes and sources can be functions of only the variables and their first spatial derivatives. To compute the source term ηj_ϕ^2 in the pressure evolution equation (see Section 5.3), the presence j_ϕ as an auxiliary variable is necessary.

The first index of the variables is the variable number as given in the list above. The second and third indices are the axial and radial positions of the quadrature points, corresponding to the first and second indices in the grid variables (see Section A.2.3).

Jacobians (i.e., derivatives with respect to the variables) of the fluxes and sources are required, and are computed in the subroutine physics_rhs_drdu.

The mass matrix for the interior equations is set in the subroutine physics_mass. The default values of the mass matrix are set to one for the diagonal entries (i.e., `mass(1,1,:,:)`, `mass(2,2,:,:)`, etc.). For most of the variables in pn.f, the mass matrix diagonal entries are changed to `r_fac`, which is a factor equal to the radial distance at each quadrature point. This factor is used to cancel the $1/r$ that occurs in the divergence in cylindrical coordinates.

A.2.5   Equilibrium

In the subroutine physics_init, the solution is initialized. Input arguments are `x` and `y`, which are arrays of axial and radial quadrature point physical coordinates, respectively. The output argument is `u`, which has three indices: the first refers to variable number, the second to the axial position, and the third to the radial position.

The case "trans_test" first calls pn_equil, which reads in an FRC equilibrium from the file specified in sel.in with the variable `equilfile`. Next, the initial axial speed is set, and the neutral density profile is initialized as described in Section 6.4.

A.2.6   Boundary conditions

The subroutine physics_boundary sets the boundary condition (BC) types for each equation. The subroutine has arguments `left`, `right`, `top`, and `bottom`, which are `edge_type` variables corresponding, respectively, to the boundaries at the minimum axial position, and maximum axial position, radial wall, and the cylindrical axis.

Within the `edge_type` derived type, there is a character variable `bc_type`, and a logical variable `static`. The variables `bc_type` and `static` are arrays with entries for each variable (10 variables in the case of pn.f). As described in Section 1.3.3, BC are either flux BC or explicit local BC. For the "trans_test" case, two flux BC types are used: "normflux" and "zeroflux". As the names imply, "normflux" allows the normal flux at the boundary to be specified and "zeroflux" sets the normal flux to zero. The explicit local BC "robin" is also used, requiring the solution to satisfy a specified boundary equation. See the boundary conditions discussion in Section 6.4.1. The variable static is set to true for all variables except for the second variable, $-A_\phi$, at the radial wall. Setting static to false indicates that a time-dependent term may be used in the robin BC. See discussion of physics_edge_mass below. Time-variation of $-A_\phi$ represents a voltage applied at the wall as discussed in Section 6.4.1.

In the subroutine physics_edge_rhs, the output argument `c` is set either to the flux for "normflux" BCs, or to the right-hand side for "robin" BCs, where the left-hand side is zero if the variable `static` is true, and is a time varying term if `static` is false. The Jacobian of these boundary equations (i.e., the derivative of `c` with respect to each variables) is set in the subroutine physics_edge_drdu.

The subroutine physics_edge_mass sets the mass matrix for the time-varying terms of the "robin" boundary equations for which the variable `static` is false. As mentioned above, for the variable $-A_\phi$, the mass matrix entry is set to one.

A.2.7   Interpreting runtime output

At runtime, an output file called sel.out is generated. An excerpt of SEL.out for the ELF baseline run for which the input deck is shown in Section A.2.7 follows.

```
---------------------------------------------------------------------
physics = pn, step_type = theta, nproc =     48, nbx =   12
xper = T, yper = F, nx =   72, ny =    8, np = 8, nq = 8
solve_type = condense
```

iout	m	it	jac	ksp	t	dt	wclock	griderr	condno
0	100	0	0	0	5.000E-02	5.00E-04	4.25E+00	6.73E-03	0.000E+00
1	110	67	6	67	5.300E-02	3.00E-04	1.03E+02	6.28E-03	1.000E+00
2	120	38	4	38	5.663E-02	5.18E-04	6.75E+01	1.13E-02	1.000E+00
3	130	40	5	40	6.308E-02	1.07E-03	8.21E+01	3.43E-02	1.000E+00
4	140	44	3	44	7.830E-02	1.55E-03	5.39E+01	6.08E-02	1.000E+00
5	150	53	3	53	9.595E-02	1.86E-03	5.57E+01	3.60E-02	1.000E+00
6	160	53	2	53	1.145E-01	1.86E-03	4.11E+01	4.48E-02	1.000E+00
7	170	55	2	55	1.331E-01	1.86E-03	4.17E+01	7.22E-02	1.000E+00
8	180	55	2	55	1.517E-01	1.86E-03	4.15E+01	5.93E-02	1.000E+00
9	190	56	3	56	1.702E-01	1.86E-03	5.85E+01	3.15E-02	1.000E+00
10	200	60	2	60	1.888E-01	1.86E-03	4.24E+01	4.29E-02	1.000E+00

The header of sel.out reflects some of the input deck options (see Section A.2.1). Also, the number of processors used for the run is shown as *nproc*. In this case, 48 processors are used. Each row of data is written when the code writes output files containing the solution data in terms of basis function amplitudes in each cell. The column labeled *iout* indicates the output number; *m* indicates the step number; *it*, the number of nonlinear iterations required; *jac*, the number of Jacobians required during the nonlinear solve; *ksp*, the number of Krylov space solver iterations required (in this case, a direct LU solver is used and *ksp=it*); *t*, the time; *dt*, the time step size; *wclock*, the wall clock time required since the last data output; *griderr*, the grid error;[1] and *condno*, the condition number for the iterative linear solver (it is one in this case because a direct LU solver is used).

---

[1]Grid error is a measure of how well-converged the spectral representation is. *griderr* reports the worst grid error for all variables in all cells. More specifically, *griderr* is a comparison of the amplitude of the highest-order basis function to the overall magnitude of the variable.

A.3   Post-processing and visualizing HiFi output

Post-processing is done using the code called "post" in the repository folder SEL/trunk/post. Post-processing is done serially. When the post code is executed, it retrieves the post.in input deck. The following post.in file can be used to produce output appropriate for viewing the ELF baseline run with the VisIt [123] visualization tool. (See also the file post.in in SEL/trunk/code_3.1.)

```
&post_input

indir="results/elf_BL"  ! directory containing output files
postout="visit"         ! directory that output should be written to
out_type="hdf5"         ! output type; hdf5 output can be read by VisIt

job_type="." ! setting job_type to "." gives the default output
                        ! specialized post-processing is possible but generally
                        ! requires customized code.

nxw0=10                 ! the number of interpolary points
nyw0=10

drawgrid=f
polar_crd=f

mfile=1000
stride=10

contour=t
/

&post_input
xt_flag=f               ! this flag can be set to true to generate 1D plots
                            ! in the "x" direction at various times at fixed
                            ! "y" position which are viewable with the xdraw
```

```
                              ! software (consult HiFi developers for more information)
yt_flag=f               ! see comment for xt_flag
/
```

After post-processing using the above input deck, .hdf5 files will be present in the directory "visit" along with .xmf files which contain the information necessary for VisIt to access the data in the .hdf5 files.[2] By opening the the family of .xmf files with VisIt, a variety options will be available, including contour plots, pseudocolor plots, etc. The variables are numbered as in the list given in Section A.2.4 — for example, the first variable, density, is read into VisIt as "U01". The second variable is represented by U02, etc.

---

[2]HiFi developers currently recommend VisIt version 2.2.0.

Appendix B

DERIVATION AND DISCUSSION OF ARTIFICIAL VISCOSITY

HiFi is a spectral element code and is subject to spurious oscillations if any of the dependent variables are not properly resolved. In many realistic applications of dissipative MHD, strong gradients (or shocks) can develop. If sufficient spatial resolution is made available near the gradient, the standard dissipative terms (derived by a Chapman-Enskog-like procedure) are sufficient to smooth the solution. In practice, it may be computationally impractical to provide enough spatial resolution everywhere in the domain. Artificial viscosity can be useful to mitigate this problem by selectively applying an artificially high dissipation in regions with steep velocity gradients.

In a plasma or neutral momentum equation, a typical viscous flux term is $\pi = -\xi(\nabla \mathbf{v} + \nabla \mathbf{v}^\mathsf{T})$, where ξ is the viscosity coefficient. An artificial viscous flux, π_a, is introduced, which depends on the square of the gradient of velocity: $\pi_a = -2\xi_a \mathbb{I} \circ (|\nabla \mathbf{v}| \circ \nabla \mathbf{v})$. Here, ξ_a is a uniform coefficient, $|\cdot|$ indicates entrywise absolute value, and "$\circ$" indicates entrywise multiplication (also called the Hadamard product). The "$\mathbb{I}\circ$" operation limits the artificial dissipation to only compressional motion which causes shocks. Without the "$\mathbb{I}\circ$" operation, both compressional and shear motion would be dissipated. In the applications presented in this dissertation, artificial viscous damping of compressional motion provided the necessary damping; in other applications, the artificial damping of shear motions could be useful. The momentum equation becomes

$$\frac{\partial(\rho \mathbf{v})}{\partial t} + \nabla \cdot (\cdots + \pi + \pi_a) = 0, \tag{B.1}$$

where "$\cdots$" represents terms omitted for simplicity.

In the pressure evolution equation, kinetic energy evolution is removed from the total energy equation to ensure conservation of energy. The artificial viscosity term must be taken into account. To remove the kinetic energy, the momentum equation is dotted with

v to get an equation for kinetic energy evolution. Dotting Eqn. (B.1) with **v**,

$$\frac{\partial}{\partial t}\frac{\rho \mathbf{v}^2}{2} + \cdots = -\mathbf{v} \cdot (\nabla \cdot \pi_a). \tag{B.2}$$

The kinetic energy is subtracted, so the term that arises in the pressure equation due to artificial viscosity is $\mathbf{v} \cdot (\nabla \cdot \pi_a)$. This term can be rewritten as

$$\mathbf{v} \cdot (\nabla \cdot \pi_a) = \nabla \cdot (\mathbf{v} \cdot \pi_a) - \pi_a : \nabla \mathbf{v}. \tag{B.3}$$

Because the first term on the right-hand side of Eqn. B.3 is a divergence, it represents a redistribution of energy rather than a source of energy. Presumably this redistribution is small and localized near the shock. Therefore, it is excluded. The second term on the right-hand side is included as a source in the pressure equation.

Appendix C

ENERGY-ANALYSIS-BASED OPEN BC

As mentioned in Section 3.1, an energy analysis approach can be used as the basis of an open BC for mixed hyperbolic-parabolic systems. To perform an energy analysis, the system in question must be simultaneously symmetrized (see Gustaffson et al. [57], Ch. 4). The basic concept of an energy-analysis-based open BC (EOBC) is presented in Section C.1. The challenge of simultaneously symmetrizing MHD is discussed in Section C.2.

C.1   EOBC concept

EOBC are based on the concept of energy analysis to ensure well-posedness as described by Hesthaven and Gottlieb [59] and Nordström and Svärd [60]. Rahunanthan and Stanescu (R&S) [61] develop a discrete method for implementing well-posed interface/boundary conditions for modeling the Navier-Stokes equations with a discontinuous Galerkin approach. The one-dimensional scalar linear advection-diffusion problem is analyzed first, closely following R&S, as a simple analogy to the more complicated 2D nonlinear Navier-Stokes system. The equation and domain are

$$\frac{\partial w}{\partial t} + a\frac{\partial w}{\partial x} = \epsilon\frac{\partial^2 w}{\partial x^2} \ , x \in [-1,1]. \tag{C.1}$$

Energy analysis is now applied. Multiplying by w, and integrating over the domain,

$$
\begin{aligned}
\frac{1}{2}\frac{d\|w\|^2}{dt} &= \int_{-1}^{1} \epsilon ww_{xx}dx - \int_{-1}^{1} aww_xdx \\
&= \epsilon\int_{-1}^{1}\left[\frac{d}{dx}(ww_x) - w_x^2\right]dx - \int_{-1}^{1} aww_xdx \\
&= \left(\epsilon ww_x - \frac{a}{2}w^2\right)_{x=1} - \left(\epsilon ww_x - \frac{a}{2}w^2\right)_{x=-1} - \epsilon\|w_x\|^2,
\end{aligned}
\tag{C.2}
$$

where $\|w\|^2 = \int_{-1}^{1} w^2dx$ is the norm of the solution. The idea with EOBC is to provide sufficient conditions at the boundaries that the solution norm does not increase or grows

slowly. In the last line of Eqn. (C.2), the last term is always negative or zero, so it does not contribute to growth of the norm. If $a > 0$, a constant or decreasing solution norm can be assured by implementing $w = 0$ at $x = -1$, and $w_x = 0$ at $x = 1$.[1]

R&S extend the approach to a 2D system of the form

$$\frac{\partial \mathbf{Q}}{\partial t} + \nabla \cdot \mathbb{F} = \nabla \cdot \mathbb{F}^\nu, \tag{C.3}$$

where $\mathbf{Q}$ is the vector of dependent variables, $\mathbb{F}$ is the advective flux vector, and $\mathbb{F}^\nu$ is the dissipative flux vector. The flux vectors are

$$\mathbb{F} = (\mathbb{A}_x \mathbf{Q} \hat{x}, \ \mathbb{A}_y \mathbf{Q} \hat{y})$$

$$\mathbb{F}^\nu = \left[\left(\mathbb{B}_{xx} \frac{\partial \mathbf{Q}}{\partial x} + \mathbb{B}_{xy} \frac{\partial \mathbf{Q}}{\partial y} \right) \hat{x}, \ \left(\mathbb{B}_{yx} \frac{\partial \mathbf{Q}}{\partial x} + \mathbb{B}_{yy} \frac{\partial \mathbf{Q}}{\partial y} \right) \hat{y} \right].$$

After linearization[2], both Navier-Stokes and dissipative MHD can be written in this form. To carry out an energy analysis, the $\mathbb{A}$ and $\mathbb{B}$ matrices must be *simultaneously* symmetric. The possibility of simultaneous symmetrizing MHD is discussed in Section C.2. Assuming simultaneously symmetrized matrices, an energy analysis similar to that shown for the advection-diffusion case yields

$$\frac{1}{2} \frac{d\|\mathbf{Q}\|^2}{dt} = \oint_S \mathbf{Q}^\mathsf{T} \hat{\mathbf{n}} \cdot \left(-\frac{1}{2} \mathbb{F} + \mathbb{F}^\nu \right) dS - \int_V \nabla \mathbf{Q}^\mathsf{T} \cdot \mathbb{F}^\nu dV, \tag{C.4}$$

where $\hat{\mathbf{n}} = n_x \hat{x}, \ n_y \hat{y}$ is the outward-pointing boundary normal, and S indicates the domain surface and V indicates the volume. As for the advection-diffusion case, the last term of Eqn. (C.4) can generally be shown to be negative or zero. The EOBC is derived from the surface integral. $\hat{\mathbf{n}} \cdot \mathbb{F}$ is written as

$$\hat{\mathbf{n}} \cdot \mathbb{F} = \mathbb{A}_n \mathbf{Q} = \mathbb{R} \Lambda^n \mathbb{R}^\mathsf{T} \mathbf{Q}, \tag{C.5}$$

---

[1]Note that this is *sufficient*, but not *necessary*. R&S argue that the sufficient condition is appropriate for interface/boundary conditions.

[2]Generally, well-posedness of the linearized problem proves well-posedness of the nonlinear problem. Linearization is common in deriving BC such as the approximate Riemann BC discussed in Section 3.2.1.

where $\mathbb{A}_n = n_x \mathbb{A}_x + n_y \mathbb{A}_y$, Λ^n is a diagonal matrix, and the symmetric matrix, $\mathbb{R}$ is a unitary diagonalizing matrix. Introducing a vector of characteristic variables, $\mathbf{W} = \mathbb{R}^\intercal \mathbf{Q}$, a sufficient condition to ensure that the surface integral is negative or zero is written

$$-\frac{1}{2}\mathbf{W}^\intercal \Lambda^n \mathbf{W} + \mathbf{W}^\intercal \mathbb{R}^\intercal \mathbb{F}^\nu \cdot \hat{\mathbf{n}} \leq 0, \tag{C.6}$$

where the first term is the hyperbolic contribution and the latter is the dissipative contribution. As discussed in detail in R&S, this can be thought of as a set of independent equations. For the ith equation, if the corresponding component of Λ^n is negative ($\Lambda^{n,i} < 0$), $W^i = 0$ is a sufficient condition for well-posedness. If $\Lambda^{n,i} > 0$, the ith component of the dissipative contribution should be set to zero.

In the approximate Riemann open BC presented in Section 3.2.1, instead of setting $\mathbf{W}$ to zero, it is specified according to ambient conditions, and the dissipative contribution to the surface integral is ignored. By limiting the dissipative contribution at the boundary as required for well-posedness, an EOBC similar to Eqn. (C.6) could essentially extend the approximate Riemann open BC to accommodate dissipative effects in MHD. However, the challenge of simultaneous symmetrization must first be overcome.

C.2   The challenge of simultaneous symmetrization of dissipative MHD

Articles by Rahunanthan and Stanescu [61] and Hesthaven and Gottlieb [59] describe the procedure of simultaneous symmetrization (SS) for Navier-Stokes. Both articles refer to earlier work by Abarbanel and Gottlieb [124] (A&G). A&G generalize the SS problem to a system of n matrices that are each $m \times m$. They provide a clever, but somewhat specialized SS prescription that succeeds for Navier-Stokes. In future research, the approach of A&G could be used to attempt SS of dissipative MHD. The greater complexity of the MHD eigensystem as compared to Navier-Stokes further complicates the already mathematically challenging SS procedure. This work is left as a matter for future research.

Appendix D

REACTION COLLISION CROSS SECTION APPROXIMATIONS

D.1 Charge exchange cross section approximation

Resonant charge exchange (CX) cross sections, σ_{cx}, are generally weak functions of the relative speed of the interacting particles. An appropriate definition for V_{cx} is given in Eqn. (5.17) of Section 5.2.1. For H-H^+ resonant CX, many authors [84, 102, 125, 126, 127] have used theory-based fits of the form $\sigma_{cx,H} = [a + b \log_{10}(V_{cx})]^2$. However, cross section data for H-H^+ charge exchange from ORNL [128] is better fit with $\sigma_{cx,H} = 1.12 \times 10^{-18} - 7.15 \times 10^{-20} \ln(V_{cx})$ m^2. A similar fit for D-D^+ resonant CX yields $\sigma_{cx,D} = 1.09 \times 10^{-18} - 7.15 \times 10^{-20} \ln(V_{cx})$ m^2. For bombarding particle energies between 0.12 eV/amu and 10 keV/amu (where amu refers to atomic mass units – about 1 for hydrogen and 2 for deuterium), there is less than 10% deviation from the ORNL data.

Data for neon resonant CX is available in Smirnov [129] for bombarding particle energies between 0.1 and 1000 eV. In this range, using the same functional form as for resonant hydrogenic CX, the formula $\sigma_{cx,Ne} = -5.65 \times 10^{-20} \ln(V_{cx}) + 7.95 \times 10^{-19}$ m^2 agrees to within a few percent with the best fit curve through the experimental data given by Smirnov. The experimental data varies by up to 50% from the best fit curve.

D.2 Ionization and recombination cross section approximations

Voronov [130] provides the following fitting formula for the ionization rates of the first 28 elements (H through Ni):

$$\langle \sigma_{ion} v_e \rangle = A \times 10^{-6} \frac{1 + P * (\phi_{ion}/T_e)^{1/2}}{X + \phi_{ion}/T_e} \left(\frac{\phi_{ion}}{T_e} \right)^K e^{-\phi_{ion}/T_e} \text{ m}^3/\text{s}, \qquad \text{(D.1)}$$

where ϕ_{ion} and T_e are represented in the same energy units, and A, P, X, and K are constants tabulated for each element. Note that the constant A has units of cm^3/s such that $A \times 10^{-6}$ gives the overall formula units of m^3/s. Voronov [130] gives the range of

validity of the formula for each element. For ionization of hydrogen, the formula is accurate to within 5% of the recommended data for electron temperatures from 1 eV to 20 keV. For ionization of neon, the formula is accurate to within 25% of the recommended data for electron temperatures from 1 eV to 20 keV.

For ions with charge Z recombining from a ground state to charge state $Z - 1$, an approximate recombination rate is [131]

$$\langle \sigma_{rec} v_e \rangle = 2.6 \times 10^{-19} \frac{Z^2}{\sqrt{T_e}} \ \text{m}^3/\text{s}, \tag{D.2}$$

where T_e is in eV. According to McWhirter [131], the formula "may be relied on to $\pm 100\%$" for electron temperatures from 1 to 15 eV.

Appendix E

CHARGE EXCHANGE COLLISION INTEGRAL DETAILS

Details of the charge exchange collision integrals required for the plasma-neutral model derivation in Section 5.2 are given here. These integrals are performed using the approach described by Pauls et al. [84]. Under the assumption that the neutral gas distribution function is dominated by neutral-neutral scattering collisions, these integrals, and the integrals of recombination and ionization operators, are required as discussed in Section 5.2.1. In contrast, as discussed at the outset of Section 5.2.1, Helander et al. [98] assume a CX-dominated neutral distribution; thus, these CX collision operator integrals are not required for the Helander model, and are replaced by terms involving the non-Maxwellian perturbation of the distribution function found through a Chapman-Enskog-like analysis.

E.1 Charge exchange collision operator

Beginning with Eqn. (5.9) for the exact charge exchange (CX) collision operator,

$$C_i^{cx} = f_n \int \sigma_{cx} v_{rel} f_i(\mathbf{v}) d\mathbf{v} - f_i \int \sigma_{cx} v_{rel} f_n(\mathbf{v}) d\mathbf{v},$$

it is now shown that a suitable approximate collision operator, as given in Eqn. (5.15), is

$$C_i^{cx} \approx \sigma_{cx} \left(v_i^* n_i f_n - v_n^* n_n f_i \right).$$

Consider the first term on the right in the expression for C_i^{cx}. It represents the conversion of neutrals to ions and will be labeled C_i^{cx+}. Recall that $v_{rel} \equiv |\mathbf{v} - \mathbf{v}'|$. σ_{cx} is a weak function of v_{rel}, and can be removed from the integral with minimal error. (Approximations of σ_{cx} are discussed in Appendix D.1.) The integral can be evaluated analytically. A Maxwellian form for f_α is assumed – $f_\alpha = n_\alpha \left(\pi v_{T\alpha}^2 \right)^{-3/2} e^{-(\mathbf{v} - \mathbf{v}_\alpha)^2 / v_{T\alpha}^2}$, where n_α is the species number density, $v_{T\alpha}$ is the species thermal speed, and $\mathbf{v}_\alpha$ is the species bulk velocity. (The substitution $\mathbf{v} \equiv \mathbf{w} + \mathbf{v}_\alpha$ applies as usual.)

$$C_i^{cx+} = \sigma_{cx} f_n(\mathbf{v}') n_i (\pi v_{th}^2)^{-3/2} \int |\mathbf{v} - \mathbf{v}'| e^{-(\mathbf{v}-\mathbf{v}_i)^2/v_{Ti}^2} d\mathbf{v}, \tag{E.1}$$

Focusing on the integral, and substituting $\mathbf{w} = \mathbf{v} - \mathbf{v_i}$ and $\mathbf{x} = \mathbf{v}' - \mathbf{v_i}$,

$$\mathcal{I}(\mathbf{x}) = \int |\mathbf{w} - \mathbf{x}| e^{-\mathbf{w}^2/v_{Ti}^2} d\mathbf{w}. \tag{E.2}$$

Writing the integral in spherical coordinates, and defining $\xi \equiv cos(\theta) \equiv \frac{\mathbf{w} \cdot \mathbf{x}}{wx}$ (such that $-d\xi = sin(\theta)d\theta$), $x \equiv \frac{|\mathbf{x}|}{v_{Ti}}$, and $w \equiv \frac{|\mathbf{w}|}{v_{Ti}}$,

$$\mathcal{I}(x) = 2\pi v_{Ti}^4 \int_0^\infty \int_{-1}^1 e^{-w^2} (w^2 + x^2 - 2wx\xi)^{1/2} w^2 d\xi dw. \tag{E.3}$$

Defining $a \equiv w^2 + x^2$, and $b \equiv 2wx$, the inner integral over ξ is

$$\mathcal{I}_\xi(w, x) = \int_{-1}^1 (a - b\xi)^{1/2} d\xi. \tag{E.4}$$

Making the substitution $y \equiv a - b\xi$ (such that $d\xi = -dy/b$), and noting that at $\xi = -1$, $y = (w + x)^2$ and at $\xi = 1$, $y = (w - x)^2$,

$$\begin{aligned}
\mathcal{I}_\xi(w, x) &= \frac{1}{b} \int_{(w-x)^2}^{(w+x)^2} y^{1/2} dy = \frac{2}{3b} y^{3/2} \Big|_{(w-x)^2}^{(w+x)^2} \\
&= \frac{1}{3wx} [(w + x)^3 - |w - x|^3].
\end{aligned} \tag{E.5}$$

Now, returning to the full integral,

$$\mathcal{I}(x) = 2\pi v_{Ti}^4 \int_0^\infty e^{-w^2} \mathcal{I}_\xi(w, x) w^2 dw = \frac{2\pi v_{Ti}^4}{3x} [\mathcal{I}_1(x) + \mathcal{I}_2(x)], \tag{E.6}$$

where $\mathcal{I}_1(x)$ and $\mathcal{I}_2(x)$ are

$$\begin{aligned}
\mathcal{I}_1(x) &\equiv \int_0^x e^{-w^2} [(w + x)^3 - (x - w)^3] \\
&= 2 \int_0^x e^{-w^2} (3x^2 + w^2) w^2 dw
\end{aligned} \tag{E.7}$$

$$\begin{aligned}
\mathcal{I}_2(x) &\equiv \int_x^\infty e^{-w^2}\left[(w+x)^3 - (w-x)^3\right] \\
&= 2x\int_x^\infty e^{-w^2}(3w^2 + x^2)w\,dw
\end{aligned} \tag{E.8}$$

After integration and simplification, the answer is

$$\mathcal{I}(x) = \pi v_{Ti}^4\left[e^{-x^2} + \sqrt{\pi}\left(\frac{1}{2x} + x\right)\operatorname{erf}(x)\right], \tag{E.9}$$

where erf is the error function. Eqn. (E.1) for C_i^{cx+} can then be written

$$C_i^{cx+} = \sigma_{cx}f_n(\mathbf{v}')n_i v_{Ti}\left[\frac{e^{-x^2}}{\sqrt{\pi}} + \left(\frac{1}{2x} + x\right)\operatorname{erf}(x)\right], \tag{E.10}$$

or simply

$$C_i^{cx+} = \sigma_{cx}f_n n_i\langle v_{rel}\rangle_i. \tag{E.11}$$

A very good approximation for $\langle v_{rel}\rangle_i$ is v_i^*,

$$\langle v_{rel}\rangle_i \approx v_i^* \equiv v_{Ti}\sqrt{4/\pi + x^2}. \tag{E.12}$$

The final expression for C_i^{cx} is approximated by

$$C_i^{cx} \approx \sigma_{cx}\left(v_i^* n_i f_n - v_n^* n_n f_i\right). \tag{E.13}$$

Likewise, C_n^{cx} is expressed as

$$C_n^{cx} \approx \sigma_{cx}\left(v_n^* n_n f_i - v_i^* n_i f_n\right). \tag{E.14}$$

E.2 0th moment of CX collision term

The 0th moment of the CX collision term is

$$\int C_i^{cx}d\mathbf{v} \approx \int \sigma_{cx}\left(v_i^* n_i f_n - v_n^* n_n f_i\right)d\mathbf{v}. \tag{E.15}$$

It is now shown that the terms on the RHS can be approximated as

$$\int \sigma_{cx} v_i^* n_i f_n = \int \sigma_{cx} v_n^* n_n f_i \approx \Gamma^{cx} \equiv \sigma_{cx} n_i n_n \sqrt{\frac{4}{\pi} v_{Ti}^2 + \frac{4}{\pi} v_{Tn}^2 + v_{in}^2} \equiv \sigma_{cx} n_i n_n V_{cx}, \quad (E.16)$$

where V_{cx} is the representative speed of CX collisions. Consider the first term on the right of Eqn. (E.15), which represents net conversion of neutrals to ions. Substituting $v_i^* \equiv v_{Ti}\sqrt{4/\pi + x^2}$, where $x = |\mathbf{v}_i - \mathbf{v}|/v_{Ti}$,

$$\int C_i^{cx+} d\mathbf{v} \approx \int \sigma_{cx} n_i f_n(\mathbf{v}) v_{Ti} \sqrt{4/\pi + x^2} d\mathbf{v}. \quad (E.17)$$

Expressing $\mathbf{v}$ as the sum of random and fluid velocities, $\mathbf{v} = \mathbf{w} + \mathbf{v_n}$, and inserting a maxwellian for f_n,

$$\int C_i^{cx+} d\mathbf{v} \approx (\pi v_{Tn}^2)^{-3/2} \sigma_{cx} n_i n_n v_{Tn} \int e^{-\mathbf{w}^2/v_{Tn}^2} \sqrt{\frac{4}{\pi} \frac{v_{Ti}^2}{v_{Tn}^2} + \frac{\mathbf{w}^2 + v_{in}^2 - 2\mathbf{w} \cdot \mathbf{v}_{in}}{v_{Tn}^2}} d\mathbf{w}. \quad (E.18)$$

Using spherical coordinates, and defining $\xi \equiv cos(\theta) \equiv \frac{\mathbf{w} \cdot \mathbf{v}_{in}}{w v_{in}}$ (such that $-d\xi = sin(\theta)d\theta$), $w \equiv \frac{|\mathbf{w}|}{v_{Tn}}$, and $v_{in} \equiv |\mathbf{v}_{in}|$,

$$\int C_i^{cx+} d\mathbf{v} \approx \frac{2}{\sqrt{\pi}} \sigma_{cx} n_i n_n v_{Tn} \int_0^\infty w^2 e^{-w^2} \int_{-1}^1 \left(\frac{4}{\pi} \frac{v_{Ti}^2}{v_{Tn}^2} + w^2 + \frac{v_{in}^2}{v_{Tn}^2} - \frac{2w v_{in}}{v_{Tn}} \xi \right)^{1/2} d\xi dw. \quad (E.19)$$

Defining $a^2 \equiv \frac{4}{\pi} \frac{v_{Ti}^2}{v_{Tn}^2}$, $b^2 \equiv \frac{v_{in}^2}{v_{Tn}^2}$, and $y_\pm \equiv a^2 + (w \pm b)^2$, the inner integral over ξ is

$$\int_{-1}^1 \left(a^2 + w^2 + b^2 - 2wb\xi \right)^{1/2} d\xi = \frac{1}{3bw} \left(y_+^{3/2} - y_-^{3/2} \right). \quad (E.20)$$

The whole integral is then

$$\int C_i^{cx+} d\mathbf{v} \approx \sigma_{cx} n_i n_n \frac{2}{3\sqrt{\pi}} \frac{v_{Tn}^2}{v_{in}} \int_0^\infty w e^{-w^2} \left(y_+^{3/2} - y_-^{3/2} \right) dw \quad (E.21)$$

According to Pauls et al. [84], an appropriate approximation is

$$\int C_i^{cx+} d\mathbf{v} \approx \Gamma^{cx} \equiv \sigma_{cx} n_i n_n \sqrt{\frac{4}{\pi} v_{Ti}^2 + \frac{4}{\pi} v_{Tn}^2 + v_{in}^2} \equiv \sigma_{cx} n_i n_n V_{cx}. \quad (E.22)$$

Numerical testing shows that this approximation is accurate to $< 3\%$.

E.3 1st *moment of CX collision term*

Consider the integral required to specify the frictional momentum transfer term, $\mathbf{R}_{in}^{cx} \equiv m_i \sigma_{cx} n_i \int \mathbf{w} v_i^* f_n d\mathbf{v}$. Substituting for v_i^* and f_n as in Appendix E.2,

$$\mathbf{R}_{in}^{cx} = m_i(\pi v_{Tn}^2)^{-3/2}\sigma_{cx}n_i n_n v_{Tn} \int \mathbf{w} e^{-w^2/v_{Tn}^2}\sqrt{\frac{4}{\pi}\frac{v_{Ti}^2}{v_{Tn}^2} + \frac{\mathbf{w}^2 + \mathbf{v}_{in}^2 - 2\mathbf{w}\cdot\mathbf{v}_{in}}{v_{Tn}^2}}d\mathbf{w}. \quad \text{(E.23)}$$

Using spherical coordinates, and defining $\xi \equiv cos(\theta) \equiv \frac{\mathbf{w}\cdot\mathbf{v}_{in}}{wv_{in}}$ (such that $-d\xi = sin(\theta)d\theta$), $w \equiv \frac{|\mathbf{w}|}{v_{Tn}}$, and $v_{in} \equiv |\mathbf{v}_{in}|$),

$$\mathbf{R}_{in}^{cx} = m_i\frac{\mathbf{v}_{in}}{v_{in}}\frac{2}{\sqrt{\pi}}\sigma_{cx}n_i n_n v_{Tn}^2 \int_0^\infty w^3 e^{-w^2}\int_{-1}^1 \xi\sqrt{\frac{4}{\pi}\frac{v_{Ti}^2}{v_{Tn}^2} + w^2 + \frac{v_{in}^2}{v_{Tn}^2} - \frac{2wv_{in}\xi}{v_{Tn}}}d\xi dw. \quad \text{(E.24)}$$

Defining $a^2 \equiv \frac{4}{\pi}\frac{v_{Ti}^2}{v_{Tn}^2}$, and $b^2 \equiv \frac{v_{in}^2}{v_{Tn}^2}$, the inner integral over ξ is

$$I_\xi = \int_{-1}^1 \xi\sqrt{a^2 + w^2 + b^2 - 2wb\xi}d\xi. \quad \text{(E.25)}$$

Substituting $\eta = a^2 + w^2 + b^2 - 2wb\xi$ such that $d\xi = -d\eta/(2wb)$ and $\xi = -(\eta - a^2 - w^2 - b^2)/(2wb)$,

$$I_\xi = \frac{1}{(2wb)^2}\int_L^U \eta^{3/2} - (a^2 + w^2 + b^2)\eta^{1/2}d\eta, \quad \text{(E.26)}$$

where $L \equiv a^2 + w^2 + b^2 + 2wb$ and $U \equiv a^2 + w^2 + b^2 - 2wb$. Then, defining $y_\pm \equiv a^2 + (w \pm b)^2$,

$$I_\xi = \frac{1}{3bw}\left[\frac{1}{5bw}\left(y_+^{5/2} - y_-^{5/2}\right) - y_+^{3/2} - y_-^{3/2}\right]. \quad \text{(E.27)}$$

The whole integral is then

$$\mathbf{R}_{in}^{cx} = m_i\frac{\mathbf{v}_{in}}{v_{in}}\frac{2}{3\sqrt{\pi}}\sigma_{cx}n_i n_n \frac{v_{Tn}^3}{v_{in}}\int_0^\infty w^2 e^{-w^2}\left[\frac{1}{5bw}\left(y_+^{5/2} - y_-^{5/2}\right) - y_+^{3/2} - y_-^{3/2}\right]dw. \quad \text{(E.28)}$$

According to Pauls et al. [84], an appropriate approximation is

$$\mathbf{R}_{in}^{cx} \approx -m_i\sigma_{cx}n_i n_n \mathbf{v}_{in}v_{Tn}^2\left[4\left(\frac{4}{\pi}v_{Ti}^2 + v_{in}^2\right) + \frac{9\pi}{4}v_{Tn}^2\right]^{-1/2}. \quad \text{(E.29)}$$

E.4 2nd moment of CX collision term

Consider the integral required to specify the random thermal energy, $Q_{in}^{cx} \equiv \frac{1}{2}\sigma_{cx}m_i \int \mathbf{w}^2 n_i v_i^* f_n d\mathbf{v}$. Taking an approach very similar to that of Appendix E.2,

$$Q_{in}^{cx} = \sigma_{cx}m_i n_i n_n \frac{2}{6\sqrt{\pi}} \frac{v_{Tn}^4}{v_{in}} \int_0^\infty w^3 e^{-w^2} \left(y_+^{3/2} - y_-^{3/2} \right) dw. \tag{E.30}$$

According to Pauls et al. [84], an appropriate approximation is

$$Q_{in}^{cx} \approx \sigma_{cx}m_i n_i n_n \frac{3}{4} v_{Tn}^2 \sqrt{\frac{4}{\pi}v_{Ti}^2 + \frac{64}{9\pi}v_{Tn}^2 + v_{in}^2}. \tag{E.31}$$

Appendix F

PLASMA-NEUTRAL PRESSURE EQUATION DERIVATION

Repeating Eqn. (5.63), the equation for plasma fluid energy evolution is

$$
\frac{\partial \varepsilon}{\partial t} + \nabla \cdot (\varepsilon \mathbf{v} + \mathbf{v} \cdot (p\mathbb{I} + \pi) + \mathbf{h}) =
$$
$$
\mathbf{j} \cdot \mathbf{E} + \mathbf{v} \cdot \mathbf{R}_i^{in} + \mathbf{v} \cdot \mathbf{R}_e^{en} + Q_i^{in} + Q_e^{en}
$$
$$
+ \Gamma_i^{ion} \left(\frac{1}{2} m_i \mathbf{v}_n^2 - \phi_{ion} \right) + Q_i^{ion} - \Gamma_n^{rec} \frac{1}{2} m_i \mathbf{v}^2 - Q_n^{rec}
$$
$$
+ \Gamma^{cx} \frac{1}{2} m_i \left(\mathbf{v}_n^2 - \mathbf{v}^2 \right) + \mathbf{v}_n \cdot \mathbf{R}_{in}^{cx} - \mathbf{v} \cdot \mathbf{R}_{ni}^{cx} + Q_{in}^{cx} - Q_{ni}^{cx}. \tag{F.1}
$$

The plasma fluid energy evolution, $\frac{\partial \varepsilon}{\partial t}$, can be written out as evolution of internal and kinetic energies: $\frac{\partial}{\partial t}(\frac{1}{\gamma-1}p + \frac{1}{2}m_i n\mathbf{v}^2)$. To identify the kinetic energy evolution, the plasma momentum equation, Eqn. (5.60), is dotted with $\mathbf{v}$:

$$
\mathbf{v} \cdot \left[\frac{\partial}{\partial t}(m_i n\mathbf{v}) + \nabla \cdot (m_i n\mathbf{v}\mathbf{v} + p\mathbb{I} + \pi) = \right.
$$
$$
\mathbf{j} \times \mathbf{B} + \mathbf{R}_i^{in} + \mathbf{R}_e^{en} + \Gamma_i^{ion} m_i \mathbf{v}_n - \Gamma_n^{rec} m_i \mathbf{v} + \Gamma^{cx} m_i (\mathbf{v}_n - \mathbf{v})
$$
$$
\left. + \mathbf{R}_{in}^{cx} - \mathbf{R}_{ni}^{cx} \right]. \tag{F.2}
$$

Using vector identities [132], it can be shown that $\mathbf{v} \cdot [\nabla \cdot (m_i n\mathbf{v}\mathbf{v})] = \nabla \cdot (\frac{1}{2}m_i n\mathbf{v}\mathbf{v}^2) + \frac{1}{2}m_i \mathbf{v}^2 \nabla \cdot (n\mathbf{v})$. Also, $\mathbf{v} \cdot [\frac{\partial}{\partial t}(m_i n\mathbf{v})] = \frac{\partial}{\partial t}(\frac{1}{2}m_i n\mathbf{v}^2) + m_i \frac{1}{2}\mathbf{v}^2 \frac{\partial n}{\partial t}$. Using these relations and using the plasma continuity equation, Eqn. (5.58), to replace $m_i \frac{1}{2}\mathbf{v}^2[\frac{\partial n}{\partial t} + \nabla \cdot (n\mathbf{v})]$ with $m_i \frac{1}{2}\mathbf{v}^2(\Gamma_i^{ion} - \Gamma_n^{rec})$, the kinetic energy evolution is found to be

$$
\frac{\partial}{\partial t}\left(\frac{m_i n\mathbf{v}^2}{2} \right) + \nabla \cdot \left(\frac{m_i n\mathbf{v}^2\mathbf{v}}{2} \right) = -\mathbf{v} \cdot [\nabla \cdot (p\mathbb{I} + \pi)] + \mathbf{v} \cdot (\mathbf{j} \times \mathbf{B})
$$
$$
+ \mathbf{v} \cdot (\mathbf{R}_i^{in} + \mathbf{R}_e^{en}) + \Gamma_i^{ion} m_i (\mathbf{v} \cdot \mathbf{v}_n - \frac{1}{2}\mathbf{v}^2) - \Gamma_n^{rec} m_i \frac{1}{2}\mathbf{v}^2
$$
$$
+ \Gamma^{cx} m_i (\mathbf{v} \cdot \mathbf{v}_n - \mathbf{v}^2) + \mathbf{v} \cdot (\mathbf{R}_{in}^{cx} - \mathbf{R}_{ni}^{cx}). \tag{F.3}
$$

Subtracting the kinetic energy evolution from Eqn. (F.1), gives an equation for the plasma pressure evolution,

$$\frac{1}{\gamma-1}\frac{\partial p}{\partial t} + \nabla \cdot (\frac{\gamma}{\gamma-1}p\mathbf{v} + \mathbf{v}\cdot\pi + \mathbf{h}) = \mathbf{v}\cdot[\nabla\cdot(p\mathbb{I}+\pi)] + \mathbf{j}\cdot\mathbf{E} - \mathbf{v}\cdot(\mathbf{j}\times\mathbf{B})$$
$$+ Q_i^{in} + Q_e^{en} + \Gamma_i^{ion}\left(\frac{1}{2}m_i\mathbf{v}_n^2 + \frac{1}{2}m_i\mathbf{v}_i^2 - m_i\mathbf{v}_i\cdot\mathbf{v}_n - \phi_{ion}\right) + Q_i^{ion} - Q_n^{rec}$$
$$+ \Gamma^{cx}m_i\left(\frac{1}{2}\mathbf{v}_n^2 + \frac{1}{2}\mathbf{v}^2 - \mathbf{v}\cdot\mathbf{v}_n\right) + \mathbf{v}_n\cdot\mathbf{R}_{in}^{cx} - \mathbf{v}\cdot\mathbf{R}_{in}^{cx} + Q_{in}^{cx} - Q_{ni}^{cx}. \qquad \text{(F.4)}$$

Appendix G

PLASMA-NEUTRAL MODEL TRANSPORT CONSIDERATIONS

In Section 5.3, which presents the HiFi plasma-neutral model implementation, the coefficients used for neutral thermal conductivity, κ_n, are discussed. Two options for κ_n are presented. The first, $\kappa_{n,hs}$, is derived using a Chapman-Enskog-like approach [11, 101] assuming neutral-neutral scattering is the leading order term in the neutral Boltzmann equation. The second, $\kappa_{n,cx-hs}$, is an approximation of the physical thermal conductivity expected when CX and neutral-neutral scattering share the role of dominance in the neutral Boltzmann equation. The issue of properly modeling neutral heat flux motivates the general discussion of transport given in this appendix.

In addition to specifically considering neutral heat flux, this appendix aims to illuminate the challenge of formally deriving transport terms. Section G.1 sketches a Chapman-Enskog-like procedure for formally deriving transport terms for the plasma-neutral model. In Section G.2, the model derived by Helander et al. [98] for partially ionized plasma is discussed with attention to the transport terms that they find. In Section G.3, the two neutral heat flux options implemented in HiFi — $\mathbf{q}_{n,hs} = \kappa_{n,hs}\nabla T_n$ and $\mathbf{q}_{n,cx-hs} = \kappa_{n,cx-hs}\nabla T_n$ — are compared to the neutral heat flux derived by Helander et al. Finally, implications of these transport considerations are summarized in Section G.4.

G.1 Approach for exactly deriving transport coefficients

Transport coefficients for the plasma-neutral model may be formally derived by extending the Chapman-Enskog approach to include reaction effects. A sketch of this procedure, presented here, gives insight into the impact of reaction physics on transport. The plasma-neutral model derivation is shown in Section 5.2; the variable definitions made there are not repeated here. Defining the operator $\mathscr{D} \equiv \frac{\partial}{\partial t} + \mathbf{v} \cdot \nabla_{\mathbf{x}} + \mathbf{a} \cdot \nabla_{\mathbf{v}}$, Eqn. (5.2) can be written as

$$\mathscr{D}(f_\alpha) = \frac{\partial f_\alpha}{\partial t}\bigg|_{collisions} = C_\alpha^{scat.} + C_\alpha^{react.}, \tag{G.1}$$

Fluid equations are found by taking moments of Eqn. (5.2). Where the distribution function deviates slightly from a Maxwellian, significant effects can arise such as viscous and thermal transport. To close the system of fluid equations, these non-Maxwellian effects must be quantified. Following the Chapman-Enskog closure procedure, the distribution function, f_α is expanded as

$$f_\alpha = f_\alpha^0 + f_\alpha^1 + f_\alpha^2 + \cdots, \tag{G.2}$$

where f_α^0 is Maxwellian, and the additional terms represent higher-order perturbations. Using only the Maxwellian and the 1st-order perturbation in Eqn. (G.1),

$$\mathscr{D}(f_\alpha^0 + f_\alpha^1) = C_\alpha^{scat.}(f^0 + f^1, f^0 + f^1) + C_\alpha^{react.}(f^0 + f^1, f^0 + f^1). \tag{G.3}$$

If the scattering collision terms are assumed dominant, the 0th-order equation for species α is

$$C_\alpha^{scat.}(f^0, f^0) = 0. \tag{G.4}$$

This is the formal approach used in this research. Other orderings are possible. For example, Helander et al. [98] choose an ordering such that, for the neutral Boltzmann equation, the 0th-order equation is $C_n^{CX}(f_n^0, f_i^0) = 0$ — i.e., CX is the dominant term. (The work of Helander et al. is summarized in Section G.2.) Another possible ordering for the neutral equation gives $C_n^{scat.}(f_n^0, f_n^0) + C_n^{CX}(f_n^0, f_i^0) = 0$ — i.e., neutral-neutral scattering and CX are the two lowest order terms.

Assuming that the ordering assumption that gives Eqn. (G.4) is made (for all species), the approach of Chapman and Cowling [101] for a single species gas is now generalized. The 1st order equation with reactions is

$$\mathbf{L}f_\alpha^1 = \mathscr{D}f_\alpha^0 - C_\alpha^{react.}(f^0, f^0), \tag{G.5}$$

where **L** represents a linear operator giving $\mathbf{L}f_\alpha^1 = C_\alpha^{scat.}(f^0, f^1)$. The terms $\mathscr{D}f_\alpha^1$, $C_\alpha^{react.}(f^0, f^1)$, $C_\alpha^{react.}(f^1, f^1)$, and $C_\alpha^{scat.}(f^1, f^1)$ are neglected as small perturbations. It is Eqn. (G.5) that must be solved to determine the correction terms, f_α^1, which, in turn, allow specification of the transport terms. Solving the system now involves 0th-order reaction terms, $C_\alpha^{react.}(f^0, f^0)$, that are not present when considering a non-reacting gas.

Viscous and thermal fluxes are represented as stress tensors ($\boldsymbol{\pi}_\alpha$) and heat fluxes ($\mathbf{q}_\alpha$),

$$\boldsymbol{\pi}_\alpha = \rho_\alpha \int (\mathbf{w}\mathbf{w} - \frac{1}{3}w^2\mathbb{I})f_\alpha^1 d^3\mathbf{w}, \tag{G.6}$$

and

$$\mathbf{q}_\alpha = \frac{1}{2}\rho_\alpha \int \mathbf{w}^2 w f_\alpha^1 d^3\mathbf{w}. \tag{G.7}$$

Note that the Maxwellians, f_α^0, make no contribution to the stress tensors and heat fluxes because, as seen in Eqns. (G.6) and (G.7), the integrals are odd in velocity space such that only asymmetric perturbations to the distribution functions are important. Similarly, only asymmetric contributions by the terms on the right-hand side of Eqn. (G.5) can cause transport. For example, the term $\mathscr{D}f_\alpha^0$ includes the effects of temperature and velocity gradients that can cause distribution function asymmetries. Assuming that their cross sections depend only on the electron random velocity, ionization and recombination only give symmetric contributions. Resonant charge exchange can give an asymmetric contribution if there is a relative velocity between the plasma and neutral species. This effect is assumed to be negligible in this research.

G.2 Summary of transport derivations by Helander et al.

Helander et al. [98] derive a model for evolution of ion and neutral fluids in a partially ionized gas. They state that a particular application of their research is a model for tokamak edge physics. By choosing an ordering that makes the CX collision term dominant in the neutral distribution function, they show that the Maxwellian component of the expanded neutral distribution function is $f_n^0 = (n_n/n_i)f_i^0$, where n_i is the ion number density and f_i^0 is the Maxwellian component of the ion distribution. They employ a Chapman-Enskog solution

procedure separately for the ion distribution (f_i) and neutral distribution (f_n). Separate solutions are possible because the kinetic equations for f_i and f_n decouple under their ordering assumption. This decoupling is established in earlier work by Catto [133].

For the ion fluid, the heat flux is identified as

$$\mathbf{q}_{i,H} = \frac{n_i + n_n}{n_i}\mathbf{q}_{i,B},\qquad(G.8)$$

where the subscripts "H" and "B" refer to Helander and Braginskii respectively. Assuming that the neutral density is a small fraction of the ion density, the Helander heat flux is approximately equal to the Braginskii heat flux. A similar result is found for the ion stress tensor: $\pi_{i,H} = \frac{n_i + n_n}{n_i}\pi_{i,B}$.

For the neutral fluid, the heat flux is

$$\mathbf{q}_{n,H} = \frac{n_n}{n_i}\mathbf{q}_{i,H} - 2.40\left(\frac{n_n k_B T}{m_i \nu_{cx}}\right)k_B \nabla T - 0.24 n_n k_B T(\mathbf{v}_n - \mathbf{v}_i),\qquad(G.9)$$

where T is the combined ion-neutral fluid temperature and ν_{cx} is the CX frequency. (See definition of ν_{cx} in Section 5.3.) The neutral stress tensor is similar. Another important result of Helander et al. is that evolution equations are not required for neutral fluid momentum and energy. Instead, T_n and $\mathbf{v}_n$ are determined as functions of the remaining variables.

The primary result of Helander et al. is their set of equations 30, which give the combined ion-neutral fluid evolution. A secondary result is the set of equations 33, describing the neutral fluid evolution. (As discussed above, these neutral fluid evolution equations are superfluous, but are given to facilitate comparison to other models.) It should be noted that, in their equations 33, the moments of ionization and recombination collision operators are present, but moments of the CX collision operator are not. Because their ordering assumption implies that $C_n^{cx}(f_n^0, f_i^0) = 0$, CX effects arise only through transport effects due to the non-Maxwellian component of the distribution functions. In contrast, for the two-fluid plasma-neutral model derived in Section 5.2.1, moments of ionization, recombination, and CX are all required.

The model derived by Helander et al. is fundamentally different than the plasma-neutral

model implemented in HiFi as discussed in Section 5.3 and derived in Section 5.2. A primary difference is that the HiFi plasma-neutral model separately evolves plasma and neutral momenta and energies whereas, in the Helander model, the neutral distribution is closely related to the ion distribution and is not separately evolved. In the HiFi plasma-neutral model, assuming that neutral temperature and velocity are similar to plasma temperature and velocity[1], the transport results of Helander et al. provide useful guidance for specifying transport in the HiFi plasma-neutral model.

G.3 Comparison of neutral heat fluxes

The neutral heat flux derived by Helander et al., $\mathbf{q}_{n,H}$, will be compared with the two neutral heat flux options in the HiFi plasma-neutral implementation — $\mathbf{q}_{n,hs}$ and $\mathbf{q}_{n,cx-hs}$. The assumptions implicit in deriving $\mathbf{q}_{n,H}$ and $\mathbf{q}_{n,hs}$ are discussed in Sections G.1 and G.2. Before presenting the comparison of the three terms, the intuition behind the *ad hoc* heat flux $\mathbf{q}_{n,cx-hs}$ is described.

As presented in Section 5.3, when neutral-neutral scattering is assumed dominant in the neutral Boltzmann equation, the thermal conductivity is $\kappa_n \propto n_n T_n / \nu_{hs}$, where ν_{hs} is the neutral-neutral scattering frequency, defined as $\nu_{hs} \equiv \bar{C}\pi d^2 n_n$. The mean-free path and scattering frequency are related by $\nu_{hs} = \bar{C}/\lambda_{hs}$, where $\bar{C} \equiv \sqrt{8k_b T_n/(\pi m_n)}$ is the mean velocity. The thermal conductivity can be related to mean-free path as $\kappa_n \propto n_n T_n \lambda_{hs}/\bar{C} \propto n_n \bar{C}\lambda_{hs}$. If an ion species with approximately the same temperature as the neutral gas is assumed, the mean-free path may be estimated as $\lambda_{cx-hs} = (n\sigma_{cx} + n_n\sigma_{hs})^{-1}$, where n is the plasma number density. Similarly, a modified frequency accounting for CX is $\nu_{cx-hs} = \bar{C}/\lambda_{cx-hs}$, which is equivalent to $\nu_{cx-hs} = \nu_{cx} + \nu_{hs}$. It is this frequency that is used in the definition of κ_{cx-hs} in Eqn. (5.82).

The three neutral heat fluxes to be compared are

$$\mathbf{q}_{hs} = \kappa_{n,hs}\nabla T \ \frac{\text{W}}{\text{m}^2}, \qquad (\text{G.10})$$

---

[1]In fact, when CX is dominant, the direct transfer of energy and momentum due to the moments of the CX collision operator described in Section 5.2.1 strongly couple the plasma and neutral temperatures and momenta.

$$\mathbf{q}_{cx-hs} = \kappa_{n,cx-hs} \nabla T \ \frac{\text{W}}{\text{m}^2}, \text{ and} \qquad (\text{G}.11)$$

$$\mathbf{q}_H = \frac{n_n(n_n + n)}{n^2} \mathbf{q}_{i,B} - 2.40 \left(\frac{n_n T_n}{m_i \nu_{cx}} \right) \nabla T - 0.24 n_n k_B T (\mathbf{v}_n - \mathbf{v}) \ \frac{\text{W}}{\text{m}^2}, \qquad (\text{G}.12)$$

where the usual subscript "n" on the heat fluxes has been dropped for readability, and it is assumed that $T \approx T_i \approx T_n$. The formulas for $\kappa_{n,hs}$ and $\kappa_{n,cx-hs}$ are given earlier in Eqns. (5.81) and (5.82). To repeat,

$$\kappa_{n,hs} = \frac{5}{2} \frac{k_b}{m_n} \frac{n_n k_b T_n}{\nu_{hs}} \ \frac{\text{W}}{\text{m eV}},$$

and

$$\kappa_{n,cx-hs} = \frac{5}{2} \frac{k_b}{m_n} \frac{n_n k_b T_n}{\nu_{cx-hs}} \ \frac{\text{W}}{\text{m eV}}.$$

In the comparisons given in this section, attention will be restricted to the component of heat flux perpendicular to the magnetic field. The perpendicular Braginskii ion heat flux is

$$q_{i,B\perp} = \frac{3.35 \times 10^{-6}}{\ln\Lambda \sqrt{m_i m_p}} T^{5/2} k_B \frac{\gamma^1 x^2 + \gamma^0}{\Delta} \nabla_\perp T \ \frac{\text{W}}{\text{m}^2}, \qquad (\text{G}.13)$$

where the formula is taken from Braginskii [11], and modified for SI units. $\ln\Lambda = 10$ is assumed, m_p is proton mass, $k_B = 1.602 \times 10^{-19}$ J/eV is Boltzmann's constant, and temperatures are in eV. $x = \omega_{ci}\tau_i$, where ω_{ci} is the ion cyclotron frequency and τ_i is the ion-ion collision frequency, and $\Delta = x^4 + \delta^1 x^2 + \delta^0$. $\gamma^0 = 2.645$, $\gamma^1 = 2$, $\delta^0 = 0.677$, and $\delta^1 = 2.7$. ω_{ci} and τ_i are as defined by Braginskii.

The parameters of HIT-SI [134], a magnetic plasma confinement experiment at the University of Washington, are used for the plotted comparisons given here. Such parameters are appropriate for this research, which is largely motivated by university-scale magnetic plasma confinement experiments. The assumed characteristic magnetic field is 0.03 T, length is 0.1 m, plasma density is $n = 10^{19}$ m^{-3}, and temperature is 10 eV. Thus, the characteristic

temperature gradient is 100 eV/m. Plots are made for two neutral densities: 10^{18} and 10^{20} m^{-3}. The relative velocity between the plasma and neutral species is assumed to be $0.1\bar{C}$.

Perpendicular heat flux is of particular interest in magnetic confinement experiments; only the perpendicular components are plotted in the following comparisons. At the HIT-SI parameters given above, for temperature ranging from 1 eV to 10 eV, Figure G.1 shows the neutral heat flux based on a hard-sphere model, the combined CX/hard-sphere model, and the Helander model; these are labeled q_hs, $q\_cx\text{-}hs$, and q_Htot, respectively. The Helander heat flux is split into the contributions from the first, second, and third terms on the right side of Eqn. (G.12); these are labeled q_H1, q_H2, and q_H3, respectively. As seen, $q\_cx\text{-}hs$ appropriately limits the heat flux whereas q_hs allows unrealistically high heat flux because CX effects are ignored. Physically, high CX frequency is associated with short neutral mean-free path. A shorter mean-free path is intuitively associated with reduced thermal diffusion. The heat flux given by $q\_cx\text{-}hs$ shows this expected reduction in thermal heat flux. The terms q_H1 and q_H2, which contain physics that not captured in $q\_cx\text{-}hs$, are not crucial and $q\_cx\text{-}hs$ reasonably approximates q_Htot.

The perpendicular heat fluxes when the neutral density is increased to $n_n = 10n = 10^{20}$ m^{-3} are plotted in Figure G.2. In this case, $q\_cx\text{-}hs$ appropriately limits the heat flux whereas q_Htot is unrealistically high because neutral-neutral elastic collisions are ignored. Just as high CX frequency limits the mean-free path in the case with $n_n = 10^{19}$ m^{-3}, high neutral-neutral scattering limits the mean-free path in this case. $q\_cx\text{-}hs$ reasonably approximates q_hs which is valid in this regime. In HIT-SI, this regime may exist only in a thin sheath near the wall; it is, however, an important regime relevant in many other applications such as the ELF thruster described in Section 6.4 and supersonic gas injection for tokamak-like magnetic confinement devices [81].

Perpendicular heat transport is expected to be a leading effect in magnetic confinement and the heat flux $\mathbf{q}_{cx-hs}$ qualitatively captures the physical effects present in $\mathbf{q}_H$ in the CX-dominated regime. A similar term π_{cx-hs} is not pursued in this research.
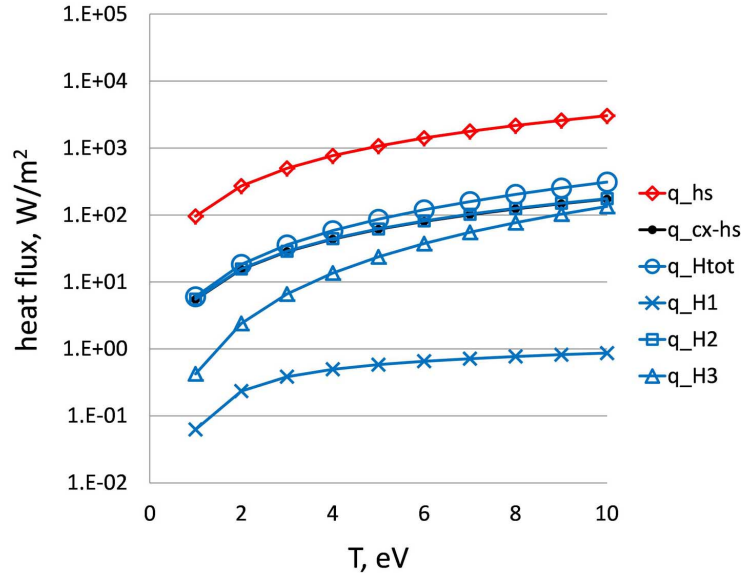
Figure G.1: Plot of perpendicular heat flux vs. T for CX-dominated regime using HIT-SI parameters. q_hs, $q\_cx\text{-}hs$, and q_Htot are the heat fluxes given by Eqns. (G.10), (G.11), and (G.12), respectively. The flux from the Helander model is split into three terms, q_H1, q_H2, and q_H3, corresponding to the first, second, and third terms on the right side of Eqn. (G.12). In this case, q_hs is unrealistically high because it does not account for CX collisions, which limit the neutral mean-free path in this case. An alternative option in the HiFi plasma-neutral model, represented here by $q\_cx\text{-}hs$, is similar to q_Htot which is derived formally for this regime, and captures CX collision effects.
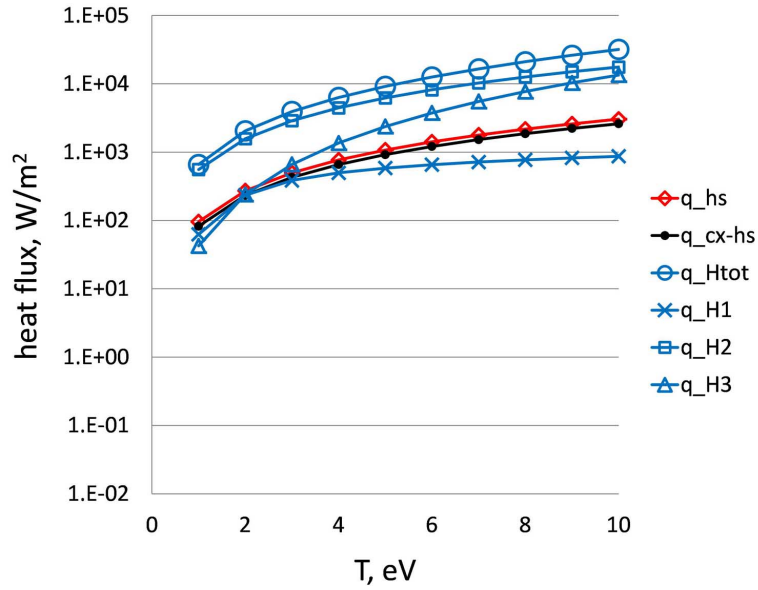
Figure G.2: Plot of perpendicular heat flux vs. T for neutral-neutral elastic-collision-dominated regime using HIT-SI parameters, but with $n_n = 10^{20}$ m^{-3}. q_hs, $q\_cx\text{-}hs$, and q_Htot are the heat fluxes given by Eqns. (G.10), (G.11), and (G.12), respectively. The flux from the Helander model is split into three terms, q_H1, q_H2, and q_H3, corresponding to the first, second, and third terms on the right side of Eqn. (G.12). In this case, q_Htot is unrealistically high because it does not account for neutral-neutral scattering collisions, which limit the neutral mean-free path in this case. $q\_cx\text{-}hs$ closely matches the physically expected heat flux, q_hs.

G.4 Summary

There is significant room for developing extensions and improvements of the transport effects included in the plasma-neutral model. The most obvious areas for improvement are the heat flux and stress tensor closures, but other terms could also be included. Researchers who wish to apply the plasma-neutral model should understand the relevant material, including the references given, and either verify that the implemented transport options are acceptable, or develop new options that ensure the validity of their simulations.

VITA

Eric Meier was born in Shreveport, Louisiana, and spent much of his childhood in Nacogdoches, Texas. At age 13, he moved with his family to Salt Lake City, Utah. In high school, he enjoyed mountain recreation in Utah, played many sports including wrestling and tennis, and developed a strong interest in physics and mathematics. He earned a BS in mechanical engineering at the University of Utah in 2000. His first job after graduating was with an aerospace company presently called Aerojet in Redmond, Washington. After two years at Aerojet, he and a fellow engineer formed Space Transport Corporation (STC) with the primary goal of capturing the Ansari X Prize. Though STC fell short of this goal, and was ultimately dissolved, the experience instilled in Eric a passion for scientific research. In 2005, he joined the Department of Aeronautics and Astronautics at the University of Washington, where he earned a MS and PhD specializing in computational plasma science.